Novel atom interferometry techniques for a cold-atom gyroscope of large Sagnac area

Matteo Altorio

SORBONNE UNIVERSITÉ
CRÉATEURS DE FUTURS DEPUIS 1257

l'Observatoire de Paris — SYRTE
Systèmes de Référence Temps-Espace

THÈSE DE DOCTORAT
DE SORBONNE UNIVERSITE

Spécialité : Physique

École doctorale n°: Physique en Île-de-France

réalisée

au SYRTE - Observatoire de Paris

sous la direction de Arnaud LANDRAGIN

présentée par

Matteo ALTORIO

pour obtenir le grade de :

DOCTEUR DE SORBONNE UNIVERSITE

Sujet de la thèse :

Novel atom interferometry techniques for a cold-atom gyroscope of large Sagnac area

soutenue le 4 Decembre 2019

devant le jury composé de :

M.	Achim PETERS	Rapporteur
M.	Gabriel DUTIER	Rapporteur
M^{me}	Agnes MAITRE	Examinatrice
M.	Patrick CHEINET	Examinateur
M.	Remi GEIGER	Encadrant de thèse
M.	Arnaud LANDRAGIN	Directeur de thèse

Acknowledgments

I wanna take this space to thank everyone who was a part of my journey in these last three years.

I wanna thank Achim Peters and Gabriel Dutier for having accepted to be the referees for this manuscript and to Agnes Maitre and Patrick Cheinet to have partecipated as jury to my defense.

When I started I was full of fear about my future and my new job in a new city without the closeness of my family and friends. What I found when I arrived in Paris was a group of people ready to help me and make me feel at home.

It is not easy to express my feelings and gratitude by writing these acknowledgment, so forgive me if I'm going to forget about you but know that I have treasured all the time I have spent with you. I can only start by thanking my family, who have held my back through all these years and have always been strong even when the distance felt was greater than the physical distance.

Next I would also like to thank Marco Barbieri for convincing me that it is worth it to do my doctorate in Paris with the SYRTE laboratory. I still remember the first interview I had with Remi Geiger and how he made me feel comfortable with just a simple skype call.

"Everything is going to be okay", I thought to myself at the time, and it did... Except for the numerous problems I had in the lab during my three years, especially with the glue, the AC unit and my clumsiness. He was always there, even if just for 5 minutes before having to leave, to discuss and help me.

Another person always ready to discuss... a lot... at 7 PM on a Friday evening... is Arnaud Landragin. Jokes aside, I am still amazed by the immense passion and knowledge he is able to display everyday. It is thanks to their guidance and experience that I was able to grow as a researcher and overcome the adversities encountered in this journey. I know these feeling are shared with Denis Savoie, the friend and colleague I shared the first part of my journey with. He showed me all the tricks on how to operate the gyro

at the best conditions, which I'm very thankful for. Hopefully I was able to pass all this knowledge to Romain Gautier with the help of my trusted chicken. I may have been a bit rough with him sometimes but I'm sure he will do an excellent job with the gyro, even better than I could. I'm sure exciting times await the GYRO team.

I cannot forget to thanks also Bess Fang who also welcomed me in the GYRO team, which had to deal first hand with my complete lack of knowledge on how to setup a laser system. It is thanks to her I have been able to made up for almost all of my shortcomings at the beginning. Then it was Leonid Sidorenkov turn to help me operate the experiment. He has pushed me not to settle for the few results already obtained but to always try to make things a little bit better.

I could not find a better team to work with... Thank you... Of course they were not the only person I met and interacted at SYRTE. I had the pleasure of also working together with Nicolas Mielec and to discuss everything pythonic and have fun with small little projects.

I also want to thank everyone else in the Atom Interferometry and Inertial Sensor group: Frank, Sebastien (sorry for all the noise I made in the lab), Carlos for the permanent who helped me many times during this three years: Theo, Tommaso, Mengzi, William, Romain, Raphael, Luc, Xavier, Romain, Ranjita, Thomas for the laugh we shared everyday between all the problems we had in the labs.

I also want to thank the electronic department (Michel, Jose, Laurent), the MUTA team (David and Bertrand), the informatics team (Pascal and Gilles), the administration (Marine) for all the time and help they gave to me. But my life was not only inside the lab, I want to also thank Giuseppe e Patrizia (aspetto a breve la buona notizia sappiatelo), Guglielmo, Tommaso, Giulia, Marcella, Elena for the many joyful evenings we shared together. I just want to give a special thanks to Gianluca, my roommate, and Carlotta, my trusted room finder. We knew each other from the university in Rome and for me, it is thanks to you two if Paris felt a bit more like home during these years.

Also a small mention to all my friends who were in Rome which never missed the opportunity to have fun with me the few time I went back to the CAPUT MUNDI.

Finally I want to express my greatest gratitude to Sofia. Our story starts way before my days in Paris but it is here where we found each other again. You were by my side while I was writing this manuscript and you never passed the chance to make me feel your support and love, even if you were in London. Thank you for everything, I love you.

Contents

Chapter 1

Introduction

1.1 Cold atom inertial sensor

During the continuous development of atom interferometry in the last 28 years, we saw the birth of a new generation of inertial sensors. Accelerometers, gravimeters, gyroscopes, gradiometers are being studied and developed in the scientific community as well as in the industry. The versatility of these sensors is shown in the wide range of results they are achieving: measurements of fundamental constants such as the fine structure constant [1, 2, 3], prospect of improved navigation systems [4, 5, 6, 7], measurement of gravity acceleration for geophysics purposes [8, 9] and also tests of fundamental physics such as test of equivalence principle [10, 11, 12, 13]. In the recent years, propositions for detecting gravitational waves have also been made [14, 15, 16, 17, 18].

1.2 Sagnac based gyroscopes

The main types of optical gyroscopes in commerce are the ring laser gyroscope (RLG) and the fiber optic gyroscope (FOG). Both technologies relies on the Sagnac effect to perform rotation rate measurement. Sagnac effect [19] couples the rotation rate applied to the interferometer with its physical area. To illustrate in a simple way the effect, we start by considering an interferometer with a circular optical guide, rotating about its center with angular velocity Ω, see Figure 1.1. During the time it takes light to cross half of the guide, the interferometer output has rotated by $\Omega\pi\frac{R^2}{c}$. Here we assume that the angular velocity is much smaller than c/R. The difference in traveling time between the two arms then becomes $\Delta t \approx 2\Omega\pi\frac{R^2}{c^2}$.

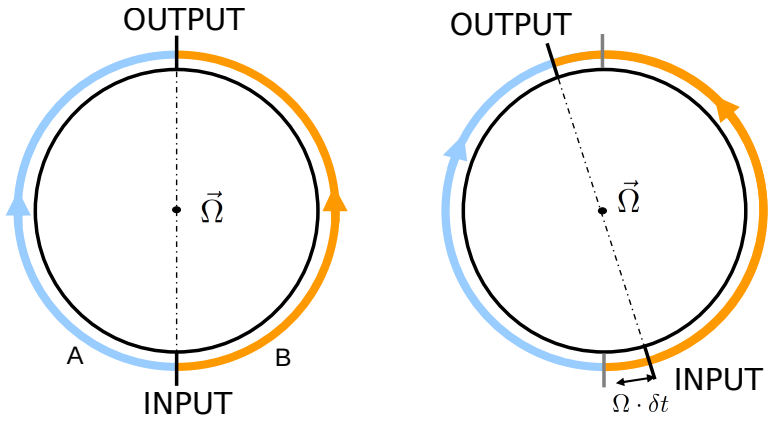

Figure 1.1: *Scheme of a rotating circular interferometer. The light enters from the input, is split in the two arms A and B and is recombined at the output. The interferometer is in rotation about its center, thus the output port moves, changing the length of the optical path.*

This leads to a phase difference such as:

$$\Delta\Phi_\Omega = \frac{2\pi c}{\lambda}\Delta t = \frac{4\pi}{\lambda c}A\Omega \tag{1.1}$$

where $\vec{A}$ is the normal vector of the physical area of the interferometer. Equation (1.1) can be generalized to other kind of particles using the De Broglie wavelength $\lambda = \frac{hc}{E}$:

$$\Delta\Phi_\Omega = \frac{4\pi E}{hc^2}\vec{A}\cdot\vec{\Omega} \tag{1.2}$$

As we can see the effect is proportional to the energy E of the particle used to produce the interference. In the case of optical gyroscope the energy of the photon is of the order of 1 eV while, for comparison, in the case of cold atom gyroscope using non relativistic ^{133}Cs atoms, the energy is of the order of 10^{11} eV.

For inertial navigation, ring laser gyroscope (RLG) are the de-facto standard thanks to their long term stability and compact size (typical Sagnac area of tens of cm^2) and wide dynamic range. Ring laser gyroscope with larger areas, up to few m^2, are also being used for geosciences. Large Sagnac areas are also achieved by fiber-optic gyroscope (FOG) reaching hundreds of m^2. Both RLG and FOG utilize optical interference, while atomic gyroscopes make use of *matter wave* interference, taking advantage of the huge energy

difference between atoms and photons. The first atomic gyroscope, which used thermal atomic beams, was realized between the beginning of the 90's [20] and the first years 2000's [21]. At SYRTE the first cold atom gyroscope was also built at the beginning of the first decade of the 2000's. It was a 6 axis gyroscope-accelerometer and it provided the basis of a compact design for cold atom inertial sensors [4, 6]. The gyroscope described in this work is the new generation of cold atom gyroscope being developed at SYRTE. It has a Sagnac area of 11 cm^2, the largest at the moment of writing. Other cold atom gyroscope are also being developed around the word, at Hanover [22], at NIST [23] or in China [24].

Type	Sagnac Area	Stability Short Term ($rad \cdot s^{-1} \cdot Hz^{-1/2}$)	Stability Long term ($rad \cdot s^{-1}$)	Integration time
Fiber, iXblue FOG 200 [25]		$5,8 \cdot 10^{-8}$	$2 \cdot 10^{-10}$	$\sim$ 8 day
RLG G-Ring (Germany) [26]	16 m^2	$3 \cdot 10^{-11}$	$6 \cdot 10^{-13}$	2 hours
Atomic Jet (Stanford) [5]	24 mm^2		$5 \cdot 10^{-10}$	2000 s
Cold atom 3 light pulse (Hanover) [22]	41 mm^2	$1,2 \cdot 10^{-7}$	$2,6 \cdot 10^{-8}$	100 s
Cold Atom 3 light pulse (SYRTE) [6]	4 mm^2	$2,4 \cdot 10^{-7}$	$1 \cdot 10^{-8}$	30 minutes
Cold Atom 4 light pulse (this work)	11cm^2	$3 \cdot 10^{-8}$	$3 \cdot 10^{-10}$	$\sim$ 8 hours

Table 1.1: *Brief summary of the state of the art for both optical and atomic gyroscopes. Integration time refers to the time needed to reach the best long term stability.*

1.3 Purpose of the thesis work

The cold atom gyroscope was already built by Thomas Lévèque [27] in 2008. The very first atomic interferometer measurements using Raman transitions were performed by Matthieu Meunier in 2013, who also implemented the first continuous measurement using a Ramsey interferometer [28, 29]. Following Meunier's work, Indranil Dutta implemented continuous measurement with a 4 pulse configuration [30]. He also performed the first measurement correlating the interferometer's phase with the signal acquired from classical sensor [31]. Denis Savoie extended Dutta's work developing a three times interleaved continuous measurement. He also implemented a system to compensate in real time the contribution to the interferometers phase due to acceleration noise. He also introduced a routine to operate the interferometer always at the middle of the fringe, thus at maximum sensitivity [32].
I started working with Denis Savoie on the long term performance of the gyroscope. To operate the sensor at its best, most of the systematic effects must be addressed and minimized. The characterization of these systematic biases has been part of the main purposes of my work. As I will show in this manuscript, the main systematic effect which leads to long term stability drift comes from the imperfect optimization of the atomic trajectory. This couples with the relative misalignment of the two Raman retro-reflection mirrors used to realize beam-splitter and mirror pulses for the atomic wave packet. After an initial optimization of the vertical trajectory in order to reduce phase shift linked with the vertical alignment of the retro reflecting Raman mirrors, we published state of the art performances for cold atom gyroscope [33]. A full characterization for both directions of the mirrors and trajectory followed soon after. The other objective of my work was the estimation of the scale factor of our large Sagnac area atom interferometer and its linearity. I implemented different indirect methods to estimate the scale factor, while finally a first direct measurement has been performed with the installation of a rotation stage below the experiment. Towards the end of my PhD I also worked on the implementation of a new 4 pulse scheme using different exchanged momentum which could lead to an improvement of the overall performances.

1.4 Plan of the Thesis

Chapter 2: Concepts of Atom interferometry

In this chapter I briefly introduce all the necessary concepts for understanding atom interferometry. I also present the 4 pulse configuration actually in use for our gyroscope,

with its relative sensitivity function. I then conclude by describing how acceleration and rotation noise affects our measurements.

Chapter 3: Experimental Set-Up

Here I illustrate the experimental apparatus: the laser systems used to cool, probe and detect the atomic cloud. I then describe the main structure of the sensor, introducing the new rotation stage implemented under the sensor. I conclude presenting a study on the contribution to the phase noise due to vibration, before and after the introduction of the rotation stage.

Chapter 4: Interleaved atom interferometry for improved sensibility

In this chapter I recall the latest results obtained with our cold atom gyroscope. I start by describing the methods implemented by previous PhD students and used by me to achieve a sensor that operates without dead time and with a high sampling rate. I then present the results achieved in terms of long term stability, which is, at the time of writing, the state of the art for a cold atom gyroscope. Using the fast sampling rate together with the high inertial sensitivity, I could perform studies of dynamic rotation in a so far unexplored range.

Chapter 5: Scale Factor and Bias of the Gyroscope

This chapter addresses the problem of characterizing the scale factor and bias of the gyroscope. Here I present various techniques and instruments to estimate indirectly the scale factor of the gyroscope. I then move on measuring directly the scale factor by using a rotation stage placed below the sensor. To improve the precision of the estimation, in the second part of the chapter I address the bias linked to non optimized atom trajectory and relative misalignments between the retro-reflecting Raman mirrors.

Chapter 6: Non equal momentum transfer

This chapter describes the methods used to remove the destructive effects of parasitic interferometers. I first present the solution implemented by previous PhD students and the relative effect on the DC acceleration sensitivity. I then introduce a new solution to prevent the recombination of secondary parasitic interferometers which consists in the use of different exchanged momentum for the two Raman laser pair collimator. I also present a new protocol to optimize the frequency ramp used to compensate DC acceleration phase shift.

Chapter 2

Basic concepts for cold atom interferometry

In this chapter I will briefly introduce the concepts of atom interferometry (AI) and cold atom inertial sensors. I will first introduce the method of using Raman transitions to create an atomic beam splitter and mirror, such that we can manipulate coherently atomic waves. I will later explain how inertial quantities such as acceleration and rotation can be measured using atom interferometry. Subsequently I will describe the 4-pulse interferometer currently in use for our gyroscope explaining why it is suitable for rotation measurements. Finally, I will present the sensitivity function associated with the 4 pulse interferometer in order to estimate how different source of noise can deteriorate our measurements.

2.1 Raman transition and light pulses

2.1.1 Principles

The schemes here presented can be described in terms of simple optical interferometer. The general scheme for AI resembles the scheme of Mach-Zehnder interferometer; instead of using coherent light which is reflected and diffracted by physical mirrors and beam splitters, we use matter wave as carrier and laser light pulses as "beam splitter and mirrors."

2.1.2 Stimulated Raman Transitions

In our gyroscope we manipulate the atomic wave-packet by mean of stimulated Raman transitions [34, 35]. Using two laser fields, $\vec{E}_1$ and $\vec{E}_2$, set close to the D_2 line of Cesium atom, we connect the Cesium hyperfine states $|g\rangle = \left|6S_{1/2}, F = 3\right\rangle$ and $|e\rangle = \left|6S_{1/2}, F = 4\right\rangle$.
Stimulated transition is a process that occurs when the atom, starting from one of the lower states e.g. $|g\rangle$, absorbs one photon of energy $\hbar\omega_1$ from one laser field and emits a photon of energy $\hbar\omega_2$ with the second laser field, being transfered coherently to the final state $|e\rangle$.

In order for this transition to take place, the two hyperfine states are coupled to an intermediate virtual level $|i'\rangle$ red-detuned by Δ from $|i\rangle = \left|6P_{3/2}, F' = 3\right\rangle$. The detuning Δ, is introduced to minimize one photon transitions to the exited state, thus limiting spontaneous emission effects that will decrease the coherence of the wave-packet. Spontaneous emissions processes decrease as $1/\Delta^2$ while the coupling efficiency to the intermediate level $|i\rangle$ decreases as $1/\Delta$, therefore an optimum condition can be found in order to maximize both coherence and coupling.

In the case of counter-propagating laser beams, the two electromagnetic fields $\vec{E}_1(t)$ and $\vec{E}_2(t)$ have opposite direction, therefore the exchanged momenta, when the atom absorbs or emits a photons, have the same sign. The total momentum transfered to the atom then, will be $\hbar\vec{k}_{eff} = \hbar(\vec{k}_1 - \vec{k}_2) \approx 2\hbar\vec{k}_1$.
The stimulated Raman transition with counter propagating beams then, associate an external momentum state, $|\vec{p}\rangle$ or $|p + \vec{\hbar}k_{eff}\rangle$, to an internal state $|g\rangle$ or $|e\rangle$, physically separating the two population into separate arms of the interferometer.

To describe the interaction between the atom and the light pulse, we start from studying the time-dependent Schrödinger equation associated with the system:

$$i\hbar\frac{\mathrm{d}}{\mathrm{d}t}\Psi(t) = \hat{H}\cdot\Psi(t) \tag{2.1}$$

The wave-function $\Psi(t)$ for our three level system can be expressed as a linear combination of the atom levels' eigenstates:

$$|\Psi(t)\rangle = C_i(t)\,|i\rangle + C_e(t)\,|e\rangle + C_g(t)\,|g\rangle \tag{2.2}$$

The operator $\hat{H} = \hat{H}_0 + \hat{V}(t)$ describes the complete Hamiltonian of the system with $\hat{H}_0$ as the non interactive Hamiltonian and with $\hat{V}(t)$ as the time dependent interaction between the atoms and the total electromagnetic field.

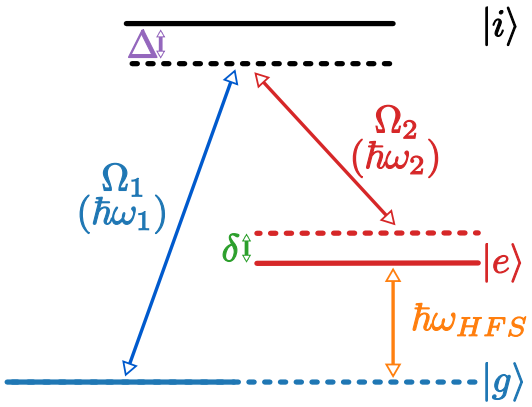

Figure 2.1: *Raman transition in a 3 level Λ-system*

The interaction operator, takes the form $\hat{V}(t) = -\vec{\hat{D}} \cdot \vec{E}$, where $\vec{\hat{D}}$ is the dipole moment operator and $\vec{E}$ is the total electromagnetic field:

$$\vec{E}(\vec{x}, t) = \vec{E}_1 e^{i(\vec{k}_1 \cdot \vec{x} - \omega_1 t + \phi_1)} + \vec{E}_2 e^{i(\vec{k}_2 \cdot \vec{x} - \omega_2 t + \phi_2)} + cc \tag{2.3}$$

We can rewrite the interaction operator in term of Rabi frequencies :

$$\hat{V}(t) = \sum_{j,k,l} \hbar\Omega_{j,k,l} = \sum_{j,k,l} -\vec{\hat{D}}_{jk} \cdot \vec{E}_l \, |j\rangle\langle k| \tag{2.4}$$

where $l = [1, 2]$ specifies the electromagnetic fields and $j, k = [e, g, i]$ specifies the state. To simplify the equations we apply the *rotating wave approximation* to our system. In brief we ignore the terms that oscillate with optical frequencies (THz) since they will average to zero faster than the terms which oscillate with the difference of optical frequencies (GHz). At the end we obtain a two level system with effective Hamiltonian [36, 37]:

$$\hat{H}_{eff} = \frac{p^2}{2M} + \left[\hbar\Omega_{eff} e^{i(\vec{k}_{eff} \cdot \vec{x} - \phi(t))} \, |g\rangle\langle e| + \hbar\Omega^*_{eff} e^{-i(\vec{k}_{eff} \cdot \vec{x} - \phi(t))} \, |e\rangle\langle g|\right] \tag{2.5}$$

where $\Omega_{eff} = \frac{\Omega_e \Omega_g}{2\Delta}$ is the *effective Rabi frequency*.
This Hamiltonian describes the transition between the two hyperfine states with an exchanged momentum $\hbar\vec{k}_{eff}$ and a phase $\phi(t)$ imprinted at the time of the pulses. The diagonalization of Eq. (2.5) yields:

$$|\Psi(t)\rangle = \tilde{C}_g(t) e^{-iE_g t/\hbar} \, |g, \vec{p}\rangle + \tilde{C}_e(t) e^{-iE_e t/\hbar} \left| e, \vec{p} + \hbar\vec{k}_{eff} \right\rangle \tag{2.6}$$

where $E_g = \frac{p^2}{2M} + \hbar\omega_g$ and $E_e = \frac{\left(p + \hbar k_{eff}\right)^2}{2M} + \hbar\omega_e$ are the energy for the two states.

Using the effective Hamiltonian in Eq. (2.6) and the above wave-function, Eq. (2.6), in Schrödinger equation Eq. (2.1) we obtain:

$$\begin{aligned} |\tilde{C}_g|^2(\tau) &= 1 - \Lambda \ \sin^2\left(\frac{\Omega_R}{2}\tau\right) \\ |\tilde{C}_e|^2(\tau) &= \Lambda \ \sin^2\left(\frac{\Omega_R}{2}\tau\right) \end{aligned} \tag{2.7}$$

where with $|\tilde{C}_{g,e}|^2(\tau)$ we describe the population in the two hyperfine state and their respective Rabi oscillation. The amplitude of these oscillation is given by $\Lambda = \Omega_{eff}^2/\Omega_R^2$, where $\Omega_R^2 = \sqrt{\Omega_{eff}^2 + \delta^2}$ is the generalized Rabi frequency and with δ we indicate the shift from 2 photon resonance which includes Doppler shift, recoil shift, and light-shift.

Resonance conditions

Since the atoms are free falling the electromagnetic field will experience some detuning due to Doppler effect. The frequency difference between the Raman lasers pair then will have to satisfy the sequent condition:

$$\hbar(\omega_1 - \omega_2) = E_g - E_e = \hbar(\omega_g - \omega_e) + \hbar\omega_R + \hbar\omega_D + \hbar\delta_{det} \tag{2.8}$$

where $\hbar\omega_R = \frac{\hbar^2|\vec{k}_{eff}|^2}{2M}$ is the recoil energy, $\hbar\omega_D = \frac{\vec{p}\cdot\vec{k}_{eff}}{M}$ is the Doppler correction and $\hbar\delta_{det}$ is a general detuning from the 2-photon resonance.

2.2 Atom optics

In the limit where $\delta \ll \Omega_{eff}$, the amplitude of the population oscillation $\Lambda \to 1$, then we can simplify equations Eq. (2.7) as :

$$\begin{aligned} |\tilde{C}_g|^2(\tau) &= \frac{1}{2}(1 + \cos(\Omega_{eff}\tau)) \\ |\tilde{C}_e|^2(\tau) &= \frac{1}{2}(1 - \cos(\Omega_{eff}\tau)) \end{aligned} \tag{2.9}$$

We now discuss two interesting cases where depending on the length of the pulse we obtain what are called *atom optics*.

π pulses - Mirror

We start by having an atom in the ground state $|g\rangle$, $|\tilde{C}_g|^2 = 1$ which interacts with our light pulse. In the case the duration of the pulse is $\tau = \tau_\pi = \pi/\Omega_{eff}$, from Eq (2.9) we obtain:

$$|\tilde{C}_e|^2(\tau_\pi) = 1 \tag{2.10}$$

for the population in the excited state while $|\tilde{C}_g|^2(\tau_\pi) = 0$ for the initial state.
This means we have successfully transferred the whole atomic population from one hyperfine state to the other. Since we also associate momentum state with our internal state, this implies that the atom in the exited state $|e\rangle$ has changed direction, producing a path spatially separated from the original trajectory, acting on the wave-packet as a mirror.

$\frac{\pi}{2}$ pulses - Beam Splitter

In the case the duration of the pulse is $\tau = \tau_{\frac{\pi}{2}} = \pi/2\Omega_{eff}$ Eq (2.9) returns:

$$|\tilde{C}_e|^2(\tau_{\frac{\pi}{2}}) = \frac{1}{2} \tag{2.11}$$

as well for $|\tilde{C}_g|^2(\tau_{\frac{\pi}{2}}) = \frac{1}{2}$. In this case we have created a superposition of both states, $|g\rangle$ and $|e\rangle$, while generating two spatially separated path, one for each atomic state. This behavior can be compared to how an optical beam splitter creates two separate outputs from a single input.

2.3 Mach-Zehnder Atom interferometry - 3 pulse scheme

With a mirror and beam splitter pulse, we now have all the tools to create an atom interferometer. An optical Mach-Zehnder interferometer requires two beam splitters, and two mirrors. With atom interferometry we can achieve the same type of configuration, by using the correct series of pulses. We start with a $\pi/2$-pulse to physically separate the two arms, a single π-pulse to reflect then conclude the sequence with a $\pi/2$-pulse to recombine the wave-packets. We can estimate the phase in one of the output ports of the interferometer, by calculating the difference of accumulated lasers phase between the two arms:

$$\Delta\Phi_{3P} = (\phi_1 - \phi_2) - (\phi_2 - \phi_3) = \phi_1 - 2\phi_2 + \phi_3 \tag{2.12}$$

Here we introduce our sign convention for the imprinted phase; if the starting state is the ground state $|g\rangle$, we apply a positive phase shift, $+\phi$. On the contrary when we shine the light pulses on the exited state $|e\rangle$, phase imprinted is negative, $-\phi$.

2.3.1 Phase shift for a constant acceleration

In the previous section we explained how we are able to create a superposition of atomic states while also separating the two wave-packets in space. As we saw the separation is proportional to the effective momentum exchanged but it also depends on the time between each light pulses. As the separation between the two wave-packets increases, the interferometer's sensitivity to 'inertial' forces grows. For the case of a 3-pulse Mach-Zehnder, subjected to a constant acceleration field $\vec{a}$ we are able to generalize the expression for the phase shift as:

$$\begin{aligned}\Phi_a &= \vec{k}_{eff} \cdot (\vec{x}_1(0) - \vec{x}_2(T)) - (\vec{x}_2(T) - \vec{x}_3(2T)) \\ &= \vec{k}_{eff} \cdot (\vec{x}_1(0) - 2\vec{x}_2(T) + \vec{x}_3(2T)) \\ &= \vec{k}_{eff} \cdot \vec{a}T^2\end{aligned} \tag{2.13}$$

The displacement of the atom on each path, is obtained by doubly integrating the acceleration $\vec{a}$, thus we obtain the phase to scale as T^2.

2.3.2 Phase shift for constant rotations - Sagnac effect

As our Mach-Zehnder atom interferometer encloses a physical area $\vec{A}$, another famous interference phenomenon can be observed [19]. Sagnac experimentally proved that when light is split and recombined after enclosing a certain area, the interference pattern at the output changes depending on the rotation rate of the apparatus [19, 38]. Sagnac discovered that such phase shift is proportional to the area $\vec{A}$ enclosed by the two path, and to the rotation rate, $\vec{\Omega}$. The general expression for Sagnac phase shift is:

$$\begin{aligned}\Delta\Psi_\Omega &= \frac{1}{\hbar c^2} \oint \left(\vec{\Omega} \times \vec{x}\; E \cdot \mathrm{d}\vec{x}\right) \\ &= \frac{2E}{\hbar c^2} \vec{A} \cdot \vec{\Omega}\end{aligned} \tag{2.14}$$

where E is the total energy of the particle used to perform interferometry.
It's important to notice that Eq. (2.14), holds true for both purely optical interferometer and matter-waves ones [39, 40, 41]. In Eq. (2.14), lies the reason why performing Sagnac interferometry with cold atoms is more advantageous with respect to optical interferometers. In fact for equal enclosed area $\vec{A}$, the energy ratio between an atom ($E_{at} \approx mc^2$)

and a photon ($E_{ph} = \hbar\omega$) gives:

$$\frac{E_{at}}{E_{ph}} \approx 10^{11} \tag{2.15}$$

This relation shows clearly the huge potential gain in sensitivity using atom interferometry compared to photon interferometry. We now proceed to calculate the phase shift linked to rotation that we can measure with a 3-pulse atom interferometer. We assume the atoms possess an initial velocity $\vec{v}_0$ and the interferometer perceives a constant rotation rate $\vec{\Omega}$ in the plane perpendicular to both $\vec{k}_{eff}$ and $\vec{v}_0$. The resulting phase shift at time t will then be:

$$\Phi(t) = -\vec{k}_{eff} \cdot \vec{x} = -\vec{k}_{eff} \cdot (\vec{v}_0 t \sin(\Omega t) + 2\vec{v}_{rec} \cos(\Omega t)) \tag{2.16}$$

where we introduced the 2-photon recoil velocity $\vec{v}_{rec} = \frac{\hbar \vec{k}_{eff}}{M}$. We now calculate the full phase shift for a 3-pulse atom interferometer, with timings $0 - T - 2T$:

$$\begin{aligned} \Phi_1 &= 0 \\ \Phi_2 &= -\vec{k}_{eff} \cdot \vec{v}_0 T \sin(\Omega T) - \vec{k}_{eff} \cdot 2\vec{v}_{rec} T \cos(\Omega T) \\ \Phi_3 &= -\vec{k}_{eff} \cdot \vec{v}_0 2T \sin(\Omega 2T) - \vec{k}_{eff} \cdot 2\vec{v}_{rec} 2T \cos(\Omega 2T) \end{aligned} \tag{2.17}$$

Following the calculation in [42], and combining Eq. (2.17) with Eq. (2.12), we can write down the phase shift for all direction, in vectorial form:

$$\Phi_{rot} = -\vec{k}_{eff}\Big(2\vec{\Omega} \times \vec{v}_0\Big)T^2 \tag{2.18}$$

From this equation, plus Eq. (2.14), we can extract the total Sagnac area for a 3-pulse interferometer:

$$A = \frac{\hbar}{M}\vec{k}_{eff} \cdot \vec{v}_0 T^2 \tag{2.19}$$

2.4 4-pulse Atom Gyroscope

The four pulse atom interferometer uses a sequence of light-pulses ($\pi/2 - \pi - \pi - \pi/2$). The scheme could be seen as two Mach-Zehnder interferometer, where the output of the first is the input of the second, but with no last(first) pulse.

2.4.1 Constant acceleration - Zero sensitivity

We now demonstrate why this is the configuration of choice to perform a cold atom gyroscope compared to a simple Mach-Zehnder. We start by calculating the phase shift

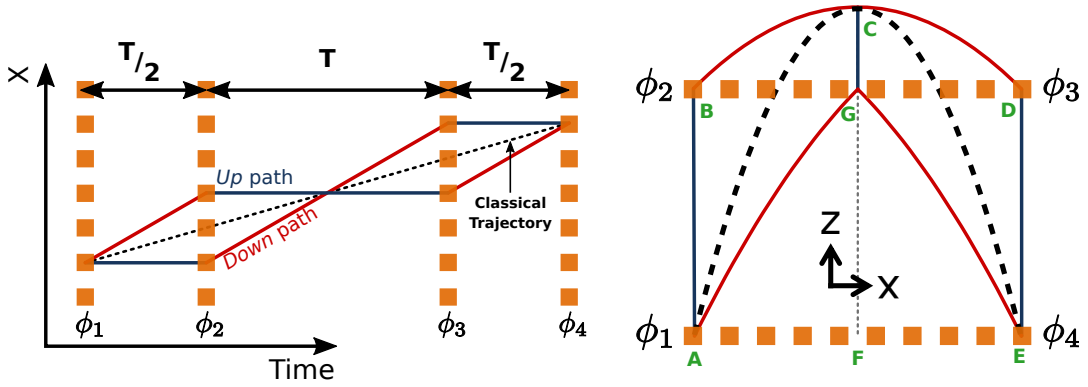

Figure 2.2: *(left): Space-time diagram of the 4 pulse butterfly interferometer. (right): Scheme of the experiment in the* xz *plane. The color represent the different momentum states.*

for the 4 pulse (see Figure 2.2):

$$\begin{aligned}\Phi_a^{4p} &= (\phi_1 - \phi_2 + \phi_3 - \phi_4)_{up} - (\phi_2 - \phi_3)_{down} \\ &= (\phi_1 - 2\phi_2 + 2\phi_3 - \phi_4) \\ &= k_{eff} \cdot (\vec{x}_1(0) - 2\vec{x}_2(T/2) + 2\vec{x}_3(3T/2) - \vec{x}_4(2T)))\end{aligned} \tag{2.20}$$

If we now substitute the usual equation of motion $\vec{x}(t) = \vec{v}_0 t - \frac{1}{2}\vec{g}t^2$, it's easy to calculate that Φ_a^{4p} goes to zero. This means the sensitivity to DC acceleration is null, hence at the output of the interferometer we have an output signal that comes purely from DC sensitivity to rotation and not a mix of rotation and acceleration.

2.4.2 Rotation Sensitivity - Sagnac area

In order to calculate the rotation phase sensitivity, we need to estimate the area enclosed by the two wave-packets. As we operate the sensor as an atomic fountain the paths of the two wave-packets fold onto themselves enclosing an area in the xz-plane.
To begin with, we introduce the velocities of the atoms in the x and z direction:

$$\begin{aligned}v_z(t) &= (v_0 - gt) \\ v_x(t) &= 2v_{rec} = \frac{\hbar k_{eff}}{M}\end{aligned} \tag{2.21}$$

where v_0 is the initial velocity of the cloud; to make the atomic cloud trajectory symmetric in space, we want to make sure the apogee of the trajectory coincide in time with

the middle of the interrogation time 2T. This means $v_z(T) = 0$ hence we fix the initial velocity to $v_0 = gT$. We can now proceed to calculate the area enclosed between the two path of the wave-packets. Since the AI is now symmetric with respect to the apogee, the total area of the interferometer will be twice the area enclosed by the point ABCGA in Figure 2.2. The total area of ABCGA, can also be divided in two separate section:

$$A_{ABCGA} = A_{ABG} + A_{BCG} \tag{2.22}$$

Since the initial velocity v_0 is much larger than the recoil velocity v_{rec} we can approximate the two areas with the areas of two triangles, we begin with A_{ABG}:

$$\begin{aligned} A_{ABG} &= \frac{1}{2} \times \overline{AB}_z \times \overline{BG}_x \\ &= \frac{1}{2} \int_0^{\frac{T}{2}} v_z(t')\mathrm{d}t' \times \int_0^{\frac{T}{2}} v_x(t')\mathrm{d}t' \\ &= \frac{3}{32} g \frac{\hbar k_{eff}}{M} T^3 \end{aligned} \tag{2.23}$$

For the other section we have:

$$\begin{aligned} A_{BCG} &= \frac{1}{2} \times \overline{GC}_z \times \overline{BG}_x \\ &= \frac{1}{2} \int_{\frac{T}{2}}^{T} v_z(t')\mathrm{d}t' \times \int_{\frac{T}{2}}^{T} v_x(t')\mathrm{d}t' \\ &= \frac{1}{32} g \frac{\hbar k_{eff}}{M} T^3 \end{aligned} \tag{2.24}$$

Finally the total area of our 4 light-pulse atom interferometry is:

$$A_{4p} = 2 \times (A_{ABG} + A_{BCG}) = \frac{1}{4} \frac{\hbar}{M} (\vec{g} \times \vec{k}_{eff}) T^3 \tag{2.25}$$

We note that, even though we made some approximation, the result correspond to the actual area of the interferometer. If we now combine Eq. (2.25) with Eq. (2.14) we obtain the DC rotation phase shift due to Sagnac effect of the 4 pulse atom interferometer:

$$\Phi_\Omega = \frac{1}{2} \vec{k}_{eff} \cdot \left(\vec{g} \times \vec{\Omega} \right) T^3 \tag{2.26}$$

It's important to notice that the phase sensitivity to rotation scales as T^3 since the initial velocity of the atom has to be equal to $\vec{g}T$, contrary to systematics effect which scale as T [43]. This property, together with the zero sensitivity to DC accelerations are what makes this *butterfly* configuration very advantageous for measuring purely rotation signals.

2.5 Sensitivity function of a 4 light pulse interferometer

To describe how our system responds to external perturbation we rely on the sensitivity function. In this section I will describe how different types of perturbation (Raman laser phase noise, acceleration noise) modify the phase reading at the output of the interferometer.

2.5.1 Laser phase sensitivity

We begin by studying the response of our system to an infinitesimal variation of the phase difference between the two Raman lasers, $\delta\phi$ [44]. Such fluctuation generates a change δP in the transition probability $P = \frac{1}{2}(1 + \cos(\Phi))$ measured with the sensor. If we assume the interferometer is operating in the middle of the fringe $\Phi = \frac{\pi}{2}$ we can write the sensitivity function as:

$$g_\phi = \lim_{\delta\phi \to 0} \frac{\delta\Phi(\delta\phi, t)}{\delta\phi} \tag{2.27}$$

If the relative phase between the Raman lasers changes with time, $\phi(t)$, we can calculate the total contribution to the interferometer's phase by integrating over time:

$$\Delta\Phi = \int_{-\infty}^{+\infty} g_\phi(t)\mathrm{d}\phi(t) = \int_{-\infty}^{+\infty} g_\phi(t)\frac{\mathrm{d}\phi(t)}{\mathrm{d}t}\mathrm{d}t \tag{2.28}$$

Since the interrogation time $2T$ is much larger than the pulse length, $2T \gg \tau$ we can write $g_\phi(t)$ as:

$$g_\phi(t) = \begin{cases} 0 & : t < 0 \\ -1 & : 0 \leq t < T/2 \\ +1 & : T/2 \leq t \leq 3T/2 \\ -1 & : 3T/2 < t \leq 2T \\ 0 & : t > 2T \end{cases} \tag{2.29}$$

It is important to notice that it is possible to take in consideration both the length and the shape of the pulse used [31, 32, 45]. We will now use the sensitivity function to calculate the contribution to the phase generated by perturbations like rotation noise and acceleration noise. To do so we need to convolve the sensitivity function with the perturbation to obtain the inertial phase noise.
To simplify the calculation we pass to the Fourier space where the convolution becomes a simple multiplication. Hence the perturbation will depend on the angular frequency

ω. The Fourier transform of $g_\phi(t)$ for a 4-pulse interferometer, takes the following form:

$$|H_\phi(\omega)|^2 = 64 \sin^2\left[\frac{\omega T}{2}\right] \sin^4\left[\frac{\omega T}{4}\right] \tag{2.30}$$

To obtain the total variance of the laser phase noise then, we need only the power spectral density, $S_\phi(\omega)$, of the noise. To do so we calculate σ_ϕ^2:

$$\sigma_\phi^2 = \int_0^{+\infty} |H_\phi(\omega)|^2 S_\phi(\omega) \frac{\mathrm{d}\omega}{2\pi} \tag{2.31}$$

2.5.2 Acceleration phase noise

To characterize the phase noise introduced by external source by means of acceleration noise is useful to study the response of the sensitivity function to acceleration. If we subjected the sensor to an acceleration $\vec{a}(t)$, the interferometers phase would evolve as:

$$\frac{\mathrm{d}^2\Phi(t)}{\mathrm{d}t^2} = \vec{k}_{eff} \cdot \vec{a}(t) \tag{2.32}$$

As in the previous section, we now pass to the Fourier space and we obtain:

$$\omega^2 \, \tilde{\phi}(\omega) = \vec{k}_{eff} \cdot \tilde{a}(t) \tag{2.33}$$

where $\tilde{\phi}$ and $\tilde{a}$ are the Fourier transform of ϕ and $\vec{a}$. If we now combine Eq. (2.33) with Eq. (2.30) we obtain the transfer function for acceleration noise:

$$\begin{aligned} |H_a(\omega)|^2 &= \frac{k_{eff}^2}{\omega^2} |H_a(\omega)|^2 \\ &= 64 \frac{k_{eff}^2}{\omega^2} \sin^2\left[\frac{\omega T}{2}\right] \sin^4\left[\frac{\omega T}{4}\right] \end{aligned} \tag{2.34}$$

As in Eq. (2.31), we can measure the power spectral density, to estimate the phase contribution of the acceleration noise:

$$\sigma_\phi^2 = \int_0^{+\infty} |H_a(\omega)|^2 S_a(\omega) \frac{\mathrm{d}\omega}{2\pi} \tag{2.35}$$

In Figure 2.3, are shown the amplitude spectral density (ASD), acquired with the use of a seismometer, and the acceleration transfer function $|H_a(\omega)|^2$. As we can see, the transfer function acts as a band-pass filter with a peak sensitivity centered around $1/2T$. The result of the numerical integration will be shown in Section 3.3

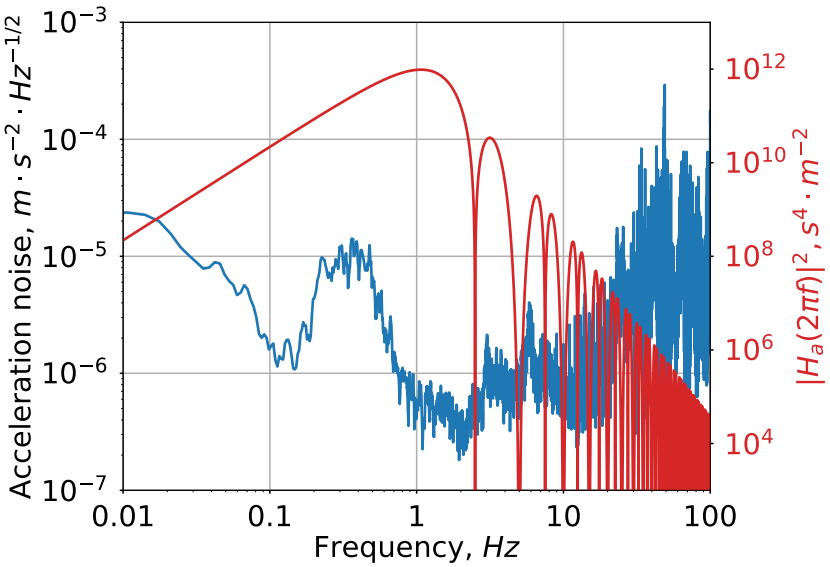

Figure 2.3: *Amplitude spectral density (ASD) of the linear acceleration noise and the acceleration transfer function $|H_a(\omega)|^2$ for a 4 pulse interferometer with interrogation time $T = 0.4$ s. The ASD was acquired with the sensor resting onto a vibration isolation platform using a seismometer.*

2.5.3 Rotation phase noise

Phase sensitivity to rotation comes from the relative angular displacement of the Raman collimator, rigidly connected to the sensor's structure, with respect to the atoms, free falling inside the vacuum chamber. A constant phase bias is due to Earth's rotation since the sensor is rotating along with it. However, as the sensor rests onto a vibration isolation platform, it is free to rotate slightly about the horizontal axis. These small rotations are one of the source of phase noise. Let us consider a rotation axis parallel to the y-axis, we can then write the displacement along the x-axis as [32]:

$$\begin{aligned} x_1 &= \theta_1\left(L - \frac{3}{16}gT^2\right) \\ x_2 &= \theta_2\left(L + \frac{3}{16}gT^2\right) \\ x_3 &= \theta_3\left(L + \frac{3}{16}gT^2\right) \\ x_4 &= \theta_4\left(L - \frac{3}{16}gT^2\right) \end{aligned} \tag{2.36}$$

where L is the distance from the axis of rotation. In this description we are considering only tangential displacement since the noise acts on the entire structure of the sensor.

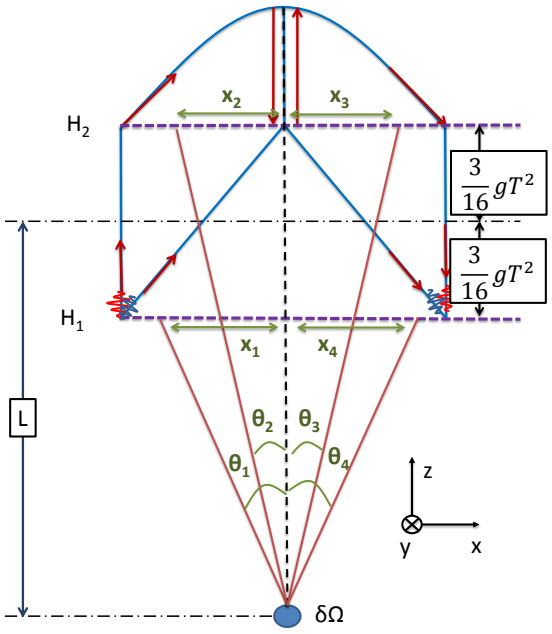

Figure 2.4: *Geometry of the 4 pulse butterfly scheme in the XZ plane. The rotation axis for the noise is distanced L from the geometrical center of the two Raman collimator.*

For a generic frequency ω and phase ψ we define rotation noise as $\Omega(t) = \Omega_\omega \cos(\omega t + \psi)$, therefore we can write $\omega(t) = \frac{\Omega_\omega}{\omega} \sin(\omega t + \psi)$. Following this definition, we can explicit the values of θ_i for all the pulses :

$$\begin{aligned}
\theta_1 &= \theta(0) = -\frac{\Omega_\omega}{\omega} \sin(\psi) \\
\theta_2 &= \theta\left(\frac{T}{2}\right) = -\frac{\Omega_\omega}{\omega} \sin\left(\omega\frac{T}{2} + \psi\right) \\
\theta_3 &= \theta\left(\frac{3T}{2}\right) = -\frac{\Omega_\omega}{\omega} \sin\left(\omega\frac{3T}{2} + \psi\right) \\
\theta_4 &= \theta(2T) = -\frac{\Omega_\omega}{\omega} \sin(2\omega T + \psi)
\end{aligned} \tag{2.37}$$

We now combine Eq. (2.20) with Eq. (2.36) to obtain an estimation of the rotation phase noise:

$$\begin{aligned}\Delta\Phi_\omega &= k_{eff}(x_1 - 2x_2 + 2x_3 - x_4)\\ &= -8k_{eff}\frac{\Omega_\omega}{\omega}\cos(\omega T+\psi)\sin\left(\omega\frac{T}{2}\right)\left[L\sin^2(\omega\frac{T}{4}) + \frac{3}{16}gT^2\cos^2(\omega\frac{T}{4})\right]\\ &= -\Omega_\omega\cos(\omega T+\psi)|H_\Omega(\omega)|\\ &= \Omega(t)|H_\Omega(\omega)|\end{aligned} \tag{2.38}$$

From Eq. (2.38) then, we define the transfer function for rotation noise $|H_\Omega|^2$:

$$|H_\Omega|^2 = -64\frac{k_{eff}^2}{\omega^2}\sin^2(\omega\frac{T}{2})\left[L\sin^2(\omega\frac{T}{4}) + \frac{3}{16}gT^2\cos^2(\omega\frac{T}{4})\right]^2 \tag{2.39}$$

As we can see, the transfer function depends on a specific L; when $L = 0$, meaning the axis of rotation passes precisely in between the two Raman collimator, the cosine term in Eq. (2.39) is null. On the contrary, When the distance of the axis of rotation from the center of the sensor is very large, $L \gg \frac{3}{16}gT^2$, the cosine term dominates the expression between square bracket. In this condition at low frequency, $\omega \to 0$, a DC terms appears in $|H_\omega|^2$, which takes the form of a constant bias in the rotation phase. This is the case for Earth's rotation as the projected rotation axis is far away from the sensor. As for acceleration noise we can estimate the variance of rotation noise following Eq. (2.31):

$$\sigma_\phi^2 = \int_0^{+\infty}|H_\Omega(\omega)|^2 S_\Omega(\omega)\frac{\mathrm{d}\omega}{2\pi} \tag{2.40}$$

where S_Ω is the power spectral density of rotation noise. Unfortunately we cannot precisely estimate the contribution to the phase introduced by rotation noise, since we cannot exactly position in space the axis of rotation. As for the acceleration, which we can measure the PSD thanks to seismometers or accelerometers, the use of a sensor to measure rotation noise, is more challenging due to the fact that measuring rotation of the order of 10^{-7} rad $\cdot$ s^{-1}Hz^{-1} can be quite challenging for commercial sensors.

2.6 Conclusion

In this chapter I briefly describe two photons stimulated Raman transition which we use to create a coherent superposition of different momentum states. This is done by generating light pulses that act like beam splitters and mirrors for the atomic wave-packets. Then I showed the calculation to estimate the phase shift of a 4-pulse interferometer due to Sagnac effect. Finally I present the sensitivity functions of the gyroscope, that allow us to estimate the impact of noise on the performance of our sensor.

Chapter 3

Experimental Set-Up

In this chapter the various components of the experimental apparatus will be briefly presented. A detailed description of the design ideas behind the construction can be found in previous thesis work [27], while in subsequent work [28, 31] the sensor gets characterized. In [32] the detection system of the experiment has been improved along side with the tilt locking systems which now can stabilize the tilt in both horizontal direction. I will begin by describing the frequency and laser system used to coherently manipulate and detect the atoms during all phases of the measurement cycle. I will, then, describe the properties of the anti-vibration stage on which the gyroscope resides. During my first year of PhD, I characterized a new rotation stage to be implemented below the sensor. This new stage allows the experiment to rotate about its vertical axis giving us the chance to measure the scale factor of the gyroscope. In collaboration with the mechanical team (MUTA) of SYRTE, I designed a system that allows the rotation stage to sustain the weight of the gyroscope and maintain a low level of vibration. In this context I will present a characterization of the vibration noise on the experiment before and after the implementation of the rotation stage. Another feature of the design is the possibility to adjust independently the tilt both of the rotation stage itself and of the sensor head, along both horizontal directions. Additionally, I will present a study on a new voice coil actuator, used for the tilt locking system on the gyroscope.

3.1 Lasers

3.1.1 Frequency chain

A central component of all the optical benches is the frequency chain which provides the necessary RF reference signals. It relies on a 100 MHz signal obtained from the

Hydrogen Maser situated in SYRTE as a master reference for a quartz oscillator. The reference frequency of the quartz oscillator is then used to synchronize and synthesize all frequencies involved with the frequency locking between lasers, such as the frequency beating between the two Raman lasers.

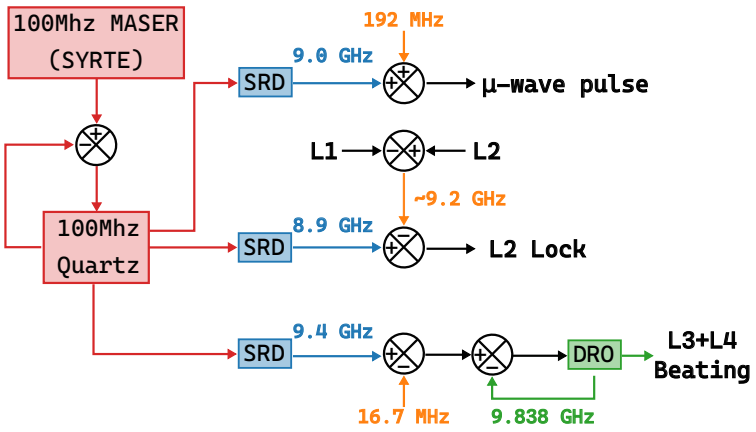

Figure 3.1: *Simplified scheme of the frequency chain which provides the reference signals for the laser locks and μ-wave selection pulse*

3.1.2 Cooling Laser system

The cooling laser system relies on two external cavity lasers (ECDL) [46]. They are used for the detection and repumper light as well as masters for injecting the 3 slave diode lasers and reference for the Raman lasers.

Master optical frequency reference, Repumper, L1 The first ECDL (L1) is locked by saturated absorption spectroscopy on the crossover transition $|6\ ^2S_{1/2}, F = 3\rangle \rightarrow |6\ ^2P_{3/2}, F' = 2/3\rangle$ and is used mainly as the repumper laser, mixed with the cooling light in the 2D-Magneto Optical Traps (MOT) and 3D-MOT. Another part of the beam is used as reference for the other lasers. The rest of the beam is used as probe repumper in the detection system.

Cooling and Detection, L2 The second ECDL (L2) is locked close to the transition $|6\ ^2S_{1/2}, F = 4\rangle \rightarrow |6\ ^2P_{3/2}, F' = 5\rangle$, thanks to its beating with L1 around 8.8 GHz which is then compared to a reference signal at 8.9 GHz generated by the frequency chain. Its light is used for the detection light sheet in the sensor and is also used to

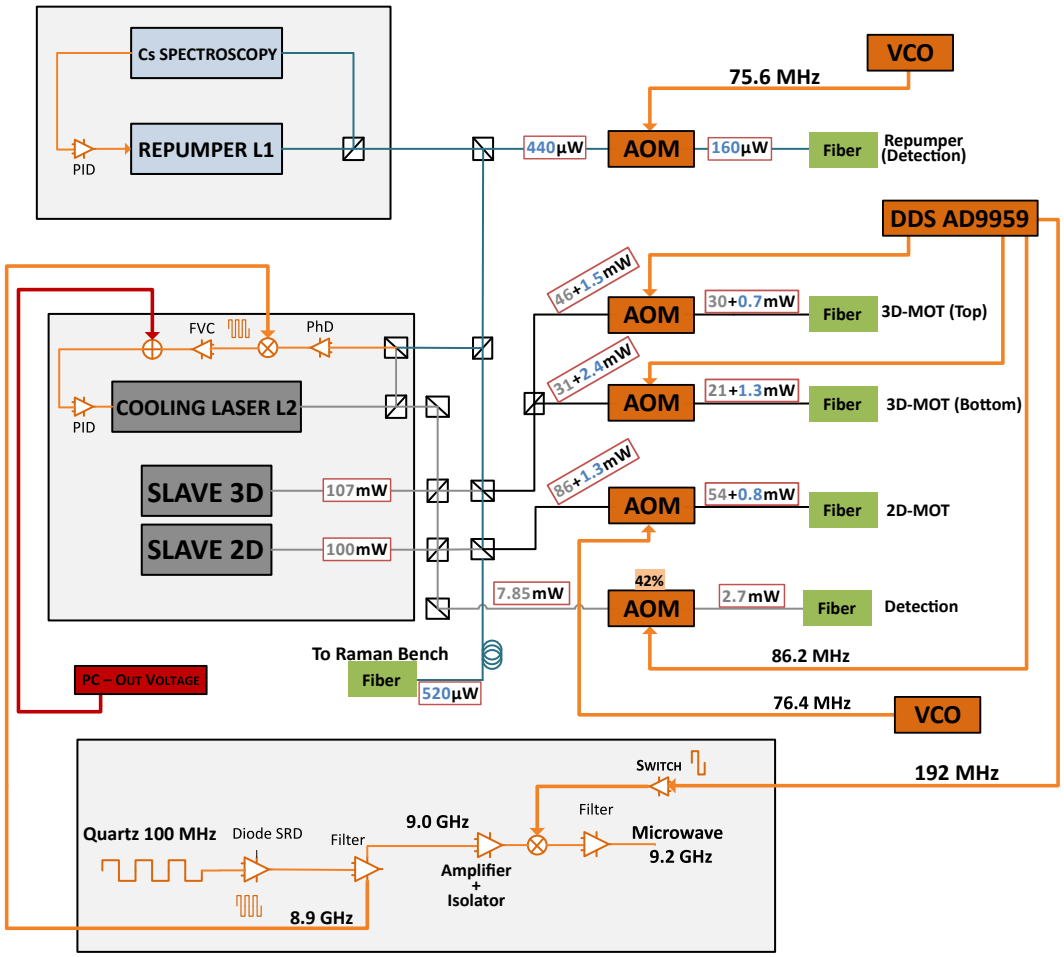

Figure 3.2: *Schematic representation of the cooling laser bench and relative frequency chain. The system is composed by two extended cavity diode laser and two slave diode laser.*

injection lock the 2 slave diodes responsible for the atom cooling inside the 2D-MOT and 3D-MOT.

2D-MOT and 3D-MOT slaves These are two slave diodes[1] both injection locked with L2. The powers are divided in 9 different fibers, 3 for 2D-MOT and 6 for the 3D-MOT.

3D MOT					
3.1	3.2	3.3	3.4	3.5	3.6
4.1mW	6.0mW	6.46mW	5.4mW	5.3mW	6.37mW
2D MOT					
6.1	6.2	6.3			
29mW	24mW	2.2mW			

Table 3.1: *Fiber input power for the 3D MOT and 2D MOT. The coupling efficiency has been measured 10 years ago and since has not been measured. Judging by the fluorescence signal we estimate a total coupling efficiency of 50%.*

3.1.3 Raman Laser system

The Raman bench is responsible for the generation of the light pulses to manipulate coherently the atomic wave-packet. It is composed by two ECDL(L3, L4) phase locked with each other, then optically amplified through the same single path tapered amplifier to reach the experiment.

L3 is locked to L1 by frequency locking their beat-note at 350 MHz, in such a way L3 is sufficiently far red detuned from the crossing transition $|6\ ^2S_{1/2}, F = 3\rangle \rightarrow |6\ ^2P_{3/2}, F' = 2/3\rangle$. This detuning $\Delta/2\pi \simeq 425$ MHz, enough to limit the spontaneous emission during the interrogation pulses.

L4 is phase locked to L3 with a variable frequency shift close to the hyperfine splitting, 9,192 GHz. The beating between the two lasers is then mixed with the dielectric resonator oscillator's (DRO) frequency, 9,383 GHz, producing a frequency of around 190 MHz. This frequency is sent to a phase lock loop where it is divided by two and then

[1] EYP-RWL-0850-00100-1500-SOT12-0000

compared with a signal at 95.55 MHz, the resulting feedback then acts on the cavity of L4.

Light amplification and pulse generation The total available power at the output of L3 and L4 ECDL is around 30 mW, which half of it is used for the locking system or is lost. To increase the total output power of the Raman bench, the two ECDLs are injected simultaneously and with the same polarization, into a *tapered amplifier*[2] (MOPA), reaching up to 350 mW after the optical isolator, using 1.6 A as forward current and depending on the power of the seed. The acousto-optic modulator (AOM) controls the length and shape of the light pulses which are then injected in the fibers leading to the Raman collimators. Thanks to a variable retarder we can inject only one fiber at a time.

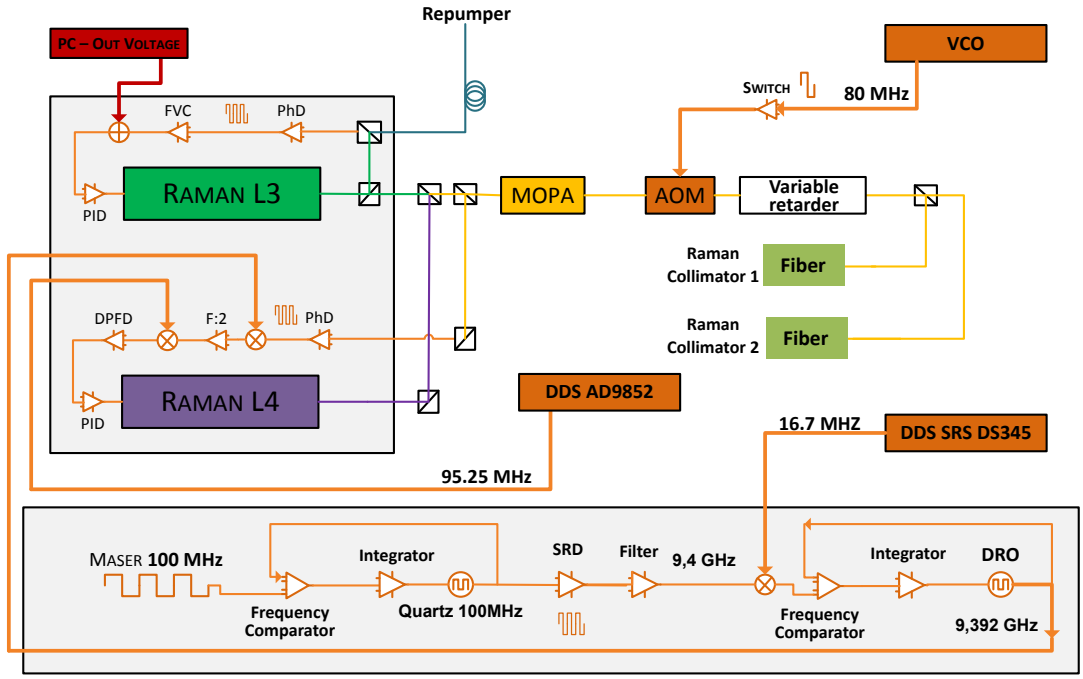

Figure 3.3: *Schematic representation of the Raman laser bench. The system is composed by two extended cavity diode laser and one Tapered amplifier. A voltage controlled variable retarder select the Raman collimator to use.*

[2]EYP-TPA-0850-02000-4006-CMT04-0000

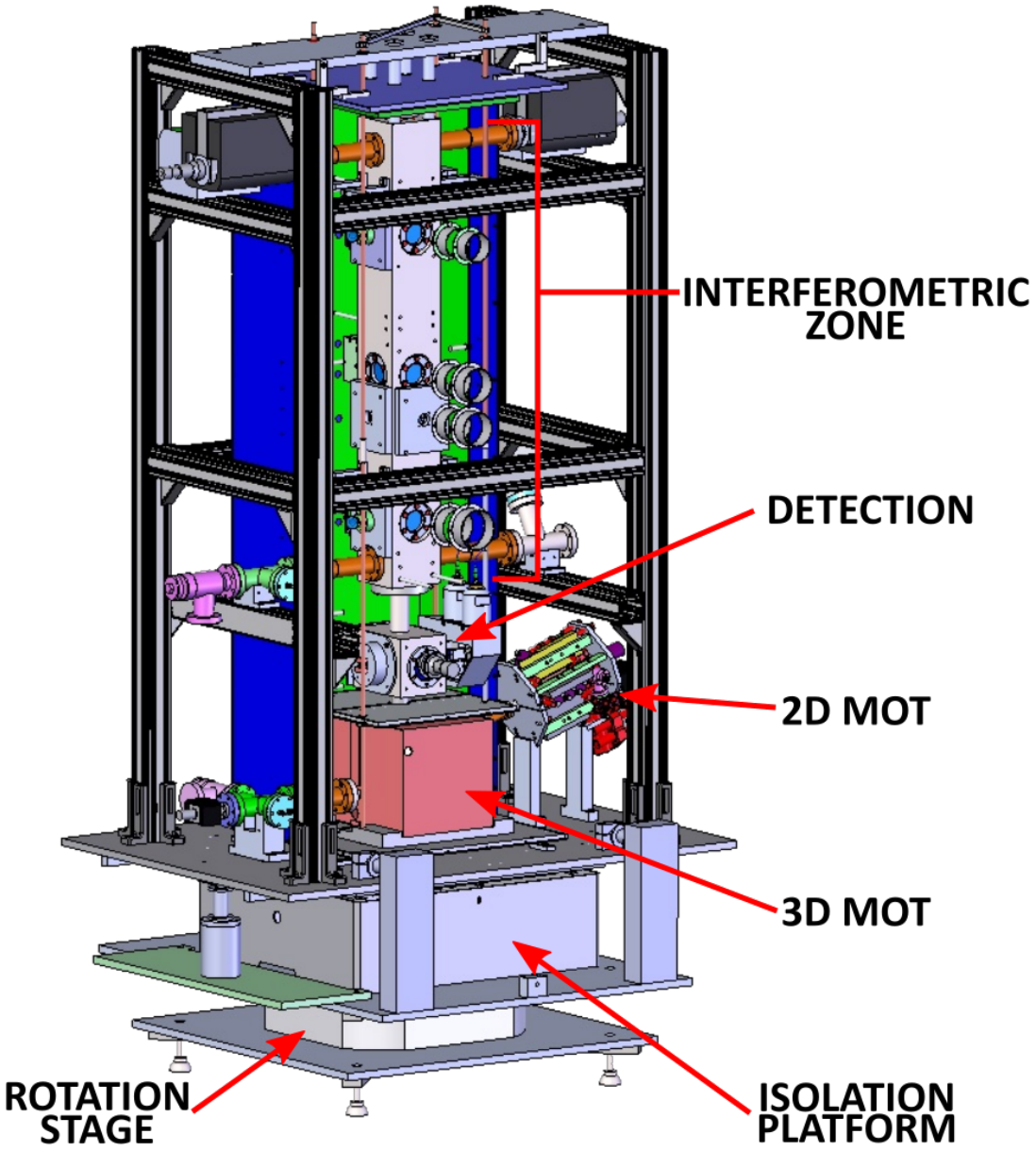

Figure 3.4: *Cad drawing of the full sensor structure highlighting the different sections of the experiment.*

3.2 Vacuum chamber - Atomic Fountain

The vacuum system is composed by four separated regions:

- **2D-MOT** Initial trapping and optimized loading of 3D MOT
- **3D-MOT** Trapping, cooling and launching of the atomic cloud
- **Interferometric zone** Probing of the atomic matter-wave with Raman Pulses
- **Detection** State population measurement by fluorescence

3.2.1 2D MOT

The scope of the 2D-MOT is to generate a flux of pre-cooled atoms that is pushed toward the 3D-MOT system. The complete scheme of the 2D-MOT is described in [27]. In short, two laser beams are used for trapping the atoms, thanks to a system of beam splitter and retro-reflection mirrors, constraining the thermal vapor in two transverse directions. A third beam is then used as a *pusher*, moving the trapped cloud toward the center of the 3D-MOT where it is re-captured and cooled down. Two pairs of rectangular coils are positioned inside the structure and produce a magnetic field gradient of 20 $\mathrm{G\,cm^{-1}}$[27]. The implementation of a 2D-MOT is useful to achieve a quick loading of the 3D-MOT.

3.2.2 3D MOT - Moving Molasses

The 3D-MOT is responsible for cooling and launching the atomic cloud.
It is composed by 6 independent laser beams, trapping the atoms along three directions in space. The beams realize 3 pairs of counter propagating beams in a $\sigma^+/\ \sigma^-$ configuration, forming two tetrahedron pointing each other, trapping the atoms at the center of the structure. Two pairs of coils provide the necessary magnetic fields; one in an anti-Helmholtz configuration for creating a B-field gradient during the trap, one in an Helmholtz configuration for compensating the residual bias field from other magnetic sources.

Cooling and Launching sequence

After the trapping phase is completed, the magnetic field is switched off in less than a 1 ms, then the atoms are maintained in an optical molasses and further cooled for 6 ms before being launched toward the interferometric region (a scheme of the full sequence can be seen in Figure 3.5). To accelerate the atoms vertically the frequency between

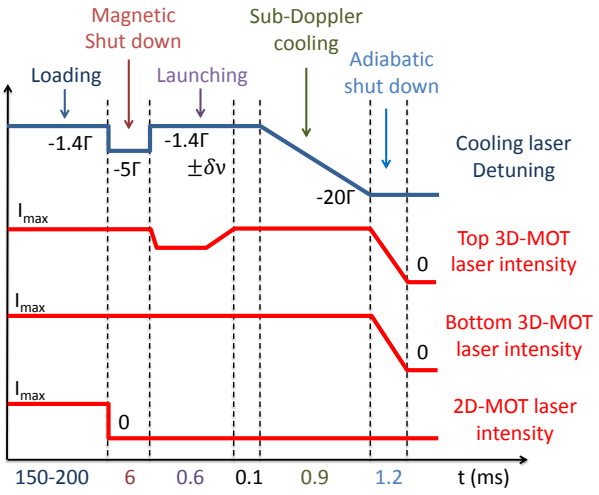

Figure 3.5: *Scheme showing the relative intensity for the MOT slave lasers and the reference frequency detuning during the trapping and launching phase.*

the top and the bottom sets of lasers get symmetrically detuned by $\pm\delta\nu$ by applying a frequency ramp to the respective AOMs. The resulting launch velocity can be calculated as:

$$v_0 = \frac{\sqrt{3}}{2}\, 2\delta\nu \cdot \lambda \tag{3.1}$$

In Figure 3.6 it is shown to see the relation between the launch velocity and the cooling laser detuning. In this work we used mostly, a launch velocity $v_0 = 5.043\ m \cdot s^{-1}$; this translates in a detuning of $\delta\nu = 3.38$MHz using Eq. (3.1). After the MOT and before the interrogation, the atoms are prepared in the $|F = 4, mF = 0\rangle$ state using a selection scheme based on the Stern-Gerlach effect (magnetic deflection of the atoms in $mF \neq 0$ states).

3.2.3 Detection Region

Above the 3D MOT is situated the Detection region, where the atomic cloud falls back after a parabolic flight in the interferometric region. The detection scheme is described in detail by [27, 28, 31] and, during the first year of my PhD, has been modified to reduce the overall detection noise [32].

In brief three light sheets, 3 cm wide each, are propagated along Y direction and then retro-reflected (see Figure 3.7); the top and bottom detection light sheets, of 1 cm height, are resonant on transition $|6\ ^2S_{1/2}, F = 4\rangle \rightarrow |6\ ^2P_{3/2}, F' = 5\rangle$, while the middle light sheet, only 0.2 cm tall, repumps atoms from $|6\ ^2S_{1/2}, F = 3\rangle$ to $|6\ ^2S_{1/2}, F = 4\rangle$

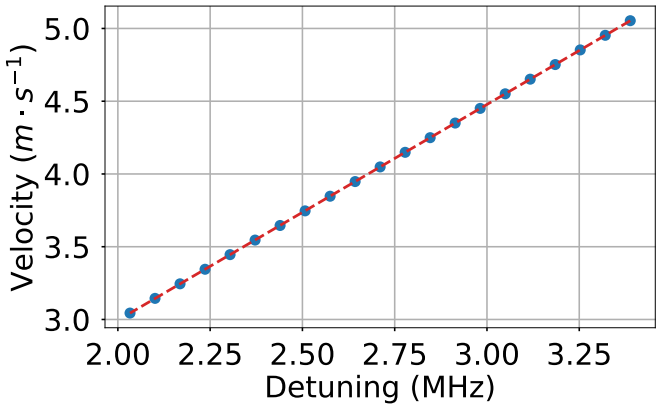

Figure 3.6: *Launch velocity versus lasers detuning. Higher velocities are not available since the cloud collides with the ceiling of the vacuum chamber. On the other hand 3.00* $m \cdot s^{-1}$ *is the lowest velocity to reach one of the Raman windows. The red dashed line is a linear fit of the data with slope* $m = 1.0048(1)\ m \cdot s^{-1} \cdot \mathrm{MHz}^{-1}$

state. Along the X direction two collection systems, gather the photons generated by fluorescence, onto a pair of bi-quadrant photodiodes[3]. The total collection efficiency for each photodiodes is 4%.

In Figure 3.8 is showed the output of the Mirror photodiode representing the time of flight of one atomic cloud. The fluorescence signal from the top sheet corresponds to the atoms only in the F=4 state, while the bottom light sheet will detect both atoms in F=4 and F=3.

Normalization and crosstalk

After the signals from each photodiodes are read with a 16bit acquisition card[4] they get integrated and processed. Since we are in the case were $I < I_{sat}$, we can assume the fluorescence to increase linearly with the number of atoms detected, we describe how the number of atoms in each state is calculated. Using a simple linear equation system we have:

$$\begin{pmatrix} N_4 \\ N_{tot} \end{pmatrix} = \begin{pmatrix} K_t & -C_{bt}K_b \\ -C_{tb}K_t & K_b \end{pmatrix} \begin{pmatrix} I_t \\ I_b \end{pmatrix} \tag{3.2}$$

where $I_{t,b}$ are the integrated signals from the *top* and *bottom* light sheets, K is a normalization factor, while $C_{tb,bt}$ are coefficients to compensate for the crosstalk between the two light sheet. In an ideal system C_{bt} and C_{tb} would be equal to 0, meaning that

[3]Hamamatsu S5870
[4]National Instrument PCIe-6341

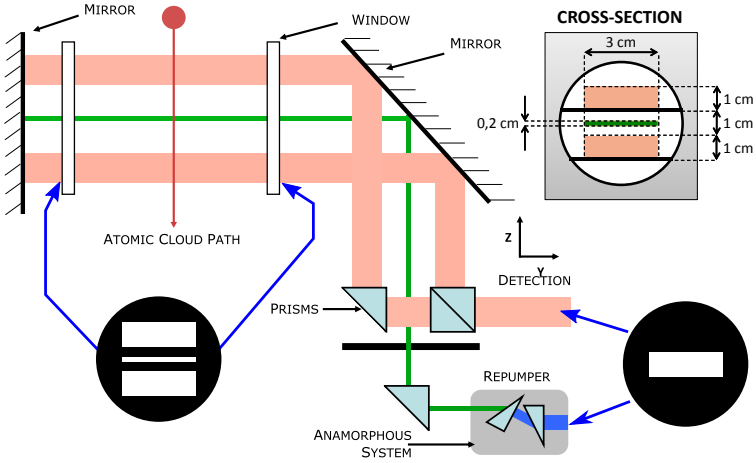

Figure 3.7: *Detection Scheme with the modification implemented in [32]. Black masks have been positioned to reduce stray light reflections and to improve the shape of the detection light-sheet.*

all photons generated by one light sheet are captured by the respective photodiodes quadrant. Since the fluorescence light from detected atoms, scatters in all direction, the bottom quadrant of the photodiodes can collect photons generated in the upper light sheet. The same effect is valid with photons generated in the lower light sheet, detected in the top quadrant. To compensate for this effects, we change the values of C_{bt} and C_{tb} by a few percent from their ideal values. By switching the initial state of the atoms, between $F = 4$ and $F = 3$ (obtained by using a microwave pulse as selection tool instead of Raman pulse), and without probing the atoms with no Raman lasers, we can finely adjust these values using the transition probability:

$$P = \frac{N_4}{N_{tot}} = \frac{N_4}{N_4 + N_3} \tag{3.3}$$

We expect to have transition probability $P = 1$ for a cloud with only atoms in F=4, since the atom count in the top and bottom light sheet should be the same. While on the other hand we expect to see a transition probability $P = 0$ in the case of an atomic ensemble prepared in the state F=3. Typical values of these crosstalk factors are usually around 15% for C_{bt} and 5% for C_{tb}.

Detection noise vs atom number

Different type of noise affect our probability measurements. The first type is linked to the technical nature of the detection. Each individual component of the detection, can

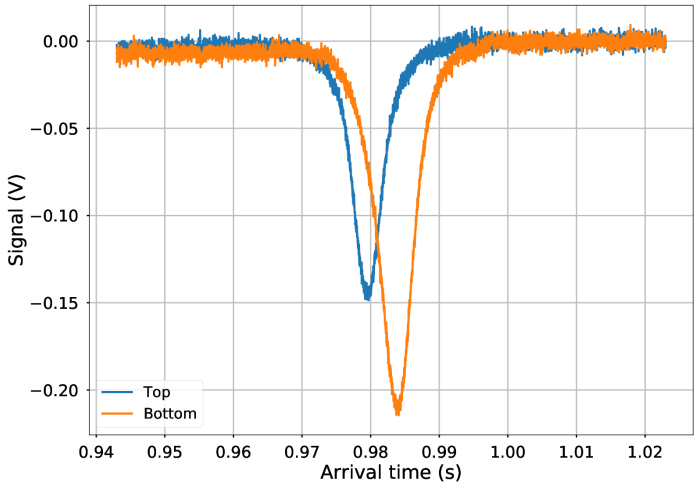

Figure 3.8: *Time of flight signals. The two colors represent the signals from different quadrant of the photodiodes. The top trace (blue) is proportional to the number of atoms in the state $F = 4$ while the bottom trace (yellow) measures the total number of atoms (that is why the signal is larger compared to the blue trace).*

contribute to the noise of the detection. As an example, the photodiodes noise, which is independent of atom number. Another example is the fluctuation in power or frequency of the probe lasers, leading to a noise which, on the contrary, scales proportionally with the number of atoms detected.
The other type of noise is more fundamental. We begin by describing the output wave function of the interferometer as $|\Psi\rangle = \alpha\,|F = 4\rangle + \beta\,|F = 3\rangle$, and the projection operator as $\Pi_4 = |F = 4\rangle\,\langle F = 4|$. The probability of measuring an atom in the state $F = 4$ is given by $P = |\alpha|^2$ and consequently $1 - P = |\beta|^2$ for an atom in the $F = 3$ state. The variance for a single probability measurement then will be:

$$\sigma_4^2 = \langle \Pi_4^2 \rangle - \langle \Pi_4 \rangle^2 = P - P^2 = P(1 - P)$$

Since the atomic cloud is composed by N independent atoms the total variance can be calculated as $\sigma_P^2 = \sigma_{N_4}^2/N$, this constitutes the ultimate limit for our detection, the quantum projection limit.
It is important, to improve the sensitivity of the sensor, to measure the source of the noise limiting us, being it technical noise, which can be improved, or if the quantum

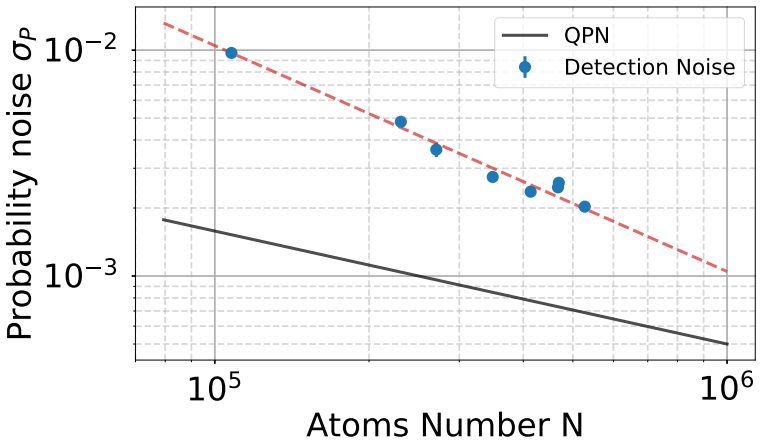

Figure 3.9: *Characterization of probability noise as a function of number of atoms. The black line indicates the quantum projection noise, while the red line is a guide (1/N) to show the trend of the blue data points.*

projection limit is reached. In Figure 3.9 a characterization of the detection noise is shown. We vary the number of atoms launched by changing the duration of the cooling sequence. We can study how the detection noise varies with a changing number of atoms detected. With the black line, we show the quantum projection noise calculated at mid-fringe ($\sigma_{P_N} = \frac{1}{2\sqrt{N}}$).
As the dashed red line shows, the trend of the blue point indicates that we are still in a regime where the limiting noise is proportional to the number of atoms. We operate between 4 and $5{\cdot}10^5$ atoms, this corresponds to a $\sigma_P \simeq 3 \cdot 10^{-3}$. Such level of probability noise translates to a signal of $1.2 \cdot 10^{-8}$ rad $\cdot$ s^{-1} for a 10% contrast. which is a typical value at which we operate.

3.2.4 Interferometric Region

Thanks to the several windows, 4 for each side of the chamber, the interferometric chamber opens up the possibility to use different interrogation time as well as different configurations, 4 pulses, 3 pulses. On one side of the chamber, all 4 windows are fitted with a mounted mirror, a black cover and an adjustable quarter-wave plate. Since the output of the collimator is linearly polarized for both Raman laser at the same time, a the quarter-wave plate is needed to achieve a **lin** $\perp$ **lin** transition scheme with counter-propagating beams. In the case of counter-propagating beam then, it becomes necessary to resolve the degeneracy between the different transfered momentum $\pm\hbar k_{eff} = \hbar(k_1 +$

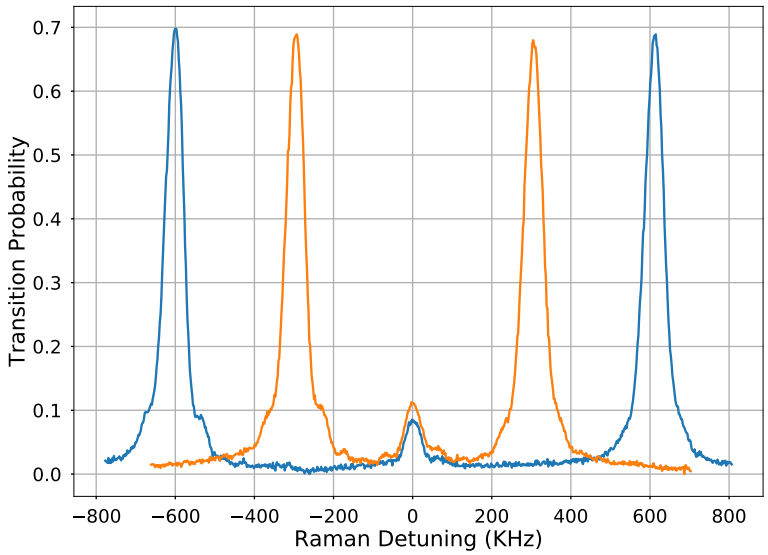

Figure 3.10: *Frequency Spectrum at different Raman windows. The blue traces is obtained at the first windows and is characterized by a larger Doppler shift between the co-propagating peak and the two counter-propagating peaks. The yellow trace is obtained at the fourth Raman windows, where the atomic cloud is closer to the apex of the ballistic trajectory, thus the counter-propagating peaks have a smaller Doppler shift. Here we used a* $\tau = 70$ *µs light pulse duration and the averaged width is* $\bar{\sigma_f} = 26.27 \pm 0.57$ kHz

k_2).

To overcome this, the Raman collimator and the relative mirrors, are tilted with an angle of 3.8° respect to the gravity acceleration $\vec{g}$, this introduces a Doppler shift as:

$$\omega_D = \vec{v}(t) \cdot \vec{k}_{eff} = \pm(v_0 - gt) \cdot \sin\theta \cdot k_{eff} \tag{3.4}$$

where v_0 is the launch velocity, t is the timing of the pulses, θ is the angle of the collimator and k_{eff} is the effective momentum exchanged. We remove the degeneracy when the Doppler shift between the peaks, becomes large enough to completely discern the Doppler width for the velocity distribution. In order to reconstruct the full Doppler width, we change the relative detuning between the two Raman lasers, L3 and L4.

In Figure 3.10 different pairs of Doppler shifts are shown; the two curves have been acquired at different windows, this translates to a different mean velocity of the atomic cloud. The parallelism between the collimator can be roughly tested by using (3.4). Initially the cloud is launched at 5.014 $\mathrm{m\,s^{-1}}$, at this velocity it reaches the first and

fourth window after respectively 0.114ms and 0.314ms. The difference between the peaks for H1 windows is around 1,2 MHz while $(v_0 - gt) \approx 4\,\mathrm{m\,s^{-1}}$, using (3.4) we find $\theta = 3.796° \pm 0.008°$.

3.2.5 Rabi oscillation

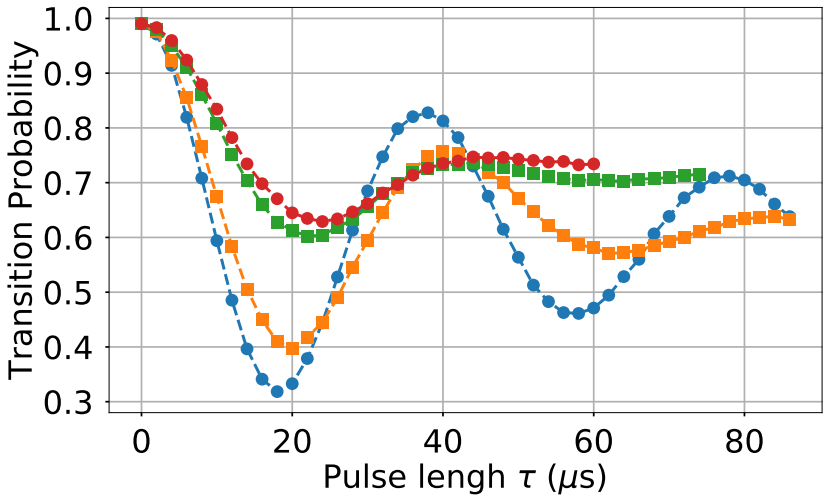

Figure 3.11: *Rabi oscillation of the $\frac{\pi}{2}$ light pulse at the bottom (circle marker) and top (square marker) Raman windows. The blue (orange) curve is acquired after a time of flight of* 114 ms (314 ms) *while the cloud is going upwards. The green (red) curve is acquired after a time of flight of* 714 ms (914 ms) *while the cloud is falling down.*

In Figure 3.11 we present the Rabi oscillation performed at the top and bottom Raman windows for a cloud going upwards and for the cloud falling down. As we can see the transfer efficiency is limited due to the velocity selectivity of the counter-propagating Raman transition. This means only the velocity classes in the cloud that satisfy the resonant condition, Eq. (2.8), are affected by the light-pulses. A clear difference is also visible between the curves obtained with the cloud going up and the curves obtained with the cloud falling down. As the cloud expands, the atoms are more sensitive to the intensity inhomogeneity of the Raman laser pairs. This effect appears as a damping factor in the Rabi oscillation which is especially visible after long time of flight (green and red curves). A solution to mitigate this effect has been studied in [47] with the use of a top-hat laser beam; in Appendix B I describe my contribution to this work.

3.3 Vibration Isolation Platform

All of the experiment rests on top of a *Minus K* platform. This platform has a resonant frequency around 0.5 Hz with a maximum load about 400 kg.

In Figure 3.12 we can see the transfer function of the *Minus K* in the 3 axis direction.

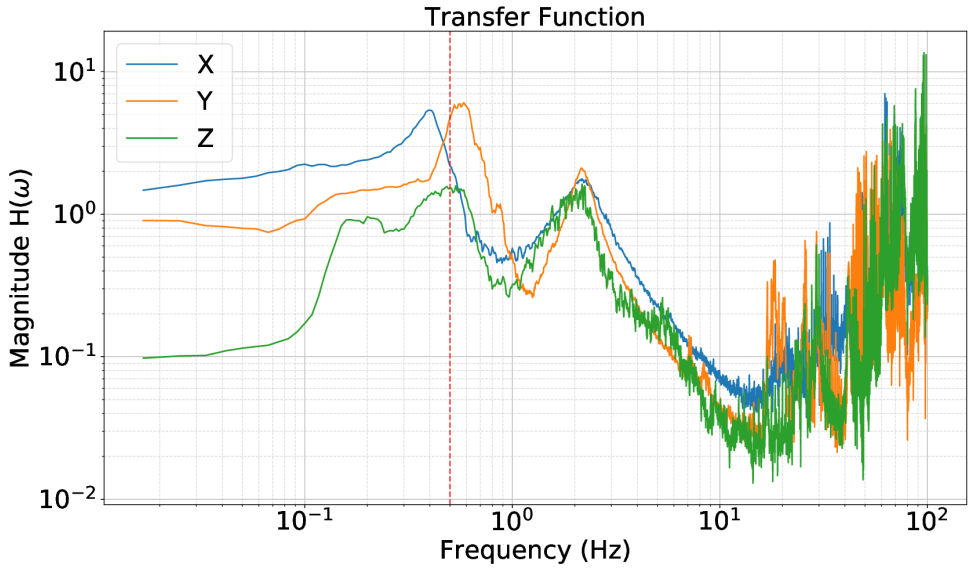

Figure 3.12: *Transfer Function Ground - Minus K. The vertical dashed red line indicates the nominal resonant frequency for the isolation platform. As we can see all three direction present a resonant peak close to this line. To adjust the position of such peak, on the horizontal direction can be done by adjusting the weights on top of it, while for the vertical direction Z, this adjustment are done by adjusting the stiffness of the internal springs.*

Such graph has been calculated by comparing the signal from a seismometer situated on the platform and one situated on the ground. As expected a peak is present around the resonant frequency of the platform, around 0.5 Hz,shown with a red dashed line. A second peak is very prominent around 2Hz; this feature is being associated with a rotation mode of the experiment. This hypothesis can be confirmed by looking at the signal of the two seismometer when both of the sensors are attached to the experiment. By taking the half difference and the half sum of the signals from the two seismometers we can distinguish which vibration measurements come from rotations instead of common accelerations.

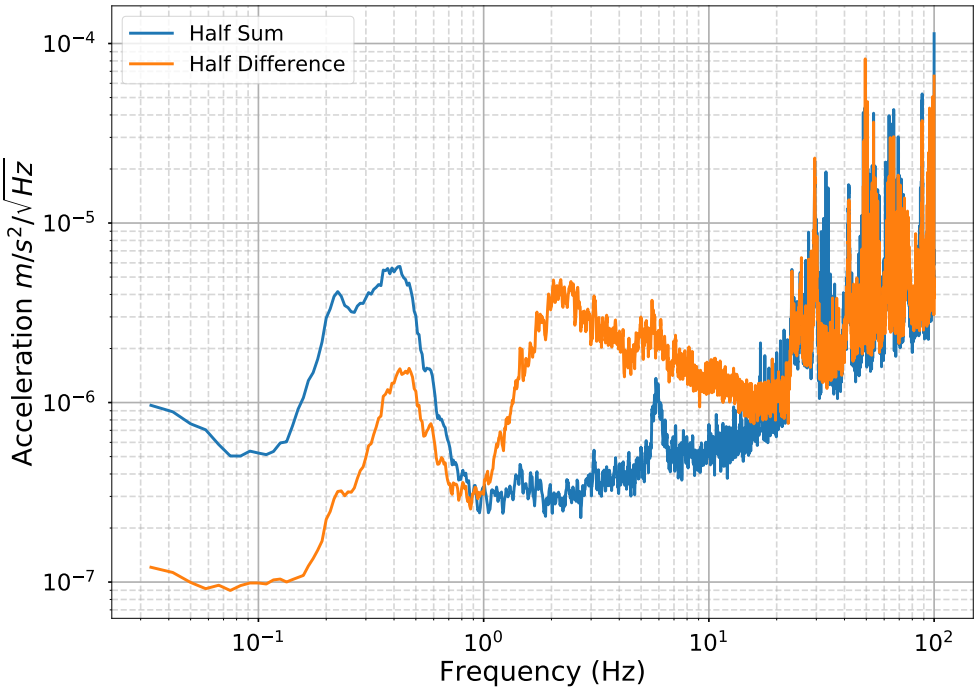

Figure 3.13: *Spectrum of acceleration (half sum, blue) and rotation (half difference, orange) noise along the horizontal axis of the Raman beams. From this graph is clear how the peak at 2 Hz, (seen also in Figure 3.12) is linked to rotational motions of the sensor.*

We can estimate how each frequency band contributes to the AI's phase by using the transfer function $|H_a(\omega)|$ of the 4-pulse AI, introduced in Section 2.5.2:

$$\sigma_\Phi^2 = \int_{f_1}^{f_2} |H_a(\omega)|^2 S_a(\omega) \frac{d\omega}{2\pi} \tag{3.5}$$

where $S_a(\omega)$ is the Power Spectral Density (PSD) of the vibration noise. As we can see, in Table 3.2 most of vibration noise contribution comes from the frequencies between 0.1 and 1 Hz while for the other frequency band the contribution is almost the same.

3.4 Rotation Stage

As it can be seen in Eq 2.26, the phase shift of the gyroscope depends on the relative alignment between the effective k vector and the North. In order to study the scale

Frequency	0.1-1	1-10	10-100	Hz
$\sigma_{\phi\ vib}$	2.15	0.89	0.51	rad

Table 3.2: *Vibration phase contribution for different frequency band. The total phase noise will be compensated in real time during the interferometer, see Sec 4.2.2.*

factor of the gyroscope or to determine possible biases, we need to be able to rotate the sensor about its vertical axis. In order to turn the whole experiment a rotating stage *ALAR-250LP* by Aerotech has been implemented. The stage is a brush-less slotless motor capable of freely rotating, with a precision of 10 μrad and a maximum payloads of 500kg. To control and supply the rotation stage we use a *Soloist HLe Controller* which is a single-axis digital servo controller with integral power supply and amplifier, which can be connected to a control computer through USB or Ethernet. To remotely drive the stage we need to *fine-tune* the servo loop gains of the controller. This operation is very critical and a wrong optimization could lead the sensor to spin uncontrollably. Since at the moment we are not able to perform a full rotation of the sensor due to the length of multiple cables, we have not yet performed the tuning of the controller in order to avoid to catastrophically pull on these. Nevertheless the controller allow us to easily know the angle of rotation, by reading the internal encoder of the motor stage, without any necessary optimization. We then utilize two brass block to lock the stage in position and a script to monitor its angle.
The stage does not provide any solution to reduce ground vibration and its requirements for planarity of the floor are pretty high, 1 μm per 50 mm. A first design to comply with this problems can be seen in Figure 3.14. The rotation stage is screwed on top of an aluminium plate on top of 4 adjustable feet, in order to ensure its axis of rotation is aligned with $\vec{g}$. A second plate is screwed on the top of the motor ring and it is used to support the vibration isolation and gyroscope setup. Both plates are reinforced with two steel bars in a cross configuration, in order to help the plates maintain their flatness.

In Figure 3.15 we can see a comparison of the vibration noise spectrum before and after the rotation stage was being implemented. The plot shows very comparable noise levels. Using (3.5) we can estimate the contribution to the phase with the new setup.
Table 3.3 shows the difference in the estimated vibration phase calculated from the acceleration measurements.

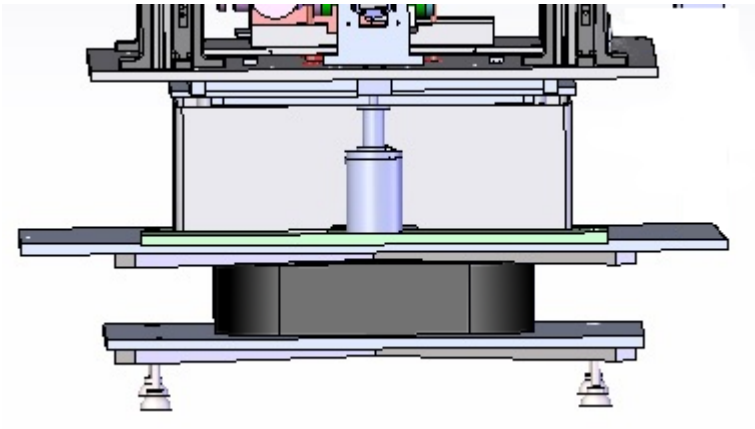

Figure 3.14: *CAD drawing of the rotation stage positioned below the isolation platform. The feet of the bottom plate can be adjusted in order to adjust the inclination of the rotation stage. In the picture is also possible to see one of the voice coil actuator used to lock the tilt of the experiment.*

Frequency	0.01-0.1	0.1-1	1-10	10-100	Tot	Hz
Minus K	0.01	2.15	0.89	0.51	3.55	rad
Minus K + Alar	0.02	2.15	0.89	0.51	3.56	rad

Table 3.3: *Vibration phase contribution for different frequency band. As we can see, the largest contribution comes from acceleration in the frequency band 0.1 and 1* Hz*, which contains the resonance of the isolation platform.*

3.4.1 New Tilt Lock coil

Fluctuation in the projection of $\vec{g}$ onto the direction of our Raman laser pair, can induce fluctuation in the trajectory of the atoms which as a consequence could bring phase shift uncounted for. Other phase shift could arise if the gyroscope is operated with an asymmetric timing configuration. This configuration, render the 4-pulse sequence sensitive to DC acceleration as seen in:

$$\Phi_{acc} = 2\vec{k}_{eff} \cdot \vec{g} T \Delta T \tag{3.6}$$

These fluctuation can introduce phase shift of $\sim$ 50 mrad for a change in projection of 10μrad. To achieve a satisfactory long term stability then, it becomes necessary to stabilize the tilt of the experiment.
A locking system has been implemented, first in the Raman lasers direction [31], then

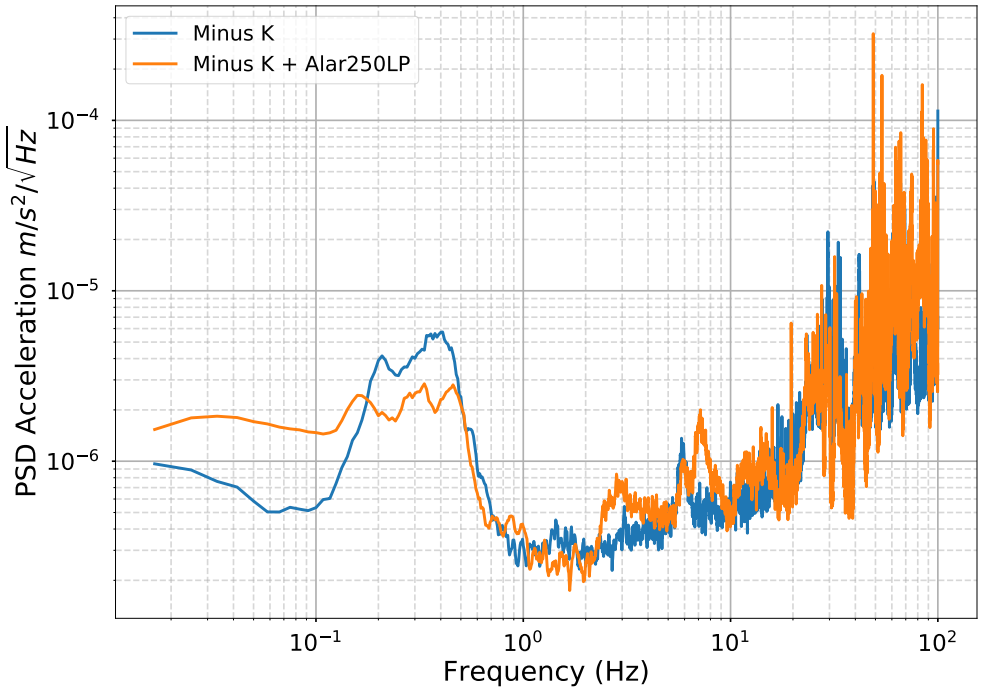

Figure 3.15: *Comparison of the acceleration noise spectrum with only the isolation platform* Minus k *(blue) and the combination of the isolation platform with the rotation stage* Alar250LP *(orange).*

in the transverse direction [32]. The system is composed by a 2 axis tiltmeter[5] and two separate voice-coil actuator. The voice-coil actuator are made in house and consist of two coils of 270 spires, with inner radius of 30 mm and with an height of 50 mm. Since the coils have to sustain 1 A as average current, support is made in aluminum to help with the heat dissipation. The locking system consists of a feedback loop, which is a simple numerical integrator, which generates a control voltage signal, based on the tilt of the experiment acquired from the tiltmeter. This signal is then sent to a *Delta Electronika ES300* power supply, which converts it to a stable current signal. The output of power supply is connected to the coil and the permanent magnet is connected to the isolation platform below the experiment. Two of these systems are implemented, one for both directions of the tiltmeter. In the direction of the Raman beams, which denote the

[5] Applied Geomechanics Incorporated 700-series HighGain version

X direction, the actuator is able to lock the tilt with a stability of 0.2 nrad $\cdot$ s^{-1} after 10 seconds [32]. In the transverse direction, denoted as Y, the actuator fails to lock if the actual tilt of the experiment drifts too far from the chosen set point. This shorter active range, is thought to be a consequence of the higher inertial mass present on the experiment along the Y direction compared to the X direction.

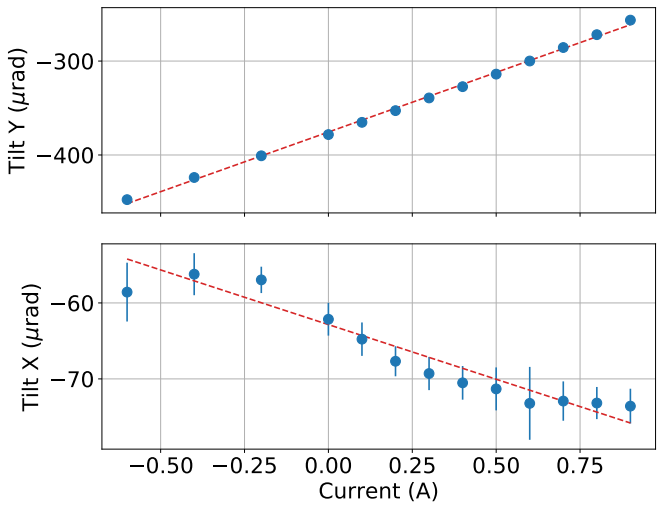

Figure 3.16: *Inclination of the experiment in the Y and X direction as a function of current. We tested the new coil design by manually changing the current in the voice-coil and measuring the inclination of the experiment. We tilted the experiment along the Y direction (top) and we obtained a scale factor of* 127.0$\pm$1.7 μrad/A*, five time higher than previous coil. The cross talk on the X direction remained the same,* 14.4 $\pm$ 1.4 μrad/A*.*

To overcome this limitation, a new design for the coil holder has been designed and tested. The new design allows to wind more spires around the support piece, while maintaining the same inner radius of the old support, effectively increasing the total field. We are able to wind around 1000 turns around this new support increasing by a factor of almost 5 the field generated. We then proceed to measure the capabilities of this new voice-coil actuator directly on the experiment. The previous actuator could achieve 23 μrad $\cdot A^{-1}$ in the Y direction with a crosstalk of 15 μrad $\cdot A^{-1}$ in the X direction [32]. With the new support we reach a scale factor of 127 μrad $\cdot A^{-1}$ while maintaining the same level of crosstalk as before, as can be seen in Figure 3.16. The implementation of this new actuator has been a decisive upgrade in the study of systematic effects linked to improper setup of the mean trajectory of the atoms as we will see in future chapter.

3.5 Conclusion

In this chapter I presented most of the elements that make up the SYRTE cold atom gyroscope. The design of the sensor is more than 10 years old but different modification and improvements have been implemented during the course of my thesis. Most notably the modification to the detection system and the implementation of the piezo-motor mirror mount, described in more details in [32], and finally the rotation stage. Most of the results I will present in the next chapter would not have been achievable if these upgrades were not implemented.

Chapter 4

Interleaved atom interferometry for improved sensitivity

In this chapter, I will present techniques that are in use on the cold atom gyroscope at SYRTE. These techniques aim to overcome the limitation imposed by having *dead time* in the scheme of operation for a cold atom sensor. I will describe a solution that has been studied and implemented on the gyroscope by previous PhD students [28, 31], which relies on the use of a *joint scheme* to eliminate dead time in the sequence of the sensor. During the first year of my PhD, I then contributed to the implementation of an *interleaved* scheme, which aims to increase the sampling rate of the gyroscope, that I will describe in this chapter.

This scheme has been setup by Denis Savoie during his thesis [32]. I have participated in the optimization and the achievement of the best performances [33]. These parts are well detailed in his manuscript. I will recall here the methods and the main results in term of stability. Thereafter, I studied the gyroscope's response to weak dynamic rotation rate. By making use of the high sampling rate, I was able to measure the weak rotation rate signals in a regime that was not studied before for a cold atom sensor.

4.1 Continuous operation

4.1.1 Joint measurement

The general sequence of operation for a cold-atom inertial sensor can be summarized in few steps: we first prepare a cold ensemble of atoms, then interrogate the ensemble with light pulses and finally we detect the output states. All of these processes are executed sequentially before the following measurement is performed. The total duration is the

cycling time, T_c.

During the cooling and the detection phases no atomic cloud is being probed inside the interferometric region. Since no measurements are being performed, these phases are then considered as *dead time* for the sensor. The presence of dead time is a major limitation for inertial sensor with cold-atoms; similarly to the Dick effect for atomic clocks [48, 49], the presence of dead time deteriorates the stability of the sensor, due to an aliasing of the noise, for example vibration noise. The loss of information also prevents the correct reconstruction of inertial signal that vary rapidly in time [50].

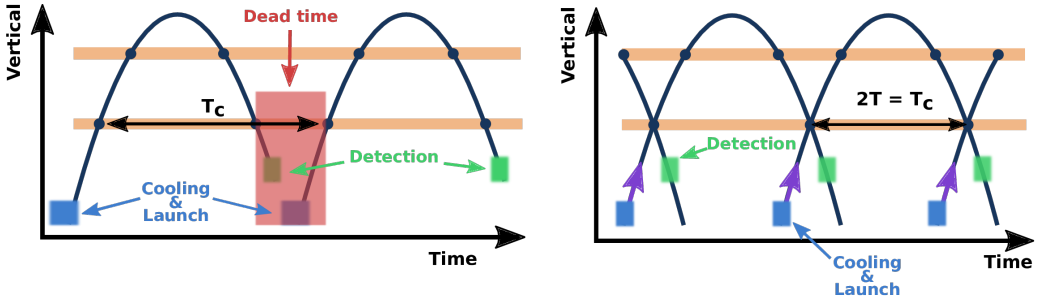

(a) *Usual sequential scheme* **(b)** *Joint Scheme*

Figure 4.1: *Comparison between the sequential scheme with dead times* **(a)** *and with continuous interrogation* **(b)**

To avoid these problems one has to setup a scheme of operation that allows the sensor to measure in *continuous*, even during the cooling and detection phases.

Once the first cloud has almost reached the bottom window before the last pulse, the new cloud is launched. By carefully matching the timings, both clouds arrive in front of the window at the same time and share the same $\pi/2$ pulse. With this method the cycling time T_c is reduced to be equal to the interrogation time $2T$.

4.1.2 Interleaved Sequence

The sampling frequency of the experiment, even after the implementation of a joint scheme, still remain fairly low due to the long flight time of the atoms inside the interferometric region. While reducing the time of flight of the atoms is a possibility, this choice leads to a reduction of the scale factor since the sensitivity scales as T^3. An improved scheme has been implemented [32] during the first year of my PhD, which relies on interleaving multiple joint sequence together. Exploiting this long flight time,

we prepare and launch a cold-atom cloud every 2T/3, where 2T is the interrogation time having then 3 independent and joint atom interferometer. A visualization of triple joint interleaved can be seen in Figure 4.2.

Interleaving higher number of interferometers was not possible due to technical lim-

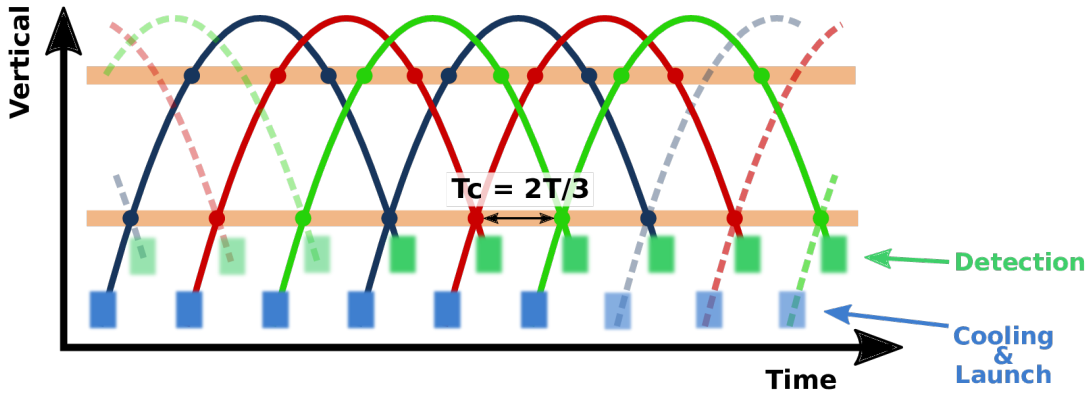

Figure 4.2: *Representation in time-space of 3 interleaved continuous atom interferometer, where each color represents a different joint sequence.*

itation given by the design of our sensor. Another limitation is the possibility to use only an odd number of interleaved sequence. This comes from the necessity to ramp the frequency of the Raman lasers to compensate for the Doppler effect. In a simple joint scheme, two consecutive interferometer share the first and last $\pi/2$-pulse. This requires the Raman lasers to be at resonance for both cloud at the same time. With our design, this condition is satisfied by changing the sign of the ramp at the moment of the light pulse. This means we acquire measurements with alternating $+k_{eff}$ and $-k_{eff}$ momentum transfered. If we were to interleave two joint scheme, we would be in a condition where interferometers with the same sign of k_{eff} share a π-pulse, see Figure 4.3. In this condition we would not be able to satisfy the resonance condition due to Doppler effect for both cloud at the same time. By extension a sequence $2n$-interleaved would be equivalent to interleaving n-times a two joint scheme, meaning that with even number of interleaved sequence, the resonance condition cannot be satisfied for all interferometers. A solution would be to implement a double diffraction scheme where there is no Doppler effect.

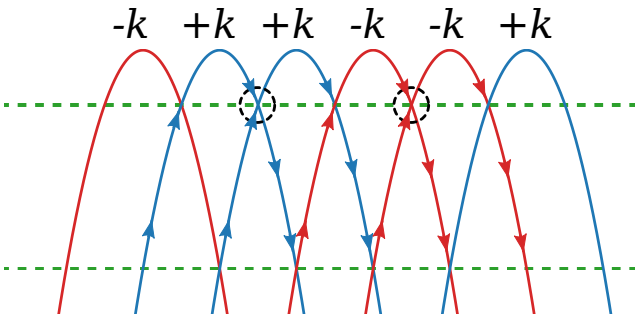

Figure 4.3: *Geometry for a double interleaved atom interferometer. As we can see in this configuration AIs with the same k_{eff} share a pulse while the wave packets have opposite mean velocities. In a simple diffraction scheme this configuration cannot be satisfied as the two clouds have different resonant conditions.*

4.2 Methods

4.2.1 Acquisition and processing based on seismometers

Our sensor is insensitive to DC acceleration, therefore a large contribution to the phase noise of the interferometer comes from vibrations (AC-accelerations), see Sec 2.4.1. To better understand this contribution, we show on the right in Figure 4.4, the correlation between the transition probability and the reconstructed vibration phase, ϕ_{vib}. To determine this vibration phase we use two separate seismometers[1]. They are rigidly fixed to the structure that holds the vacuum chamber and are positioned in proximity of the Raman retro reflection mirrors. We can independently estimate the rotation and the horizontal acceleration, using linear combination of the signal recorded during the interrogation time 2T, see Figure 4.6. To do so, we combine the measured vibration signal with the transfer function of our sensor to estimate the phase noise linked to the vibration of the mirrors and rotation of the apparatus, as explained in Sec. 3.3. As shown in Figure 4.4, the vibration phase ϕ_{vib} can sample multiple periods of the interference fringes. This leads a significant number of occurrence to accumulate around the maximum and minimum of the fringes, as can be seen in the histogram on the left side of Figure 4.4. The sensitivity of the interferometer around these extremes vanishes. Effectively operating without *dead-times* requires to overcome this problem.

[1] Trillium Compact Seismometer - 108 Hz-120.2 s bandwidth

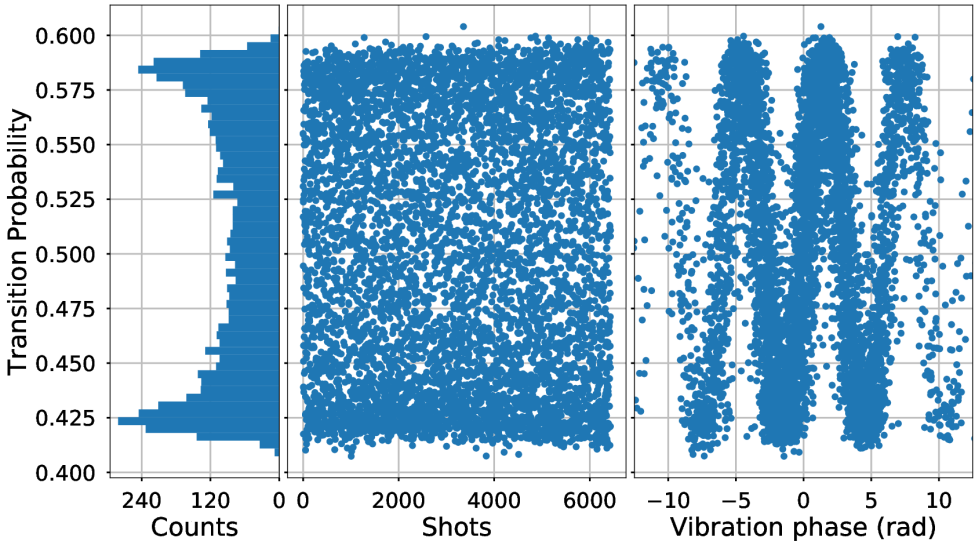

Figure 4.4: *Acquisition of 6100 points. On the left, the distribution of probability shows the expected twin-horned shape. On the right, we can see the reconstructed fringes using vibration phase as* x*-axis. The span of the vibration phase* ϕ_{vib} *is as estimated in Section 3.3*

4.2.2 Real-time Compensation of vibration noise

The ideal condition would be to operate the sensor in the linear regime, that is the middle of the fringe, to maximize the sensitivity of the sensor. To operate at the middle of the fringe we first need to reduce the contribution from the vibration noise to the AI phase such as to fit into the center of a single fringe. A possible solution is to correct the relative phase between the Raman lasers [51] just before the last pulse, in order to compensate ϕ_{vib} *in real time*.

This operation, requires a finite amount of time to be performed, due to the time needed to integrate the signals and the response time of DDS, which is controlled by a GPIB interface. We apply a phase correction 15 ms before the end of the interrogation time 2T to compensate for this limitation. The vibration noise is recorded until this time, and the missing part, to complete a 2T long acquisition, is filled with an average of the signal from 15 ms before the correction timing. We have verified that the error in the estimation of the correction with this method is negligible (70 mrad per shot) at the moment [32].

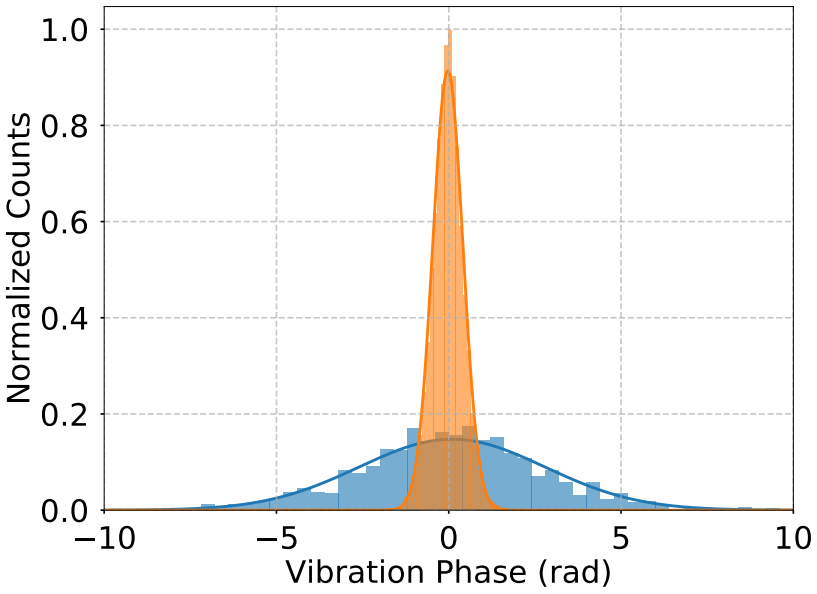

Figure 4.5: *Distribution of the reconstructed vibration phase in the case of uncompensated measurements (blue, $\sigma = 2.70$rad) and for compensated in real time measurements (orange, $\sigma = 0.44$rad) .*

In Figure 4.5 we show the difference between the measured distribution for the vibration phase in the case of uncompensated acceleration noise versus the compensated one. In the case where the AI operates without real time compensation, the measurements have a standard deviation of 2.70 rad (blue counts) while in the compensated case we have a standard deviation of 0.44 rad. The use of the signal from a classical sensor to real time compensate the vibration, acts as a filter for the vibration noise. This technique exploits the best feature of classical and quantum sensor: the accuracy and long term stability of the atom interferometer and the large bandwidth of classical sensors.

4.2.3 Mid Fringe Lock

As showed in the previous section, real-time compensation of vibration noise constrain the measurements inside a single fringe. This method, do not compensate for DC-phase shift and do not prevent the phase of the AI from drifting during an acquisition. These shifts are generally caused from systematics effects such as the fluctuations of lightshift or alignment between the Raman retro-reflection mirrors. A locking system has been put in place to steer the AI toward the middle of the fringe and stabilize it there for the

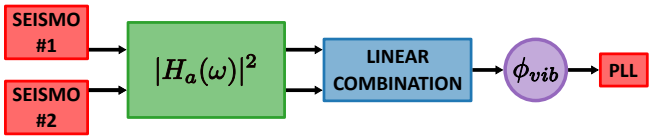

Figure 4.6: *Simple scheme to illustrate how ϕ_{vib} is calculated. The individual signals from the seismometers are first convolved with the transfer function $|H_a(\omega)|$ and then are combined together. The resulting vibration phase ϕ_{vib} is then sent to the PLL for compensation.*

whole duration of the acquisition. To estimate the average DC phase shift we alternate measurements between the two sides of the fringe. This is done by applying additional π phase-shift between each shot. The error signal of this locking scheme is calculated from the difference of transition probability between consecutive measurements.

This phase locking loop is a pure integrator. The feedback for the $i+1$ measurement can be described as follow:

$$\phi_{i+1}^{MFL} = G\sum_{j=0}^{i}(-1)^j(P_j - P_{j-1}) = G\ (-1)^i\ (P_i - P_{i-1}) + \phi_{i-1}^{MFL} \tag{4.1}$$

where ϕ_{i-1}^{MFL} is the phase jump applied to the *i-1* measurement, G is the gain of the lock, P_i is the transition probability. We adjust the value of the gain G in order for the sensor to need less than a minute to reach a locking point. With this magnitude of effective gain the sensor needs few hundreds shots to reach a stable locking point, as can be seen in Figure 4.7 in the first 30 seconds. The full phase shift added to the atom interferometer then is:

$$\phi_i^{DDS} = \phi_i^{vib} + \phi_i^{MFL} + (-1)^i \times \frac{\pi}{2} \tag{4.2}$$

4.3 Sensitivity of the Gyroscope

In the previous section we have presented how we overcome the limitation of dead-time and operate the sensor in the linear regime, thus at the best sensitivity. To demonstrate the effectiveness of these techniques we measure Earth rotation rate continuously for 30 hours and evaluate the performance of our AI sensor. In Figure 4.8 we can see the extracted time-trace for the total phase of the interferometer after the real time correction

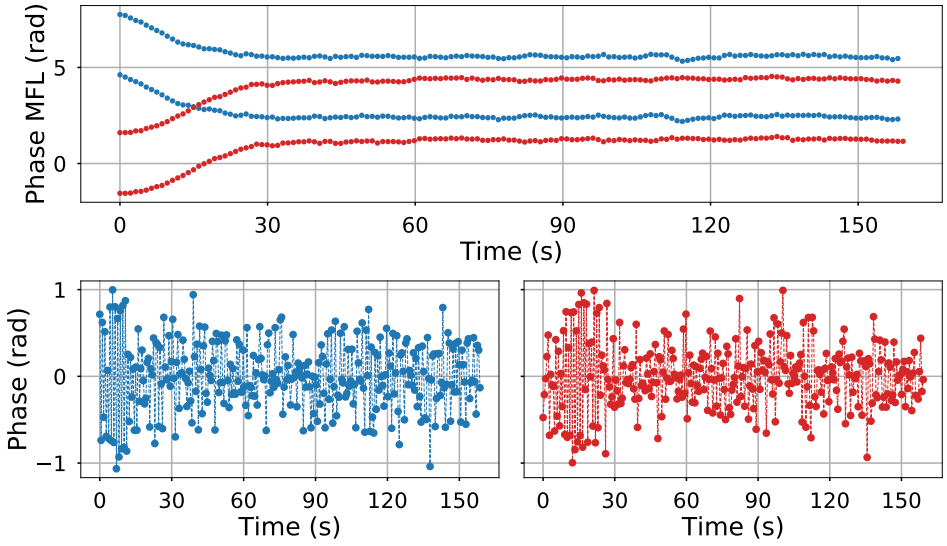

Figure 4.7: *(Top) Time trace of ϕ^{MFL} showing how the lock converges to a stable point. The two colors represent the two sign of the momentum transfer, blue for $+k_{eff}$ and red for $-k_{eff}$. Each momentum then is divided in two subset depending on the sign of $(-1)^n \times \frac{\pi}{2}$ to separate which side of the fringe we are probing. (Bottom) Time traces of the atomic phase for $+k_{eff}$ and $-k_{eff}$. The graphs show how the measurements have a larger dispersion, shot to shot, while the interferometer is not yet locked ($t < 30$ s).*

of the phase. In order to suppress systematic effects that don't depend on the direction of $\vec{k}_{eff}$, such as 1 photon light shift, we rely on the k_{eff} reversal techniques. A single measurement then becomes the combination of two measurements done with opposite sign of effective exchanged momentum, $\pm k_{eff}$. This operation allows us to isolate phase shifts that are solely linked to inertial effects, such as rotation and acceleration. In our experiment we switch the sign of k_{eff} every shot, effectively interleaving the two independent acquisition. The switch between momentum is obtained by changing the sign of the frequency ramp used to compensate the Doppler shift. The total phase is calculated by combining the atomic phase, recovered from the transition probability, and the MFL phase used to steer the interferometer towards the center of the fringe. For a single k_{eff} it will be:

$$\Phi_i = \phi_i^{at} + \frac{1}{2}(\varphi_i^{MFL} + \varphi_{i-1}^{MFL}) = \frac{(-1)^i}{2A}(P_i - P_{i-1}) + \frac{1}{2}(\varphi_i^{MFL} + \varphi_{i-1}^{MFL}). \tag{4.3}$$

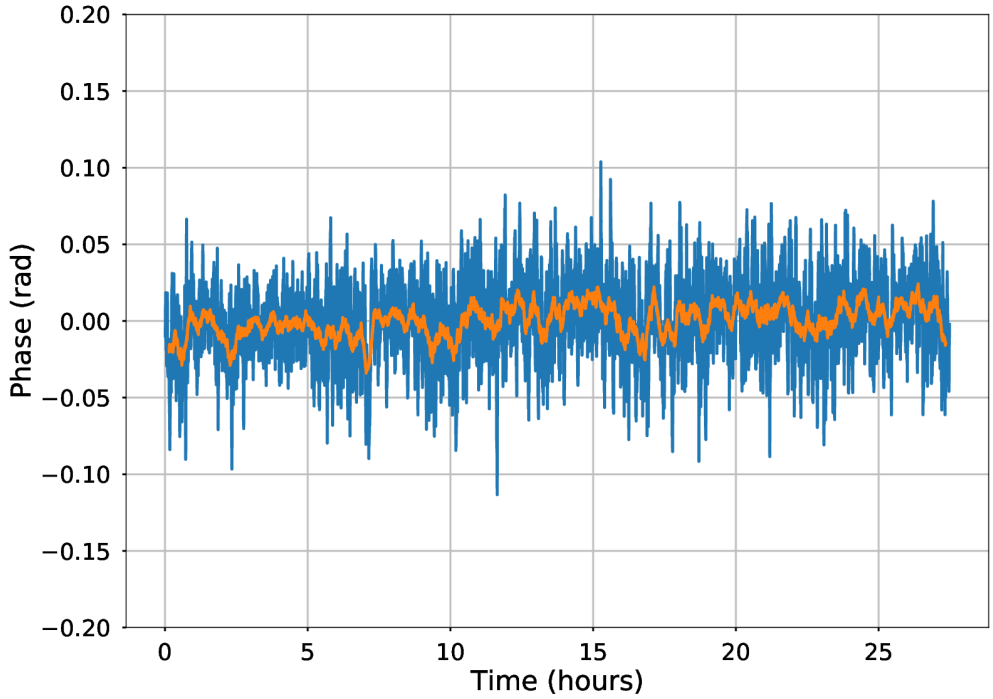

Figure 4.8: *Moving average of Earth's rotation rate signal. The blue (orange) trace is obtained by using a window of 100 (1000) seconds.*

Operating at the center of the fringe, allows us to reconstruct the atomic phase with a linear approximation instead of using an inverse trigonometric function, but in this way there is a residual error.

4.3.1 Sensitivity with interleaved scheme

In Figure 4.9 we can observe the Allan standard deviation (ADEV) for a portion of 11.3 hours extracted from Figure 4.8. The graph shows how we are able to reach a stability of $3 \times 10^{-10}\text{rad} \cdot \text{sec}$ after 10 000 sec of integration time [33]. This translates in a stability improvement of factor 3 compared to our previous result in 2016 [30]. The black line shows also a sensitivity at 1 second of $3 \times 10^{-8}\text{rad} \cdot \text{sec}^{-1} \cdot \text{Hz}^{-1}$.
This will give us the ability to study new systematics effect in the $10^{-9}\text{rad} \cdot \text{sec}^{-1}$ range within a reasonable integration time of 1000 seconds. As is shown in Figure 4.9, the improvement in the performance is directly linked to our capability of averaging the

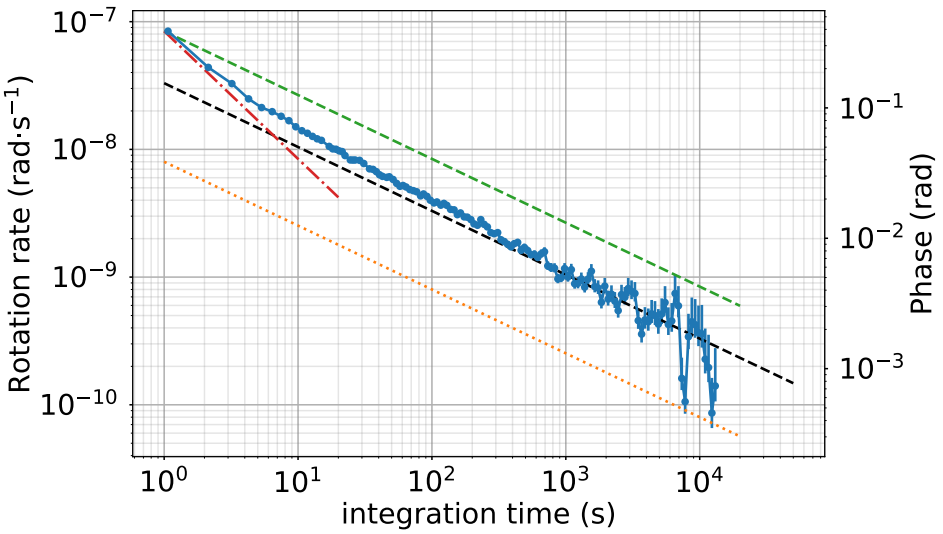

Figure 4.9: *Allan Deviation plot showing the stability of the experiment for triple joint interleaved operation. The dashed lines are guide for the eye describing the different behavior of the noise. The red line has a slope equals to* $1/\tau$*. This is characteristic of correlated noise which is linked to continuous measurement. The green line decreases as* $1/\sqrt{\tau}$ *and represents the normal uncorrelated noise due to phase noise and uncompensated acceleration noise.The orange dotted line represented the detection noise which corresponds to a limit of* 8×10^{-9} rad $\cdot$ sec^{-1} $\cdot \sqrt{\tau}^{-1}$.

rotation noise as τ^{-1} up to $\sim$7 seconds. This ability derives directly from the continuous measurement in which successive phase measurements are correlated. After 7 seconds, it reaches the regime of $1/\sqrt{\tau}$ characteristic of uncorrelated white noise.
When averaging for longer period of time, deviations from the $\tau^{-\frac{1}{2}}$ regime may appear, as seen in Figure 4.10.

To avoid these deviations, and the degradation of the AI sensor performances, a deep and comprehensive study of all the systematic effects is necessary. Currently one of the main limitation arises from the use of two separated Raman beams. As I will discuss in the next chapter small misalignment in the parallelism between the mirrors could lead to significant phase shift which impacts the long-term stability of the gyroscope.

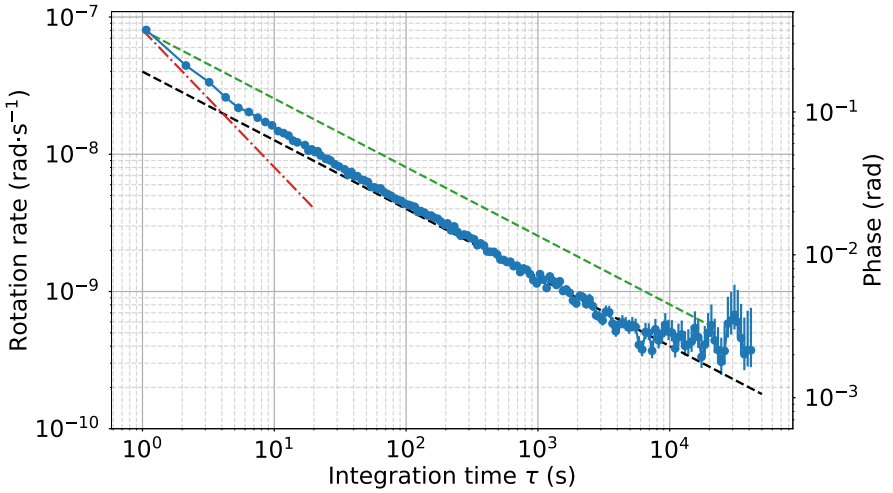

Figure 4.10: *Allan Deviation showing the full data acquisition of 22 hours. After 10 000 seconds we can see the stability of the sensor deviating from the normal regime of* $1/\sqrt{\tau}$

4.3.2 Interpretation of vibration noise averaging in a joint scheme

Non-continuous operation

The accumulated phase at the output of the interferometer for a single measurement can be written as:

$$\Phi = \phi_b(0) - 2\phi_t(T/2) + 2\phi_t(3T/2) - \phi_b(2T) \tag{4.4}$$

where 2T is the total interrogation time, $\phi_{b,t}$, denotes the difference of phase between the Raman lasers, imprinted on the atomic wave packet a the moment of the pulse (b and t refers to bottom and top Raman laser pairs). The above equation can be rewritten as:

$$\begin{aligned}\Phi &= \phi_t(0) - 2\phi_t(T/2) + 2\phi_t(3T/2) - \phi_t(2T) \\ &\quad + [(\phi_b(0) - \phi_t(0)) - (\phi_b(2T) - \phi_t(2T))] \\ &= \phi_t^{acc} + k_{eff}L(\theta_b(0) - \theta_b(2T)) \qquad (4.5) \\ &= \phi_t^{acc} + k_{eff}L\Delta\theta \qquad (4.6)\end{aligned}$$

with $L = \frac{3}{8}gT^2$ being the distance the wave packet travels between the $\pi/2$ and π pulses[2], ϕ_t^{acc} indicates the linear acceleration seen by only the top mirror. With $L\Delta\theta$ we indicate

[2]This distance is valid only if the cloud is at the apogee at time T

by how much the top mirror rotates with respect of the bottom mirror between the two $\pi/2$-pulses. Using (4.6), we can estimate the mean phase after N measurements as:

$$\overline{\Phi}_N = \frac{1}{N}\sum_{i=0}^{N-1}\Phi_i = \frac{1}{N}\sum_{i=0}^{N-1}(k_{eff}L\Delta\theta_i + \tilde{\varphi}_i) \tag{4.7}$$

where $\Delta\theta_i = \theta_b(i2T) - \theta_b((i+1)2T)$ and $\tilde{\varphi}_i$ represents other type of noise contributions such as detection noise, laser phase noise and uncompensated vibration noise(ϕ^{vib}). We now look at the variance of the phase shift:

$$\sigma^2_{\overline{\Phi}_N} = \mathrm{Var}\left(\frac{1}{N}\sum_{i=0}^{N-1}\Phi_i\right) = \mathrm{Var}\left(\frac{1}{N}\sum_{i=0}^{N-1}(k_{eff}L\Delta\theta_i + \tilde{\varphi}_i)\right) = \frac{1}{N^2}\sum_{i=0}^{N-1}\mathrm{Var}\left(k_{eff}L\Delta\theta_i + \tilde{\varphi}_i\right) \tag{4.8}$$

Here we assumed all the measurements to be independent from each other.
Then assuming the variance of rotation noise and $\tilde{\varphi}$ to be Gaussian white noise:

$$\sigma^2_{\overline{\Phi}_N} = \frac{1}{N}(\sigma^2_{\Delta\theta} + \sigma^2_{\tilde{\varphi}}) \tag{4.9}$$

The standard deviation then decreases as $\tau^{-1/2}$ characteristic of uncorrelated noise.

Continuous Operation

In the case for a joint operation scheme we can rewrite the equation (4.7) as such:

$$\overline{\Phi}_N = \frac{1}{N}\sum_{i=0}^{N-1}(k_{eff}L[\theta_b(iT_c) - \theta_b((i+1)T_c)] + \tilde{\varphi}_i) \tag{4.10}$$

where now $\Delta\theta_i$ depends on the cycling time which now coincides with the interrogation time $2T$. While in the non-consecutive operation each measurement is uncorrelated since separated by dead time, here each interferometer share one pulse, making the results correlated. Expanding the series in equation (4.10) most of the terms in $\Delta\theta_i$ cancel each other resulting in the equation for the mean phase shift as:

$$\overline{\Phi}_N = k_{eff}L\frac{(\theta_b(0) - \theta_b((N+2)T_c))}{N} + \frac{1}{N}\sum_{i=0}^{N-1}\tilde{\varphi}_i \tag{4.11}$$

As for the variance we can rewrite equation (4.8), minding that this time we deal with correlated measurement.

$$\sigma^2_{\overline{\Phi}_N} = \frac{2}{N^2}\sigma^2_{\Delta\theta} \quad + \quad \frac{1}{N}\sigma^2_{\tilde{\varphi}} \tag{4.12}$$

We can see that, with a continuous operation scheme, if the correlated noise is dominating for short integration time (small N), the standard deviation of the rotation noise

decreases as $1/N$. This regime is maintained until the uncorrelated noise becomes dominant, at which point the signal falls back to the white noise regime of $1/\sqrt{N}$.

To better understand this effect a signal was simulated using two independent traces

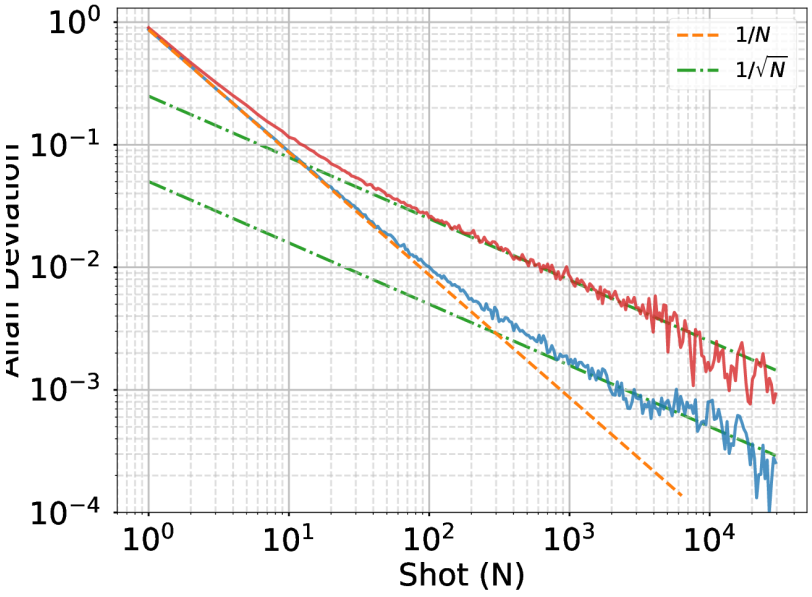

Figure 4.11: *Allan deviation of simulated phase data for different level of uncorrelated noise. The red line is simulated to have 5 times more noise than blue trace. The dashed lines are guides to the eyes showing the two different behavior:* $1/\tau$ *(orange),* $1/\sqrt{\tau}$ *(green).*

of the same length, that simulates correlated and uncorrelated noise. The first trace is created by using a function that generates random white noise and stores it into an array. Each element of the array, then, is combined with the preceding one, generating correlation between each point. To generate simple uncorrelated noise we create a different array with the same white noise generator. The final trace is obtained by the sum of these traces. In Figure 4.11, we show the aforementioned traces for two different levels of uncorrelated noise. As we can see, with the same level of correlated noise, the change of regime between $1/\tau$ and $1/\sqrt{\tau}$ is ruled solely by the amount of uncorrelated noise present in our measurements.

4.4 Measurements of weak dynamic rotation rates

The high sampling rate together with the high sensitivity, makes possible to use our sensor in order to measure the effect of weak dynamic rotation rates. Let us consider the case where the sensor is rotating about the normal of the interferometric area at a rate $\Omega_D(t)\vec{e}_y$ with $\Omega_D(t) = \dot{\theta}(t)$.
As first step we rewrite the equation of motion, moving from the classical reference frame of the lab, to the rotating frame of the Raman lasers as:

$$\begin{cases} x(t)_{cl} = & \frac{\hbar k_{eff}}{2M} t \\ z(t)_{cl} = & g(Tt - \frac{t^2}{2}) \end{cases} \Rightarrow \begin{cases} X(t) = & x(t)_{cl}\cos\theta(t) + z(t)_{cl}\sin\theta(t) \\ Z(t) = & z(t)_{cl}\cos\theta(t) - x(t)_{cl}\sin\theta(t) \end{cases} \tag{4.13}$$

The phase shift equation for a 4-pulse AI is:

$$\Phi_{dyn} = \varphi(0) - 2\varphi(\frac{T}{2}) + 2\varphi(\frac{3}{2}T) - \varphi(2T) \tag{4.14}$$

where the phase at each individual pulse can be rewritten with $\varphi(t) = k_{eff}X(t)$ as:

$$\varphi(t) = k_{eff}\left[\frac{\hbar k_{eff}}{2M}\ t\ \cos\theta(t) + g(Tt - \frac{t^2}{2})\sin\theta(t)\right] \tag{4.15}$$

Considering weak periodic rotation characterized by small angular $\theta(t) = \theta_0\sin(\omega t)$ where the amplitude $\theta_0 \ll 1$, we neglect the first term in equation (4.15).
We can then rewrite equation (4.14) using the second term of (4.15):

$$\Phi_{dyn} = \frac{3}{4}k_{eff}g\theta_0\left(\sin\left(\omega\frac{3T}{2}\right) - \sin\left(\omega\frac{T}{2}\right)\right)T^2 \simeq \frac{3}{4}k_{eff}g\Omega_0T^3 \tag{4.16}$$

where we put ourselves in the case of slow rotation, ($\omega T \ll 1$), and writing $\theta_0\omega$ as Ω_0. It's important to notice that equation (4.16) has a factor of $\frac{3}{4}$, contrary to the general Sagnac formula for a 4 pulse gyroscope

$$\Phi_S = \frac{1}{2}\vec{k}_{eff}(\vec{g}\times\vec{\Omega})T^3. \tag{4.17}$$

This difference comes from the intrinsic nature of our sensor, which is not a simple gyroscope, but a gyroscope-accelerometer. If the sensor rotates coherently with the Earth, no change in the projection of $\vec{g}$ would be measured. The sensor, then, will be only sensitive to Sagnac effect which scales with a factor $\frac{1}{2}$. If the sensor is subject to rotation in the Earth reference frame, it will measure a phase shift which is the combination of Sagnac effect and modulation in time of the projection of $\vec{g}$. This phase shift Φ_{acc}^{AC} scales with a factor of $\frac{1}{4}$ [52] which summed with the Sagnac phase shift gives:

$$\Phi_{dyn} = \Phi_S + \Phi_{acc}^{AC} = \frac{3}{4}k_{eff}g\Omega_0T^3. \tag{4.18}$$

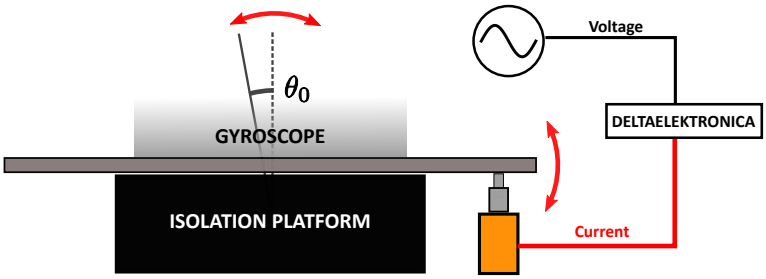

Figure 4.12: *Representation of the loop used to apply a modulated signal through the voice-coil actuator used to lock the inclination of the apparatus. Using a function generator a sinusoidal signal is sent to a programmable power supply. The generated current will then modify the inclination of the experiment through the voice-coil actuator.*

4.4.1 How to apply weak dynamic rotation rate

To apply weak dynamic rotation, $\Omega_0 = \theta_0 \sin(\omega t)$ we rely on the tilt lock system. We connect a waveform generator to a programmable power supply [3] as shown in Figure 4.12. This power supply converts the modulation from voltage to current, feeding it to one of the voice-coil actuator which locks the sensor tilt in the X direction. Normally this power supply is controlled by the main experiment computer, which is responsible for the tilt locking loop. In this case we need to manually take care of using the correct offset for our modulated signal. This allows us to maintain the sensor's tilt around the usual locking point on average during the measurement of dynamic rotation rate.

4.4.2 Classical sensor

The objective of these type of measurements is to reconstruct a modulated signal with our AI sensor and to verify its quality. To do so we compare the signal from the cold atom sensor with the signals measured by classical sensors. On the experiment are present different type of classical sensor: a tiltmeter and an accelerometer, both of which measure the variation of projection of gravity acceleration on the horizontal axis, $a(t) = g\theta(t)$. The other type of sensor is a seismometer, that instead of measuring acceleration is sensitive to velocity changes, which can be considered as the *integrated* projection of gravity acceleration, $v(t) = \int a(t)\mathrm{d}t$. Prior to use the AI sensor to measure weak dynamic rotation rate, we proceed to calibrate the response of the classical sensor to such weak modulation. Using the scale factor given by the manufacturers, we move to

[3] Delta Elektronika ES 030-10

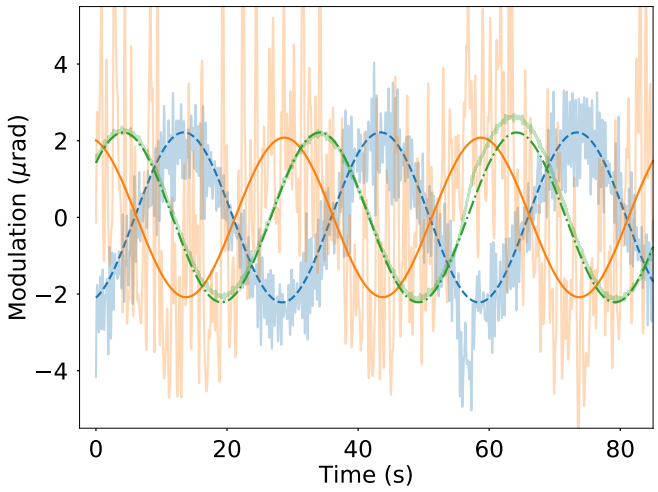

Figure 4.13: *Tilt measurement of the gyroscope, with a modulation of 30 seconds period. 3 different sensors have been used: Tiltmeter (yellow trace), Titan accelerometer (blue), Trillium seismometer (green)*

estimate the amplitude θ_0 of the effective modulation applied to the AI sensor apparatus. In Figure 4.13 we show the signals recorded by the three classical sensors for a modulation period of 30 seconds and their respective fit. The accelerometer and the tiltmeter are in anti-phase due to a change in sign of the accelerometer. The difference of phase for the seismometer is due to the integration of the signal plus the specific time response of the sensor, which can be seen in Figure 4.15.
For a 30 seconds modulation the reconstructed amplitudes from each individual sensor are consistent with each other within the error extracted by the fit as shown in Table 4.1 and the estimated error of the scale factor from the manufacturer.

	30 s	100 s	200 s
Seismometer	2.2145 ± 0.0003	1.83 ± 0.00002	0.75543 ± 0.00001
Accelerometer	2.216 ± 0.001	2.264 ± 0.001	2.273 ± 0.001
Tiltmeter	2.094 ± 0.004	2.330 ± 0.002	2.197 ± 0.001

Table 4.1: *Extracted amplitude θ_0 in* μrad *for different periods but same amplitude of tilt modulation.*

We repeat the measurement using longer modulation period, 100 and 200 seconds, but keeping the same voltage amplitude on our waveform generator. The measured amplitude of the modulation for the tiltmeter and accelerometer didn't change as expected.

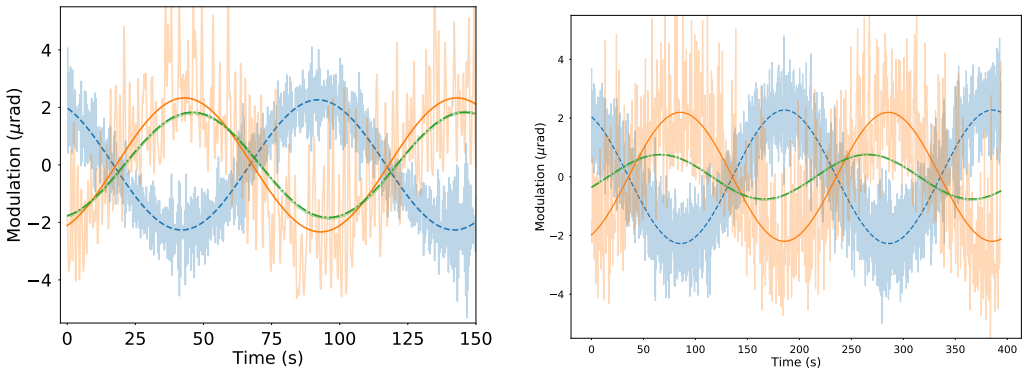

(a) *100 seconds modulation* **(b)** *200 seconds modulation*

Figure 4.14: *Comparison of measured amplitude for different modulation periods for the three classical sensors: Tiltmeter (yellow trace), Titan accelerometer (blue), Trillium seismometer (green).*

The seismometers on the other hand presented a decreased amplitude compared to the 30 seconds signal, as seen in Figure 4.14. We compare the results from the seismometers with the frequency response graph provided by the manufacturer in Figure 4.15.

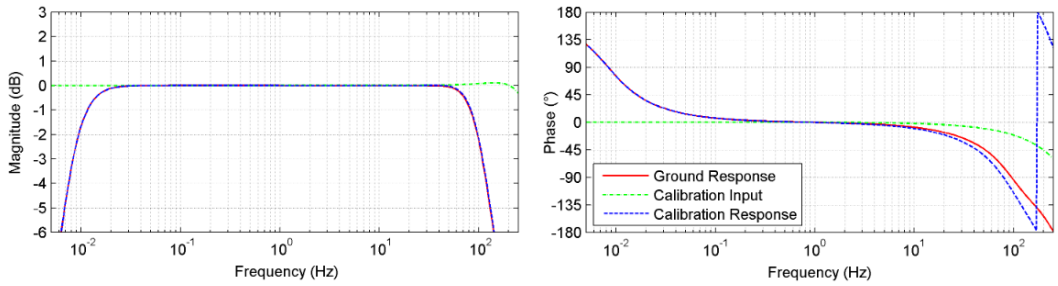

Figure 4.15: *Frequency and phase response of Nanometrics Trillium Seismometer as provided by the manufacturer.*

The graph shows a clear decrease in the magnitude for frequency smaller than 0.03 Hz together with a significant phase delay coming from the high pass filter of the seismometers.
We then concentrate our study of dynamic measurement in a frequency range where both seismometer and AI works simultaneously.

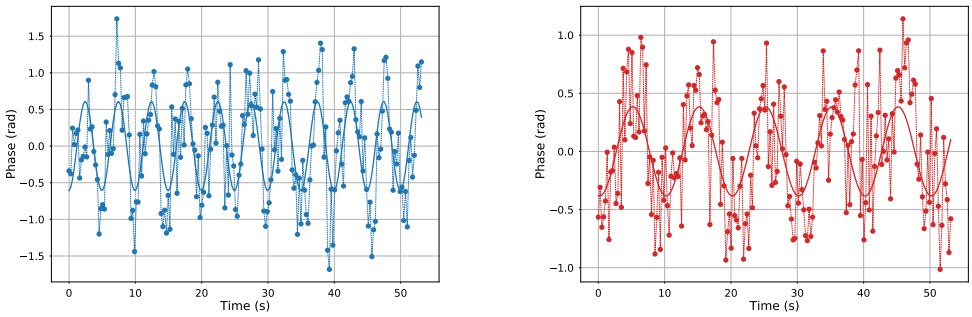

(a) *5 seconds* **(b)** *10 seconds*

Figure 4.16: *Time trace and sinusoidal fit of the atomic phase. The phase is presented centered around zero by removing the offset value extracted from the fit.*

4.4.3 AI sensor

Following (4.16) we can write the total phase shift of the gyroscope:

$$\Phi(t) = \Phi_{Earth} + \Phi_{dyn}(t) = \frac{1}{2}\vec{k}_{eff} \cdot (\vec{g} \times \vec{\Omega}_E)T^3 + \frac{3}{4}\vec{k}_{eff}(\vec{g} \times \vec{\Omega}_D(t))T^3 \tag{4.19}$$

where we reintroduced $\vec{\Omega}_D = \Omega_0 \cos(\omega t)\vec{e}_y$. The phase shift Φ_E due to Earth rotation is a constant offset and the phase shift due to induced AC acceleration are negligible at this moment.

At the end of every cycle, the AI sensor returns a measurement about the change of angle (due to the applied rotation rate), averaged over the duration of the interrogation time $2T = 801$ms.

Then Φ_{dyn} can be rewritten as:

$$\Phi_{dyn}(iT_c) = S\frac{1}{2T}\int_{iT_c}^{2T+iT_c} \Omega_D \, \mathrm{d}t = S\Omega_0 \cos[\omega(iT_c + T)] \times \frac{\sin(\omega T)}{\omega T} \tag{4.20}$$

with $S = \frac{3}{4}k_{eff}gT^3$.

As the interrogation time is not infinitely small compared to the period of oscillation the measurement gives a reduced amplitude due to the averaging of the signal. This attenuation of the amplitude is expressed by the latest term in (4.20) and is a function of the modulation period. For modulation of 5 seconds period the measured signal corresponds to 0.96 of the original signal while it correspond to 0.99 for 10 seconds modulations.

In Figure 4.16 we see the evolution of the atomic phase in time for modulation of 5 and 10 seconds. The phase signal is recovered from the transition probability divided

by the fringe amplitude:

$$\Phi_{at} = \frac{P_i}{A} \tag{4.21}$$

The estimation of the amplitude and its uncertainty is done by fitting the probability distribution using a twin horned distribution, see Appendix A; typical operation values are $A = 0.06 \pm 0.002$. By fitting the time traces, we extract the amplitude of the applied modulation. The reconstructed amplitudes differ greatly from the values measured with the seismometers data due to the real time compensation removing useful information from the data.

To extract properly the modulation, we have to reconstruct the full raw signal sensed by the AI. To do so we add back the vibration phase noise that was compensated by the RTC loop. In Figure 4.17, the result of this operation can be seen. The modulated

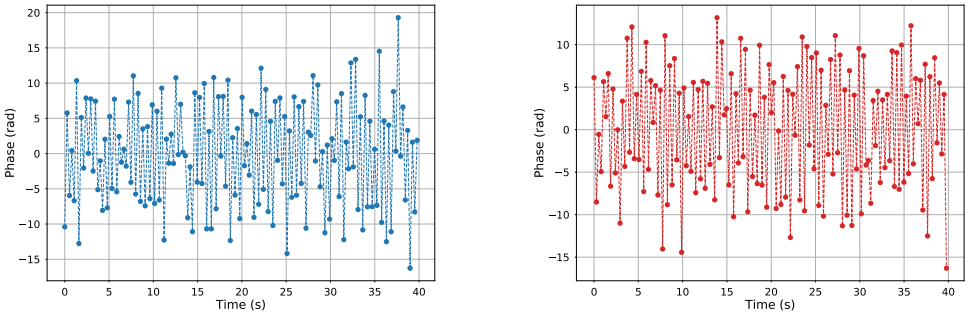

(a) *5 seconds* **(b)** *10 seconds*

Figure 4.17: *Time trace of the reconstructed atomic phase recombined with the compensated vibration phase ϕ_{rtc}. No clear sinusoidal modulation are visible after the recombination as the vibration noise spans multiple* rad

signal is not clearly visible anymore as in Figure 4.16 due to the large amplitude of the vibrations. We thus rely on using FFTs to analyze the traces. We use two similar approaches, the first is to apply an FFT to the full extent of the time trace; the second is to cut the time trace in smaller portion to which we apply the FFT routine, then compute the average of all the FFTs. The first approach allows us to gain in frequency resolution sacrificing the signal to noise ratio. The second approach on the other hand, prioritize lowering the level of noise, by averaging multiple FFTs, while not having the best possible frequency resolution.

The result obtained, by applying the FFTs routines describe above, are in good agreement with Eq. (4.20). In Table 4.2, the results of these routines applied on the AI data

are shown. We are able to recover the amplitude of the simulated signal within the bound imposed by Eq. (4.20).

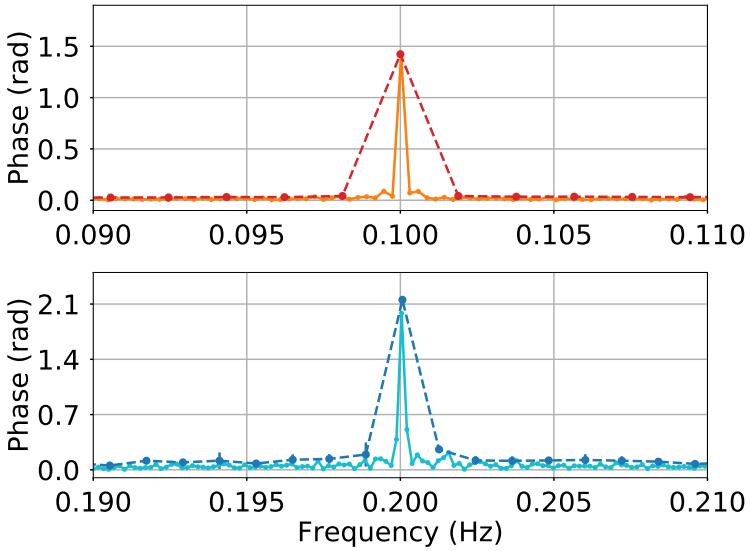

Figure 4.18: *FFTs of the modulated signals for 10 seconds (Top) and 5 seconds (Bottom) periods. In dashed are showed the averaged FFTs which present a great reduction in frequency resolution but allow us to present a statistical uncertainty on the measurements. In solid lines are shown the full traces FFTs with our full frequency resolution.*

4.5 Conclusion

In this chapter, I presented the principle of continuous and interleaved operation for our gyroscope. This method allowed us to improve the sensitivity of the experiment, reaching an unprecedented sensitivity of 3×10^{-8} rad $\cdot$ s^{-1} $\cdot$ Hz$^{-1/2}$.

While testing a five times interleaved sequence we notice that the atomic clouds entering the interrogation region where de-pumped to another state. The cause was the scattering light from the detection. In fact an ascending atomic cloud has barely surpassed the detection region while another cloud is being detected, scattering light in all directions. Another problem that future iteration will have to solve is posed by the position of the 3DMOT with respect of the interrogation region. With the current design, the atomic cloud is always in the line of sight of the 3DMOT. Scattered photons that leaks in the interferometric region heat up the cloud during its flight. This translates

	5 s	**10 s**
	Averaged	
Full Phase (Atomic phase plus RTC phase)	0.246 ± 0.004	0.325 ± 0.008
Seismometers	0.281 ± 0.002	0.359 ± 0.002
	Full trace	
Atoms without RTC phase	0.058	0.088
Full Phase (Atomic phase plus RTC phase)	0.226	0.322
Seismometers	0.257	0.354

Table 4.2: *Extracted values of θ_0 from the FFT in μ*rad*. The uncertainties for the averaged FFTs are the statistical errors calculated from the averages.*

in a loss of contrast and an increase in lightshift [32].
At the moment the apparatus can operate with maximum 3 interleaved joint sequences. This number is imposed by the geometry of the apparatus and it will be improved in future generation of the design. Considering the typical loading time of a 3D-Mot from a 2D-Mot and the subsequent launching scheme, we can expect to reach a sampling rate higher than 10 Hz. Even though we reached state of the art performance we are still limited by different noise source. One limitation is given by residual vibration that are not well estimated by the seismometers. At the time of writing, the two seismometer are placed outside the magnetic shields, this gives a limit on the estimation of vibration close to the Raman retro reflection mirror. A new mirror mount has been designed in order to bring the seismometers closer to the mirrors, in order to improve our ability to measure and compensate vibration noise. The high sampling rate, nevertheless, opened up the possibility to study dynamic signal. This in conjunction with the large sensitivity gave us the capability to measure and reconstruct weak dynamic rotation rate signals.

Chapter 5

Scale Factor and bias of the Gyroscope

The scope of cold atom inertial sensor is to develop a new generation of instruments of potentially better accuracy than existing ones. To do so, it is necessary to know accurately the link between phase measurements and physical quantities, that is the scale factor and the bias from systematic effects. In this chapter, I will present the first characterization of the gyroscope's bias and scaling factor.
I will present the different methods we developed to separate bias contribution to the AI phase from scale factors ones. To this end, we take advantage of our knowledge of Earth's rotation rate and its projection on the oriented area of the atom interferometer. By turning the gyroscope around its vertical axis, I was able to measure the variation of the rotation phase from its maximum value when the sensor is oriented to North to its zero value when it was orientated to West/Est. I will present the setup modification and its characterization together with a first estimation of the bias and scaling factor. Subsequently I will present a study regarding what we think to be one of the major systematic effect: the coupling between the non-perfect wavefront of the Raman laser and the transversal velocities of atoms [6].
A method to align with μrad precision the 3 laser beams in a Mach-Zehnder like configuration of atom interferometer gyroscope was presented in [53], however the residual systematic shift was not evaluated in this study. In the case of two separated Raman pair collimators, we will see the effect depends at first order only on the misalignment of the retro-reflection mirrors used. I will later present a method to characterize and minimize the systematics effect, without the implementation of ultra cold-atoms sources.

5.1 Gyroscope scale factor

In the case of our sensor with a 4 pulse atom interferometer, the scale factor can be written like:

$$\Phi = \frac{1}{2}T^3\left(\vec{g} \times \vec{k}_{eff}\right) \cdot \vec{\Omega}_E \tag{5.1}$$

Let's explicit Eq. (5.1):

$$\Phi_{rot} = \frac{1}{2}k_{eff}g\Omega_E \cos(\theta_0)\cos(\theta_L)\cos(\theta_N)\mathrm{T}^3 \tag{5.2}$$

where θ_N represents the orientation of the AI area's normal relative to the geographical North direction. Since the Raman beams are not perpendicular with $\vec{g}$, a term $\cos(\theta_0)$ arises. Lastly we need to take into account in the latitude at which the sensor is situated with the term $\cos(\theta_L)$.

Quantities	Symbol	Values	
Gravity acceleration	g	9.8092795(1)	$\mathrm{m \cdot s^{-2}}$
Effective momentum exchanged	k_{eff}	$1.4743251924(5) \cdot 10^7$	$\mathrm{m^{-1}}$
Raman collimator inclination	θ_0	3.79(1)°	deg
Interrogation time	2T	800	ms
Earth's rotation rate	Ω_E	$7.2921150(1) \cdot 10^{-5}$	$\mathrm{rad \cdot s^{-1}}$
Laboratory Latitude (GPS)	θ_{lat}	48.83573(1)°	deg
Sensor bearing to North	θ_N	33-38(?)°	deg

Table 5.1: *Table reporting the values used in the estimation of the sensor's scale factor. We also report the values regarding Earth's rotation rate, the latitude of the sensor and its estimated latitude.*

Most of the terms of Eq. (5.2) are known with great accuracy such as Earth rotation rate, Ω_E, and the gravity acceleration, g, which can be known with a precision up to 10^{-9}. The latitude θ_L of the experiment is obtained by GPS localization and the inclination of the Raman beam is measured trough spectroscopy.
The orientation, θ_N, of the experiment towards the geographical North is the only quantity with a large uncertainty. In this section I will present how we measured the scale factor of the gyro-accelerometer.

5.1.1 Latitude estimation

To locate any point on the surface of the Earth a set of coordinate, usually latitude and longitude, together with a specific reference frame are needed. The simplest set of coordinates around the globe would be using spherical coordinates, associating a polar angle to the latitude and an azimuthal angle to the longitude.
While this type of approximation could work for simple application, it fails when higher precision is needed, as in the case of navigation or in the case of large geophysical investigation, which involves large portion of Earth's surface. The reason why the spherical approximation fails on large scales, is due to Earth's rotation and the viscous composition of its inner layer. Due to centrifugal forces, the planet bulges around the equatorial plane and consecutively flattens around the North and South poles. The most reasonable approximation for the shape of the Earth, then becomes an oblate ellipsoid which rotates about its smaller axis. Nowadays, the World Geodetic System (WGS), fixes the characteristics of this ideal ellipsoid, such as major axis and ellipticity, to create a reference system for cartography and navigation systems, such as GPS. With this peculiar reference system, new definitions for the latitude arise. As we can see from Figure 5.1,

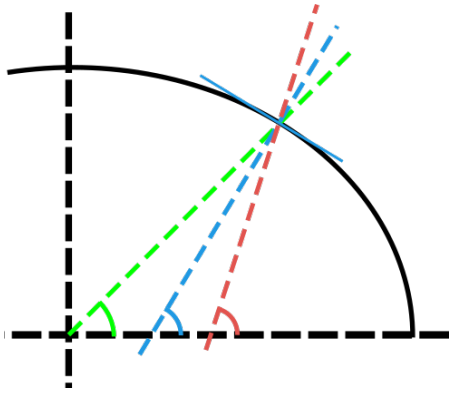

Figure 5.1: *Visual representation of the different type of latitude: geocentric in green, Geodetic in blue and Astronomical in red. The difference are exaggerated to better present the possible differences.*

for the same point P on the surface of the ellipsoid, two different latitude angle can be calculated. The first and most intuitive is the *geocentric* latitude θ, which is the angle between the equatorial plane and the line connecting the center of the ellipsoid to the point P (green line in Figure 5.1). The second is the *geodetic* latitude ϕ, which is the angle between the equatorial plane and the normal of the ellipsoid in the point P, (blue line). If no specification is made, when speaking about latitude one should always refer

to the Geodetic latitude. What we are interested in, is the latitude that best describes what is the *"down direction"*, given by the gravity acceleration. Physically this direction is defined by a simple plumb line and the angle it forms with the equatorial plane is called *Astronomical latitude* (red line).

In normal condition, the astronomical latitude, or true vertical, does not coincide exactly with the normal of the reference ellipsoid. This is due to the local distribution of land mass. The presence of mountains or sea bodies can change *locally* the direction of the true vertical. The difference between the two latitude is generally below 10 arc-seconds in low land areas such as Paris metropolitan area. This difference is negligible as it is equivalent to a phase shift less than 10 mrad.

5.1.2 Estimation of the initial bearing to north, θ_N

As shown in Table 5.1, θ_N is the quantity with the largest relative uncertainty. We need then to measure with better accuracy the orientation of the AI sensor. The apparatus has been initially aligned compared to the walls of the room, roughly 10 years ago. Unfortunately, given the age of the building, there is no plan showing precisely its alignment with the cardinal points. To estimate its orientation then, we relied on GPS measurements. By measuring the positions at two extremities of the laboratory we can

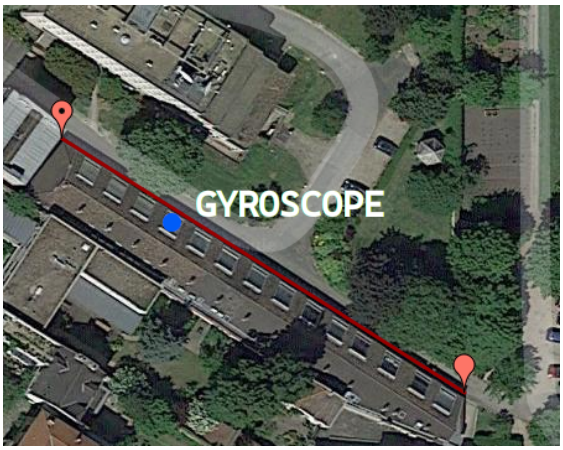

Figure 5.2: *Representation of GPS point used to measure orientation of the building and relative position of the gyroscope.*

extract the bearing of the building with this formula:

$$\theta_N = \arctan 2(\, \sin\Delta\lambda \cos\varphi_2 \,,\; \cos\varphi_1 \sin\varphi_2 - \sin\varphi_1 \cos\varphi_2 \cos\Delta\lambda) \tag{5.3}$$

where arctan2 is a *2-argument arctangent*[1], $\varphi_{1,2}$ are the latitude of the two points and $\Delta\lambda$ is the difference in longitude. Using Eq. (5.3) we obtain that the building is oriented 123.8° with half a degree of statistical error. We then proceeded to measure the relative alignment of the experiment with the lab walls.
We shine a laser pointer perpendicular to the laboratory's wall onto a small mirror glued to the collimator of the experiment. The measured relative misalignment is $1.26° \pm 0.15°$. Adding up this contribution we have $35.1° \pm 0.5°$ as an initial estimation of the orientation of the experiment. We now use the phase of the AI sensor to try to estimate its own orientation.

5.1.3 Variation of interrogation time T

The first test we did to estimate the orientation of the sensor, was to change the interrogation time of the sensor. By changing interrogation time we can observe how the total phase of the interferometer changes and then extract θ_N. We change the interrogation time T by small quantities, dT, of the order of tenths of milliseconds. These changes are small compared to the total interrogation time, thus we can rewrite Eq. (5.2) as:

$$\mathrm{d}\Phi = \frac{3}{2} k_{eff} g \Omega_E \cos(\theta_0) \cos(\theta_L) \cos(\theta_N) \mathrm{T}^2 \mathrm{dT} \tag{5.4}$$

To change the interrogation time T we must operate with caution. To make sure the wave packet recombines we need to maintain the spacing $\left[\frac{\mathrm{T}}{2} - \mathrm{T} - \frac{\mathrm{T}}{2}\right]$ within the 4 pulses. In addition, to minimize unpredictable wavefront problems, we symmetrically shift the timings relative to the apex of the parabolic trajectory. This is done to be sure the centers of the ascending and the descending cloud are positioned in the same spot relative to the mirror and collimator.

In Figure 5.3 we can see the results from two different sets of measurements done at a distance of few hours. This was done in order to be certain the measurements were consistent with each other, independently from the methods used.
The blue points, in Figure 5.3, represents data obtained with an acquisition locked at midfringe, which is already presented in Section 4.2.3. The red points are obtained by scanning the relative phase between the Raman lasers with a fixed phase jump of 30°, while still compensating for vibration noise in real time. As with measurements locked at mid-fringe, we alternate the sign of the exchanged momentum k_{eff} to reduce systematic effects. At the end of the acquisition we separate the two traces to process

[1] $\mathrm{arctan2}(x, y) = \arctan \frac{y}{x}$

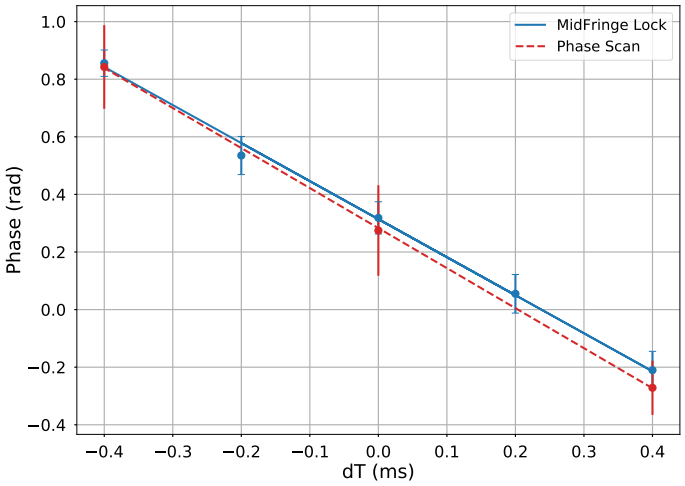

Figure 5.3: *Phase shift* $\mathrm{d}\Phi$ *as function of* dT. *The two datasets are acquired on the same day at a few hours apart. The blue points represents measurements acquired by locking the AI in the middle of the fringe. Red points are acquired by scanning the relative phase of the Raman laser with a constant phase shift. The error bars in both case are the standard deviation of the phase.*

them independently. Subsequently we divide the data points in packets containing the same amount of measurement. We then extract a phase measurement from each packet by using a sinusoidal fit.
Once all the packets are processed, we obtain our inertial signal by taking the half difference between the results of $\pm k_{eff}$. The final phase values are then obtained by doing a weighted average of the recombined phases and the error bar is simply the trace's standard deviation. The weight used for the average are calculated from the uncertainties given by the fit routine and properly propagated when the two traces are recombined. An example of fringe fitting and the relative extracted inertial signal can be seen in Figure 5.4.

Once all the measurements for different T have been acquired we proceed to extract the slope $\frac{\mathrm{d}\Phi}{\mathrm{dT}}$ with a linear fit. By inverting Eq. (5.4) we can then recover θ_N and then calculate the total phase of the AI, Φ_{rot}.

As can be seen from the Table 5.2, over the span of few weeks, the extracted values for θ_N have fluctuated. A possible explanation, although only partial, is the possibility

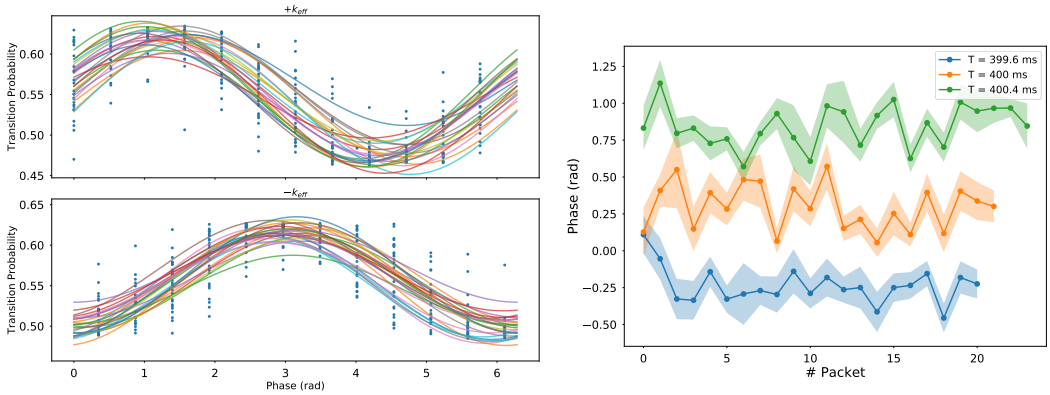

(a) *Fringe fitting T=400.4 ms* **(b)** *Extracted phases with confidence region*

Figure 5.4: *Phase extraction by fitting packets of 12 consecutive points. On the left are shown the fitted fringes for T=400.4 ms. On the right are shown the extracted phases versus packet number. The weighted averages of this traces are shown in Figure 5.3*

	θ_N	Φ_{rot}
23rd January	$35.8° \pm 2.3°$	179.4 ± 5.2 rad
23rd January MFL	$37.4° \pm 2.1°$	176.1 ± 5.0 rad
1st February	$37.8° \pm 1.3°$	175.1 ± 3.1 rad
5th March	$41.5° \pm 1.5°$	166.1 ± 3.9 rad

Table 5.2: *Values of θ_N and relative interferometer phase Φ_{rot} acquired in the first 3 months of 2018.*

the AI sensor was rotating around its vertical axes. The experiment is floating on top of an anti-vibration platform, so its orientation is not fully constraint. Small rotation are still possible, caused probably by some cables pulling on the experiment. I will present a method to monitor and measure these rotations in the next section.

5.1.4 Proximity sensors

To verify possible fluctuation of the orientation around the vertical axis of the sensor, I set up a system that monitors the relative alignment of the isolation platform, on which the sensor sits, compared to its base. To do so, I used two separate inductive proximity sensor[2]. These sensors work by applying a high frequency voltage through a small coil

[2]DW-AS-509-M12-390

positioned on the tip. When a metal target comes in the proximities of the coil, the inducted current in the target, will modify the amplitude of the high frequency signal. These changes are then converted into an usable output signal with the help of the integrated circuit. In Figure 5.5 is shown the response curve of the sensors for different

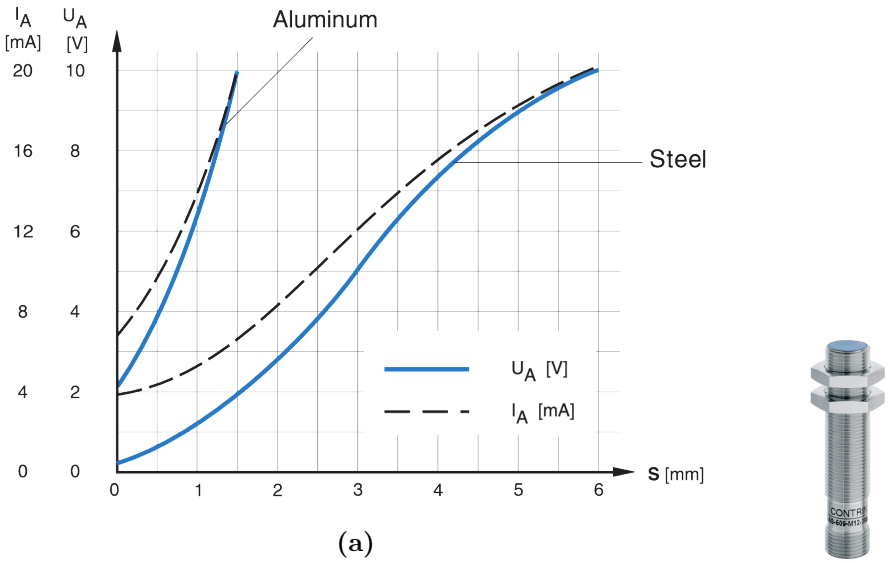

Figure 5.5: **(a)** *Current/Voltage response curve provided by the manufacturer. Since the sensor works by responding to inducted current generated inside a target, we can see on the left how the sensor has different response depending on the material of the target.* **(b)** *Picture of proximity sensor.*

targets' material given by the manufacturer. We use target of 10x20x30 mm size, made of steel to maximize the range of measurement. Since the measurement depends on the material which is made the target and its sensitivity to induced magnetic fields, the characterization of the sensors can change from target to target. We make sure then, that the pairing sensor-target remain the same during all the measurements. Moreover the response is non linear and depends on the actual distance that we don't know a priori. This is why we have to characterize the response of the sensors directly with our set up. We then glue the sensors onto a translation stages and record the distance from the target as a function of the voltage signal acquired. In Figure 5.6b we present the respective calibration curves and fit lines for the two sensors. To fit the data points we rely on a polynomial fit up to the 5-th order. The estimated error associated with this fit is less than 5 mV in the central linear section of the curve, up to 9 mV on the outer parts of the curve. These translate to uncertainties in the position of 3 μm for the

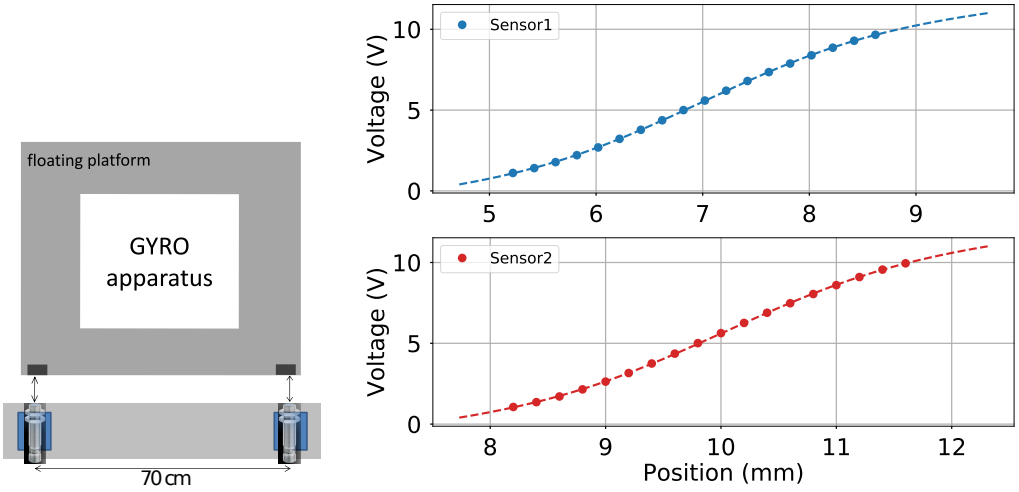

(a) (b)

Figure 5.6: **(a)** *Scheme of the setup. The two sensors are distant 70 cm from each other and locked in place on top of a rail.* **(b)** *Characterization of the response of the proximity sensors using steel target. Using a translation stage and an oscilloscope the distance and the relative voltage have been recorded.*

central part and 4 μm in the outer part.

The next step is to measure the angle of the experiment using the proximity sensors. To do so we mount the two sensors, with relative translation stage, onto a rail and adjust the distance between them. To maximize the sensitivity to small rotation, we place the two metal target at opposite extremes of one side of the floating platform, distanced by 70 cm. The rail is mounted and fixed onto two brass pillar with a collective weight of 30 kg which rest directly on the floor of the laboratory. This whole setup is kept isolated from the experiment in order to not bring any vibration from the ground to the AI sensor. The heavy pillars have been chosen to prevent any accidental displacement of the rail and affecting, as a consequence, the proximity measurements. Once the rail is brought in the vicinity of the floating platform, the distance of the two sensors is adjusted thanks to the micro-metric screws on the translation stage. We do this adjustment to position the sensors in the middle of their linear regime, in order to maximize voltage response in both directions. To finally extract the angle from the two distance measurement we use a simple geometrical formula $\theta = \arctan\left(\frac{D_1 - D_2}{L}\right)$ where $D_{1,2}$ is the measured distance read from the sensor and L is the distance between the two, as seen in Figure 5.6a.

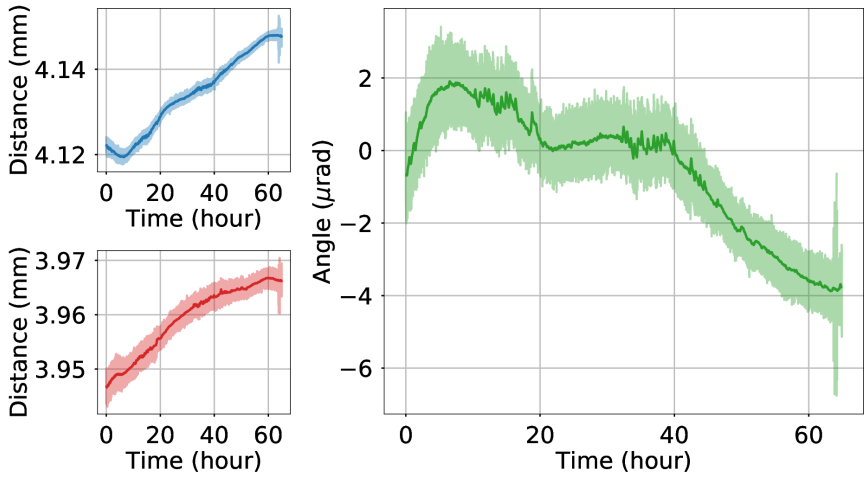

Figure 5.7: *Raw data (lighter trace) and moving average with 10 minutes windows (darker trace) from proximity sensors (blue for sensor 1 and red for sensor 2) and calculated angle (green). The small spikes between 10-20 and 30-40 hours are the air-conditioning cycle starting.*

In Figure 5.7 is shown the reconstructed angle variation for an acquisition over the weekend. It is possible to see that both sensors start to measure a continuous drift that lasts until the end of acquisition 65 hours later. This translates to a total rotation drift of 6 μrad in the span of 3 days. We associate this small and slow rotation with temperature fluctuation inside the isolation box that envelop completely the apparatus.

This box is put in place to insulate the sensor from acoustic vibration, but, thanks to the inside covers made of foam, it also act as a thermal isolator. Using multiple thermocouples, we measured increases of °2C compared to room temperature inside the isolation box. During the installation of the proximity sensor rail, the box was left open for a couple of days and then was closed just before the acquisition started.

The drift seen in Figure 5.7 is probably due to the relaxation of the spring inside the isolation platform, linked to the small temperature fluctuation. Such small rotations, nevertheless, cannot explains the large shift in the rotation phase observed between consecutive days while we changed interrogation time. With the implementation of this proximity sensor, we can look at different methods to extrapolate the orientation of the experiment. In the next section I will present how we implemented one of such methods.

5.1.5 Estimation changing orientation by small angles $\mathrm{d}\theta$

The implementation of these proximity sensors creates a new opportunity to evaluate the angle θ_N. By applying small rotation about the vertical to the isolation platform, which we are now able to measure precisely, we can extract the bearing to North of the gyroscope. We define this small rotation as $\mathrm{d}\theta$ and rewrite Eq. (5.2) as:

$$\mathrm{d}\Phi = \frac{1}{2} k_{eff} g \Omega_E \cos(\theta_0) \cos\left(\tilde{\theta}_L\right) \sin(\theta_N) \mathrm{d}\theta \tag{5.5}$$

The difficulty of this approach lies in applying a force in a controlled way, without introducing extra noise in the interferometric measurements. The apparatus, while is isolated from the ground vibration, is very susceptible to any exterior forces applied on it. The idea is to pull or push the sensor on one corner of the structure that holds the sensor head, making it rotate around its vertical axis.
The solution found to execute this idea reliably was to connect two corners of the structure to a mirror mount using very thin strings, as is displayed in Figure 5.8. By adjusting the horizontal screw of the mirror mount, we can apply small rotation to the sensor in both direction without affecting the tilt of the sensor and the performance of the measurement.
As Figure 5.8a shows, the signals from the proximity sensors are acquired in continuous

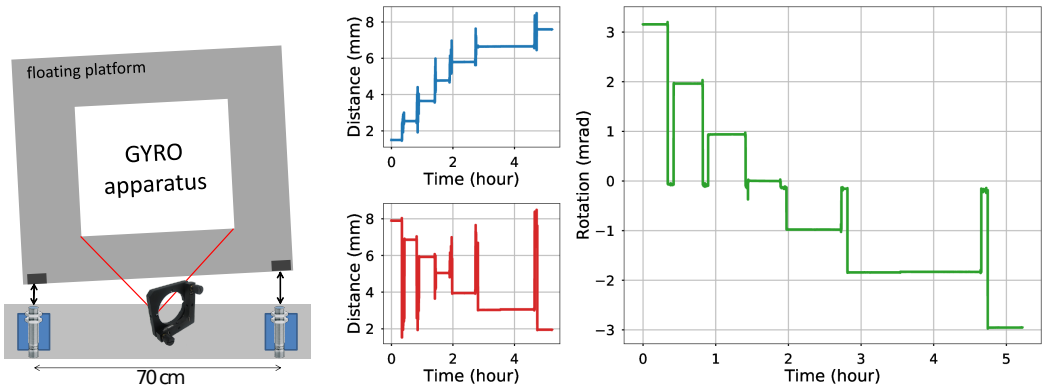

(a) **(b)**

Figure 5.8: **(a)** *Scheme of the strings and mirror setup. The mirror mount is fixed on the rail, while the strings are attached to two corners of the Gyro apparatus and one side of the mirror mount.* **(b)** *Extraction of the 7 values for the gyroscope's angle used in Figure 5.9.)*

while the interferometer is operating. From the individual traces it is clear the two cor-

ners of the isolation platform are moving in opposite directions. This translates to a net rotation of the gyroscope up to ± 3 mrad. The values of the angle $\mathrm{d}\theta$ are then extracted by averaging each section of the rotation trace. After each rotation, the platform stabilize itself and we proceed to measure the phase $\mathrm{d}\Phi$ of the atom interferometer. The result is shown in Figure 5.9. In Table 5.3 are then shown the extracted values of θ_N and the relative rotation phase Φ_{rot}. Compared to changing the interrogation time T,

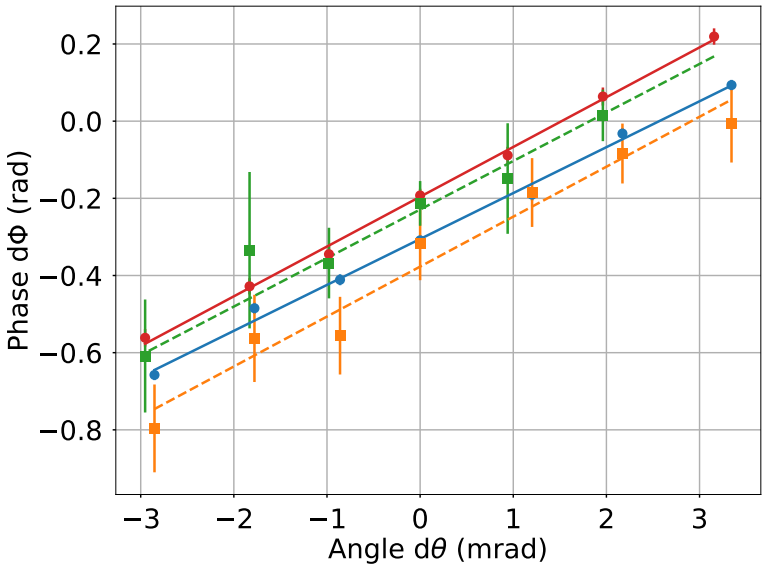

Figure 5.9: *Changes of phase shift* $\mathrm{d}\Phi$ *as function of the angle* $\mathrm{d}\theta$ *on different days. The square marker represents measurement acquired by scanning the fringe. Round marker are measurements obtained by locking the AI to the middle of the fringe. The data set blue and orange correspond to measurements acquired on the* 20^{th} *of March 2018 while green and red were acquired on the* 23^{rd} *of March 2018*

the measured orientation of the experiment fluctuates less within the confidence interval. However, with this level of uncertainty, it is still not possible to estimate the total scale factor of the gyroscope. As I will explain in the next section, due to the periodicity of the gyroscope measurements we cannot distinguish different measurements which are distanced with multiples of π. The uncertainty on the scale factor, using the best measurement of θ_N from Table 5.2 or Table 5.3, is larger than π, therefore we cannot estimate without ambiguity the value of the full scale factor.

		θ_N	Φ_{rot}
20^{th} March	Phase Scan	$35.7° \pm 3.6°$	179.9 ± 8.1 rad
	MFL	$32.5° \pm 1.1°$	187.0 ± 2.31 rad
23^{rd} March	Phase Scan	$34.6° \pm 2.1°$	182.5 ± 4.6 rad
	MFL	$35.6° \pm 0.9°$	180.2 ± 2.0 rad

Table 5.3: *Extracted θ_N and relative Φ_{rot} extracted from $\frac{d\Phi}{d\theta}$ in March 2018*

5.1.6 Variation of the bearing to North using a rotation stage

To overcome the difficulties in the estimation of the scale factor, we decided to implement a rotation stage below the sensor. With this new equipment (described in Section 3.4), we are now able to directly measure the full scale factor of the gyroscope. The stage allows us to rotate freely the experiment about the vertical axis giving us a direct read of the rotation angles. By measuring ϕ_{rot} at different angles and using a sinusoidal fit, we can measure the scale factor by extracting the amplitude of the modulated signal independently from the bias, which should stay constant.

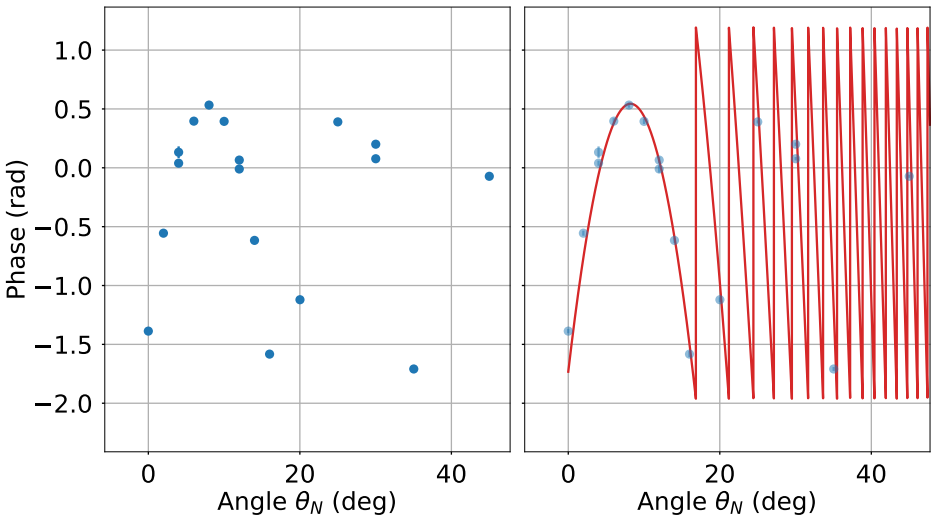

Figure 5.10: *(left) Extracted Phase versus the orientation of the sensor. The point are folded between 0 and π. (right) Visual guide showing how many times the fit curve has been folded. By counting how many times the curves jump, we are able to determine the number of π to add.*

In Figure 5.10 we can see how the phase evolves for a θ_N between 0° and 40°.
By looking at Eq. (5.2) one would expect a sinusoidal response as a function of θ_N. As

we can see in Figure 5.10 the points after 20 degree appear to be randomly distributed between 0 and π. This is a consequence of the under-sampling over the $\sim$70 fringes when changing the orientation of the sensor from North to East. To reconstruct the full scale factor, then, the measurements must be *unfolded*. To do this, we need to determine the number of π-period we have to add (subtract) from our measurements to reconstruct a proper sinusoidal signal. Knowing all of this problematic, we start to acquire measurements with the gyroscope aligned closely to North. At this orientation, the sensor is close to one of the extrema of $\Phi(\theta_N)$, thus we can perform multiple measurements being sure to remain within the same π period.

After acquiring 10 data points at different orientations, between 0° and 8° we can fit the extracted measurement with a cosine curve, fixing the amplitude of the curve to the expected value of the scale factor. This amplitude is estimated from the values in Table 5.1 with an uncertainty of 2 mrad. In Figure 5.10 we show the extracted cosine with a periodicity of π applied to it. A script then calculates the number of π-period needed to unfold the data points. This procedure, fit and calculation of the periodicity, is then repeated with each new measurement. In fact, small phase shift can lead to a wrong calculation of the periodicity, especially around East/West where the number of fringes per angle of rotation increases. In Figure 5.11 the unfolded data points are presented. In the graph are also shown two different fit curves: one obtained by fixing the amplitude to the expected value of the scale factor and leaving bias and phase parameters free(which was used to unfold the points). The second one is obtained by leaving the amplitude free, together with the other parameters, in the fitting routine. As we can see from

	Amplitude Fixed	Amplitude Free
Offset - Bias (rad)	-1.28 ± 0.13	0.633 ± 0.12
Phase - θ_N (deg)	$-8.19° \pm 0.06°$	$-7.84° \pm 0.03°$
Scale Factor (rad)	221.642	219.91 ± 0.11

Table 5.4: *Comparison of the extracted values for the sinusoidal curves in Figure 5.11. Column* Fixes *shows the value obtained by constraining the amplitude to the expected value for the gyroscope's scale factor. Column Free shows the result of the fit leaving as free parameters all three components.*

Table 5.4 and the inset in Figure 5.11, the two fitted curves produce different results. To better understand the nature of this discrepancy we need to complete a rotation about the vertical in order to better estimate the scale factor, by measuring the phase at South, where the phase shift is at its minimum, and the bias, by measuring the phase at East

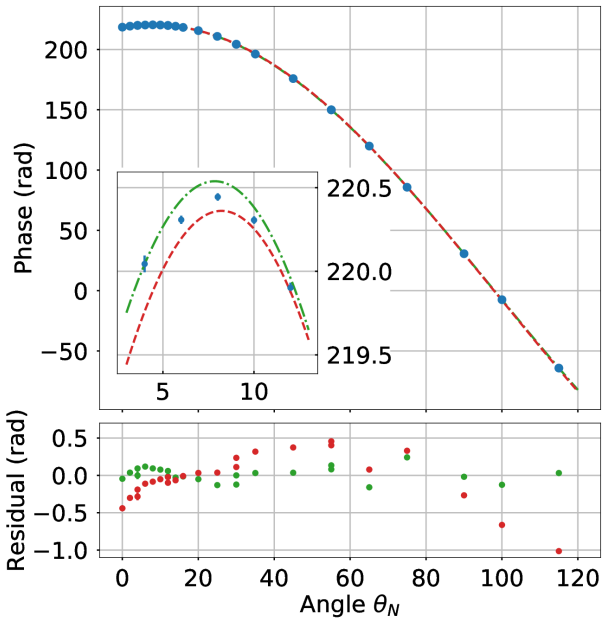

Figure 5.11: *Reconstructed phase versus the orientation of the experiment. In red is shown a fit with only bias and phase as free parameters, while the amplitude is fixed to the expected value for the scale factor. The green dash-dotted line represents a fit where also the amplitude is left free. In the inset is shown a magnification of the curves around the maximum (normal of the sensor's area aligned with North). To better show the difference between the fit curves and the data point, on the bottom are plotted the residual of the fit routines. The error bars in the plot are smaller than the marker size at this scale.*

and West and comparing the results. Unfortunately at this time, it was only possible to rotate the experiment up to 120°, due to the length of the fibers connecting the optical benches with the sensors. Other improvements, that can be made with this limitation, are the minimization of the long-term fluctuation of the bias. For example to change the orientation we need to open the isolation box around the sensor head for several minutes. The temperature, inside the box and around the sensor, then constantly fluctuates for long period of times, leading to diverse effects that worsen the stability of the sensor. One major effect that we have encountered, is the drift in the alignment of the Raman retro-reflection mirrors. In the next section, I will show how this misalignment affects the performances of the sensor and I will present the solution we put in place to reduce such effect.

5.2 Bias associated with an imperfect alignment of the retro-reflection mirrors

In this section I present how the parallelism between the Raman retro-reflection mirrors is controlled and optimized. Later on, I will present how these misalignments, combined with an improper mean trajectory of the atomic cloud, can lead to systematic effects in the phase estimation. Such phase shift are considered as one of the limiting factor in the current sensor's performance; it becomes critical to implement protocols in order to minimize such effects and reduce possible drifts in time.

5.2.1 Interferometer contrast

A misalignment between the Raman mirrors can be seen as using two distinct k-vectors. These two vectors have different directions but same modulus. We introduce θ as the relative angle between the two effective vector, then we can rewrite them as:

$$\begin{aligned} \vec{k}_b &= k_{eff}\hat{e}_r \\ \vec{k}_t &= k_{eff}(\hat{e}_r \cos\delta\theta + \hat{e}_\theta \sin\delta\theta) \end{aligned} \tag{5.6}$$

where $\hat{e}_r$ is the unit vector aligned with the direction of $\vec{k}_b$ and $\hat{e}_\theta$ is the unit vector perpendicular to $\hat{e}_r$ along the plane defined by $(\vec{k}_b, \vec{k}_t)$. In the case of perfectly aligned beams, we fall back on the condition $\vec{k}_b = \vec{k}_t = \vec{k}_{eff}$.

As a consequence of this misalignment, the wave-packets in the two arms of the interferometer will not perfectly overlap during the last pulse. We can calculate the distance, $\delta\vec{r}$, between the two wave packet as a function of the angle $\delta\theta$ between the retro-reflection mirrors. We begin by writing the position of the two wave-packets relative to the mean trajectory, at the end of the interrogation sequence:

$$\begin{aligned} \vec{x}_{up} = &\quad 2v_{rec}T((2-\cos\delta\theta)\hat{e}_r - \sin\delta\theta\hat{e}_\theta) \\ \vec{x}_{down} = &\quad 2v_{rec}T(\cos\delta\theta\hat{e}_r + \sin\delta\theta\hat{e}_\theta) \end{aligned} \tag{5.7}$$

with v_{rec} being the one photon recoil velocity and where $\vec{x}_{up(down)}$ describes the path followed by the wave-packet after the first pulse. From Eq. (5.7), we calculate the distance between the wave-packets at the moment of the last pulse:

$$\delta\vec{x} = 2v_{rec}T(\delta\theta^2)\hat{e}_r - 4v_{rec}T(\delta\theta)\hat{e}_\theta \simeq -4v_{rec}T(\delta\theta)\hat{e}_\theta \tag{5.8}$$

where at the moment we are interested only in the effect at first order in $\delta\theta$.

Given the finite temperature of the atomic cloud, Eq. (5.8) imposes a constraint on the maximum misalignment possible between the two mirrors. In fact, to generate interference between the two wave-packet, the distance $||\delta\vec{x}||$ has to be smaller than the coherence length ($L_{coh} = \frac{\hbar}{2M\sigma_v}$).
As the misalignment between the mirror increases, we can observe a decrease in the interferometer's contrast.

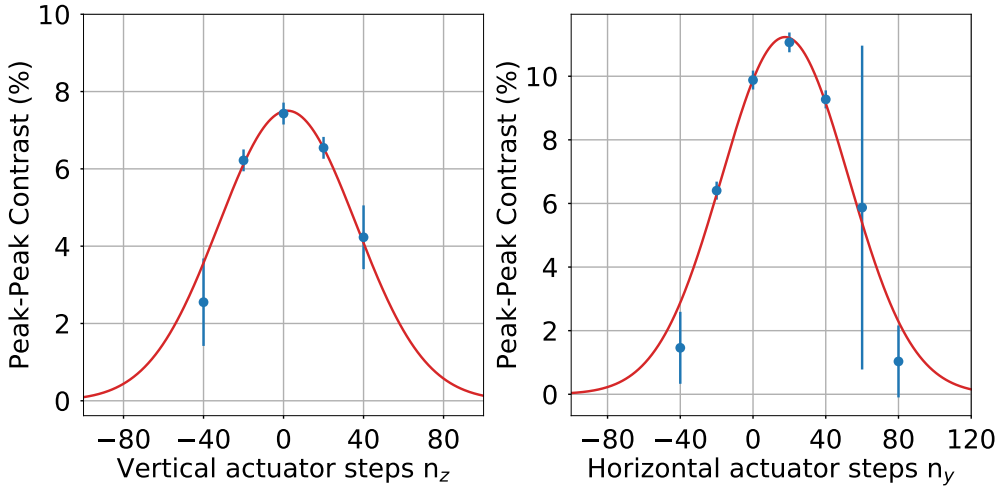

Figure 5.12: *Contrast as function of angle θ between the mirrors. On the left is presented the vertical direction. The contrast curve is centered around $n_z = 2(1.3)$ with a standard deviation of $\sigma_{\theta,z} = 34.4(2.6)$. On the right we show the results obtained by scanning the horizontal direction. Here the contrast is maximal at $n_y = 17.60(0.99)$ with standard deviation $\sigma_{\theta,y} = 34.9(1.5)$. The horizontal profile is higher since it was acquired after optimizing the vertical alignment.*

Therefore, an initial alignment can be performed by looking at how the contrast evolves as we scan the tilt of the mirrors. To do so, the bottom Raman retro-reflection mirror is equipped with a piezo-motor mount[3], which gives us the ability to finely adjust the relative alignment between the mirrors in both horizontal and vertical direction. These linear actuators have a nominal step size of $\sim$ 20nm. We measured the effective tilt applied to the mirror to be 0.3μrad by using an autocollimator before mounting the piezo controlled mount on the gyroscope. In Figure 5.12, is shown the changes of the interferometer's contrast as function of the piezo-motor actuator's step, for both the vertical and the horizontal direction. Each data point is obtained by fitting the

[3]Physik Instrumente Piezo Mike Linear Actuator N-470

probability distribution using a *"twin horned"* function[4]. As we can see the mirror in the horizontal position was distant roughly 20 steps (~ 6 μrad) from the optimal position. Using a Gaussian function we extract the standard deviation of the two curves: $\sigma_{\theta,z} = 34.4(2.6)$ for the vertical and $\sigma_{\theta,y} = 34.9(1.5)$ for the horizontal direction. From the standard deviation we can estimate the coherence length L_{coh} of our cloud, by using Eq. (5.8):

$$L_{coh} = 2\sqrt{2} v_{rec} \mathrm{T} \sigma_\theta \tag{5.9}$$

where the factor $1/\sqrt{2}$ rises from the convolution of two Gaussian function of same width. For both direction we obtain a coherence length of ~ 40 nm which is compatible with the length measured in the past using different methods as time of flight or Raman spectroscopy.

5.2.2 Bias estimation

Another quantifiable effect linked to the misalignment of the retro-reflection mirrors, is a net phase shift which leads to a bias in our measurements. To estimate this phase shift we rewrite the interferometer transfer function, keeping in consideration the different directions of the exchanged momentum by using the notation introduced in Eq. (5.6):

$$\begin{aligned} \Phi &= \varphi_b(0) - 2\varphi_t(\frac{T}{2}) + 2\varphi_t(\frac{3T}{2}) - \varphi_b(2T) = \\ &= \vec{k}_b \cdot \vec{x}(0) - 2\vec{k}_t \cdot \vec{x}(\frac{T}{2}) + 2\vec{k}_t \cdot \vec{x}(\frac{3T}{2}) - \vec{k}_b \cdot \vec{x}(2T) \end{aligned} \tag{5.10}$$

where we use the subscript $\{b, t\}$ to specify which of the two Raman laser pairs is being used.

We write the equation of motion[5] for each point of interest, in the laboratory reference frame:

[4] More information regarding how we estimate the amplitude, offset, probability noise and relative uncertainties can be found in Appendix A.

[5] We neglect the motion induced by Earth's rotation in this description

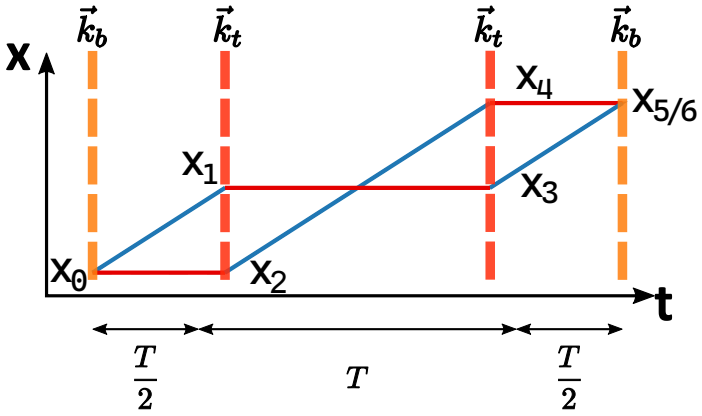

Figure 5.13: *Scheme showing the notation used in Eq. (5.11). The blue and red colors represent the internal states of the atom.*

$$
\begin{aligned}
\vec{x}_0 &= x(0) = 0 \\
\vec{x}_1 &= \left[\vec{x}_0 + \vec{v}_0\frac{T}{2} + \frac{1}{2}\vec{g}\left(\frac{T}{2}\right)^2\right] + \frac{\hbar\vec{k}_b}{M}\frac{T}{2} \\
\vec{x}_2 &= \left[\vec{x}_0 + \vec{v}_0\frac{T}{2} + \frac{1}{2}\vec{g}\left(\frac{T}{2}\right)^2\right] \\
\vec{x}_3 &= \left[\vec{x}_0 + \vec{v}_0\frac{3T}{2} + \frac{1}{2}\vec{g}\left(\frac{3T}{2}\right)^2\right] + \frac{\hbar\vec{k}_b}{M}\frac{3T}{2} - \frac{\hbar\vec{k}_t}{M}T \\
\vec{x}_4 &= \left[\vec{x}_0 + \vec{v}_0\frac{3T}{2} + \frac{1}{2}\vec{g}\left(\frac{T}{2}\right)^2\right] + \frac{\hbar\vec{k}_t}{M}T \\
\vec{x}_5 &= \left[\vec{x}_0 + 2\vec{v}_0T + \frac{1}{2}\vec{g}\,(2T)^2\right] + \frac{\hbar\vec{k}_b}{M}2T - \frac{\hbar\vec{k}_t}{M}T \\
\vec{x}_6 &= \left[\vec{x}_0 + 2\vec{v}_0T + \frac{1}{2}\vec{g}\,(2T)^2\right] + \frac{\hbar\vec{k}_t}{M}T
\end{aligned}
\tag{5.11}
$$

The terms in square bracket represent the ballistic trajectory of the mean position for the atomic cloud, while $\vec{v}_0$ is the mean velocity at the first pulse and $\vec{g}$ is the gravity acceleration. The second terms describe the recoil velocity caused by the Raman light-pulses, where M is the mass of Cs atoms.

The difference of phase at the output of the interferometer then becomes:

$$\begin{aligned}
\delta\Phi = & \left(\vec{k}_b\vec{r}_0 - \vec{k}_t\vec{r}_1 + \vec{k}_t\vec{r}_3 - \vec{k}_b\vec{r}_5\right) - (\vec{k}_t\vec{r}_2 - \vec{k}_t\vec{r}_4) = \\
= & \ \vec{k}_b \cdot (\vec{r}_0 - \vec{r}_5) + \vec{k}_t \cdot (\vec{r}_3 + \vec{r}_4 - \vec{r}_1 - \vec{r}_2) = \\
= & \ 2T\left(\vec{k}_t - \vec{k}_b\right) \cdot (\vec{v}_0 + \vec{g}\,T) + \frac{\hbar T}{M}\left(2\vec{k}_t\vec{k}_b - \vec{k}_b^2\right) = \\
= & \ 2Tk_{eff}[(\cos\delta\theta - 1)\hat{e}_r + \sin\delta\theta\hat{e}_\theta] \cdot (\vec{v}_0 + \vec{g}T) + \frac{\hbar}{M}k_{eff}^2 T(2\cos\delta\theta - 2)
\end{aligned} \tag{5.12}$$

If we now consider only the first order in θ, we obtain:

$$\Phi = 2Tk_{eff}\ \hat{e}_\theta \cdot (\vec{v}_0 + \vec{g}T)\ \delta\theta \tag{5.13}$$

This equation gives us another description for the loss of contrast due to the misalignment of the mirrors, discussed in the previous section. The velocity dispersion of the cloud, due to a finite temperature, can lead to different phase shifts among different velocity classes. As the detection integrates the signal over all possible velocity classes, if the range of the phase shift is in the order of 2π, destructive interference will decrease the total signal recorded.

By finely tuning the modulus and direction of the launch velocity, thus $\vec{v}_0 = -\vec{g}T$, we are able to completely minimize Eq. (5.13). With this adjustment the atomic cloud reaches the apogee of its ballistic trajectory at time T, thus in the middle of our interrogation time. This means the ascending and descending wave-packet are interrogated at the same position in the interrogation region, avoiding any wavefront induced phase shift generated by a non perfect alignment of the mirrors. The idea is to exploit such phase shift, in order to study and implement a new procedure which simultaneously adjust atomic trajectory and mirrors' parallelism.

5.2.3 Mirrors alignment and Trajectory optimization

We start by rewriting Eq. (5.13), highlighting the different components of the scalar product:

$$\delta\Phi = 2Tk_{eff}(\delta\theta_y\delta v_y + \delta\theta_z\delta v_z) \tag{5.14}$$

where we indicate with $\delta\theta_{y,z}$ the misalignment component in the experimental frame, and with $\delta v_z = v_z + g\mathrm{T}$ and $\delta v_y = v_y$ the respective velocity components. As we can see the phase shift components in the y and z direction are independent from each other. This allows us to study individually the two effects by changing only one component at a time. The main idea is to use the piezo-motor mirror mount to scan the alignment of the mirrors for different values of the $\delta v_{z,y}$ in order to find a common point for all sets that minimizes the phase shift.

Optimum vertical mirror alignment

To reliably change the velocity along the vertical direction, we can rely on different approaches: we could vary the launch velocity while monitoring the timings. Or we could change the timings of the interferometer to add an effective initial velocity $\delta v_z = g\delta t$. Since we have better control over the timing of the experiment we opt to modify the timing of the pulses. As we can see in Figure 5.14, for both launch velocities we are

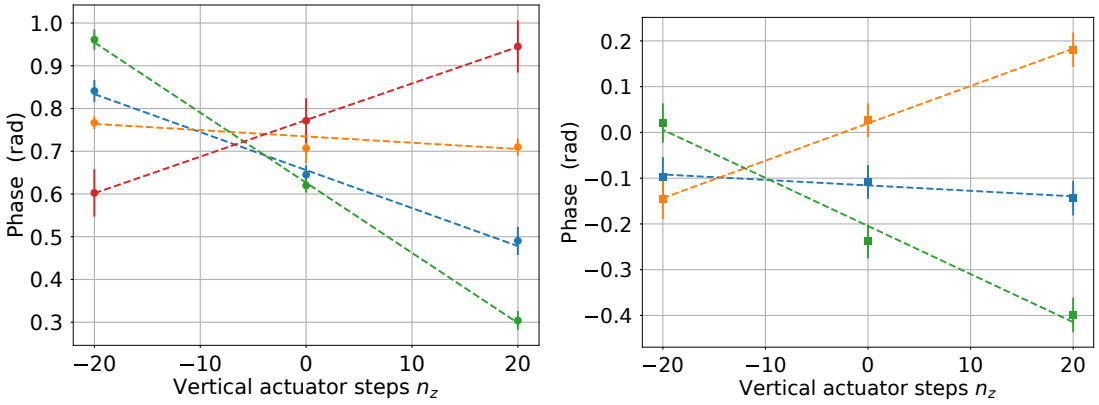

(a) *Launch velocity* $v_l = 5.041\ \mathrm{mm \cdot s^{-1}}$ **(b)** *Launch velocity* $v_l = 5.043\ \mathrm{mm \cdot s^{-1}}$

Figure 5.14: *Trajectory adjustment for the vertical direction. Each line in the two plot represents different timing for the first* $\pi/2$*-pulse separated by* $\delta t_1 = 0.25$ ms*:* 114.25 ms *(green),* 114.0 ms *(blue),* 113.75 ms *(orange),* 113.5 ms *(red). A change* $\delta t_1 = 0.25$ ms *in the timings corresponds to a change of velocity of* $\sim$2.5 $\mathrm{mm \cdot s^{-1}}$*. To demonstrate the reproducibility of the method we performed the optimization routine for two different launch velocities which differs by* 2 $\mathrm{mm \cdot s^{-1}}$*. Comparing the orange data set from figure* **(a)** *(slope* 1.20(37) $\mathrm{rad \cdot step^{-1}}$*) with the blue data set from* **(b)** *(*1.47(53) $\mathrm{rad \cdot step^{-1}}$*) we observe they have compatible slopes, thus the method works consistently for both launch velocities.*

able to pinpoint, within few actuator steps, the optimum alignment between the two retro-reflector mirrors.

We now proceed to compare the optimum position obtained by the adjustment of the trajectory and the position obtained by maximizing the contrast of the interferometer. In this case we can compare only Figure 5.14a since it has been acquired on the same day as Figure 5.12. On the contrary, the data-points shown in Figure 5.14b have been acquired few months prior. Since the piezo-motor mount do not provide an absolute reading about the position of the tilting screw, possible human errors as well alignment's drift

may have changed the reference point of Figure 5.14b with Figure 5.14a over time. The optimal positions between the two methods have a difference of 8 actuator steps, which corresponds to a difference of ∼2.4 μrad.

Optimum Vertical trajectory

As discussed in previous sections, this approach gives us the possibility to also estimate the correct initial velocity to satisfy $v_z = -gT$, in order to be insensitive to drift in the mirrors' alignment. To do so, we show the slopes $\frac{\delta\Phi}{\delta\theta}$, extracted from Figure 5.14, as a function of the initial velocities. As shown in Figure 5.15, by fitting the respective lines, we extract the optimal value for the vertical velocity, as the velocity which put the phase shift at zero. The two lines present compatible slopes within the error bars: 3.82 ± 0.04 mrad $\cdot$ step$^{-1} \cdot$ (mm/s)$^{-1}$ for launch velocity of $v_l = 5.043$ mm $\cdot$ s^{-1} and 3.46 ± 0.13 mrad $\cdot$ step$^{-1} \cdot$ (mm/s)$^{-1}$ for $v_l = 5.041$ mm $\cdot$ s^{-1}. This demonstrates how consistent is the method for different launch velocities.

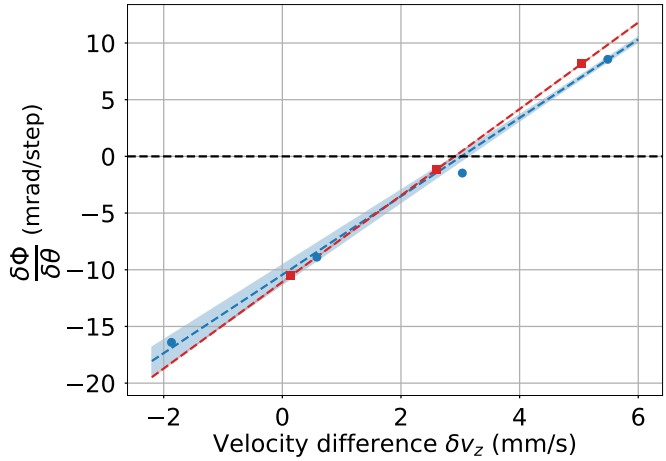

Figure 5.15: *Phase shift as function of velocities. In blue the results obtained from a launch velocities* $v_l = 5.041$ mm $\cdot$ s^{-1}*, with a slope of* 3.46 ± 0.13 mrad $\cdot$ step$^{-1} \cdot$ (mm/s)$^{-1}$*. In red the velocities with* $v_l = 5.043$ mm $\cdot$ s^{-1}*, and slopes* 3.82 ± 0.04 mrad $\cdot$ step$^{-1} \cdot$ (mm/s)$^{-1}$*. The shaded areas show the confidence region at one sigma for the blue results.*

Optimum horizontal mirror alignment

Changing velocity in the y-direction proved to be more challenging, compared to the vertical direction. Since we do not have a *control knob* that allows us to change the

transverse direction we have to rely on different methods to induce transversal velocities. If we assume the vertical axis of the sensor to be always aligned with the local direction of the acceleration of gravity, no transverse velocities should be present in the experiment. To induce a change in the horizontal velocities δv_y, we changed the projection of gravity acceleration along the y axis; to do so we varied the sensor's tilt along this same axis.

To apply large rotation to the sensor, we didn't rely only on the tilt lock setup since the range of the voice-coil is only $\sim$50 μrad. To reach inclination close to 1 mrad, in order to make the effect as visible as possible, we proceed to change the mass distribution present on top of the isolation platform. By changing the position along the y-direction of 10 kg lead weights we can reach transverse velocities of the order of $\pm$3.5 mm (corresponding to a tilt of $\pm$0.7 m rad).

The need to manually adjust the tilt though, has a large impact on the measurement performed after this operations. Opening the thermal-isolation box for the time it's needed to adjust the tilt, changes by roughly half a degree the temperature inside the box. This creates a continuous modulation in the temperature which could lead to a drift in the alignment of the mirrors. To avoid this we decided to measure the effects for only three different tilt which are obtained by moving the least amount of free weights.

In Figure 5.16a we show the measurement obtained for 3 different tilt value in the y

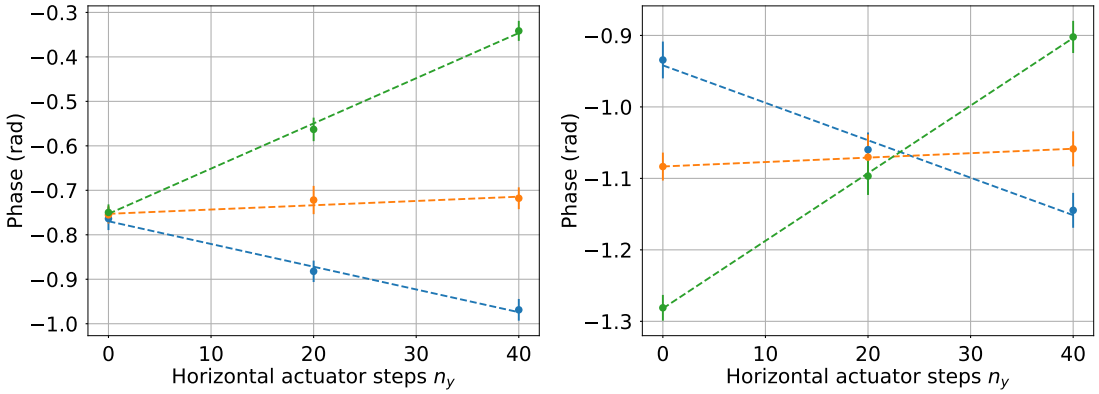

(a) **(b)**

Figure 5.16: *Trajectory adjustment for the horizontal direction. The two plot show the same measurement, without(left) and with(right) phase correction from the proximity sensors. The optimal mirror position in the corrected graph is* $n_y = 23.1(5)$*, compatible with the measured position in Figure 5.12*

direction. By comparing this graph with the curve obtained in 5.12, we see a discrepancy of 20 actuators steps, ($\sim$6 μrad), in the position of the optimal value between the two

methods. By repeating the measurements multiple times, we notice a small rotation of the isolation platform caused by the adjustment of the weight distribution. This rotation has been discovered after the implementation of the proximity sensor, discussed in Section 5.1.4. The maximum rotation we measured was about $\sim 0.2°$ which using Eq. (5.2) translates into phase shift of the order of 500 mrad. Knowing the direction and the angle of these rotations, we are able to correct the phase measurements, as seen in Figure 5.16b.
After the measurements are corrected, we estimate the optimal position to be at $n_y = 23.1(5)$ steps, which compared with the values obtained from contrast curve in Figure 5.12, reveal a difference of 1.7 μrad.

Optimum horizontal trajectory

Similarly to the vertical case, we can estimate the optimal transverse velocity, thus the optimal inclination of the sensor in the y direction. In Figure 5.17 we show the slopes $\frac{\delta\Phi}{\delta\theta}$ as a function of the transverse velocities. We are then able to estimate the optimal velocity($v_y = -0.618(27)\text{mm} \cdot \text{s}^{-1}$), in order to vertically launch our atomic cloud.

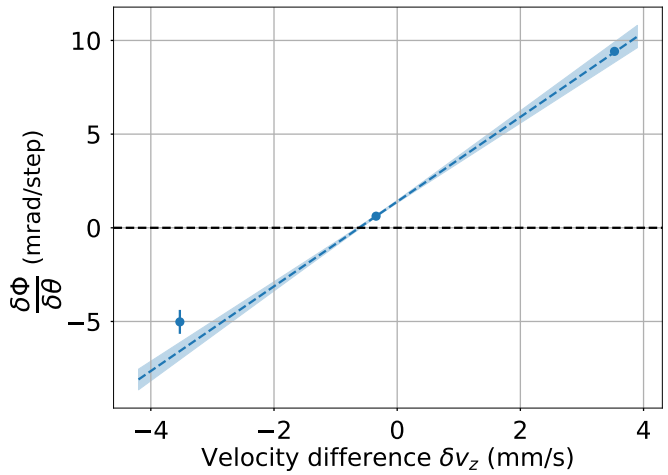

Figure 5.17: *Phase shift as function of transverse velocity. The shaded area is one sigma confidence region. The slope of the linear fit is* 2.26 ± 0.08 mrad $\cdot$ step^{-1} $\cdot$ (mm/s)$^{-1}$

5.3 Conclusion

In the first part of the chapter, I presented the first study regarding the scale factor of the cold atom gyroscope. I first started by investigating different methods to estimate the initial orientation of the gyroscope to North. This task proved to be difficult, as the results obtained presented fluctuations in some systematics from day to day which we were not able to understand. These fluctuation prevented us to measure without ambiguity the scale factor of our sensor and to estimate the biases affecting it.
To overcome these difficulties, we proceed to setup a rotating stage below the gyroscope, in order to measure *directly* the scale factor and the bias.
I then presented the preliminary results regarding a direct measurement of the scale factor obtained by rotating the sensor head by 120°. We measure 219.91 ± 0.11 rad, while from the calculation we expect $221.642(exact)$ rad. Although agreement is marginal we differ from the expected value by 15σ due to statistical uncertainties. During the redaction of this manuscript, we identified a problem when we turn the gyroscope. The central axis of the rotation stage was not well aligned with the vertical axis. This caused the isolation platform to rotate under the weight of the sensor, causing phase shift which impacted the estimation of the gyroscope's scale factor. The complete and corrected picture will be showed in the manuscript of the next PhD student, Romain Gautier.

In the second part of the chapter, I presented, a new protocol which optimizes the alignment of the mirrors and the trajectory of the atomic cloud in both vertical and transversal direction. We are now able of aligning the Raman retro-reflection mirrors to μrad precision in *both* direction. To reach levels of stability below $10^{-10}\text{rad} \cdot \text{s}^{-1}$ we plan to exchange the mirror mounts inside the sensor's magnetic shield with more rigid one, to maintain for longer period an optimal alignment. We also plan to implement an *"on the fly"* characterization of the phase shift, by automatically scanning the mirror every $N{\sim}10^4$ shots of the interferometer in order to minimize the phase shift. The characterization would automatically move the piezo controlled mirror by ± 40 steps from the optimal position. If a slope is detected we will adjust the velocity in order to compensate the phase shift. To be effective such characterization has to be performed in a limited amount of time in order to not affect the performance of the sensor.

This systematic effect is not limited to 4-pulse geometry but could affect other atomic interferometers which utilize spatially separated laser beams. As an example, proposals of ground-based gravitational wave detectors in the 0.1 to 10 Hz frequency band shall employ a similar interferometer configuration as that presented here, but with

atom interferometric sensors spatially distributed along a common laser baseline in a gradiometer setup [18, 54].

Chapter 6

4 light pulse atom interferometer with non equal momentum transfer

The increase of probability noise σ_P is a known problem in atom interferometry. One of the major source of the increase are *parasitic interferometers*. These AI are generated by imperfection in the pulses used to realize beam-splitters and mirrors. Since they follow different paths compared to the main interferometer, their scale factor to inertial forces is different.

Solutions to mitigate this problem, are highly connected to the scheme used in the interferometer [55]. In our 4 light-pulse configuration, the imprecision in performing a correct *pi*-pulse, leads to the generation of 2 secondary parasitic interferometer. In this chapter I will present the different methods we use in the gyroscope, to eliminate these effects, in order to recover a good signal to noise ratio (SNR). I will first describe the solution introduced by previous PhD students [31, 32], which relies on shifting the timings of the π-pulses. Due to this shift, only the main interferometer is recombined at the last $\pi/2$-pulse while the parasitic interferometers are not. While the implementation of such solution is fairly easy, it fades the intrinsic zero-sensitivity to DC acceleration of the 4-pulse butterfly scheme. I will show how we can minimize this unwanted side-effect by optimizing the frequency ramp, which is already in use to compensate for Doppler frequency shift. Later in the chapter I will introduce a different interrogation scheme which mitigates the effects of parasitic interferometer, while maintaining zero sensitivity to DC acceleration. The scheme relies on the use of non equal momentum transer and the π pulses [56]. I will then describe how this configuration has been implemented and

I will present the latest result demonstrating the effectiveness of this scheme.

6.1 Parasitic Interferometer

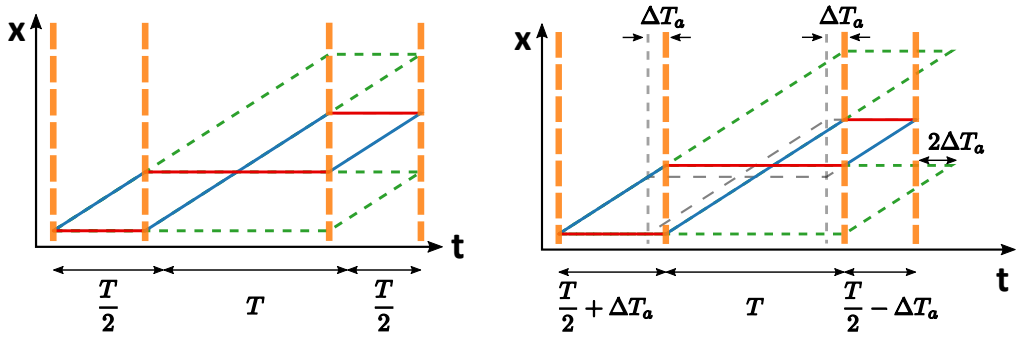

(a) *Symmetric 4-pulse interferometer* **(b)** *Asymmetric 4-pulse interferometer*

Figure 6.1: *Space-Time diagram showing the path of the main interferometer (solid line) and of the parasitic interferometers (dashed green lines). On the left,* **(a)***: in the normal 4-pulse configuration all of the path recombines at the last $\pi/2$-pulse (vertical dashed orange lines). On the right,* **(b)***: By shifting the two π-pulses in time by ΔT_a, only the main interferometer recombines at the last $\pi/2$-pulse.*

Due to its size and the multiple velocity class present in the cloud, the efficiency of our Raman lasers pairs is not 100%. As a consequence, part of the atomic cloud do not interact with our $\pi/2$ and π pulses. In our 4-pulse interrogation scheme, this phenomenon generates a pair of secondary interferometers which recombine at the same time as the primary interferometer. The main effect connected to this secondary interferometers is the increase of probability noise σ_P. The signal at the output of the interferometer then, will be a combination of different fringe patterns, one for each interferometers. This mixture of signals is translated in probability noise in our detection system, thus decreasing the signal to noise ratio of our measurements. As discussed in [57, 58], a possible method to recover good level of SNR, consists in translating the two central π-pulses by ΔT_a in an asymmetric way with respect to the apogee, as seen in Figure 6.1b; with this modification, the parasitic interferometers do not recombine as the two paths overlap at a different time while the total paths of the main interferometer remain unchanged. To the shift in time ΔT_a, we associate a distance ΔX which measure the separation between the point of recombination of the primary interferometer and the

point of recombination of the parasitic AI. This distance can be estimated as:

$$\Delta X = 2\Delta T_a \frac{\hbar k_{eff}}{M} = 4\Delta T_a v_{rec} \tag{6.1}$$

To recover the best signal to noise ratio then, the separation ΔX between the recombination point, has to be larger than the coherence length of the wave packet, $\Delta X \geq 2 \cdot L_{coh}$:

$$\Delta T_a \geq L_{coh} \frac{M}{\hbar k_{eff}} = \frac{L_{coh}}{2v_{rec}} \tag{6.2}$$

From the previous chapter 5.2.1, we estimate the coherence length to be of the order of 40 nm, which translates to a minimum shift of $\Delta T_a = 6$ μs.

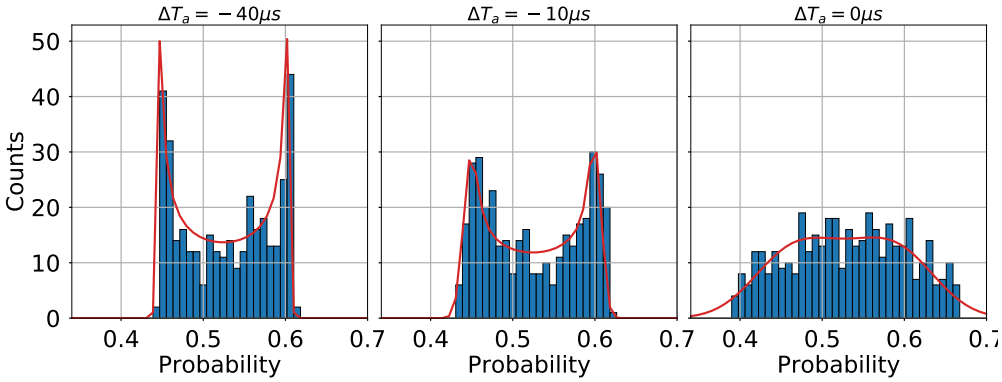

Figure 6.2: *Probability distribution for different values of the time shift ΔT_a. As we can see as the time shift decreases, the feature of the distribution are blurred by the probability noise until they completely disappear.*

To visualize the increase of σ_P linked to the *parasitic interferometer*, we show in Figure 6.2 the probability distribution for three different values of the time-shift ΔT_a={-40 μs, -10 μs, 0 μs}. As we can see for large ΔT_a, hence σ_P is small, the distribution presents two sharp features at the extremities, and low count number at the center. As ΔT_a goes to zero, thus σ_P increases, we see how the *sharp* features fade into the main body of the distribution. To estimate correctly the SNR of these distributions, we use a statistical method [59] that allows us to measure and separate amplitude noise from phase noise. The full description regarding this statistical tool and the uncertainties associated with it, is described in Appendix A. Using the *"twin-horned"* function that comes with this tool, we are able to determine all three parameters independently of the phase of the sensor.

In Figure 6.3, we show how the probability noise evolves as a function of the time shift

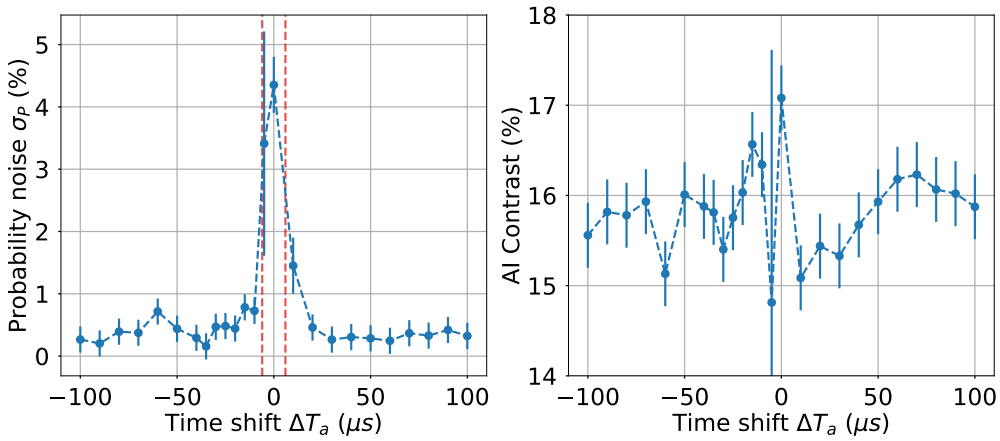

Figure 6.3: *Probability noise (left) and interferometer contrast (right) as function of the time shift ΔT_a. As we can see from the graph on the right the interferometer contrast remains constant within the error bars. The graph on the left shows how fast the probability noise decreases once ΔT_a is bigger than 6 μs (red dashed vertical lines).*

ΔT_a. As expected, σ_P is maximal when we do not introduce any asymmetry in the 4 pulse scheme. For $\Delta T_a > 6$ μs, σ_P decreases rapidly until it reaches a level of less than 1%. The figure shows also how the contrast of the interferometer stays the same, independently from the time shift ΔT_a. This proves our fit function is capable of estimating, separately and independently, all three parameters. A more in depth study on the goodness of the extracted parameters and their uncertainties is presented in Appendix A.

6.2 DC acceleration sensitivity and ramp optimization

As discussed in the previous section, to prevent the simultaneous recombination of the parasitic interferometers with the primary one, the central π-pulses are translated in time by ΔT_a. This shift deteriorates the intrinsic zero sensitivity to DC acceleration by introducing a phase shift proportional to ΔT_a. We calculate then this contribution by adjusting the timing in Eq. (2.20):

$$\Delta\Phi_{\Delta T_a} = \phi_1(0) - 2\phi_2(T/2 \pm \Delta T_a) + 2\phi_3(3T/2 \pm \Delta T_a) - \phi_4(2T) \tag{6.3}$$

which results in:

$$\Delta\Phi_{\Delta T_a} = \pm 2T\Delta T_a\left(\vec{k}_{eff} \cdot \vec{g}\right) \tag{6.4}$$

To mitigate this phase shift alternating measurements with opposite sign of $\pm\Delta T_a$ can be acquired, averaging in post process the measured phase shift. Another possible solution,

is inspired by cold-atom gravimetry, which utilizes frequency ramps to measure gravity [60, 61]. This technique aims to compensate the gravity induced phase shift by scanning the relative frequency of the two Raman lasers, thus inducing an ulterior phase shift with opposite sign.

6.2.1 Frequency ramp

With the atoms constantly in free fall, their velocity steadily changes during the interrogation phase. To compensate the relative Doppler effect then, we sweep the frequency of one of the Raman laser by chirping the reference frequency of the phase lock loop (PLL). We use a linear ramp $2\pi f(t) = \alpha \cdot t$ with α being the ramp rate expressed in Hz/s. This change of frequency introduce a phase shift which cumulates with time and can be described as:

$$\Delta\Phi_\tau = \int_{\tau_{i-1}}^{\tau_i} 2\pi f(t)\mathrm{d}t = 2\pi\alpha\Big(\tau_i^2 - \tau_{i-1}^2\Big) \tag{6.5}$$

where τ_i indicates the timing of the i-th pulse. If we sum the contribution from each pulse, using Eq. (6.5) together with Eq. (6.4), we obtain the total phase shift for DC acceleration of the gyroscope as:

$$\Delta\Phi = 2T\Delta T_a\Big(\vec{k}_{eff}\cdot\vec{g} - 2\pi\alpha\Big) \tag{6.6}$$

By carefully choosing α then, we can compensate the gravity induced phase shift. From Eq. (6.6) we can extract the general expression for α:

$$\alpha = \frac{\vec{k}_{eff}\cdot\vec{g}}{2\pi} \tag{6.7}$$

6.2.2 Ramp optimization

In previous work [28, 31, 32], the techniques used to estimate the optimal value of α required to setup a 3-pulse interferometer using *only one* Raman laser pair collimator. By utilizing this scheme the sensor was operated as a pure accelerometer, measuring the projection of gravity acceleration onto the Raman laser pair axis. Once the sensor is set up to operate with 3-pulse, two different set of measurements with different interrogation times $T_{1,2}$ are performed. The two measurements will give:

$$\begin{aligned}\Phi_{T_1} &= \Big(\vec{k}_{eff}\cdot\vec{g} - 2\pi\alpha\Big)T_1^2\\ \Phi_{T_2} &= \Big(\vec{k}_{eff}\cdot\vec{g} - 2\pi\alpha\Big)T_2^2\end{aligned} \tag{6.8}$$

By taking the difference of the two equation we obtain:

$$\left(\vec{k}_{eff} \cdot \vec{g} - 2\pi\alpha\right) = \frac{\Phi_{T_1} - \Phi_{T_2}}{T_1^2 - T_2^2} \tag{6.9}$$

The old optimization routine, requires to minimize the right hand term of Eq. (6.9) for multiple values of T_1 and T_2. By increasing the difference between the interrogation times, the precision in the estimation of the ramp rate increases. By combining different acquisitions, it is possible to estimate $\alpha = -\vec{k}_{eff} \cdot \vec{g}$ with an accuracy of 10^{-4} g levels. The value of α was then estimated to be ~ 1.525 MHz $\cdot$ s^{-1} and it becomes our reference value for future estimation, α_0.

While this method could reach good levels of accuracy, it has its limitations. The estimation of the ramp is limited directly by the level of precision to which we can discern the two phases $\Phi_{1,2}$. Another limitation is the time needed to complete such procedure. In fact it requires multiple acquisitions at different interrogation time for different values of the frequency ramp. Moreover, once the optimal ramp has been found, the procedure has to be repeated on the second Raman laser pair collimator in order to verify the parallelism between the mirrors.

To reduce the time needed in order to tune the frequency ramp, a new procedure has been developed and implemented. We leverage our capability to interleave multiple measurements with opposite sign of ΔT_a. As the phase shift written in Eq. (6.6) is also directly proportional to the phase shift ΔT_a, we proceed to acquire multiple sets of measurements with a combination of different ΔT_a and different values for α. In Figure 6.4a we present the results obtained for three different ramp rate values, in order to show how sensitive this operation is. The first ramp rate being used is our reference ramp α_0, while the other two are deviation of $\pm 0.4\%$ from the reference value. For each ramp, we acquire multiple values of $\pm\Delta T_a$, to clearly show how the phase shift is proportional to the value of the time shift.

In order to determine the optimal ramp rate, we extract the various slopes $\frac{\Delta\Phi}{\Delta T_a}$ and we display them as a function of the ramp rate in Figure 6.4b. To estimate the correct ramp rate we need to pinpoint the values of α that nullify the phase shift $\frac{\Delta\Phi}{\Delta T_a}$. From Figure 6.4b and using a linear fit, we measure the optimal ramp rate to compensate DC acceleration phase shift is $\alpha = 1.5232(1)$ MHz $\cdot$ s differing by only 1.6 kHz $\cdot$ s from our reference ramp.

This new procedure proves to be a good alternative to operate the sensor as a pure accelerometer. Nevertheless the use of asymmetric 4-pulse configuration does not appear to be the ideal solution in order to remove the destructive interference from parasitic interferometer. In fact, with only 0.05% deviation from the optimal value, our reference

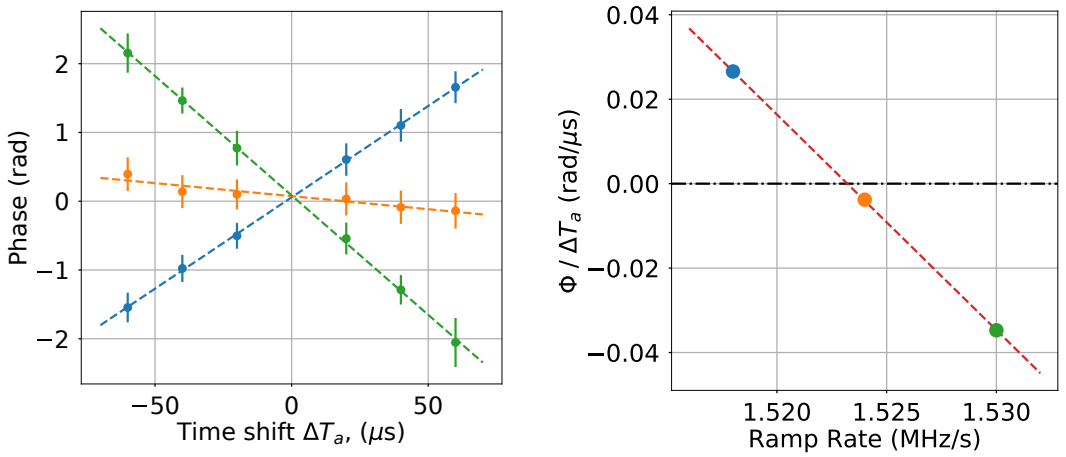

(a) *Result for different ramp* **(b)** *Slopes versus ramprate*

Figure 6.4: *On the left: Phase shift for different values of the frequency ramp as a function of the asymmetric time shift* ΔT_a*. In yellow is depicted the reference frequency ramp* $\alpha_0 = 1.5248\ \mathrm{MHz}\cdot\mathrm{s}^{-1}$*. In blue (green) we show a frequency ramp* 0.4% *higher (lower) than* α_0*. No measurements have been performed at* $\Delta T_a = 0$ *due to the increased probability noise. On the right: Phase shift* $\Phi/\Delta T_a$ *as a function of the applied ramp rate (error bars covered by the marker): slope* $-5.104(16)\ \mathrm{rad}\cdot\mu\mathrm{s}^{-1}/\mathrm{MHz}\cdot\mathrm{s}^{-1}$*. By minimizing the absolute value of* $\Phi/\Delta T_a$ *we determine the optimal ramp rate to be* $\alpha = 1.5232(1)\ \mathrm{MHz}\cdot\mathrm{s}^{-1}$.

ramp introduces 100 mrad phase shift at $\Delta T_a = 40\ \mu s$, meaning we still have to alternate between measurements with opposite sign of ΔT_a to compensate for this.

6.3 Non Equal k_{eff} momentum transfer

A different solution to mitigate the interference of parasitic interferometers is proposed in [57]. By choosing distinct combination of exchanged momentum and light-pulse timing, it is possible to recover good signal to noise level by not recombining parasitic interferometer. Contrary to the method presented earlier in the chapter, this 4-pulse scheme with different exchanged momentum between the $\pi/2$-pulses and π-pulses, retains the inherent zero sensitivity to DC acceleration phase.

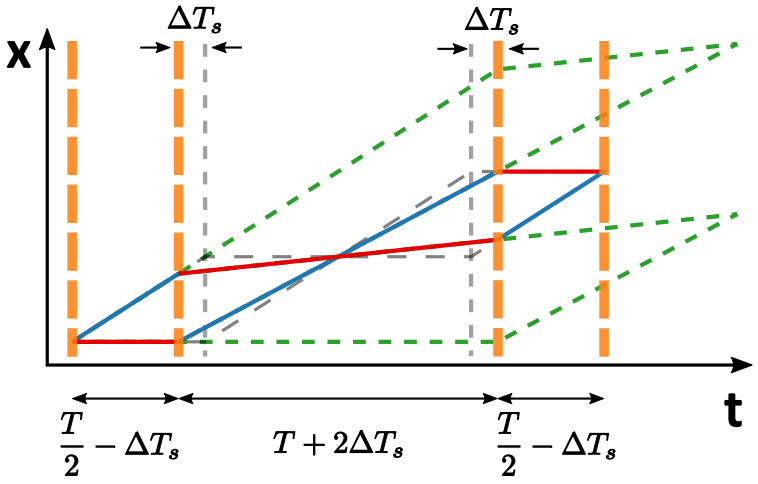

Figure 6.5: *Space-Time diagram showing the path of the interferometer with non equal momentum transfer, with the π-pulses symmetrically shifted in order to recombine the main interferometer. The gray dashed lines represent the symmetric 4-pulse interferometer with equal momentum exchanged. The secondary parasitic interferometer are shown with the green dashed lines.*

6.3.1 Change of exchanged momentum modulus

In order to precisely change the modulus of $\vec{k}_{eff}$ for either π or $\pi/2$ pulses we exploit the Raman pairs' collimator system. The top collimator is responsible only for the π-pulses; by changing the angle of input, compared to the bottom Raman collimator, we can modify the modulus of the effective momentum exchanged k_{eff}. By using a micrometric screw positioned on top of the collimator mount, we can apply rotations $\Delta\theta$ in the vertical direction with a precision of $2 \cdot 10^{-6}$ rad. To estimate the tilting angle applied to the collimator, we use this simple relation $\Delta\theta = \arctan(\Delta X/D)$, where D=10 cm is the distance between the pivot of the mount and the screw and ΔX indicates the displacement of the micrometric screw on the mount. Since we will apply only small rotation, less than 40 mrad to the top Raman pair collimator, it is possible to rewrite the relation between the two k-vector taking the bottom one as a reference

$$k'_t = k_{eff} \cos\Delta\theta \simeq k_{eff}(1 - \frac{\Delta\theta^2}{2}) = k_{eff} - \Delta k \tag{6.10}$$

where we indicate the difference in exchanged momentum as $\Delta k = k_{eff} \cdot \Delta\theta^2/2$.

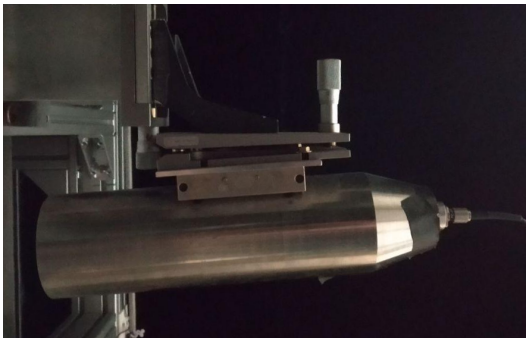

(a)

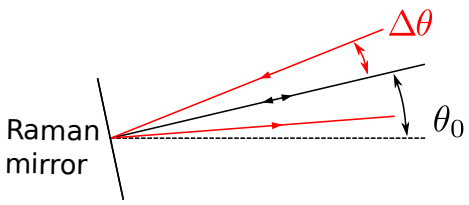

(b)

Figure 6.6: **(a)** *Collimator with micro-metric screw to adjust the tilt of the laser beam.***(b)** *Scheme of the retro-reflection*

Closing the interferometer

In order to recombine the two wave packets at the output of the interferometer, we shift the two π-pulses symmetrically, with respect of the apogee, by ΔT_s, as shown in Figure 6.5. To calculate the value of such shift we determine the position of the two wave packet at the output of the interferometer:

$$\begin{aligned} x_{up} &= \frac{\hbar\vec{k_b}}{M}(2T) - \frac{\hbar\vec{k_t'}}{M}\left(\frac{3T}{2} + \Delta T_s\right) + \frac{\hbar\vec{k_t'}}{M}\left(\frac{T}{2} - \Delta T_s\right) \\ x_{down} &= \frac{\hbar\vec{k_t'}}{M}\left(\frac{3T}{2} + \Delta T_s\right) - \frac{\hbar\vec{k_t'}}{M}\left(\frac{T}{2} - \Delta T_s\right) \end{aligned} \tag{6.11}$$

We then impose the two clouds to be completely overlapped:

$$\Delta x = x_{up} - x_{down} = (T)k_b - (T + 2\Delta T_s)k_t' = 0 \tag{6.12}$$

If we now combine the definition in (6.10) with equation in (6.12) we find the relation between the relative change of exchanged momentum and the time-shift we need to apply to our middle pulses:

$$\frac{1}{2}\frac{\Delta k}{k_{eff}\left(1 - \frac{\Delta k}{k_{eff}}\right)} = \frac{\Delta T_s}{T} \tag{6.13}$$

Since the ratio between Δk and k_{eff} is small we rewrite the (6.13) as

$$\frac{1}{2}\frac{\Delta k}{k_{eff}} \simeq \frac{\Delta T_s}{T} \tag{6.14}$$

The change of momentum, also displace the parasitic interferometer by a distance $\Delta X = 2T\frac{\hbar}{M}\Delta k$; as for Eq. (6.1) we impose this distance to be larger than the coherence

length and we obtain the minimum change of momentum needed to kill the parasitic interferometer:

$$\frac{\Delta k}{k_{eff}} = \frac{L_{coh}}{2Tv_{rec}} \sim 1.5 \cdot 10^{-5} \tag{6.15}$$

6.3.2 Zero sensitivity to DC acceleration

Following the procedure used in the previous chapter we now demonstrate how, using this scheme, the sensor remain insensitive to DC acceleration. We start again by writing the equation of motion for the two wave-packet along the two path:

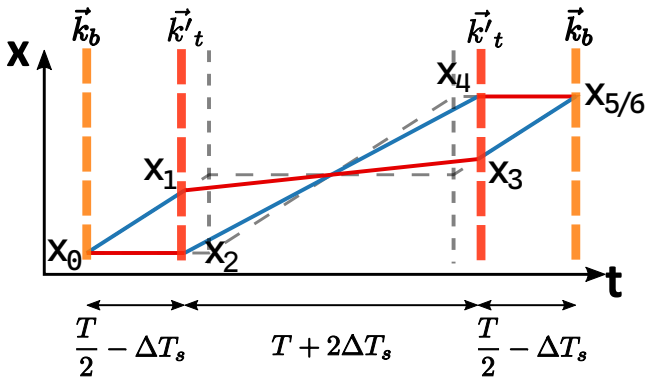

Figure 6.7: *Scheme showing the notation used in Eq. (6.16). The blue and red colors represent the internal states of the atom while the gray dashed lines represent the path of the 4 pulse interferometer with equal momentum.*

$$\begin{aligned}
x_1 &= \left[\vec{v}_0\left(\frac{T}{2} - \Delta T_s\right) + \frac{\vec{g}}{2}\left(\frac{T}{2} - \Delta T_s\right)^2\right] + \frac{\hbar\vec{k_b}}{M}\left(\frac{T}{2} - \Delta T_s\right) \\
x_2 &= \left[\vec{v}_0\left(\frac{T}{2} - \Delta T_s\right) + \frac{\vec{g}}{2}\left(\frac{T}{2} - \Delta T_s\right)^2\right] \\
x_3 &= \left[\vec{v}_0\left(\frac{3T}{2} + \Delta T_s\right) + \frac{\vec{g}}{2}\left(\frac{3T}{2} + \Delta T_s\right)^2\right] + \frac{\hbar\vec{k_b}}{M}\left(\frac{3T}{2} + \Delta T_s\right) - \frac{\hbar\vec{k'_t}}{M}(T + 2\Delta T_s) \\
x_4 &= \left[\vec{v}_0\left(\frac{3T}{2} + \Delta T_s\right) + \frac{\vec{g}}{2}\left(\frac{3T}{2} + \Delta T_s\right)^2\right] - \frac{\hbar\vec{k'_t}}{M}(T + 2\Delta T_s) \\
x_5 &= \left[\vec{v}_0(2T) + \frac{\vec{g}}{2}(2T)^2\right] + \frac{\hbar\vec{k_b}}{M}(2T) - \frac{\hbar\vec{k'_t}}{M}(T + 2\Delta T_s)
\end{aligned} \tag{6.16}$$

where we fixed x_0 to zero for convenience.
We then calculate the phase-shift accumulated along the paths and take the difference:

$$\begin{aligned}\Phi &= \left(\vec{k_b}\cdot\vec{x}_0 - \vec{k'_t}\cdot\vec{x}_1 + \vec{k'_t}\cdot\vec{x}_3 - \vec{k_b}\cdot\vec{x}_5\right) - \left(\vec{k'_t}\cdot\vec{x}_2 - \vec{k'_t}\cdot\vec{x}_4\right) = \\ &= -\vec{k_b}\cdot(\vec{x_5}) + \vec{k'_t}\cdot(\vec{x_3}+\vec{x_4}-\vec{x_2}-\vec{x_1}) = \\ &= \left[\vec{k'_t}(T+2\Delta T_s) - \vec{k_b}T\right]\cdot\left(2(\vec{v}_0+\vec{g}T) + \frac{\hbar\vec{k_b}}{M}\right)\end{aligned} \tag{6.17}$$

If we use the condition (6.12) for overlapping wave-packet, it is easy to see how equation (6.17) goes to zero. This result shows how, the implementation of non equal k_{eff} momentum transfer, is a better solution to avoid the recombination of parasitic interferometer, while still maintaining zero-sensitivity to DC acceleration.

6.3.3 Probability noise and ramp optimization

To demonstrate the validity of Eq. (6.14), we proceed to measure the contrast of the interferometer as a function of the symmetric time shift ΔT_s. In Figure 6.8 we show the measurement repeated for a values of $\Delta\theta$ equals to 10 mrad and 20 mrad, which requires a ΔT_s of respectively 10 μs and 40 μs.

By fitting the two curves with a Gaussian profile we extract the center of the profiles $10.6 \pm 0.1\mu$s for 10 mrad (blue curve) and $41.20 \pm 0.15\mu$s for 20 mrad (red curve). The extracted values differ from the expected ones by 5% for 10 mrad and 3% for 20 mrad. By using Eq. (6.14), and the relation $\frac{\Delta k}{k_{eff}} = \frac{\Delta\theta}{2}$ we can estimate an initial misalignment between the collimator of 0.3 mrad that was not measured before. In Figure 6.8, on the bottom, is also shown the probability noise, σ_p, for these measurement. Contrary to the asymmetric time-shift case, we can see how σ_p remains relatively flat for all time-shift measured, meaning the adverse effect from parasitic interferometer are completely removed.

To better compare the two schemes, we repeat the ramp optimization procedure with the non equal momentum configuration. To do so, we sum up the two different time shift, ΔT_a and ΔT_s, for each combination of ΔT_a and ramp. As we can see in Figure 6.9, the results are visually similar, with the notable exception that with non equal momentum exchange we are now able to measure phase shift without any asymmetric time shift ΔT_a. This will lead us to an improved rejection of the DC acceleration phase noise.

In order to estimate how well we are rejecting DC-acceleration, we set our self at $\Delta T_a = 0$ with a $\Delta\theta$ equals to 20 mrad. We then proceed to measure the output phase of the interferometer for different values of the ramp. We subsequently acquire the same set of measurements with $\Delta\theta = 30$ mrad.

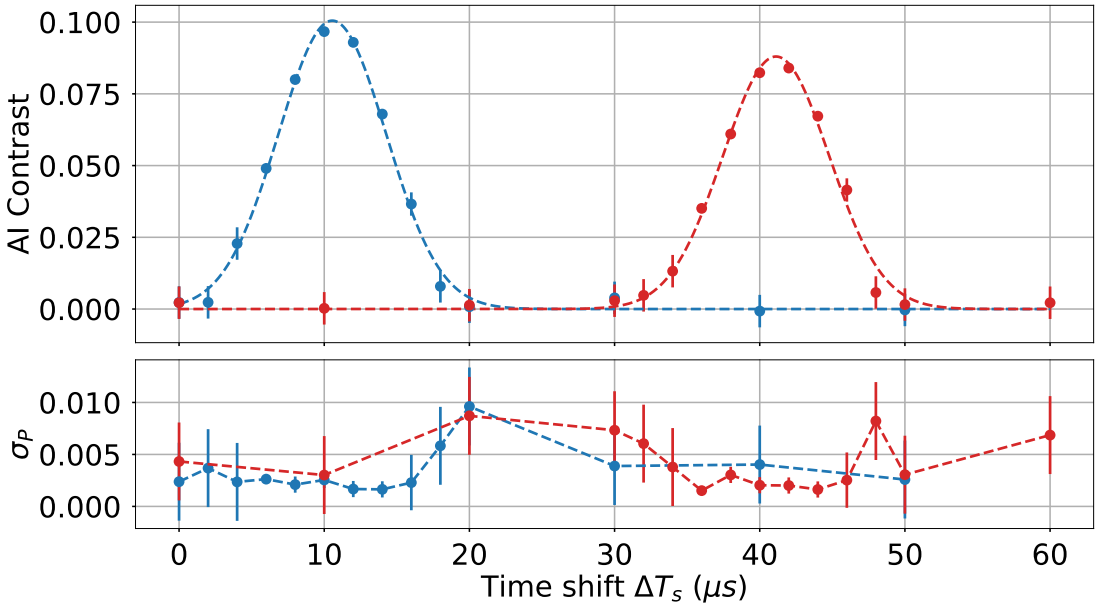

Figure 6.8: *(Top) Interferometer contrast as a function of the time-shift ΔT_s for two different vertical tilt of the collimator: $\Delta\theta$ = 10mrad, showed in blue, $\Delta\theta$ = 20mrad, showed in red. (Bottom) In this panel is shown the probability noise σ_p linked to the contrast curves shown above.*

In Figure 6.10, are then showed the results of these sets of measurements. By fitting the data points we extract for both sets a variation of phase of $\sim$ 0.1 rad per 6% of ramp variation. Analogously, from Figure 6.4a, for a $\Delta T_a = 40\ \mu s$, the asymmetric interferometer presents a phase shift of 2.5 rad per 0.8% of total ramp variation. If we compare the results, these translate to a suppression factor for DC accelerations of 180 for the non equal momentum transfer scheme compared to the asymmetric configuration. In other words, the residual sensitivity measured can be compared to an interferometer with $\Delta T_a = \frac{40}{180}\ \mu s = 0.22\ \mu s$ time shift, which could be linked to the small initial misalignment between the Raman laser pair collimator showed in Figure 6.8.

6.3.4 Sensitivity to rotation - Scale factor

The introduction of non equal exchanged momentum, as depicted in Figure 6.5, changes the path of the diffracted wave packet in order to avoid the simultaneous recombination of the main interferometer with the parasitic ones. Contrary to the asymmetric case,

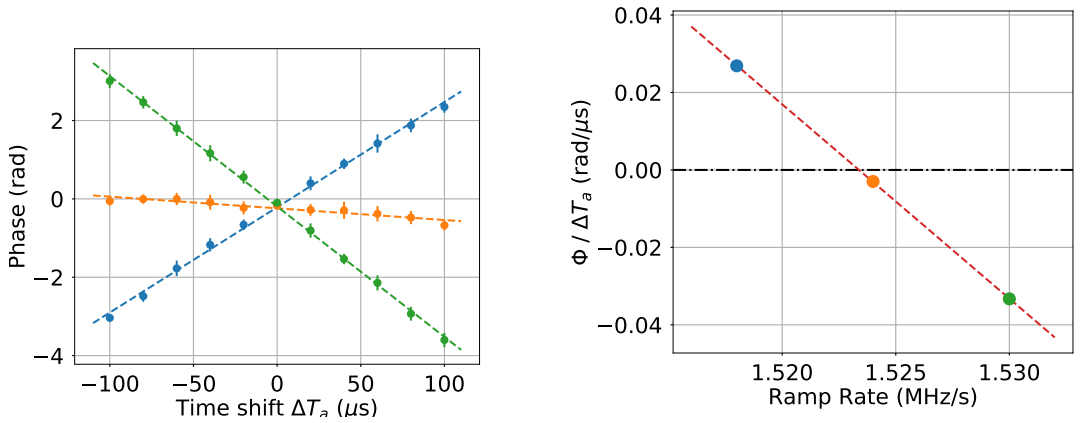

(a) (b)

Figure 6.9: *On the left: Phase shift for different values of the frequency ramp as a function of the asymmetric time shift ΔT_a. In yellow is depicted the reference frequency ramp $\alpha_0 = 1.5248$ MHz $\cdot$ s^{-1}. In blue (green) we show a frequency ramp 0.4% higher (lower) than α_0. It's important to notice that this are different sets of measurement with respect to Figure 6.4a. A key difference is the ability to measure the interferometer's phase at $\Delta T_a = 0$. On the right: Phase shift $\Phi/\Delta T_a$ as a function of the applied ramp rate. By minimizing the absolute value of $\Phi/\Delta T_a$ we can determine the optimal ramp rate to be $\alpha = 1.5234$ MHz $\cdot$ s^{-1} with an uncertainty smaller than 100 Hz.*

this leads to a change in the size of the area opened by the interferometer. We now want to characterize how this change, linked to Δk modifies the scale factor of the gyroscope, thus its sensitivity to rotation. We then rewrite the equation for the phase shift as :

$$\Phi_{\Omega_E} = k_b x(0) - 2k_t x(T/2 - \Delta T_s) + 2k_t x(3T/2 + \Delta T_s) - k_b x(2T) \tag{6.18}$$

We can write the mean position of the atoms as $x(t) = \frac{1}{3}\Omega_E g t^3$. Using the definition (6.14) we can write the positions as:

$$\begin{aligned} x(0) &= 0 \\ x\left(\frac{T}{2} - \Delta T_s\right) &= \frac{1}{3} g \Omega_E \left(\frac{T}{2}\right)^3 (1-\epsilon)^3 \\ x\left(\frac{3T}{2} + \Delta T_s\right) &= \frac{1}{3} g \Omega_E \left(\frac{3T}{2}\right)^3 \left(1 + \frac{1}{3}\epsilon\right)^3 \\ x(2T) &= \frac{1}{3} g \Omega_E (2T)^3 \end{aligned} \tag{6.19}$$

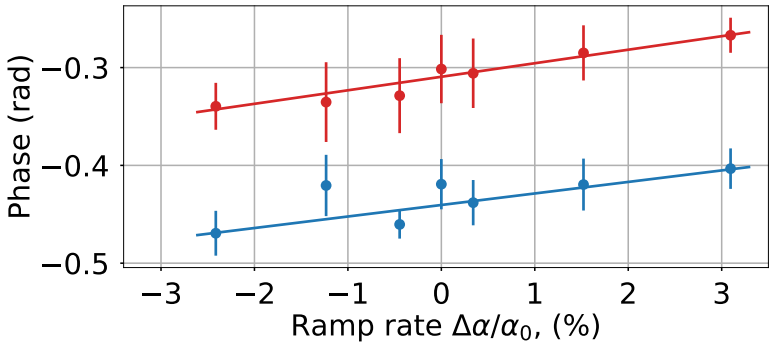

Figure 6.10: *Interferometer phase as a function of the ramp rate. In red (blue) are shown the results for an angle $\Delta\theta$ equals to 20 (30)* mrad.

where we introduce the definition $\epsilon = \frac{\Delta k}{k_{eff}}$.
Combining Eq. (6.18) with Eq. (6.19) we obtain at first order in ϵ:

$$\Phi_{\Omega_E} \simeq \frac{1}{2} k_{eff} g T^3 \Omega_E \left[-1 + \frac{2}{3}\epsilon \right] \tag{6.20}$$

At the time of writing, only preliminary measurements have been acquired. To better understand this effect we need to perform multiple measurements spanning a full turn of the sensor, to compare the results with the scale factor measurement obtained with an asymmetric configuration. Unfortunately, as we have shown in the previous chapter, at the moment we can only perform 1/3 of a full rotation of the sensor also we need to improve the precision at which we estimate the scale factor as this correction is in the order of $\sim 10^{-4}$.

6.4 Conclusion

In this chapter I showed how, due to imperfect light pulses, parasitic interferometers are generated, thus leading to an increase of probability noise in our measurements. The default solution to mitigate this problem has been until now the introduction of a small asymmetry in the light pulses' scheme. The drawback of this method though, is the reintroduction of sensitivity to DC acceleration noise, in the 4-pulse configuration.

I demonstrated how we are able to reduce the phase contribution of gravity acceleration, by adjusting the frequency sweep between the Raman laser pair, a method commonly used in cold atom gravimeter [9, 62, 63, 64].

I studied and characterized a new routine for estimating the optimal ramp rate which makes use of the full sensitivity of our sensor, without any modification to the apparatus. By alternating measurements with different asymmetric time shift I was able to estimate the optimal ramp rate within 100 Hz which corresponds to an estimation of gravity acceleration as $\sigma g/g = 10^{-4}$. This approach, while still producing good results, cannot compensate for phase shift linked to fluctuation of DC acceleration from shot to shot.

In the second part of the chapter, I presented a scheme which operates with different momentum exchanged between the $\pi/2$ and the π-pulses. This scheme, as for the asymmetric one, prevents the recombination of the parasitic interferometer in conjunction with the main interferometer, but on the contrary it maintains zero sensitivity to DC acceleration. By using this novel scheme, I showed how we are able to reject by a factor of 180 the DC acceleration without the need to interleave measurements with time asymmetry $\pm\Delta T_a$. In the future perspective of having a sensor operating with high number of interleaved measurements, the implementation of non equal exchanged momentum would also remove the complexity of designing of a sequence with alternating time asymmetry. The use of non equal momentum exchange can also be extended to horizontal gravity gradiometers in order to compensate the gravity gradient term in a gravitational wave detectors [56, 65, 66].

Chapter 7

Conclusion

This manuscript presented the implementation of new techniques to improve the accuracy and stability of the SYRTE cold atom gyroscope of 11 cm^2 Sagnac area. After an introduction to the main theoretical concepts of cold atom interferometry with stimulated Raman transition, I presented the core of the experimental apparatus and the modifications that I implemented. Previous PhD thesis detailed the implementation of continuous operation and interleaved operations in our cold atom sensor. I participated in setting up interleaved atom interferometry with real time compensation of vibration noise which allowed us to reach a sensitivity 3×10^{-8} $\mathrm{rad} \cdot \mathrm{s}^{-1} \cdot \mathrm{Hz}^{-1/2}$ together with a sampling rate of nearly 4 Hz. This sensitivity level currently represents the state of the art for cold atom gyroscopes. Moreover interleaving is a general technique for atom interferometry, as it allows to achieve high sampling rates without compromising the sensitivity of the sensor that scales with the interrogation time. This technique is in particular important when targeting time varying signals as in inertial navigation for example. To illustrate this, I used the interferometer to measure time varying rotation rate signals of the order of 10^{-7} $\mathrm{rad} \cdot \mathrm{s}^{-1}$ with periods of few seconds which was so far unexplored range for cold atom interferometer. This result is published in [33].

I also presented a first study of the scale factor and the systematic effects of the gyroscope. Since the orientation of the sensor compared to North was known with very low precision, I used different techniques to estimate the bearing to North of the sensor. Thus, I gradually improved our estimation of the gyroscope's scale factor. The best result were obtained by using a rotation stage, hence by measuring directly the phase shift associated with Earth's rotation. This gave us the first estimation of the scale factor, although the results significantly deviate from the expected value. At the time of writing multiple limitations have been identified and are being addressed by ongoing

measurements. These measurements, made available by the implementation of the rotation stage, should allow us to perform a test of the Sagnac effect for matter wave at the 10^{-4} level of relative accuracy, which would improve by 2 orders of magnitude compared to previous experiments involving matter waves.

To further improve the estimation of the bias of the gyroscope, I set up a new protocol in order to optimize the trajectory of the wave-packets. By using a piezo controlled mirror mount we are now able to characterize the coupling between the atomic trajectory and the relative misalignment of the Raman laser mirrors. A preliminary characterization of this effect was done during the last year of PhD of Denis Savoie (my first year of PhD) [32]. In this manuscript I have shown a more complete and in depth characterization of this systematic effect. Accurate control of the trajectory of the atoms and the relative alignment of the mirrors enabled us to demonstrate a stability of 3×10^{-8} rad $\cdot$ s^{-1} after 10 000 seconds of integration time, which represents the state of the art of atomic gyroscopes.

The last chapter describes the mitigation of the DC-acceleration bias of the gyroscope. I presented a novel technique which rejects more efficiently this contribution while preventing the recombination of parasitic interferometers. At the time of writing this manuscript a complete characterization of this method is undergoing, in particular focusing on the correction to the gyroscope scale factor.

Perspectives The performance of our cold atom gyroscope can be further improved by addressing different points that currently limit our sensitivity and stability. On the one hand the short term sensitivity of the sensor is limited by residual vibration noise. On the other hand the long term stability is affected by wave front aberration coupled to an imperfect trajectory of the atoms, which is linked to thermal expansion.

Different approaches can be used to mitigate the effects of vibration noise: first we can increase the number of interleaved sequences. By introducing three times interleaved, we saw a clear improvement in rejection of vibration phase contribution. Because the main noise source is between 0.1 Hz and 1 Hz increasing the number of interleaving should improve our ability to correlate measurement between each other, yielding a scaling of the sensitivity as $1/\tau$ for longer period of time than the current $\sim$7 s. At the moment the number of interleaved sequence is limited by the design of the sensor. As this limitation is purely geometrical, e.g. multiple atom cloud entering the detection region, a new physical design is required to solve this problem, which is currently un-

der study. Regarding the limitation imposed by the resonance condition for the Raman lasers pair, a solution could be the implementation of a double diffraction scheme [55], thus removing the need to compensate for Doppler effect.
A second approach would be to directly mitigate the vibration on the sensor by using an active isolation platform [67, 68, 69, 70]. This solution would allow us to reduce vibration noise in the frequency band where the gyroscope is more sensitive. Designing an active isolation platform requires first to study the frequency response of the structure holding the sensor. This will be presented in the PhD thesis of Romain Gautier.

Improving the short term sensitivity will allow us to characterize faster the systematic effects, in particular the effect linked to the misalignment of the Raman retro-reflection mirrors coupled to the trajectory of the atoms, which is currently limiting the long term stability. To this end we anticipate to perform an on the fly characterization of this effect. Efficiently performing this characterization requires to increase the span to which we misalign the mirrors beyond the $\sim$15 μrad range allowed by the finite temperature of the cloud. Therefore a colder atom ensemble is desirable. More generally a colder atom source would mitigate the effects of wavefront aberration coupled to atomic trajectories, which is a common problem in atom interferometry [63, 71, 72]. To achieve temperatures below the level of optical molasses and on the order of hundreds of nK, we plan to use degenerate Raman sideband cooling [73, 74, 75]. This is the ideal solution since it is compatible with our existing 3D-MOT design and, most importantly, it is compatible with interleaved atom interferometry at high sampling rate.

Appendix A

Method to estimate the visibility and amplitude noise of the interferometer

The goal of this appendix is to show how we estimate the probability noise and the amplitude of the fringes independently from the general phase of the interferometer. The method here discussed has been introduced in [76] and used in different studies [59, 77, 78].

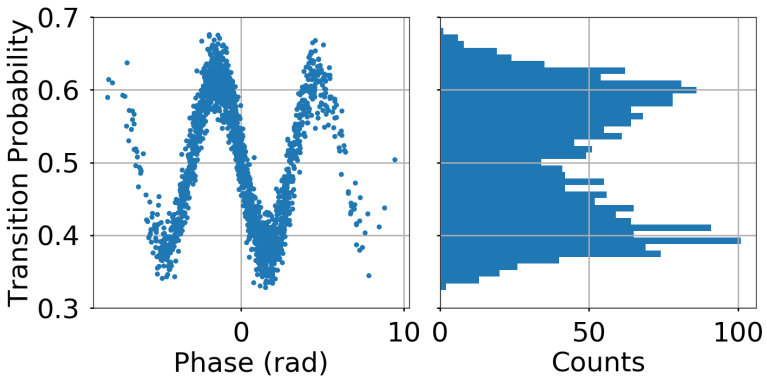

Figure A.1: *Simulated data illustrating of the method used to obtain a simulated probability distribution. We generate an interferometer fringe (left) with 12% Amplitude and* $\sigma_p = 2.5\%$*. On the right we see the histogram with step size* $\Delta x = 0.9\%$*, describing the probability distribution of the fringe.*

Principles

The output probability P depends on the interferometer's phase Φ as:

$$P(\Phi) = P_0 + A\cos(\Phi) + \tilde{P} \tag{A.1}$$

where with $\tilde{P}$ we indicate the normally distributed detection noise. The probability density function (PDF) associated to Eq. (A.1), seen in Figure A.1, can be described as the convolution of two separate distribution functions. The first is the PDF of the cosine term of Eq. (A.1) and, assuming the phase Φ to be uniformly distributed between $[0, \pi]$, can be written as:

$$f(x) = \begin{cases} \frac{1}{\pi\sqrt{1-\left(\frac{P_0-x}{A}\right)^2}} & \text{if } x \in]P_0 - A, P_0 + A[\\ 0 & \text{otherwise} \end{cases} \tag{A.2}$$

where $x = P_0 + A\cos(\Phi)$. The second distribution is simply the normal distribution of our probability noise:

$$f_P = \frac{1}{\sigma_p\sqrt{2\pi}} \exp\left(-\frac{x^2}{2\sigma_P^2}\right) \tag{A.3}$$

Since the histogram in our calculation returns a discrete distribution for our measurements we can rewrite Eq. (A.2) as follows:

$$\mathcal{F}(x) = \begin{cases} \frac{1}{\Delta x}\left[\arccos\left(\frac{P_0-x}{A}\right) - \arccos\left(\frac{P_0-(x+\Delta x)}{A}\right)\right] & \text{if } x \in [P_0 - A, P_0 + A] \\ 0 & \text{otherwise} \end{cases} \tag{A.4}$$

were we introduced Δx as the step-size of the bin used for the histogram. In the case where Δx becomes very small Eq. (A.4) tends to Eq. (A.2). This function is characterized by two distinct peaks at $x = P_0 \pm A$, as we can see on the left in Figure A.2, thus the name of *"twin-horn"* distribution.

We can now write the convolution product using Eq. (A.4) and Eq. (A.3):

$$\mathcal{B}(x) = \mathcal{N} \int_{-\infty}^{+\infty} \mathrm{d}x' \left[\arccos\left(\frac{P_0 - x}{A}\right) - \arccos\left(\frac{P_0 - (x+\Delta x)}{A}\right)\right] \times \frac{1}{\sigma_P} \exp\left(-\frac{(r-r')^2}{2\sigma_P^2}\right) \tag{A.5}$$

where $\mathcal{N}$ is a normalization factor. In Figure A.2 we see three different simulated probability distributions and the respective twin-horn function generated using the same parameters as the simulation. As we can see the function $\mathcal{B}(x)$ well describes the probability distribution presented in the figure.

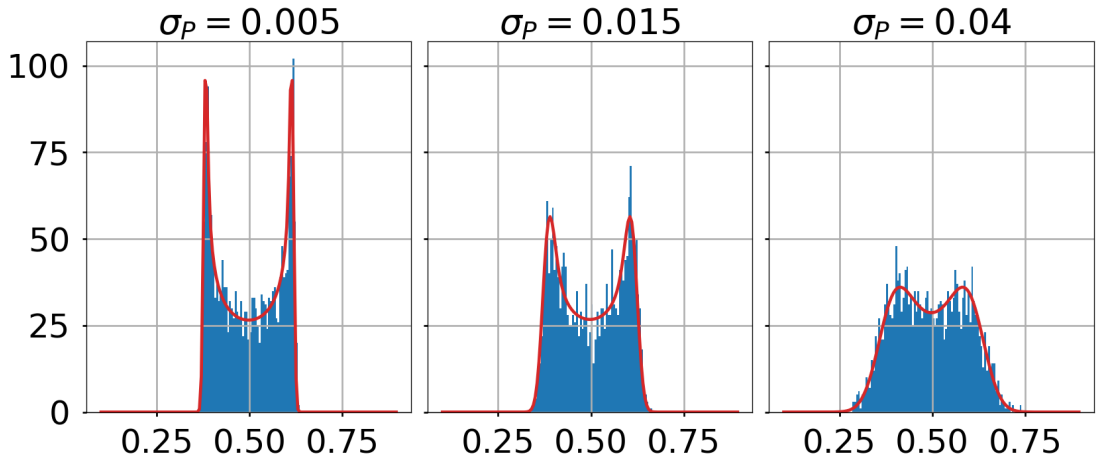

Figure A.2: *Simulated* twin-horned *distribution of 2000 points with amplitude* $A = 12\%$ *and step-size* $\Delta x = 0.5\%$. *As the probability noise* σ_p *increases, the two peaks fade and the characteristic twin-horned shape is gradually lost.*

Study of the uncertainties

In order to obtain statistically relevant uncertainties we rely on bootstrapping. This method relies on the generation of simulated data in order to statistically estimate the wanted parameters. Following this idea I chose to simulate multiple datasets with typical amplitudes A that we can find with the gyroscope data, and a wide range of possible values of probability noise σ_p. As the minimization function allows us to choose different values for Δx, we decided to study how the choice of the bin size affects the estimation of the parameters.

In Figure A.3 I present the results obtained for three different values of Δx. Furthermore I show the extracted values for the amplitude and the probability noise σ_p as a function of the theoretical signal to noise ratio SNR $= A/\sigma_p$. I simulated 4 different fringe amplitudes over a range of twelve values of σ_p. In order to reach a good statistical relevance I randomly generate 50 datasets composed of 500 shots for each combination of parameter $[A, \sigma_p]$.
As we can see choice of Δx plays an important role in the estimation of the parameters. With a high number of bins, hence a smaller step-size, the evaluation of the amplitude and more importantly of the SNR is more reliable across the whole range of theoretical SNR values. For larger values of step-size the minimization routine fails consistently in the estimation of the theoretical SNR. Using large step-size then, lead to an overestima-

tion of the probability noise since the amplitude is well estimated even with large Δx. Regarding the amplitude we can see that, in the case of lower SNR, the extracted values fluctuates leading to larger error bars. In conclusion this study allowed us to better have a statistical calibration for the typical error bar that we can associate to our extracted fringe's parameter. For values of SNR ≥ 10 we see that we can reliably associate absolute uncertainties between 0.1% and 0.4% for high values of SNR depending also on the value of the amplitude. For lower values of estimated SNR the absolute uncertainties increases ranging between 0.5% to 2%.

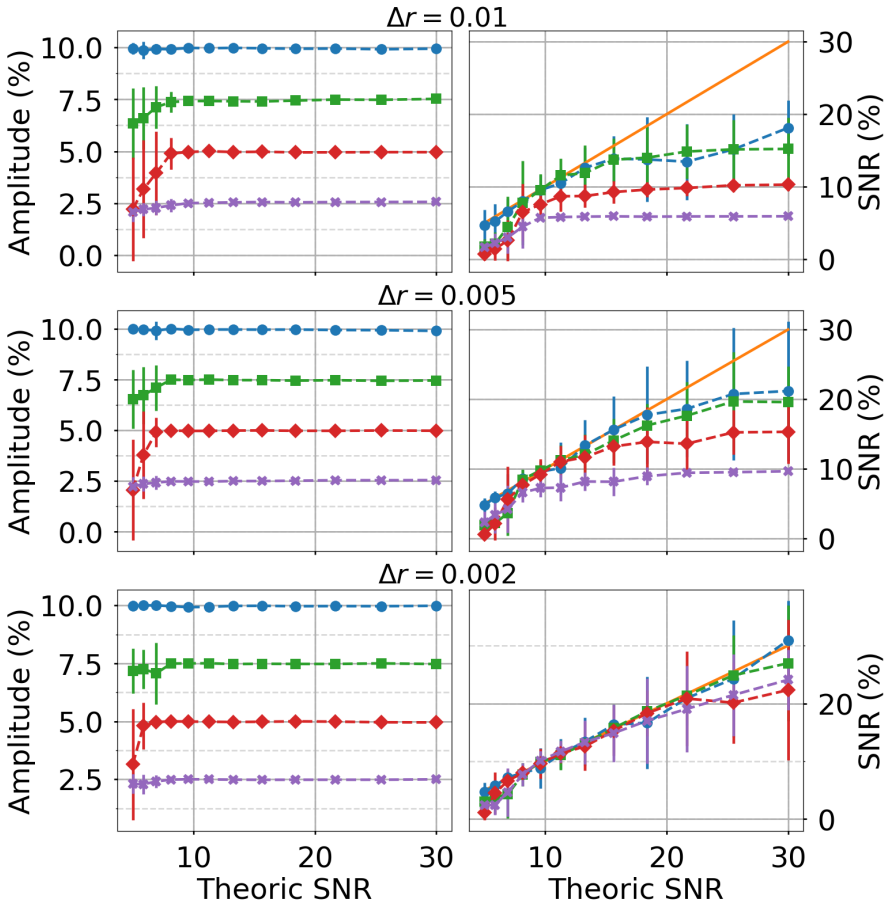

Figure A.3: *Uncertainties study regarding the estimation of the amplitude A and probability noise σ_p using a minimization routine. We repeated the study for different values of the step-size used to calculate the probability distribution. We simulated 50 datasets of 500 point for each mark in the graphs in order to extract a statistically relevant mean and standard deviation. The solid orange line in the graphs of the right column indicates the expected value of the measured SNR.*

Appendix B

Publications

Study of temporal pulse shaping
B.Fang, N.Mielec, D.Savoie, M.Altorio, A.Landragin and R.Geiger
"Improving the phase response of an atom interferometer by means of temporal pulse shaping"
New J. Phys. 20 023020

During my first year of PhD I worked on the study regarding temporal pulse shaping and its influence on the performance of an atom interferometer. In particular we showed how with smooth pulses we are able to reject high frequency fluctuation of the phase noise or frequency noise of the Raman laser pair used in the experiment. To do so, I implemented an arbitrary pulse shape generator together with Bess Fang. The first measurement I performed is showed in Figure 4 of the paper, where using co-propagating Raman transitions, I realized a Ramsey interferometer with Ramsey time $T = 20$ ms. To study the transfer function $H(\omega)$ I measured in quadrature the phase response of the interferometer to both high and low frequency sinusoidal phase modulation using different pulse shapes. I later studied the frequency selectivity of the different pulse shapes using Raman spectroscopy, shown in Figure 6 of the paper. The measured spectra are in agreement with the theoretical expectation, showing the spectroscopy shapes are the Fourier transform of the temporal pulse shape.

Implementation of a top-hat laser beam on the gyroscope
N.Mielec, M.Altorio, R.Sapam, D.Horville, D.Holleville, L.A.Sidorenkov,
A.Landragin and R.Geiger
“Atom interferometry with top-hat laser beams”,

Appl. Phys. Lett. 113, 161108 (2018), p. 161108

During the second year of my PhD I worked with Nicolas Mielec on the implementation and characterization of a top-hat laser beam. While the optical assembly and characterization was performed by Nicolas, I took care of the characterization on the atom interferometer. In particular I measured the local Raman intensity using the cold atom ensemble, shown in Figure 2 of the paper. Subsequently I compared the top-hat collimator with our Gaussian collimator by performing a 3-pulse interferometer, observing a clear improvement in the contrast of the interferometer, as show in Figure 3 of the paper. I then compared the Rabi oscillation using the two type of collimator, seen in Figure 4, showing a clear improvement in the oscillation after long time of flight using the top-hat laser beam.

Other publications:

D.Savoie, M.Altorio, B.Fang, L.A.Sidorenkov, R.Geiger, A.Landragin
"Interleaved atom interferometry for high-sensitivity inertial measurements"
Science Advances 4.12 (2018)

M.Altorio, L.A.Sidorenkov, R.Gautier, A.Landragin, R.Geiger,
"Accurate trajectory alignment in cold-atom interferometers with separated laser beams"
In preparation

New Journal of Physics
The open access journal at the forefront of physics

Deutsche Physikalische Gesellschaft DPG
IOP Institute of Physics

Published in partnership with: Deutsche Physikalische Gesellschaft and the Institute of Physics

OPEN ACCESS

RECEIVED
28 July 2017

REVISED
15 December 2017

ACCEPTED FOR PUBLICATION
21 December 2017

PUBLISHED
7 February 2018

PAPER

Improving the phase response of an atom interferometer by means of temporal pulse shaping

Bess Fang, Nicolas Mielec, Denis Savoie, Matteo Altorio, Arnaud Landragin and Remi Geiger[1]

LNE-SYRTE, Observatoire de Paris, PSL Research University, CNRS, Sorbonne Universités, UPMC Univ. Paris 06, 61 avenue de l'Observatoire, F-75014 Paris, France

[1] Author to whom any correspondence should be addressed.

E-mail: bess.fang@obspm.fr **and** remi.geiger@obspm.fr

Keywords: atom interferometry, metrology, pulse shaping

Abstract

We study theoretically and experimentally the influence of temporally shaping the light pulses in an atom interferometer, with a focus on the phase response of the interferometer. We show that smooth light pulse shapes allow rejecting high frequency phase fluctuations (above the Rabi frequency) and thus relax the requirements on the phase noise or frequency noise of the interrogation lasers driving the interferometer. The light pulse shape is also shown to modify the scale factor of the interferometer, which has to be taken into account in the evaluation of its accuracy budget. We discuss the trade-offs to operate when choosing a particular pulse shape, by taking into account phase noise rejection, velocity selectivity, and applicability to large momentum transfer atom interferometry.

1. Introduction

Precision measurements rely on a careful analysis of the relevant noise sources and systematic effects. In the field of inertial sensors, instruments based on light-pulse atom interferometry allow measurements of gravito-inertial effects such as linear accelerations [1–3], rotations [4–6], Earth gravity field [7, 8] and of its gradient [9] or curvature [10]. They have also been used for precise determinations of fundamental constants [11, 12] and tests of the weak equivalence principle (see, e.g. [13–21]), and have been proposed for gravitational wave detection in the sub-10 Hz frequency band [22, 23]. These sensors most often use two counter-propagating laser beams to realize the beam splitters and mirrors for the atomic waves associated to two different momentum states. The stability and accuracy of the sensors critically depends on the control of the intensity and of the relative phase of these two lasers, both spatially and temporally. For example, the spatial profile of the relative laser phase is the main source of systematic effects in most accurate atomic gravimeters [7, 8], and is an important concern in the design of future gravitational wave detectors based on atom interferometers (AIs) [24].

The temporal shape of the light-pulses (i.e. of the laser intensity) driving an AI determines the efficiency of the beam splitters and mirrors acting on the two momentum states of the AI. More precisely, for velocity selective transitions, the transfer efficiency of the pulse is given by the convolution between the velocity distribution of the atoms and the Fourier transform of the pulse shape [25]. Efficient transitions (i.e. high contrasts) can thus be achieved by temporally shaping the pulse intensity and phase, as shown in [26, 27]. Moreover, when driving an interferometer with large momentum transfer (LMT) atom optics, it has been shown that pulses of Gaussian temporal shape significantly improve the transfer efficiency with respect to rectangular pulse shapes [28, 29]. Adiabatic rapid passage (see, e.g. [30]) was also considered in LMT interferometry, but was shown to require stringent control of the laser phase noise compared to pulse shaping [31].

In addition to the influence on the contrast of the interferometer, the temporal shape of the pulse is expected to affect the (frequency-dependent) response of the interferometer to phase fluctuations, which is an important source of instability in AIs. Furthermore, as the phase response of the AI is modified, pulse shaping should introduce a correction to the scale factor of the interferometer, which has to be accounted for in the accuracy budget of atomic sensors.

In this article, we study the phase response of an AI driven by arbitrary temporal light pulse shapes. Our main interest is to highlight the strong difference in the phase response of an AI driven by rectangular and smooth pulse shapes. We concentrate on a few pulse shapes that are representative for the optimization of the following criteria: rejection of high-frequency laser phase (or frequency) noise, velocity selectivity of the pulse, and applicability to LMT interferometry. Experimentally, we focus on the comparison of the phase sensitivity function (section 2) and of the rejection of laser phase noise (section 3) between the two mostly employed rectangular and Gaussian pulses, in order to validate our calculations. In addition to the rectangular and Gaussian pulses, we discuss two other representative pulse shapes: (i) the GSinc pulse, which is the product of a Gaussian and a cardinal sine, and (ii) the Gaussian-Flat pulse (labeled GFlat thereafter) which is a flat pulse with Gaussian edges. For completeness of the presentation, we study in section 4 the influence of pulse shaping on the frequency selectivity, in line with previous works [26, 27]. Finally, we present in section 5 a correction to the interferometer scale factor associated with pulse shaping, and discuss its relevance for different precision measurements involving AI based sensors. We conclude our paper with a discussion of the trade-offs to operate when selecting a given pulse shape for a particular application (section 6).

2. Sensitivity function with arbitrary pulse shape

2.1. Theory

The sensitivity function was first introduced to study the degradation of an atomic clock due to the phase noise of the local oscillator [32], but the idea is more general. It describes the response of an atom interferometer phase to infinitesimal changes of external parameters. We investigate here the response of the AI phase $\delta\Phi$ to an instantaneous variation $\delta\phi(t)$ of the relative phase between the two lasers driving the AI, occurring at a given time t. As in previous works [33], we define the sensitivity function as

$$g(t) = \lim_{\delta\phi\to 0} \frac{\delta\Phi(\delta\phi, t)}{\delta\phi(t)}. \tag{1}$$

It can be calculated for an interferometer composed of perfect beam splitters and mirrors using

$$g(t) = \sin\left(\int_{t_0}^{t} \Omega(t')\mathrm{d}t'\right), \tag{2}$$

where $\Omega(t)$ is the Rabi frequency seen by the atoms during the interferometric sequence [34], with $\Omega(t) = 0$ for $t < t_0$. The overall shape of $g(t)$ depends on the AI configuration, i.e. on the number of light-pulses. In this work, our main interest lies in the effect of temporal pulse shape. Therefore, we consider without loss of generality, a two-light pulse interferometer, i.e. a Ramsey configuration. For a Ramsey sequence with two rectangular $\pi/2$ pulses characterized by a Rabi frequency Ω_R and duration τ separated by Ramsey time T, the sensitivity function reads

$$g(t) = \begin{cases} \sin\left(\Omega_R \times \left(t + \frac{\tau}{2}\right)\right) & \text{for } -\frac{\tau}{2} < t < \frac{\tau}{2} \\ 1 & \frac{\tau}{2} < t < T - \frac{\tau}{2} \\ \sin\left(\Omega_R \times \left(t - T + \frac{3\tau}{2}\right)\right) & T - \frac{\tau}{2} < t < T + \frac{\tau}{2} \end{cases}, \tag{3}$$

where the origin of the time axis is (arbitrarily) aligned with the center of the first light pulse.

We show $g(t)$ as a dashed line in figure 1(a). In the limit of infinitely short laser pulses, $g(t)$ is box-like, as the interferometer copies the phase jitter of the interrogation laser ($g(t) = 1$) between the two laser pulses.

We show in figure 1(b) a zoom of of the rising slope (i.e. during the first $\pi/2$ pulse) of $g(t)$ for a sequence based on rectangular pulses (blue dashed line) and Gaussian pulses (red dashed–dotted line). We have chosen to use the same peak intensity in our calculation (and our experiments later), and adjust the pulse duration to obtain the desired Rabi angle. This is motivated by the fact that the peak laser intensity depends on the total power available, which is often the limiting experimental factor. The main difference in the sensitivity function takes place around $t = -\tau/2$, where τ denotes the duration of the rectangular $\pi/2$ pulse. The sudden intensity variation of a rectangular pulse gives rise to a fast rise in the sensitivity function, and a discontinuity in its derivative. This fast rise is in contrast with the gradual change induced by a smooth intensity variation of a Gaussian pulse. Such a difference results in different spectral behaviors of $g(t)$ for the two pulse shapes, as we will discuss in section 3.

2.2. Measurement of the sensitivity function for rectangular and Gaussian pulses

We measure $g(t)$ using the experimental setup described in [6, 35]. Briefly speaking, we use an atomic fountain to prepare cold cesium-133 atoms. At each experimental cycle, about 10^6 atoms are prepared into the

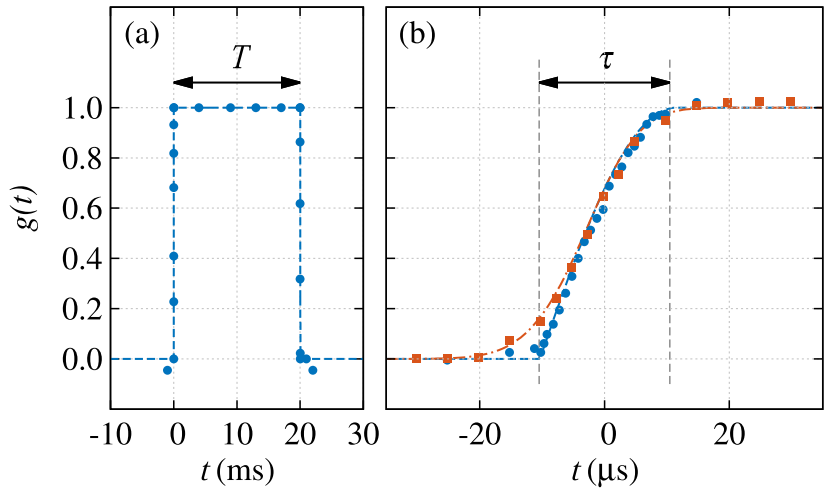

Figure 1. Sensitivity function $g(t)$ of a Ramsey sequence. (a) Complete $g(t)$ for two rectangular $\pi/2$ pulses separated by Ramsey time T. (b) Zoom on the rising slope for rectangular (blue) and Gaussian (red) pulses. We compare calculations (lines) according to equation (3) and our measurements (points). Errorbars on the measurements are smaller than the plot symbol.

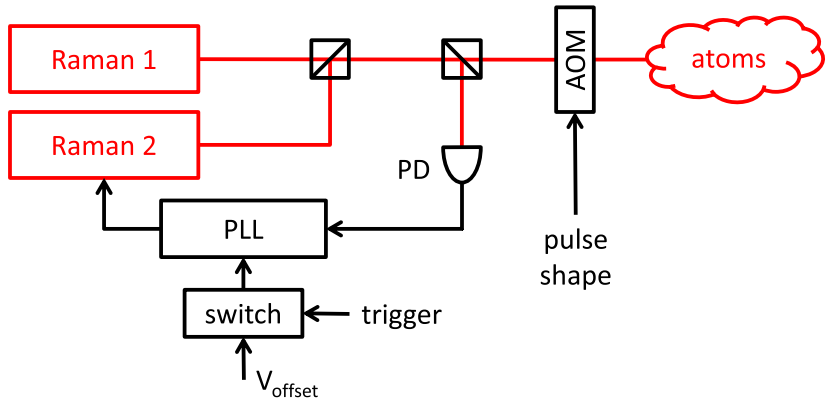

Figure 2. Schematic of the phase jump control. The beat note of two lasers (Raman 1 and 2) is detected on a fast photodiode (PD) and phase locked onto a reference signal at the Cs ground-state hyperfine splitting frequency of about 9.192 GHz. Phase jumps are implemented by sending a DC voltage V_{offset} to the feedback port of the PLL through a voltage controlled switch. By appropriately attenuating the radio-frequency signal driving the AOM, arbitrary temporal profiles of laser pulses can be sent onto the atoms.

magnetically insensitive $|F = 4, \quad m_F = 0\rangle$ ground state and launched into the interferometric zone. The Ramsey pulses are realized via stimulated Raman transitions, using a doubly seeded tapered amplifier [36]. The seeding external cavity diode lasers have a fixed phase relation by means of an optical phase locked loop (PLL) close to the Cs clock transition frequency. Both lasers are about 500 MHz red-detuned from the excited state of the D_2 line to reduce spontaneous emissions during the Raman transition. At the end of the interferometer sequence, the population in each of the hyperfine ground states N_3 and N_4 is detected by fluorescence, and the transition probability is obtained by $P_4 = N_4/(N_3 + N_4)$.

The laser phase jump is implemented by applying a DC voltage V_{offset} to the feedback port in the PLL through a voltage controlled switch, which is triggered at different times. See figure 2 for the control schematics. The voltage offset corresponds to a phase jump of about 340 mrad. The switch has a delay of 0.3 μs, whereas the PLL has a locking bandwidth of 1.6 MHz. Thus, the total delay in the phase jump implementation is under 1 μs, much shorter than the duration of the rectangular $\pi/2$ pulse $\tau = 21$ μs (peak Rabi frequency $\Omega_R/2\pi = 12$ kHz).

We shape the Raman light pulses by attenuating the radio-frequency signal driving the acousto-optic modulator (AOM), which controls the intensity of the Raman pulses shone on the atoms. A commercial direct digital synthesizer (Rigol 4620) is used to generate a waveform that takes into account the desired waveform (e.g. a Gaussian pulse) as well as the response of the chain of a voltage-controlled attenuator followed by an RF amplifier. This response is calibrated against a monitor photodiode in order to ensure that the intensity of the Raman pulses follows the desired waveform.

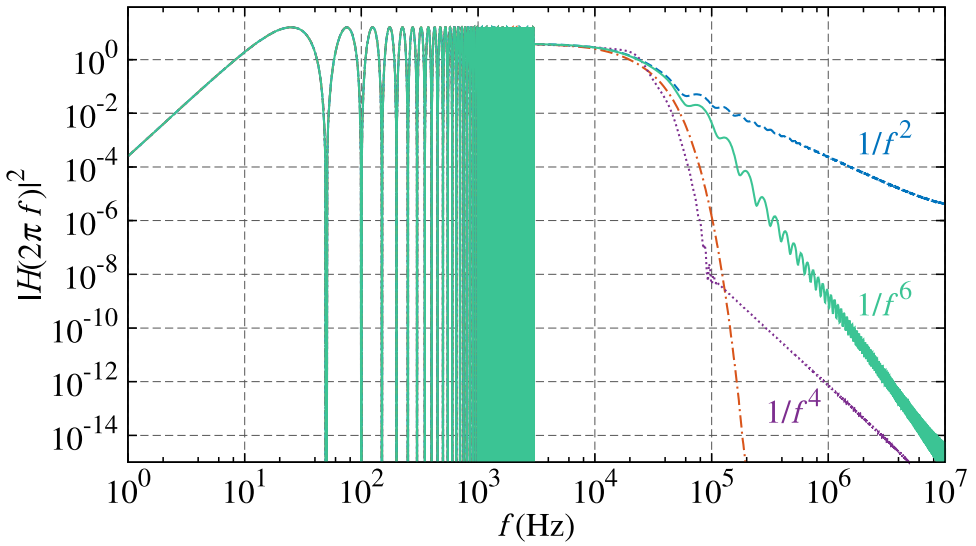

Figure 3. Transfer function $|H(2\pi f)|^2$ for a 3 pulse AI with $T = 20$ ms driven by different pulse shapes: rectangular (blue dashed line), Gaussian (red dashed–dotted line), GSinc (purple dotted line), and GFlat (green solid line). The peak Rabi frequency is the same for all pulse shapes.

With a Ramsey time of $T = 20$ ms, the phase noise of the clock sequence is about 30 mrad Hz $^{-1/2}$, which enables a mid-fringe operation of the interferometer. We further stabilize the phase offset of the interferometer by applying a mid-fringe lock [37], which converts the measurement of the atomic transition probability directly to the interferometric phase. This technique is immune to variations in the probability offset and reduces the sensitivity to the noise in the fringe amplitude, thereby allowing a robust measurement of the interferometric phase.

To compare the experimental data with the calculations, we offset the measured phase shift to 0 and normalize by 340 mrad to obtain the experimental $g(t)$. We display our measurements in figure 1(a) for the complete $g(t)$ with rectangular pulses [33]. Figure 1(b) shows the rising slope for rectangular (circles) and Gaussian (rectangulars) pulses. The relative phase uncertainty of each measurement is below 4 mrad, i.e. smaller than the plot symbol. The time axis for the experimental data is shifted by 0.22 μs to account for the delay through the switch and the PLL. Our measurements confirm the temporal form of $g(t)$ given by equation (3), and well resolve the differences between the two pulse shapes implemented.

3. Frequency response of the AI to pulse shaping

3.1. Calculations

The impact of the sensitivity function on the interferometer phase noise can be more easily understood in Fourier space. According to [33, 35], the variance of the interferometric phase noise can be expressed as

$$\sigma_\Phi^2 = \int_0^\infty \frac{\mathrm{d}\omega}{2\pi} \, |H(\omega)|^2 S_\phi(\omega), \tag{4}$$

where the transfer function $H(\omega) = \omega|G(\omega)|$, $G(\omega)$ is the Fourier transform of the sensitivity function $g(t)$, and $S_\phi(\omega)$ is the power spectral density of the Raman laser phase noise.

We plot in figure 3 the transfer function $|H(2\pi f)|^2$ as a function of frequency f for a 3 light pulse sequence ($\pi/2$–π–$\pi/2$) for various pulse shapes: rectangular (blue dashed line), Gaussian (red dashed–dotted line), GSinc (purple dotted line), and GFlat (green). The peak Rabi frequency is the same for all pulse shapes. The calculation is analytic for rectangular pulse and numerical for the other pulse shapes. The Gaussian pulse is truncated at 6 standard deviations on both sides. The definition of the GSinc and GFlat pulse shapes is given in appendix A.

Independent of the pulse shapes used, the transfer function $|H(2\pi f)|^2$ is oscillatory with arches spanning $1/T$, i.e. 50 Hz for our choice of $T = 20$ ms. This is illustrated at low frequency up to 3 kHz, beyond which we plot the mean value over 3 kHz in order to illustrate the general frequency dependence of the envelope.

The difference between the four pulse shapes lies mainly in the low-pass cut-off occurring near the peak Rabi frequency (here 12 kHz). For a rectangular pulse, the high-frequency noise is filtered out with a $1/f^2$ scaling of H^2, whereas the use of smoother pulses warrants a significantly faster decay, and therefore a better suppression of high-frequency noise. In particular, Gaussian pulses give rise to the strongest high-frequency cut-off in H^2. The

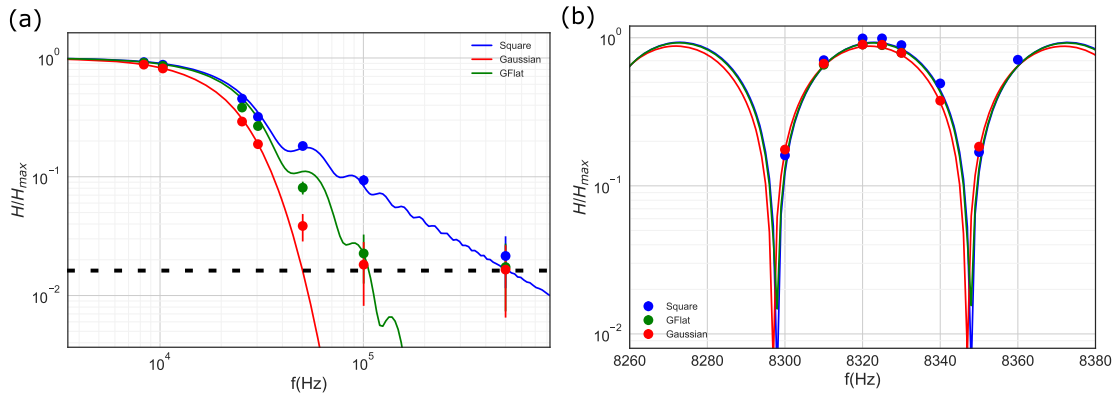

Figure 4. Transfer functions for a Ramsey sequence $\pi/2$–$\pi/2$ with a Rabi frequency of 8.3 kHz, and a Ramsay time of 20 ms. Three pulse shapes are considered: rectangular (total duration of 30 μs), Gaussian, and GFlat. (a) Asymptotic behavior of $H(\omega)$, where the experimental and theoretic data are the maxima of the arches. (b) A zoom around the Rabi frequency. The errorbars correspond to statistical errors at the 68% confidence interval. The dashed horizontal line in (a) corresponds to the noise floor of our measurements.

GSinc pulse gives a similar behavior as the Gaussian pulse around the peak Rabi frequency, before following a $1/f^4$ scaling at high frequency. The frequency at which the slope changes is determined by the width of the Gaussian relative to the length of the sine cardinal (the smaller the width of the Gaussian, the further the change of slope). The GFlat pulse gives rise to $1/f^6$ scaling in H^2 beyond the peak Rabi frequency.

To understand the asymptotic behavior of the transfer function qualitatively, we performed calculations with various pulse shapes, including temporally asymmetric pulses, and using different shapes for the $\pi/2$ and π pulses. We found that the high frequency behavior is first determined by the steepness of $g(t)$ at the beginning of the first $\pi/2$ and the end of the last $\pi/2$ pulses. Even faster decay of the transfer function is then related to the steepness of $g(t)$ at the end of the first $\pi/2$ pulse, the beginning of the last $\pi/2$ pulse, and the π pulse. Further details on this qualitative interpretation in line with equation (2) can be found in appendix B.

3.2. Measurements of the transfer function

We measure the transfer function $H(\omega)$ for different pulse shapes by realizing a Ramsey sequence ($\pi/2$–$\pi/2$) using co-propagating Raman transitions, with a Ramsey time of $T = 20$ ms, and a Rabi frequency of 8.3 kHz. To measure the transfer function, we follow the approach of [33]: we apply a sinusoidal phase modulation of angular frequency ω starting at the first Raman pulse and lasting during the whole interferometer, and measure its effect on the phase of the atom interferometer. We perform two measurements corresponding to two quadratures of the phase modulation, which are added quadratically in order to extract the value of $H(\omega)$. The maximum of $H(\omega)$ corresponds to a phase shift of 1.05 rad. The relative uncertainty of the phase measurements are at the level of 1%. To show the asymptotic behavior of $H(\omega)$, we measure the position of the maxima of the transfer function over several decades. The measurements are shown in figure 4(a) , together with the calculation presented in the previous subsection, without free parameters. The experimental data and the calculation agree well within the uncertainties of the experimental parameters ($\sim$10% on the Rabi frequency and $\sim$10% on the position of the maxima at frequencies above 10 kHz). In particular, the measurements resolve the difference in asymptotic behavior of the three pulse shapes. We also observe that the positions of the zeros of the transfer function are indistinguishable for all pulse shapes at frequencies lower than the Rabi frequency, as illustrated around 8.3 kHz in panel (b).

3.3. Experimental demonstration of noise rejection

To demonstrate experimentally the robustness of smooth pulses against high-frequency laser phase noise (compared to rectangular pulses), we realize Ramsey sequences ($\pi/2$–$\pi/2$) with additional relative phase noise in the Raman lasers. The difference between the Ramsey sequence and the 3-pulse sequence ($\pi/2$–π–$\pi/2$) only lies in the low frequency behavior of the transfer function (at $f \sim 1/T$), while the high frequency behavior (for f on the order of and higher than the Rabi frequency) is the same for both sequences. We concentrate on the comparison between Gaussian and rectangular pulse shapes. Adding phase noise is achieved by sending a noisy signal (instead of a switchable DC voltage as illustrated in figure 2) into the feedback port of the PLL. We generate a white noise using a commercial synthesizer, filtered into the 40–300 kHz band pass and amplified using a commercial low-noise amplifier. By varying the amplifer gain, we control the additional phase noise of the Raman lasers, giving rise to the power spectral density shown in figure 5(a). For each noise level, we measure the short-term phase stability of a Ramsey sequence ($T = 20$ ms) with rectangular (circles) and Gaussian

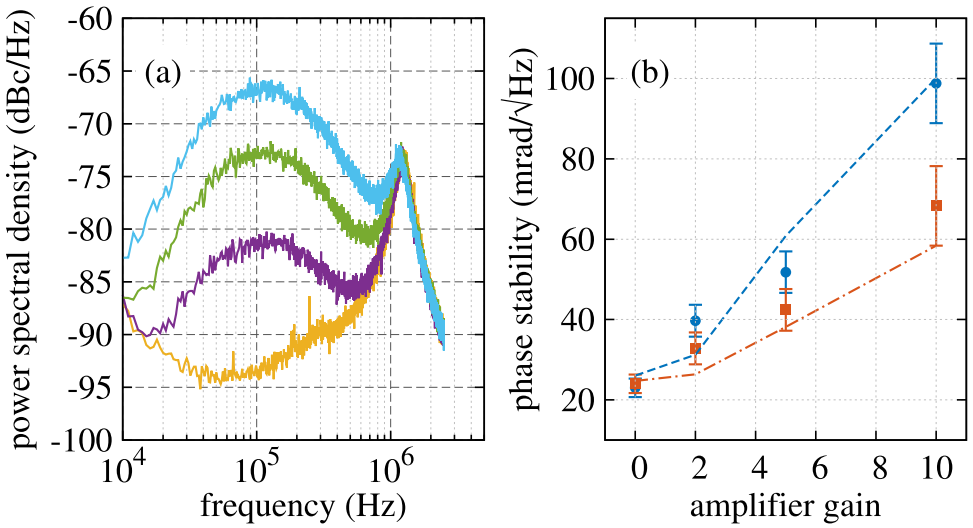

Figure 5. (a) Power spectral density of the laser phase noise recorded with a spectral analyzer with a resolution bandwidth of 1 kHz. The yellow line shows the spectrum without additional noise (gain = 0 in the low-noise amplifier), whereas the purple, green and cyan lines correspond to increasing noise levels (amplifier gain = 2, 5, and 10). (b) Short-term phase stability of a Ramsey interferometer. We overlay our measurements (points) with calculations (lines) for rectangular (blue) and Gaussian (red) pulses. The errorbars correspond to statistical errors at the 68% confidence interval.

(rectangulars) pulses, as shown in figure 5(b). In comparison, Gaussian pulses consistently rejects a significant fraction of the additional noise.

We calculate numerically the induced phase noise according to equation (4), by numerically integrating over the 10 kHz–2.5 MHz range. The contribution of frequencies out of this band is negligible. The total noise is $\sigma = \sqrt{\sigma_{\rm det}^2 + \sigma_\Phi^2}$, where $\sigma_{\rm det} = 22$ mrad Hz$^{-1/2}$ is our measured detection noise. To account for the uncertainty in the absolute phase noise level applied to the interferometer, we multiply the phase noise PSD of figure 5(a) by a global factor. This factor is obtain by matching the calculation and measurement for upper right point in figure 5(a), which is almost exclusively influenced by phase noise (and not detection noise). Apart from this global factor common to both pulse shapes, there are no free parameters. The calculation follows well the experimental data, and shows how the Gaussian pulse rejects the high frequency phase noise, above the Rabi frequency.

3.4. Discussion and applications to inertial sensors and optical clocks

The strong rejection of the relative laser phase noise by a smooth pulse (Gaussian, GSinc, GFlat) at frequencies higher than the Rabi frequency will help designing optical PLLs for AI experiments, as it relaxes the requirements on the PLL bandwidth. Regarding the limitation to the sensitivity of cold atom gravimeters due to Raman laser phase noise, we calculate the noise rejection in state of the art instruments. For the work presented in [38], we compute a phase noise of 7.5 mrad per shot (assuming a π rectangular pulse with a duration of 15 μs), in agreement with the measured short term stability. Using a GFlat pulse yields a noise of 6.1 mrad, and a Gaussian pulse reduces this contribution to 5.9 mrad per shot. For the work presented in [39], the rectangular pulse corresponds to a phase noise of 1.1 mrad per shot, which will be reduced to 0.5 mrad per shot when using GFlat or Gaussian pulses.

In AIs driven by Bragg diffraction, the relative phase noise between the two Bragg lasers is not a concern, since the two momentum states used in the two interferometer arms correspond to the same internal energy state. However, because of propagation delay from the atoms to the mirror which retro-reflects the Bragg lasers, the laser frequency noise converts into phase noise on the AI [40]. Such noise is a major concern in long baseline AI gradiometers, e.g. in gravitational wave detectors based on AIs [23, 41]. Smooth pulses can therefore relax the requirements on the laser frequency noise at high frequencies (above the Rabi frequency, i.e. above typically 10–100 kHz).

We also investigate the potential interest of temporally shaping pulses to improve the stability of optical clocks. The stability of optical clocks critically depends on the frequency stability of the interrogation laser [42], the design of which requires careful attention [43]. In that context, we found that pulse shaping in clocks is less interesting than in AIs. The reason is that the relevant transfer function for the measurement of frequency (instead of phase) is $|G(\omega)|^2 = |H(\omega)|^2/\omega^2$, which scales as ω^{-4} (for a rectangular pulse) after the cut-off given by the pulse Rabi frequency Ω_0. For white frequency noise, the contribution of high frequencies ($\omega > \Omega_0$) is

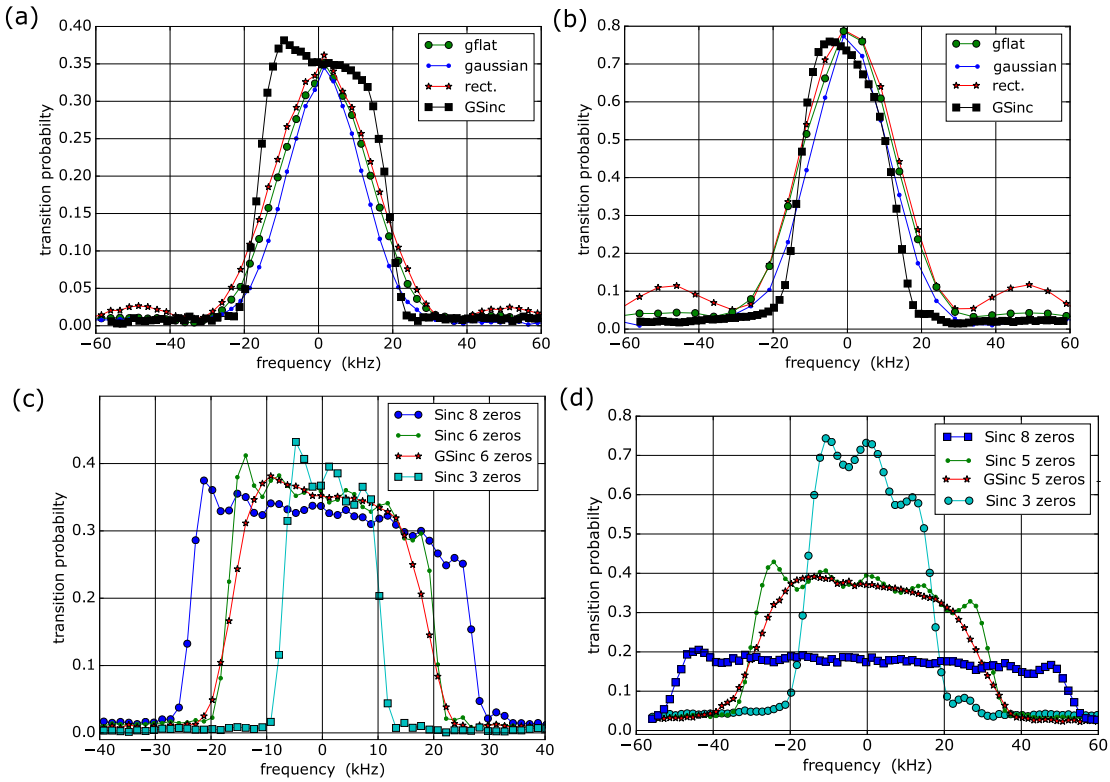

Figure 6. Spectroscopy of different pulse shapes. (a) $\pi/2$ pulse. (b) π pulse. In both cases, the duration of the rectangular pulse is 30 μs. The peak power is the same for all pulse shapes in (a), and the same for all pulse shapes in (b). In (c), the total duration of each pulse is 300 μs and the peak power is varied to perform a $\pi/2$ pulse. In (d), the peak power is kept constant and the pulse duration is kept constant to 150 μs. The maximum measured probabilities for the $\pi/2$ and π pulse are different from the ideal values of, respectively, 0.5 and 1 because of experimental imperfections (inhomogeneous Rabi frequency and imperfect normalization of the transition probability).

thus 1/3 of that of low frequencies ($\omega < \Omega_0$), in power of the noise. Therefore, faster decay (than ω^{-4}) of the transfer function does not significantly impact the stability. Pulse shaping can however be used to relax the constraints on potential spurious high frequency noise components in the clock laser, e.g. in field applications or compact clock design [44].

4. Frequency selectivity of the pulse

We investigate in this section the frequency selectivity of the pulse shapes studied in this article, in line with previous works [26, 27]. We measure the influence of the pulse shape on the frequency selectivity of the pulse, by varying the Raman laser frequency difference and measuring the transition probability. The results are presented in figures 6(a) and (b) for a $\pi/2$ pulse and a π pulse correspondingly, for the four pulse shapes investigated in the previous section: rectangular, Gaussian, GFlat, and GSinc.

The GSinc pulse is technically more difficult to implement than the other pulse shapes as it requires the introduction of phase jumps of π at the points in time corresponding to the zeros of the power envelope in order to reverse the sign of the effective Rabi frequency (see figure A2 in the appendix for the time trace of the Sinc pulse). The π phase jumps are applied on the relative phase between the two Raman lasers through the phase lock loop, in a similar way as for the measurement of the sensitivity function presented in section 2.2. For the data presented in panels (a) and (b), the GSinc is the product of a Gaussian and of a Sinc function with 5 zeros on each side of the maximum (see appendix A). The total duration of the pulse is 300 μs, and the peak power is the same as for all pulse shapes. The standard deviation of the Gaussian multiplying the Sinc function is 1/6 of the total duration (i.e. 50 μs).

The experimental data are in agreement with the theoretical expectation, shown in figure 7, that the spectroscopy is the Fourier transform of the pulse shape. In particular, the side lobes associated to the rectangular pulse are absent in the GFlat, Gaussian, and GSinc pulses. The measurements also resolve the larger width of the GFlat pulse compared to the Gaussian pulse. Finally, the GSinc pulse clearly shows sharper edges than the other pulse shapes. The asymmetry in the GSinc spectroscopy is not fully understood: we think that it is

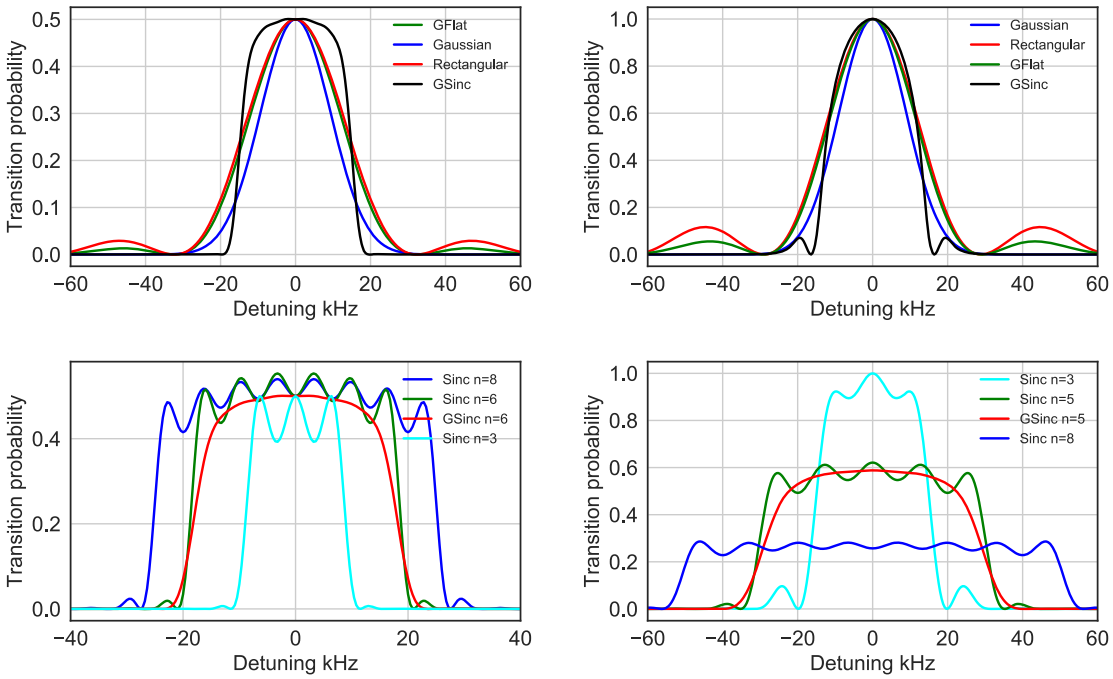

Figure 7. Calculations of the line shapes. The panels correspond to the measurement shown in figure 6. The parameters are fixed to the values measured in the experiment (pulse duration, peak Rabi frequency). Note that the maximal probability of transition in this ideal calculation is 0.5 for the $\pi/2$ pulses and 1 for the π pulses.

due to a nonlinearity in the acousto-optic modulator which is driven for a longer duration for the GSinc pulse (300 μs) compared to the other pulse shapes (the spectroscopy were less asymetric when using shorter pulses).

We investigate experimentally in further details the influence of the number of zeros in the Sinc pulse on the sharpness of the spectroscopy. The results are shown in figures 6(c) and (d). Panel (c) shows the measurements for a $\pi/2$ pulse where the total duration of all pulses is kept constant to 300 μs, and the peak power is varied. Panel (d) shows measurements were the peak power is kept constant and the pulse duration is kept constant to 150 μs.

In conclusion, the Sinc and GSinc pulses exhibit an almost flat response to detuning, and a sharper decay than the other pulse shapes. They therefore optimizes the velocity acceptance of the pulse, at the expense of more complexity in the implementation.

5. Scale factor of the interferometer

The finite duration of the light pulses influences the scale factor of atom interferometers, i.e. their response to inertial effects. The interferometer phase Φ is related to the relative laser phase $\phi(t)$ through the sensitivity function as $\Phi = \int g(t)\frac{\mathrm{d}\phi}{\mathrm{d}t}\mathrm{d}t$. Without loss of generality, we look at the example of a Mach–Zehnder-like interferometer sequence, where there are three light pulses ($\pi/2$–π–$\pi/2$ pulses) separated by T between each consecutive pulse pairs. See figure 8 for an illustration. The finite duration τ of the $\pi/2$ (rectangular) pulses modifies the scale factor of an atom accelerometer from $\Phi = k_{\mathrm{eff}}\,T^2 a$ to $\Phi = \mathcal{S}_{\mathrm{rec}} a$, with $\mathcal{S}_{\mathrm{rec}} = k_{\mathrm{eff}}(T + \tau/2)\left(T + \left(\frac{4}{\pi} - \frac{3}{2}\right)\tau\right)$ [45][2]. For experiments where the inertial effect is inferred from a phase measurement, such a change of scale factor has to be taken into account when evaluating the accuracy budget.

Furthermore, by modifying the temporal pulse shape, the scale factor $\mathcal{S}$ differs from that of rectangular pulses $\mathcal{S}_{\mathrm{rec}}$. Since τ/T is typically on the order of 10^{-4} or smaller, the relative correction $\frac{\mathcal{S}-\mathcal{S}_{\mathrm{rec}}}{\mathcal{S}_{\mathrm{rec}}}$ scales linearly with τ/T, and can be evaluated numerically with the appropriate form of $g(t)$. For example, for $T = 100$ ms and a peak Rabi frequency of 12.5 kHz ($\tau = 10$ μs rectangular pulse), this correction amounts to 9.4×10^{-6} for a sequence of Gaussian pulses, 6.8×10^{-6} for GSinc pulses and 4.2×10^{-7} for GFlat pulses.

[2] The correction in the main text corresponds to equation (2.45) on page 38 with T defined as the time elapsed between the center of adjacent pulses.

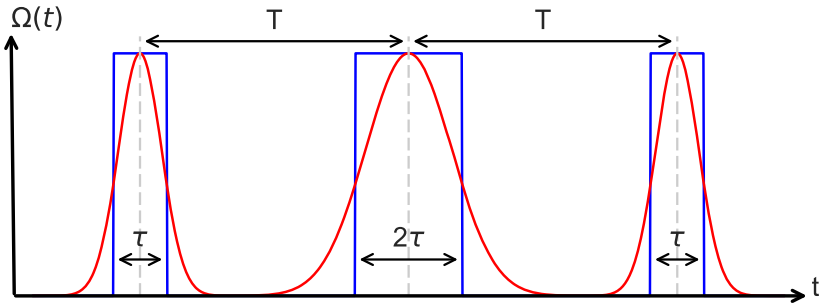

Figure 8. Illustration of the three-pulse interferometer sequence for rectangular and Gaussian pulse shapes. The pulse separation T denotes the time elapsed between the center of two consecutive light pulses, and τ is the duration of the $\pi/2$ rectangular pulse.

Table 1. Summary of the properties of the pulse shapes studied in this article. The bandwidth is defined as the two-photon detuning (in units of the peak Rabi frequency) where the transition probability falls to 50% and 95% of its maximum value. The phase noise rejection (weak/strong) is defined according to the decay of the transfer function above the Rabi frequency, as shown in figure 3.

Pulse	Bandwidth (50% | 95%)	LMT	Noise rejection	Ease of implementation
Rectangular	1.73 | 0.49	Not suitable	Weak, $1/f^2$	Easiest
Gaussian	1.31 | 0.36	Suitable	Strong	Medium
GSinc	1.73 | 1.01	Suitable	Strong	Difficult
GFlat	1.65 | 0.47	Suitable	$1/f^6$	Medium

6. Discussion

We summarize the properties of the four pulse shapes studied in this article in table 1. We report (i) the velocity selectivity of a $\pi/2$ pulse (defined as the bandwidth in units of the peak Rabi frequency, see appendix A), (ii) the suitability for LMT interferometry, (iii) the rejection of phase noise at high frequencies (according to section 3), and (iv) the ease of implementation. The main focus of this article was on the phase noise rejection. Details on the velocity selectivity are given in appendix A.

Regarding LMT applications [28, 29], we extended the numerical calculations performed in [46] to implement arbitrary pulse shapes, and computed the Rabi oscillations for 10 $\hbar k$ LMT atom optics. We found that all smooth pulse shapes (Gaussian, GSinc, GFlat) support LMT beam splitters for pulse durations of few inverse peak Rabi frequency, in contrast to the rectangular pulse.

Regarding the ease of implementation, the rectangular pulse is the most simple as it only requires a digital signal to drive, typically, a voltage controlled oscillator. The implementation of the Gaussian or the GFlat pulse shapes require a waveform generator and can be realized with relative ease. The GSinc pulse (characterized by negative values in the Rabi frequency) can be implemented experimentally by setting π phase shifts at the points of zero crossing. It requires a waveform generator in combination with a sufficiently fast phase modulation, and is thus more challenging to implement.

Disregarding the implementation of the pulse shapes, the GSinc pulse is suited for all applications, as it presents the largest velocity acceptance, can efficiently perform LMT transitions, and rejects high frequency laser phase noise. In comparison, although the GFlat pulse has a reduced velocity acceptance, it fulfills all other criteria, and can therefore be considered as a good compromise for various applications.

As a final note in this discussion, we remark that the interest of using an optical cavity to drive the light pulses in an AI has been raised recently [46, 47]. The power enhancement at the cavity resonance requires sufficient finesse $\mathcal{F}$, which modifies the intensity build up time $\tau_{\mathrm{cav}} = 2\mathcal{F}L/c$, and therefore the temporal shape of the pulse. The effect on the pulse shape will be particularly important in long-baseline gradiometers using AIs in an optical cavity, as planned in [41], where τ_{cav} may be of the order of the pulse duration (i.e. few μs). We computed the sensitivity function for such a cavity-like pulse shape (see appendix C), which shows a $1/f^4$ high-frequency behavior.

7. Conclusion

We investigated the influence of temporally shaping the light pulses on the response of an AI. The main focus of our study was on the modification of the AI sensitivity function to phase, at frequencies of the order of and higher than the effective Rabi frequency. We demonstrated that smooth pulse shapes allow for a significant

rejection of high frequency phase fluctuations compared to rectangular pulses. We also presented the modification of the scale factor of the AI due to pulse shaping, which has to be considered in the evaluation of systematic effects of AI sensors. We finally discussed the trade-offs between the different representative pulse shapes considered in the article. One important conclusion of our study is that the rejection of high frequency phase fluctuations can be achieved with a minor effect on the velocity acceptance of the pulse by employing, for example, a GFlat pulse shape, which can also efficiently perform LMT beam splitters.

In the context of LMT interferometry, future work should study the modifications of the sensitivity function for AIs driven by LMT beam splitters (see [48] for a preliminary analysis) and the influence on the rejection of the laser frequency noise, as has been done, for example, for laser intensity noise induced light shift [49].

Acknowledgments

We acknowledge the financial support from Ville de Paris (project HSENS-MWGRAV), FIRST-TF (ANR-10-LABX-48-01), Centre National d'Etudes Saptiales (CNES), DIM Nano-K, and Action Spécifique du CNRSGravitation, Références, Astronomie et Métrologie (GRAM) and Sorbonne Universités (project LORINVACC). BF is funded by Conseil Scientifique de l'Observatoire de Paris, NM by Ville de Paris, DS by Direction Générale de l'Armement, and MA by the EDPIF doctoral school. We thank Azer Trimèche for his work on the programming of the arbitrary waveform generator used in this work, Pierre Dussarrat for pointing the GSinc pulse to our attention, and Leonid Sidorenkov for his contributions in the completion of this work.

Appendix A. Definition of the pulse shapes

We define the time-dependent Rabi frequency as

$$\Omega(t) = \Omega_0 f(t), \tag{A1}$$

with Ω_0 the peak Rabi frequency. The pulses are defined by the function $f(t)$ with maximal amplitude 1.

The GSinc pulse is defined as

$$f(t) = \mathrm{sinc}(\pi t/t_1) \times \mathrm{e}^{-\frac{1}{2}\frac{t^2}{\alpha^2 t_1^2}}. \tag{A2}$$

With $\mathrm{sinc}(x) = \sin(x)/x$, t_1 the time of the first zero of the sinc, αt_1 the standard deviation of the Gaussian modulation. The total pulse duration is defined as $2nt_1$. In figure 3 the parameters of the GSinc pulse are $n = 6$ and $\alpha = 2.4$.

The GFlat pulse is even and defined as

$$f(t) = \begin{cases} 1 & \text{if} \quad t < t_0, \\ \mathrm{e}^{-\frac{1}{2}\frac{(t-t_0)^2}{r^2 t_0^2}} & \text{if} \quad t > t_0, \end{cases} \tag{A3}$$

where t_0 is the half length of the plateau, and rt_0 is the standard deviation of the Gaussian. The total pulse duration is defined as $2t_0 + 2nrt_0$. In the main text, we consider GFlat pulses with $r = 1$ and $n = 6$.

The pulse shapes are illustrated in figure A1.

In section 4 we study experimentally several Sinc pulse shapes with different number of zeros on each side of the maximum. As an illustration of implementation of such pulses, a time trace of a Sinc pulse with 8 zeros on each side of the maximum is shown in figure A2.

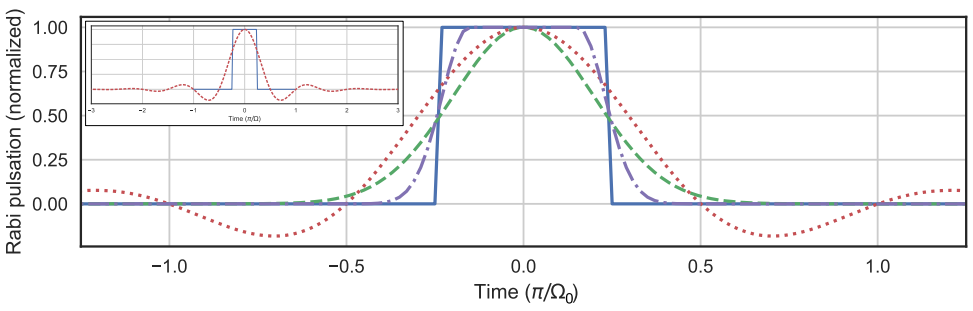

Figure A1. Illustration of the different pulse shapes considered in this article: rectangular (plain blue line), Gaussian (green dashed), GFlat (violet dotted–dashed), GSinc (dotted red). Note that the peak Rabi frequency is kept constant for all pulse shapes. For ease of illustration, we have cropped the GSinc pulse to its center part in the main panel. The inset shows the full GSinc pulse shape. The time axis is in units of the inverse Rabi frequency.

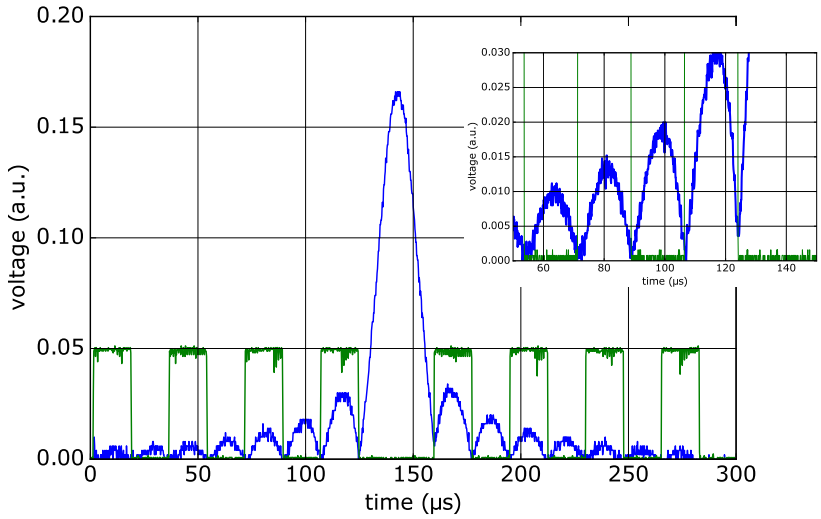

Figure A2. Time trace of the sinc pulse with 8 zeros on each side of the maximum. The blue line shows the voltage recorded by the photodiode which monitors the power of the Raman beam. The green trace shows the digital signal which triggers phase jumps of π applied to the phase lock loop. The inset is a zoom on the zeros of the power and on the phase jumps.

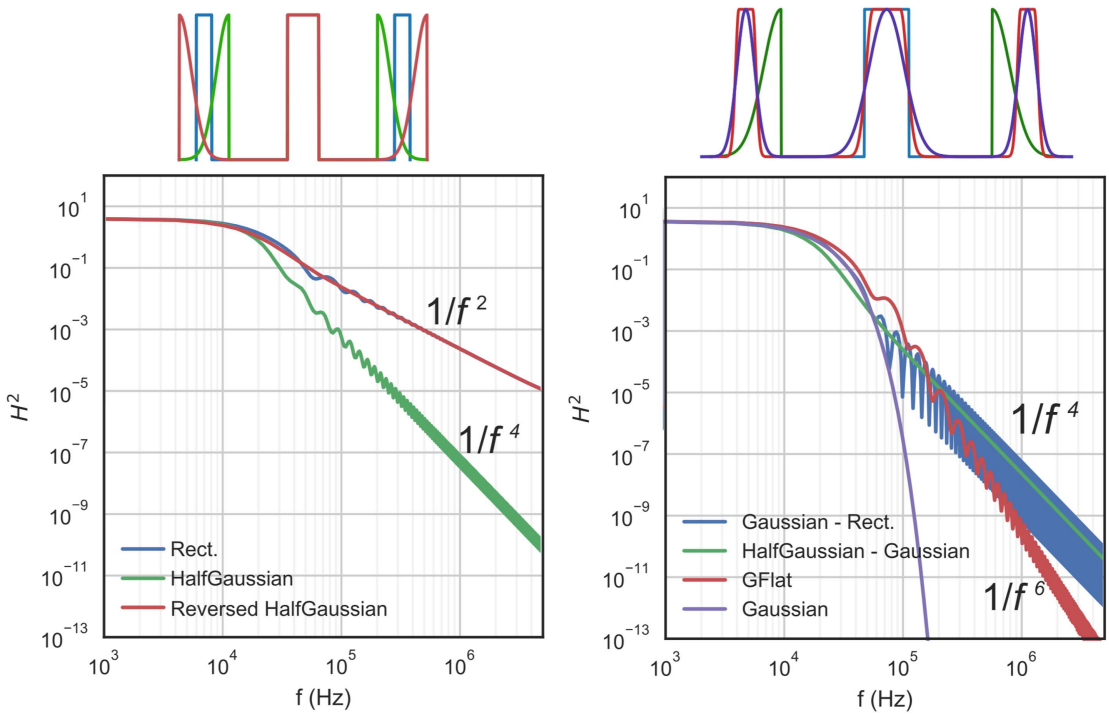

Figure B1. Illustration of the behavior of $|H(2\pi f)|^2$ at high frequency using different sequences of pulses. The calculations are for a 3 pulse interferometer with 12 kHz peak Rabi frequency and $T = 20$ ms, using different pulse shapes. The top panel shows the considered pulse sequences. Left: evolution from the $1/f^2$ scaling to the $1/f^4$ scaling, which occurs when smoothing the outer parts of the interferometer pulses, i.e. the beginning of the first $\pi/2$ pulse and the end of the last $\pi/2$ pulse. Right: evolution from the $1/f^4$ scaling to even faster decays when smoothing the inner parts of the interferometer pulses.

Appendix B. Details on the qualitative study of the influence of the pulse shape on the transfer function

The high frequency behavior of the transfer function can be qualitatively understood from the pulse shape according to the position of the pulses in the interferometric sequence. We recall that the transfer function is $|H(\omega)|^2 = \omega^2|G(\omega)|^2$, where $G(\omega)$ is the Fourier transform of $g(t)$, which is itself the sine of the integral of the time-dependent Rabi frequency, see equation (2). We define $I(t) = \int_{-\infty}^{t} \Omega(u)\mathrm{d}u$.

Our first observation, illustrated in figure B1(left), is that a decay faster than $1/f^2$ can be obtained by smoothing the beginning of the first $\pi/2$ and the end of the last $\pi/2$ pulses. At these points in time, where

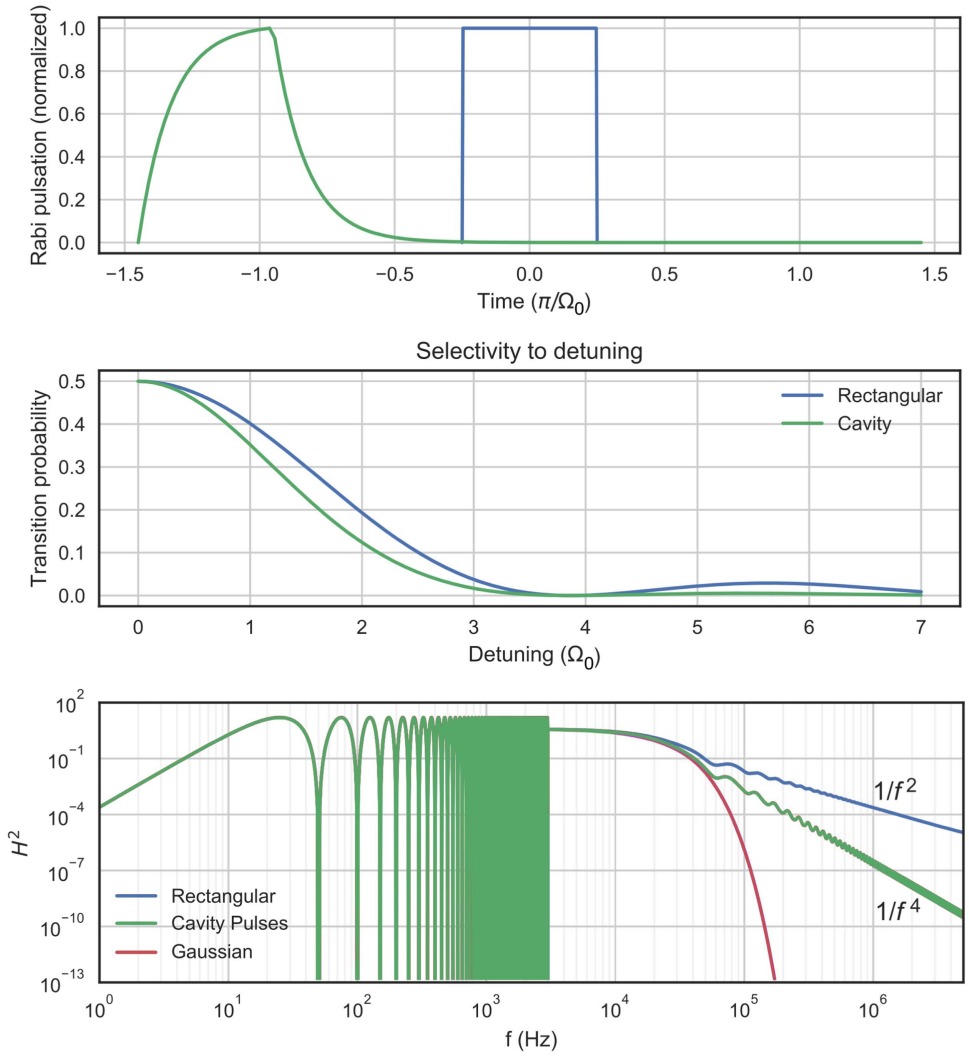

Figure C1. (Top) Shape of a cavity-like pulse and (middle) selectivity to detuning for a $\pi/2$ pulse. Here $\tau_{cav} = 5\ \mu$s. We show the shape of a rectangular pulse for comparison. Bottom: $|H(2\pi f)|^2$ in a 3 pulse interferometer with 12 kHz peak Rabi frequency and $T = 20$ ms. We show here again the response of the rectangular and Gaussian pulses for the ease of comparison.

$I(t) \simeq 0$, the sensitivity function can be Taylor-expanded as $g(t) \simeq I(t) + O(I(t)^3)$. A rectangular pulse results in a triangular form of $I(t)$, giving rise to a $1/f^2$ dependence in $|G(2\pi f)|$ and hence to a $1/f^2$ dependence in $|H(2\pi f)|^2$. In contrast, smooth pulses are characterized by a slower growth of $I(t)$ and hence a faster decay of $|H(2\pi f)|^2$. This is illustrated in figure B1(left) by calculating the transfer function using half Gaussian pulses for the $\pi/2$ pulses and a rectangular π pulse.

Evolution from $1/f^4$ to a faster decay is governed by the end of the first $\pi/2$ pulse, the beginning of the last $\pi/2$ pulse, and the beginning and end of the central π pulse. At these positions, $I(t) \simeq \pi/2$, and the sensitivity function can be approximated by $g(t) \simeq 1 - \frac{1}{2}I(t)^2 + O(I(t^4))$. Here the leading order of the time-dependence is quadratic, which explains why the influence of this part of the pulses has a weaker influence on the high frequency behavior. The rectangular π-pulse, for example, results in a parabolic shape of $I(t)$, yielding a $1/f^4$ dependence of $|H|^2$. Figure B1(right) illustrates the need to smooth these parts of the pulses in order to obtain a decay faster than $1/f^4$ in the transfer function.

Appendix C. Transfer function for an atom interferometer in an optical cavity

We present in figure C1 the temporal shape (top), the velocity selectivity (middle) and the transfer function for a pulse shape resembling the response of an optical cavity. We assumed an intensity build up time of $\tau_{cav} = 5\ \mu$s. Compared with rectangular pulses (blue), cavity pulses is more selective to detuning but rejects better the high-frequency laser phase noise.

ORCID iDs

Remi Geiger https://orcid.org/0000-0003-4678-7139

References

[1] Canuel B *et al* 2006 *Phys. Rev. Lett.* **97** 010402
[2] Geiger R *et al* 2011 *Nat. Commun.* **2** 474
[3] Rakholia A V, McGuinness H J and Biedermann G W 2014 *Phys. Rev. Appl.* **2** 054012
[4] Gustavson T L, Landragin A and Kasevich M A 2000 *Class. Quantum Grav.* **17** 2385
[5] Tackmann G, Berg P, Schubert C, Abend S, Gilowski M, Ertmer W and Rasel E M 2012 *New J. Phys.* **14** 015002
[6] Dutta I, Savoie D, Fang B, Venon B, Alzar C G, Geiger R and Landragin A 2016 *Phys. Rev. Lett.* **116** 183003
[7] Louchet-Chauvet A, Farah T, Bodart Q, Clairon A, Landragin A, Merlet S and Pereira Dos Santos F 2011 *New J. Phys.* **13** 065025
[8] Freier C, Hauth M, Schkolnik V, Leykauf B, Schilling M, Wziontek H, Scherneck H-G, Müller J and Peters A 2016 *J. Phys.: Conf. Ser.* **723** 012050
[9] McGuirk J M, Foster G T, Fixler J B, Snadden M J and Kasevich M A 2002 *Phys. Rev.* A **65** 033608
[10] Rosi G, Cacciapuoti L, Sorrentino F, Menchetti M, Prevedelli M and Tino G M 2015 *Phys. Rev. Lett.* **114** 013001
[11] Bouchendira R, Cladé P, Guellati-Khélifa S, Nez F and Biraben F 2011 *Phys. Rev. Lett.* **106** 080801
[12] Rosi G, Sorrentino F, Cacciapuoti L, Prevedelli M and Tino G 2014 *Nature* **510** 518
[13] Varoquaux G, Nyman R A, Geiger R, Cheinet P, Landragin A and Bouyer P 2009 *New J. Phys.* **11** 113010
[14] Schlippert D, Hartwig J, Albers H, Richardson L L, Schubert C, Roura A, Schleich W P, Ertmer W and Rasel E M 2014 *Phys. Rev. Lett.* **112** 203002
[15] Zhou L *et al* 2015 *Phys. Rev. Lett.* **115** 013004
[16] Bonnin A, Zahzam N, Bidel Y and Bresson A 2013 *Phys. Rev.* A **88** 043615
[17] Duan X-C, Deng X-B, Zhou M-K, Zhang K, Xu W-J, Xiong F, Xu Y-Y, Shao C-G, Luo J and Hu Z-K 2016 *Phys. Rev. Lett.* **117** 023001
[18] Aguilera D *et al* 2014 *Class. Quantum Grav.* **31** 115010
[19] Barrett B, Antoni-Micollier L, Chichet L, Battelier B, Lévèque T, Landragin A and Bouyer P 2016 *Nat. Commun.* **7** 13786
[20] Rosi G, D'Amico G, Cacciapuoti L, Sorrentino F, Prevedelli M, Zych M, Brukner C and Tino G M 2017 *Nat. Commun.* **8** 15529
[21] Overstreet C, Asenbaum P, Kovachy T, Notermans R, Hogan J M and Kasevich M A 2017 arXiv:1711.09986
[22] Dimopoulos S, Graham P W, Hogan J M, Kasevich M A and Rajendran S 2009 *Phys. Lett.* B **678** 37
[23] Geiger R 2016 Future gravitational wave detectors based on atom interferometry *An Overview of Gravitational Waves: Theory, Sources and Detection* ed G Auger and E Plagnol (Singapore: World Scientific) pp 285–313 (https://arxiv.org/abs/1611.09911)
[24] Hogan J M *et al* 2011 *Gen. Relativ. Gravit.* **43** 1953
[25] Kasevich M, Weiss D S, Riis E, Moler K, Kasapi S and Chu S 1991 *Phys. Rev. Lett.* **66** 2297
[26] Luo Y, Yan S, Hu Q, Jia A, Wei C and Yang J 2016 *Eur. Phys. J.* D **70** 262
[27] Dunning A, Gregory R, Bateman J, Cooper N, Himsworth M, Jones J A and Freegarde T 2014 *Phys. Rev.* A **90**
[28] Müller H, Chiow S and Chu S 2008 *Phys. Rev.* A **77** 023609
[29] Szigeti S S, Debs J E, Hope J J, Robins N P and Close J D 2012 *New J. Phys.* **14** 023009
[30] Santos F P D, Marion H, Bize S, Sortais Y, Clairon A and Salomon C 2002 *Phys. Rev. Lett.* **89** 233004
[31] Kovachy T, Wey Chiow S and Kasevich M A 2012 *Phys. Rev.* A **86** 011606(R)
[32] Dick G J 1987 *Proc. 19th Annu. Precise Time Time Interval* vol 19, p 133
[33] Cheinet P, Canuel B, Santos F P D, Gauguet A, Yver-Leduc F and Landragin A 2008 *IEEE Trans. Instrum. Meas.* **57** 1141
[34] Bize S 2001 Tests fondamentaux à laaide dahorloges à atomes froids de rubidium et de césium *Theses* Université Pierre et Marie Curie—Paris VI p 49, equation (4.21) (https://tel.archives-ouvertes.fr/tel-00000981)
[35] Meunier M, Dutta I, Geiger R, Guerlin C, Alzar C L G and Landragin A 2014 *Phys. Rev.* A **90** 063633
[36] Lévèque T, Gauguet A, Chaibi W and Landragin A 2010 *Appl. Phys.* B **101** 723
[37] Merlet S, Gouët J L, Bodart Q, Clairon A, Landragin A, Santos F P D and Rouchon P 2009 *Metrologia* **46** 87
[38] Hu Z-K, Sun B-L, Duan X-C, Zhou M-K, Chen L-L, Zhan S, Zhang Q-Z and Luo J 2013 *Phys. Rev.* A **88** 043610
[39] Gouët J L, Mehlstäubler T, Kim J, Merlet S, Clairon A, Landragin A and Santos F P D 2008 *Appl. Phys.* B **92** 133
[40] Gouët J L, Cheinet P, Kim J, Holleville D, Clairon A, Landragin A and Santos F P D 2007 *Eur. Phys. J.* D **44** 419
[41] Canuel B *et al* 2014 *E3S Web Conf.* **4** 01004
[42] Quessada A, Kovacich R P, Courtillot I, Clairon A, Santarelli G and Lemonde P 2003 *J. Opt. B: Quantum Semiclass. Opt.* **5** S150
[43] Nicholson T L, Martin M J, Williams J R, Bloom B J, Bishof M, Swallows M D, Campbell S L and Ye J 2012 *Phys. Rev. Lett.* **109** 230801
[44] Koller S, Grotti J, Vogt S, Al-Masoudi A, Dörscher S, Häfner S, Sterr U and Lisdat C 2017 *Phys. Rev. Lett.* **118** 073601
[45] Cheinet P 2006 Conception and realisation of a cold atom gravimeter *Theses* Université Pierre et Marie Curie—Paris VI (https://tel.archives-ouvertes.fr/tel-00070861)
[46] Riou I, Mielec N, Lefèvre G, Prevedelli M, Landragin A, Bouyer P, Bertoldi A, Geiger R and Canuel B 2017 *J. Phys. B: At. Mol. Opt. Phys.* **50** 155002
[47] Hamilton P, Jaffe M, Brown J M, Maisenbacher L, Estey B and Müller H 2015 *Phys. Rev. Lett.* **114** 100405
[48] Decamps B 2016 Atom interferometry: experiments with electromagnetic interactions and design of a Bose–Einstein condensate setup *PhD Thesis* Université Toulouse III—Paul Sabatier (https://tel.archives-ouvertes.fr/tel-01447591)
[49] Cladé P, Plisson T, Guellati-Khélifa S, Nez F and Biraben F 2010 *Eur. Phys. J.* D **59** 349

Atom interferometry with top-hat laser beams

N. Mielec,[1] M. Altorio,[1] R. Sapam,[1] D. Horville,[2] D. Holleville,[1] L. A. Sidorenkov,[1] A. Landragin,[1] and R. Geiger[1,a)]
[1]*LNE-SYRTE, Observatoire de Paris, Université PSL, CNRS, Sorbonne Université, 61 Avenue de l'Observatoire, 75014 Paris, France*
[2]*GEPI, Observatoire de Paris, Université PSL, CNRS, 5 Place Jules Janssen, 92190 Meudon, France*

(Received 10 August 2018; accepted 6 October 2018; published online 18 October 2018)

The uniformity of the intensity and the phase of laser beams is crucial to high-performance atom interferometers. Inhomogeneities in the laser intensity profile cause contrast reductions and systematic effects in interferometers operated with atom sources at micro-Kelvin temperatures and detrimental diffraction phase shifts in interferometers using large momentum transfer beam splitters. We report on the implementation of a so-called top-hat laser beam in a long-interrogation-time cold-atom interferometer to overcome the issue of inhomogeneous laser intensity encountered when using Gaussian laser beams. We characterize the intensity and relative phase profiles of the top-hat beam and demonstrate its gain in atom-optic efficiency over a Gaussian beam, in agreement with numerical simulations. We discuss the application of top-hat beams to improve the performance of different architectures of atom interferometers. *Published by AIP Publishing.*
https://doi.org/10.1063/1.5051663

Inertial sensors based on light-pulse atom interferometry address various applications ranging from inertial navigation,[1–3] metrology,[4–6] gravimetry,[7–13] gradiometry,[14,15] and tests of fundamental physics,[16–21] to gravitational wave astronomy.[22,23] Light-pulse atom interferometers rely on the coherent transfer of momentum from the photons of counter-propagating laser beams to free falling atoms in order to split, deflect and recombine the matter-waves. The sensitivity and the accuracy of the instruments thus crucially depend on the relative phase uniformity of the laser beams realizing these atom-optic functionalities. State-of-the-art cold-atom sensors typically use sources at few μK temperatures, interrogation times of several hundreds of milliseconds, and two-photon transitions.[5,10,24] Inhomogeneities in the laser intensity across the atom cloud degrade the atom optic efficiency, which causes a decrease in interferometer contrast and hence a lower signal to noise ratio, as well as systematic effects.[25] Such detrimental effects are amplified in interferometers employing large momentum transfer (LMT) techniques (in which several momenta are transferred to the atoms),[21,26] in particular, because of diffraction phase shifts.[27] The problem of intensity inhomogeneity can be mitigated by employing Gaussian beams with a size much larger than that of the atom cloud, at the cost of reduced peak intensity.

In this work, we report on the implementation of a *collimated* top-hat laser beam (i.e., with uniform intensity distribution in the central part[28]) as a solution to circumvent the problems encountered in atom interferometers employing Gaussian beams.

Beamshaping is a topic of intense development, with applications ranging from micro-lithography, optical data storage, to optical tweezers, where different approaches are followed to produce structured light patterns. For application in atom interferometry, the requirement for the relative phase homogeneity motivates a scheme where the counter-propagating beam pair is obtained by retro-reflection (the retro-distance typically lying in the ten-centimeters-to-meter scale). The interrogation laser beams are thus required to be well collimated over such distances. This requirement of the beam shaping technique amounts to achieving a flat phase profile.

The simplest form of shaping the intensity distribution of a laser beam, apodization, results in significant loss of optical power (for example, the optimal transformation of a Gaussian beam into a beam with a flat intensity profile sacrifices 64% of power). More efficient techniques involve diffractive optical elements, such as spatial light modulators (SLMs), in order to produce focused light patterns[29] or collimated structured beams when multiple SLMs are cascaded.[30] However, the bulkiness of the optical setup, the potential drift of the beam-shaping performance linked to the use of an active material, and the limited incident peak intensity make such solutions cumbersome for atom interferometry experiment. Instead, passive refractive techniques based on aspheric optical elements[31] seem favorable, owing to their compactness, stability, and efficiency.

Our passive top-hat collimator solution is based on a recently released commercial beamshaper from the Asphericon Company (model TSM-25–10-S-B), see Fig. 1(a). The beamshaper shall receive at its input a Gaussian beam of 10 mm $1/e^2$-diameter and produce a top-hat beam of 15 mm full width at half maximum (FWHM), with a region of about 14 mm where the intensity varies by less than 10% (Ref. 32). The beamshaping is done with multiple aspheric optics, based on principles similar to those of Ref. 31. The advertized uniformity of the intensity plateau is 0.056 rms, with a phase inhomogeneity of $\lambda/3$ peak-valley (PV) and $\sim\lambda/20$ rms, allowing the beam to propagate without deformation on distances of several meters.[32] We inject the beamshaper with a home-made fiber collimator made of 3 simple lenses, to produce a Gaussian beam of 9.95 ± 0.05 mm $1/e^2$ diameter. At the output of the beamshaper, the top-hat beam is

a)Electronic mail: remi.geiger@obspm.fr

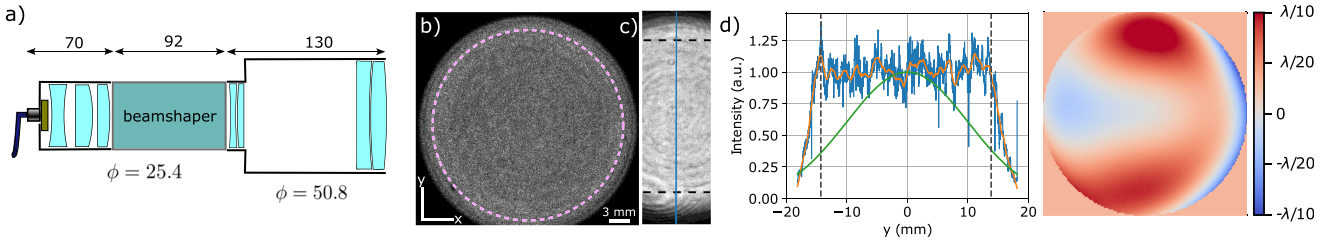

FIG. 1. (a) Schematic view of the optical system with the input collimator, the beamshaper, and the expander (dimensions in mm, ϕ denoting the diameter of the optics). (b) Image of the top-hat beam on a paper screen. The dashed purple line is a circle of 28 mm diameter. (c) Image obtained with a beamprofiler, after 40 cm of propagation. Between the 2 dashed lines separated by 28 mm, the uniformity of the plateau is 0.11 rms. (d) (blue) Vertical line profile of the top-hat beam shown in (c); the intensity has been normalized to the mean plateau intensity (orange). Moving average over 1 mm (green). Theoretical profile of a Gaussian beam with 40 mm $1/e^2$ diameter. (e) Relative phase of the top-hat beam with 70 cm propagation difference, in a disk of 28 mm; the deviation is $\lambda/5$ (PV) and $\lambda/28$ (rms).

magnified by a factor of two with two achromatic doublets, in order to reach a useful region of 28 mm. The optical system can be mounted conveniently during an experiment. The power transmission of the input collimator plus the beamshaper is 91%, while that of the full system is 85%. The quality of the generated top-hat beam mainly depends on the input beam size (which must fall within the 10 mm diameter specification at the 10% level[32]) and its collimation.

To align the top-hat collimator, we image the beam on a paper screen and optimize the intensity profile by moving the input fiber placed on a 5-axis mount. We target a flat circular intensity profile maintained over a propagation distance of at least 150 cm. Figure 1(b) shows the beam imaged on the paper screen at the output of the expander. While this method is convenient for the alignment procedure, it is not suited for a precise measurement of the intensity uniformity of the beam because of the speckle produced on the paper screen. We use a large-area beamprofiler ($11.3 \times 6.0\,\mathrm{mm}^2$) to measure the uniformity of the plateau. Figure 1(c) shows the stitched images acquired by scanning the beamprofiler in front of the beam after 40 cm of propagation. The beam exhibits a qualitatively flat plateau. Large diameter rings concentric to the beam are attributed to the beamshaper. The uniformity of the plateau over a diameter of 28 mm is 0.11 rms and the FWHM is 31.7 ± 0.2 mm. Figure 1(d) shows a profile of the vertical cut through the middle of the beam (along the blue line). The orange line is a moving average over 1 mm of the profile, shown here to illustrate lower frequency inhomogeneities. For comparison, the green line shows a Gaussian beam with 40 mm diameter at $1/e^2$ (as used in Ref. 24) and same peak intensity as the top-hat beam.

In an atom interferometer, the relative phase between two counter-propagating laser beams is imprinted on the atomic wave-function during the light pulses. This relative phase contains a term associated with the free propagation, $\varphi(x, y, 0) - \varphi(x, y, 2L)$, where L is the distance between the atom cloud and the retro-mirror.[33] We measured such a relative phase field for our top-hat beam using an asymmetric Michelson interferometer with the difference of its arms set to $2L$. At the output, the interference pattern carries the 2D relative phase map, which we recover using Fourier analysis.[34] A lower bound on the accuracy is set by the planarity of the mirrors and the beamsplitter used in the interferometer, specified to be $\lambda/10$ peak-valley (PV). The relative phase map in a pupil of 28 mm diameter corresponding to the useful part of the beam is shown in Fig. 1(e), for a difference in propagation distance $2L = 70$ cm. We find relative phase inhomogeneities of $\lambda/5$ PV and a $\lambda/28$ rms. Additional phase maps for further propagation distances are given in the supplementary material. Our characterization shows that the top-hat beam is suitable for high-precision atom interferometry, where relative wavefront inhomogeneities are an issue.[13,25,33,35]

We implemented the top-hat beam on a cold-atom gyroscope-accelerometer experiment. The setup has been described in previous works[24,36] and we recall here the main features which are relevant to this study. Laser-cooled cesium atoms (at a temperature of 1.2 μK) are launched vertically with a velocity of up to 5.0 $\mathrm{m\,s}^{-1}$. After a selection step of the $m_F = 0$ magnetic sublevel, we realize the atom interferometer by means of two-photon stimulated Raman transitions from counter-propagating laser beams, which couple the $|F = 3, m_F = 0\rangle$ and $|F = 4, m_F = 0\rangle$ clock states. The direction of the Raman beams is nearly horizontal. We use two beams separated vertically by a distance of 211 mm. The top-hat collimator was set up at the position of the top beam, while the bottom beam is a Gaussian beam of 40 mm diameter at $1/e^2$ [Fig. 2(a)]. The state of the atoms at the output of the interferometer is finally read out using fluorescence detection.

We first probe the intensity profile of the top-hat beam by applying a Raman pulse of fixed duration τ at different

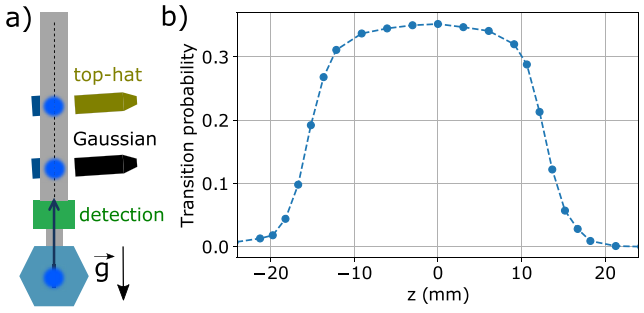

FIG. 2. (a) Sketch of the experiment. (b) Measurement of the local Raman lasers intensity with a cold atom cloud, by recording the transition probability versus time-of-flight. The duration of the Raman pulse is fixed ($\tau = 9$ μs) and set close to that of a $\pi/2$ pulse, where the sensitivity to intensity fluctuations on the plateau is maximum. The horizontal axis (z) is obtained by multiplying the TOF with the mean velocity of atoms in the beam ($3.0\,\mathrm{m\,s}^{-1}$).

times as the atoms travel on their way up. The atoms are launched with a velocity of 4.7 m s^{-1} and their mean trajectory intersects the center of the beam after a time of flight (TOF) of 170 ms. After this relatively short TOF, the size of the cloud is still close to that of the initially launched atoms ($\simeq$1.5 mm rms radius) and much smaller than the beam size. The transition probability, $P \propto \sin^2(\Omega(z)\tau/2)$, is determined by the local value of the two-photon Rabi frequency, $\Omega(z)$, and can thus be used as a probe of the local intensity of the beam (here, z denotes the direction parallel to gravity). Figure 2(b) shows the transition probability versus the relative position of the cloud inside the beam. We observe a qualitatively flat intensity profile in the center, with a width consistent with the optical characterization reported in Fig. 1.

The size of a cold atom cloud increases over free propagation due to finite temperature. This results in an inhomogeneous atom-light coupling when the cloud size approaches the waist of the Gaussian beam, thereby decreasing the interferometer contrast. The intensity homogeneity of the top-hat beam allows in principle to improve on this effect. To illustrate this improvement, we operate a 3 light-pulse interferometer sequence with a pulse separation time $T = 1$ ms, after a long TOF of 855 ms to bring forward the effect of the atom cloud expansion. For a quantitative comparison, the difference in height between the two beams (211 mm) was matched by the respective change in launch velocity, in order to obtain nearly the same TOFs when crossing the Gaussian and top-hat beams. Figure 3 presents the comparison and shows the advantage of the top-hat beam.

To assess the limitations to the gain in atom-optic efficiency offered by our top-hat beam over our Gaussian beam, we recorded Rabi oscillations after various TOFs, when the launched atom cloud crosses the beams on its way up and on its way down. Figure 4(a) shows the Rabi oscillations on the way up after a TOF of 170 ms and on the way down after a TOF of 855 ms for the top-hat and Gaussian beams. On the way up, the cloud size is smaller than the beam sizes and the Rabi oscillations have a similar shape for the Gaussian and top-hat beams, as expected. The transfer efficiency of $\sim$70% is limited by the velocity selectivity of the two-photon transition, given by the finite Rabi frequency (i.e., laser power)

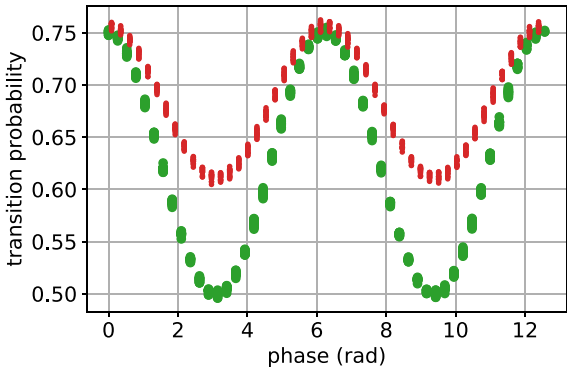

FIG. 3. Interference fringes for a 3-pulse interferometer sequence with a pulse separation time $T = 1$ ms, after a TOF of 855 ms. Red: Gaussian beam. Green: top-hat beam. The interference fringes are scanned by varying the relative Raman laser phase at the third light pulse. The same optical power was used for the Gaussian and the top-hat beams.

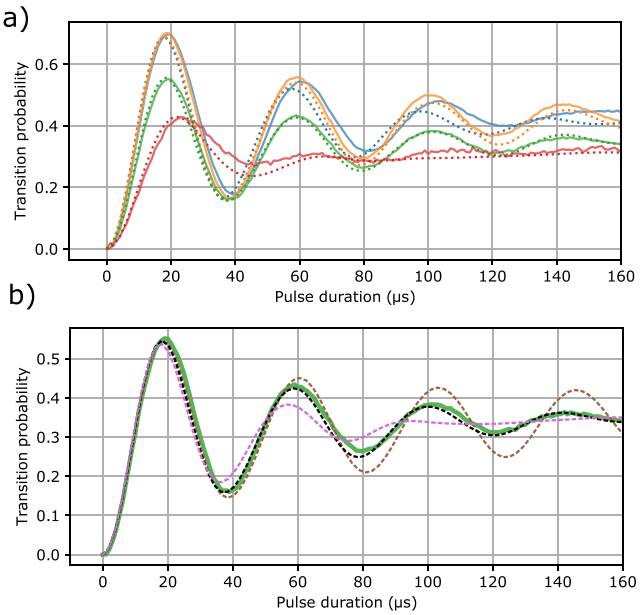

FIG. 4. Rabi oscillations. (a) Plain lines: measured oscillations on the way up after 170 ms of TOF (blue and orange for Gaussian and top-hat, respectively) and on the way down after 855 ms of TOF (red and green). Dotted lines: numerical simulation. (b) Green plain line: measured Rabi oscillation in the top-hat beam after 855 ms of TOF [the same as in (a)]. Dashed: numerical simulation for various levels of rms intensity noise on the top-hat (brown: 0%, black: 8.3%, violet: 15%).

and the velocity spread of the atoms in the direction of the beams. On the contrary, on the way down, the Rabi oscillation in the top-hat beam (green) is significantly improved with respect to that in the Gaussian beam (red), owing to the homogeneity of the two-photon Rabi frequency from the top-hat beam. To model the Rabi oscillations, we employ a Monte-Carlo simulation where we generate an ensemble of atoms with individual velocities following the distribution measured with the Doppler-sensitive Raman transitions (corresponding to a 3D temperature of 1.2 μK), and propagate them in the Raman beams. The details of the model are given in the supplementary material. The model reproduces well the data and allows one to assess the residual intensity inhomogeneities of the top-hat beam. Figure 4(b) shows the measured Rabi oscillation confronted to a simulation where the intensity noise of various levels is added on the top-hat profile.[37] The data match best with the numerical simulation assuming an inhomogeneity of 8.3% rms, consistent with the optical characterization of the intensity inhomogeneities of 11% reported in Fig. 1.

Finally, we demonstrate that the top-hat beam is suited for high-sensitivity atom interferometry, by running a 3-pulse atom interferometer sequence with a pulse separation time $T = 147$ ms. The first $\pi/2$ pulse is realized in the Gaussian beam (on the way up, TOF = 170 ms), while the second and third pulses are realized in the top-hat beam (TOF = 317 and 464 ms). For such long interrogation time, the interferometer is highly sensitive to vibration noise producing at its output a typical rms phase shift of more than π rad. Running the interferometer results in a random sampling of the fringe pattern by vibration noise, which appears blurred without additional knowledge on the vibration noise at each run. To extract the contrast, we follow the method of

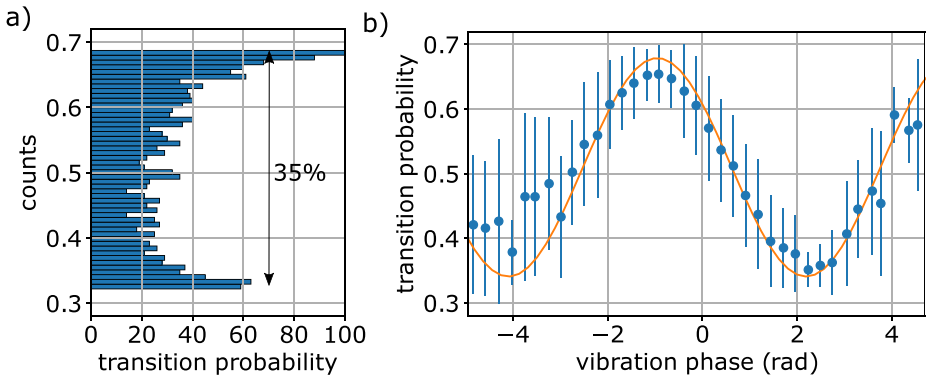

FIG. 5. Performance of the 3-pulse interferometer with $2T = 294$ ms. (a) Histogram of the transition probability showing a contrast of 35%. (b) Transition probability versus the vibration phase calculated from the data for a broadband seismometer. The data points are sorted along the x-axis and binned in intervals of 262 mrad width. The imperfect estimation of the vibration phase by the seismometer translates into phase noise and consequently into probability noise when binning. Error bars denote a standard deviation of 1. The orange plain curve shows a sinusoidal fit where the fringe amplitude is set to the value of 35% extracted from (a).

Ref. 2 and compute the histogram of the transition probability data [Fig. 5(a)], from which we extract a contrast of 35%. Furthermore, we recover the interference fringes by correlating the atom interferometer output with the phase calculated from vibration data acquired with two broadband seismometers,[24,38] see Fig. 5(b). The uncertainty (1σ) on the fitted phase is 80 mrad, corresponding to a horizontal acceleration uncertainty of 2.5×10^{-7} m s^{-2}. Although the measurement sensitivity is limited by residual vibration noise, this experiment shows that the top-hat beam is compatible with high-sensitivity inertial measurements based on long-interrogation-time cold-atom interferometry.

In conclusion, we have set up and characterized a collimated top-hat laser beam and reported on its implementation for a long interrogation time cold-atom interferometer. Our top-hat beam features a constant intensity over a region of 28 mm with rms variations of about 10%. We expect that the intensity homogeneity offered by top-hat beams compared to Gaussian beams will be beneficial to various atom interferometer geometries which we discuss below. We present additional advantages in the supplementary material.

The intensity homogeneity of the interrogation beams will allow reducing or canceling important systematic effects in cold-atom interferometers, such as the two photon light shift.[39] It can also be used to improve the efficiency and the stability of atom launching techniques based on the coherent transfer of photon momenta, such as in Bloch oscillations.[4,6,21] Moreover, this beamshaping solution could be adapted for atom interferometers with baselines of several meters as in Ref. 21.

Employing a single top-hat beam can be used to build compact, yet precise, cold-atom inertial sensors. For example, a $D = 28$ mm a wide homogeneous intensity profile should allow one to run a fountain interferometer with a total interferometer time of $2T \simeq 2 \times \sqrt{2D/g} = 151$ ms, if the atoms are launched from the bottom of the beam. Moreover, the design of gyroscopes, where the atoms travel through successive laser beams with a velocity transverse to the momentum transfers[25,40,41] could be simplified with a single top-hat beam.

Homogeneity of the intensity profile should reduce the diffraction phase shifts encountered in LMT Bragg diffraction.[42–44] For example, a variation of 1% of laser intensity in $4\hbar k$ Bragg diffraction amounts to a variation in the diffraction phase of about 84 mrad.[27] The rms intensity uniformity of our top-hat beam is between 8% and 11% over a region of 28 mm [Fig. 1(c)]. Keeping a 10% rms intensity variation within a Gaussian beam requires working within a reduced portion around the center, which translates into using only 25% of the total power. This suggests that the efficiency and the accuracy of LMT beam splitters should be significantly improved by employing top-hat beams.

See supplementary material for additional data regarding intensity profiles (Fig. S1) and relative phase maps (Fig. S2) for various propagation distances, for the impact of relative phase inhomogeneities on the atom interferometer bias, for the details of the model of Rabi oscillations, and for numerical examples of the gain in contrast with top-hat beams compared to Gaussian beams for specific interferometer geometries.

We thank Josiane Firminy and Faouzi Boussaha for their realization of engraved aspheric phase plates in an early design of the beamshaper conducted in the beginning of this project. This work was supported by Ville de Paris (Project No. HSENS-MWGRAV), FIRST-TF (ANR-10-LABX-48-01), Centre National d'Etudes Saptiales (CNES), Sorbonne Universités (project LORINVACC), Action Spécifique du CNRS Gravitation, Références, Astronomie et Métrologie (GRAM), and the European Union's Horizon 2020 research and innovation programme under the Marie Sklodowska-Curie Grant Agreement No. 660081. We thank Laurence Pruvost for fruitful discussions.

[1]B. Canuel, F. Leduc, D. Holleville, A. Gauguet, J. Fils, A. Virdis, A. Clairon, N. Dimarcq, C. J. Bordé, A. Landragin, and P. Bouyer, Phys. Rev. Lett. **97**, 010402 (2006).
[2]R. Geiger, V. Ménoret, G. Stern, N. Zahzam, P. Cheinet, B. Battelier, A. Villing, F. Moron, M. Lours, Y. Bidel, A. Bresson, A. Landragin, and P. Bouyer, Nat. Commun. **2**, 474 (2011).
[3]P. Cheiney, L. Fouché, S. Templier, F. Napolitano, B. Battelier, P. Bouyer, and B. Barrett, Phys. Rev. Applied **10**, 034030 (2018).
[4]R. Bouchendira, P. Cladé, S. Guellati-Khlifa, F. Nez, and F. Biraben, Phys. Rev. Lett. **106**, 080801 (2011).

[5]G. Rosi, F. Sorrentino, L. Cacciapuoti, M. Prevedelli, and G. M. Tino, Nature **510**, 518 (2014).
[6]R. H. Parker, C. Yu, W. Zhong, B. Estey, and H. Müller, Science **360**, 191 (2018).
[7]A. Peters, K. Y. Chung, and S. Chu, Metrologia **38**, 25 (2001).
[8]Z.-K. Hu, B.-L. Sun, X.-C. Duan, M.-K. Zhou, L.-L. Chen, S. Zhan, Q.-Z. Zhang, and J. Luo, Phys. Rev. A **88**, 043610 (2013).
[9]P. Gillot, O. Francis, A. Landragin, F. P. D. Santos, and S. Merlet, Metrologia **51**, L15 (2014).
[10]C. Freier, M. Hauth, V. Schkolnik, B. Leykauf, M. Schilling, H. Wziontek, H.-G. Scherneck, J. Müller, and A. Peters, J. Phys. Conf. Ser. **723**, 012050 (2016).
[11]S.-K. Wang, Y. Zhao, W. Zhuang, T.-C. Li, S.-Q. Wu, J.-Y. Feng, and C.-J. Li, Metrologia **55**, 360 (2018).
[12]Y. Bidel, N. Zahzam, C. Blanchard, A. Bonnin, M. Cadoret, A. Bresson, D. Rouxel, and M. F. Lequentrec-Lalancette, Nat. Commun. **9**, 627 (2018).
[13]R. Karcher, A. Imanaliev, S. Merlet, and F. Pereira dos Santos, pre-print arXiv:1804.04909 (2018). [physics.atom-ph].
[14]J. M. McGuirk, G. T. Foster, J. B. Fixler, M. J. Snadden, and M. A. Kasevich, Phys. Rev. A **65**, 033608 (2002).
[15]F. Sorrentino, A. Bertoldi, Q. Bodart, L. Cacciapuoti, M. de Angelis, Y.-H. Lien, M. Prevedelli, G. Rosi, and G. M. Tino, Appl. Phys. Lett. **101**, 114106 (2012).
[16]S. Dimopoulos, P. W. Graham, J. M. Hogan, and M. A. Kasevich, Phys. Rev. Lett. **98**, 111102 (2007).
[17]S. Lepoutre, A. Gauguet, G. Trénec, M. Büchner, and J. Vigué, Phys. Rev. Lett. **109**, 120404 (2012).
[18]D. N. Aguilera, H. Ahlers, B. Battelier, A. Bawamia, A. Bertoldi, R. Bondarescu, K. Bongs, P. Bouyer, C. Braxmaier, L. Cacciapuoti *et al.*, Classical Quantum Gravity **31**, 115010 (2014).
[19]L. Zhou, S. Long, B. Tang, X. Chen, F. Gao, W. Peng, W. Duan, J. Zhong, Z. Xiong, J. Wang, Y. Zhang, and M. Zhan, Phys. Rev. Lett. **115**, 013004 (2015).
[20]M. Jaffe, P. Haslinger, V. Xu, P. Hamilton, A. Upadhye, B. Elder, J. Khoury, and H. Mller, Nat. Phys. **13**, 938 (2017).
[21]P. Asenbaum, C. Overstreet, T. Kovachy, D. D. Brown, J. M. Hogan, and M. A. Kasevich, Phys. Rev. Lett. **118**, 183602 (2017).
[22]W. Chaibi, R. Geiger, B. Canuel, A. Bertoldi, A. Landragin, and P. Bouyer, Phys. Rev. D **93**, 021101 (2016).
[23]J. M. Hogan and M. A. Kasevich, Phys. Rev. A **94**, 033632 (2016).
[24]I. Dutta, D. Savoie, B. Fang, B. Venon, C. Garrido Alzar, R. Geiger, and A. Landragin, Phys. Rev. Lett. **116**, 183003 (2016).
[25]A. Gauguet, B. Canuel, T. Lévèque, W. Chaibi, and A. Landragin, Phys. Rev. A **80**, 063604 (2009).
[26]T. Mazzoni, X. Zhang, R. Del Aguila, L. Salvi, N. Poli, and G. M. Tino, Phys. Rev. A **92**, 053619 (2015).
[27]M. Büchner, R. Delhuille, A. Miffre, C. Robilliard, J. Vigué, and C. Champenois, Phys. Rev. A **68**, 013607 (2003).
[28]F. Gori, Opt. Commun. **107**, 335 (1994).
[29]V. Pal, C. Tradonsky, R. Chriki, N. Kaplan, A. Brodsky, M. Attia, N. Davidson, and A. A. Friesem, Appl. Opt. **57**, 4583 (2018).
[30]H. Ma, Z. Liu, P. Zhou, X. Wang, Y. Ma, and X. Xu, J. Opt. **12**, 045704 (2010).
[31]J. A. Hoffnagle and C. M. Jefferson, Appl. Opt. **39**, 5488 (2000).
[32]See https://www.aspericon.com/en/asphere/shape-it-til-you-make-it-top-hat-beam-shaping-with-aspheres/ for "Aspericon Website" (last accessed October 9, 2018).
[33]A. Louchet-Chauvet, T. Farah, Q. Bodart, A. Clairon, A. Landragin, S. Merlet, and F. P. D. Santos, New J. Phys. **13**, 065025 (2011).
[34]M. Takeda, H. Ina, and S. Kobayashi, J. Opt. Soc. Am. **72**, 156 (1982).
[35]V. Schkolnik, B. Leykauf, M. Hauth, C. Freier, and A. Peters, Appl. Phys. B **120**, 311 (2015).
[36]M. Meunier, I. Dutta, R. Geiger, C. Guerlin, C. L. Garrido Alzar, and A. Landragin, Phys. Rev. A **90**, 063633 (2014).
[37]We varied the spatial frequencies of the added intensity noise and found no substantial difference in the simulation results as long as the spatial period was smaller than about 1/10 of the beam size. In the simulation reported in Fig. 3, the spatial period of the noise is 1/100 of the beam size.
[38]S. Merlet, J. LeGouët, Q. Bodart, A. Clairon, A. Landragin, F. Pereira Dos Santos, and P. Rouchon, Metrologia **46**, 87 (2009).
[39]A. Gauguet, T. E. Mehlstäubler, T. Lévèque, J. Le Gouët, W. Chaibi, B. Canuel, A. Clairon, F. P. Dos Santos, and A. Landragin, Phys. Rev. A **78**, 043615 (2008).
[40]G. Tackmann, P. Berg, C. Schubert, S. Abend, M. Gilowski, W. Ertmer, and E. M. Rasel, New J. Phys. **14**, 015002 (2012).
[41]Z.-W. Yao, S.-B. Lu, R.-B. Li, J. Luo, J. Wang, and M.-S. Zhan, Phys. Rev. A **97**, 013620 (2018).
[42]S.-W. Chiow, T. Kovachy, H.-C. Chien, and M. A. Kasevich, Phys. Rev. Lett. **107**, 130403 (2011).
[43]P. A. Altin, M. T. Johnsson, V. Negnevitsky, G. R. Dennis, R. P. Anderson, J. E. Debs, S. S. Szigeti, K. S. Hardman, S. Bennetts, G. D. McDonald, L. D. Turner, J. D. Close, and N. P. Robins, New J. Phys. **15**, 023009 (2013).
[44]B. Estey, C. Yu, H. Müller, P.-C. Kuan, and S.-Y. Lan, Phys. Rev. Lett. **115**, 083002 (2015).

PHYSICS

Interleaved atom interferometry for high-sensitivity inertial measurements

D. Savoie*, M. Altorio*, B. Fang, L. A. Sidorenkov, R. Geiger†, A. Landragin

Cold-atom inertial sensors target several applications in navigation, geoscience, and tests of fundamental physics. Achieving high sampling rates and high inertial sensitivities, obtained with long interrogation times, represents a challenge for these applications. We report on the interleaved operation of a cold-atom gyroscope, where three atomic clouds are interrogated simultaneously in an atom interferometer featuring a sampling rate of 3.75 Hz and an interrogation time of 801 ms. Interleaving improves the inertial sensitivity by efficiently averaging vibration noise and allows us to perform dynamic rotation measurements in a so far unexplored range. We demonstrate a stability of 3×10^{-10} rad s^{-1}, which competes with the best stability levels obtained with fiber-optic gyroscopes. Our work validates interleaving as a key concept for future atom-interferometry sensors probing time-varying signals, as in onboard navigation and gravity gradiometry, searches for dark matter, or gravitational wave detection.

INTRODUCTION

Quantum sensing relies on the manipulation of internal or external degrees of freedom in atoms, molecules, optomechanical devices, and photonic or solid-state systems and covers various applications such as magnetometry (*1*–*3*), the definition of frequency standards (*4*, *5*), short-range force measurements (*6*), or electromagnetic measurements (*7*, *8*). Inertial sensors based on the coherent manipulation of superpositions of momentum states in atom interferometers have been developed for more than 25 years (*9*–*11*), with the goal of addressing various applications. Examples of remarkable achievements are tests of fundamental physics (*12*–*16*), metrology (*17*), or absolute gravimetry (*18*–*21*). These precision measurements of gravito-inertial effects directly take benefit from the inherent accuracy and long-term stability of cold-atom sensors. These two properties can eventually be combined with the high bandwidth of relative sensors, which is at the basis of sensor fusion (*22*). This approach is reminiscent of atomic clocks, where probing the stable atomic energy structure is used for stabilizing a microwave or optical oscillator (*4*, *5*) or for tests of fundamental physics.

The extension of applications of cold-atom inertial sensors to measurement of time-varying signals has been challenged by their reduced sampling rate, which originates from their sequential operation and from the long interrogation time of the atoms that is required to achieve high inertial sensitivity. This limitation is, for example, an obstacle for applications to inertial navigation (*23*) or to fundamental research related to dark matter detection (*24*) or gravitational wave astronomy (*25*, *26*). In this study, we report on the interleaved operation of a cold-atom inertial sensor, which operates with a sampling frequency of 3.75 Hz and features a high inertial sensitivity, as given by the 801-ms interrogation time of the atoms in the interferometer. The method of interleaving, which we demonstrate for both static and dynamic rotation rate measurements, can be generalized to other atom interferometer architectures and therefore paves the way to the development of high-bandwidth and high-sensitivity cold-atom inertial sensors.

Besides an increase in sensor bandwidth, we show that interleaving allows us to efficiently average vibration noise (as $1/\tau$, where τ is the integration time), which represents the most important noise source in cold-atom inertial sensors. As a consequence, we demonstrate a record rotation rate sensitivity of 3×10^{-8} rad s^{-1} $Hz^{-1/2}$. Such a high-sensitivity level allows us to characterize the systematic effects of a cold-atom gyroscope in a so far unexplored range (*27*, *28*) and to stabilize them at the few 10^{-10} rad s^{-1} level. Previous research on atomic beam gyroscopes has already demonstrated excellent sensitivities (*29*) and long-term stabilities close to the state-of-the-art optical gyroscopes (*30*). As the long-term instability of gyroscopes is a limiting factor in inertial navigation systems, achieving the performance of the best fiber-optic gyroscopes (*31*) was a long-standing goal, which we attain for the first time with a cold-atom sensor.

RESULTS

Experimental setup

Experimental sequence and principle of the gyroscope

The core of the experimental setup used in this work has been described in (*32*) and is sketched in Fig. 1. The essential techniques are given in Materials and Methods, with further details in the Supplementary Materials. In short, we laser-cool cesium atoms to a temperature of 1.2 μK and launch them vertically at a velocity of 5.0 m s^{-1}. After a selection step of the $m_F = 0$ magnetic sublevel, we interrogate the atoms in the interferometer and finally detect their state at the output of the interferometer, on their way down, using fluorescence detection. We realize the light-pulse atom interferometer using two-photon stimulated Raman transitions with counter-propagating laser beams, which couple the $|F = 3, m_F = 0\rangle$ and $|F = 4, m_F = 0\rangle$ clock states of the cesium atom.

According to the Sagnac effect, the rotation sensitivity is proportional to the area between the two arms of the interferometer. Our gyroscope is based on a fountain configuration with four light pulses to create a folded geometry owing to gravity (*33*). The symmetric four-pulse fountain configuration allows us to achieve a large area (11 cm^2 in this work) and leads to a vanishing sensitivity to constant linear accelerations. The interferometer phase shift, Φ, can be calculated from the relative phase between the two Raman lasers, $\Delta\varphi_{laser}(t) = \vec{k}_{eff} \cdot \vec{r}_{b,t}(t) + \Delta\varphi(t)$, which is imprinted on the diffracted part of the matter wave at the time t of the pulse. It reads

$$\Phi = \vec{k}_{eff} \cdot \left[\vec{r}_b(0) - 2\vec{r}_t\left(\frac{T}{2}\right) + 2\vec{r}_t\left(\frac{3T}{2}\right) - \vec{r}_b(2T) \right] + \Delta\Phi^0 \quad (1)$$

LNE-SYRTE, Observatoire de Paris, Université PSL, CNRS, Sorbonne Université, 61 Avenue de l'Observatoire, 75014 Paris, France.
*These authors contributed equally to this work.
†Corresponding author. Email: remi.geiger@obspm.fr.

where $\vec{k}_{\mathrm{eff}}$ is the two-photon wave vector, $\vec{r}_{\mathrm{b,t}}(t)$ is the position of the mirror retroreflecting the Raman lasers with respect to the center of mass of the free-falling atoms (subscripts {b, t} for bottom and top mirror; see Fig. 1), and $2T$ is the total interrogation time. The last term $\Delta\Phi^0$ is a controllable laser phase shift independent of inertial effects. The phase shift associated to the stationary Earth rotation rate $\vec{\Omega}_{\mathrm{E}}$ is given by

$$\Phi_{\Omega} = \frac{1}{2}\vec{k}_{\mathrm{eff}} \cdot (\vec{g} \times \vec{\Omega}_{\mathrm{E}}) T^3 \qquad (2)$$

where $\vec{g}$ is the acceleration of gravity (*34*).

Interleaved operation

We use a sequence of joint interrogation of successive interferometers, which is obtained by using the same π/2 Raman pulse for the atom clouds entering and exiting the interferometer zone (*32*). Consequently, the sensor can operate without dead times. The interleaved operation, which is reminiscent from the atom juggling technique of (*35*), is then implemented by extending this joint sequence to a multiple-joint sequence, as proposed in (*36*). The sequence of Raman pulses is given in Fig. 1. If we denote $2T = 801$ ms as the total duration of the interferometer, then we launch an atom cloud every $T_c = 2T/3 = 267$ ms, which supposes that a cloud is laser cooled while three previously launched clouds are interrogated in the interferometer. Because of timing constraints, the loading time of the magneto-optical trap (MOT) is limited. The atoms are loaded in the MOT during 55 ms, and we detect 2×10^5 atoms at the end of the interferometer. The light scattered from the MOT atoms causes incoherent photon absorption and emission from the interrogated atoms and therefore a loss of contrast (*36*). The contrast of the interferometer is 7.4%, limited by the expansion of the cloud during the free fall in the Raman beams of Gaussian profile and by the light scattered from the MOT.

Technical upgrades

We implemented several key upgrades of our setup compared to (*32*). First, we improved the detection noise, which was limiting the sensitivity in (*32*). The equivalent one-shot phase noise is now 71 mrad, corresponding to a rotation noise of 8 nrad s^{-1} $\mathrm{Hz}^{-1/2}$. Second, we implemented a real-time compensation of linear acceleration noise (*22*) and a servo loop to operate the interferometer at mid-fringe, i.e., in its linear range. These techniques are described in Materials and Methods. These upgrades result in a sensor that effectively operates without dead times, as statistically very few points sit on the top or bottom of a fringe, where the sensitivity vanishes.

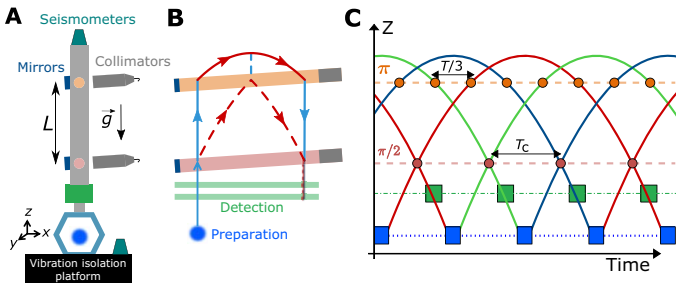

Fig. 1. Principle of the experiment. (**A**) Sketch of the experiment, where the atoms are laser cooled (blue cloud) and launched vertically, interrogated by two Raman beams (brought from the gray collimators and retroreflected on the blue mirrors), and detected on their way down (green box). The distance between the Raman beams is $L = \frac{3}{8} g T^2 \simeq 59$ cm. (**B**) Diagram of the atom interferometer in the (*xz*) plane (not to scale), with the blue and red lines labeling the $|\vec{0}\rangle$ and $\hbar\vec{k}_{\mathrm{eff}}$ momentum states, respectively. The dashed and plain lines show the two paths of the matter waves in the interferometer, which enclose an area of 11 cm^2. (**C**) Trajectories of the successively launched atom clouds in interleaved operation. Each interferometer has an interrogation time $2T = 801$ ms, and the cycle time is $T_c = 2T/3 = 267$ ms. The π/2 pulses are shared between the atom clouds entering and exiting the interferometer.

Rotation rate acquisition

Figure 2 shows a 32.5-hour acquisition of rotation rate measurements obtained between 23 and 25 September 2017. To obtain this series of data, we alternated the direction of the Raman wave vector ($\pm\vec{k}_{\mathrm{eff}}$) and computed the half-difference of two successive measurements to reject noninertial ($\vec{k}_{\mathrm{eff}}$-independent) effects, such as AC Stark shifts (see Materials and Methods and section S1 for the details of the sequence and section S2 for the raw data). In the following, we will analyze the sensitivity and the stability of the gyroscope from this acquisition.

Efficient averaging of vibration noise and record sensitivity

Vibration noise is the most important source of sensitivity degradation in cold-atom inertial sensors of large area [i.e., using long interrogation time and/or large momentum transfer techniques (*37*)]. Efficient vibration isolation at low frequencies (below a few hertz) is technically challenging [e.g., (*38*)] and not suited for field applications. We will show that interleaving allows us to reduce the impact of this key noise source.

In our sensor, the impact of inertial noise can be analyzed by considering a center of rotation located at the top Raman beam: Inertial noise then appears as linear acceleration noise of both mirrors plus rotation noise of the bottom mirror. The rotation noise translates into random variations of the angle $\theta_{\mathrm{B}}(t)$ of the Raman beam with respect to a geostationary reference frame (*34*) and affects the interferometer phase as $[\theta_{\mathrm{B}}(2T) - \theta_{\mathrm{B}}(0)]$ (Eq. 1). In joint measurements, in which π/2 pulses are shared (occurring at times 0 and $2T$), the contribution of rotation noise cancels out when averaging N successive measurements (see Materials and Methods for a derivation). Therefore, the gyroscope sensitivity should improve as τ^{-1}, where $\tau = 2NT$ is the integration time, instead of $\tau^{-1/2}$ in the case of uncorrelated measurements affected by rotation noise.

Besides averaging rotation noise, the interleaved operation of our sensor allows us to reduce the impact of residual linear acceleration noise: Because our sampling frequency ($1/T_c = 3.75$ Hz) is higher than the frequencies at which the acceleration noise mostly contributes (around 0.5 Hz; see table S1), correlations appear between successive

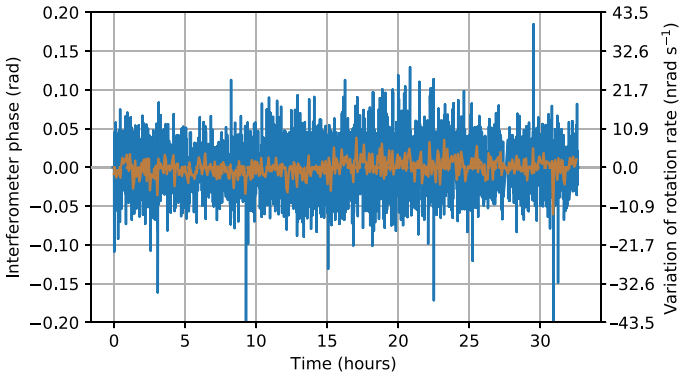

Fig. 2. Rotation rate measurement during 32.5 hours. In the blue (orange) trace, each data point is the average over segments of 26.7 s (267 s) of raw inertial phase measurements. The right axis translates inertial phase to rotation rate using the scale factor of the gyroscope to stationary Earth rotation (from Eq. 2).

measurements, yielding a scaling of the sensitivity that approaches τ^{-1} (rather than $\tau^{-1/2}$).

Figure 3 shows the Allan deviation of the gyroscope stability for an 11.3-hour portion of night data of Fig. 2. The improvement of the sensitivity as τ^{-1} for integration times up to $\simeq 7$ s is clear. The stability then gradually enters the $\tau^{-1/2}$ regime characteristic of uncorrelated white noise, corresponding to a sensitivity of 3×10^{-8} rad s^{-1} Hz$^{-1/2}$. This sensitivity, which improves by more than a factor of 3 on our previous result (*32*), establishes the new record for cold-atom gyroscopes. As a comparison, our short-term sensitivity competes favorably with that of the best fiber-optic gyroscopes (*31*). This sensitivity enables us to study several systematic effects affecting a cold-atom gyroscope for the first time in the range of low 10^{-9} rad s^{-1}.

Systematic effects and gyroscope long-term stability

A systematic shift specific to the interleaved interrogation originates from the light scattered from the MOT toward the atoms interrogated in the interferometer (*36*). The MOT scattered light is close to resonance and induces a loss of contrast and a differential light shift (AC Stark shift). The influence of induced light shifts is reduced by the spin-echo–like four-pulse sequence and by the use of $\vec{k}_{\mathrm{eff}}$ reversal: Alternating $\pm\hbar\vec{k}_{\mathrm{eff}}$ momentum transfers changes the sign of the inertial phase shift but not the one of the clock terms (e.g., differential light shift), which are rejected when taking the half-difference of two measurements (as done in Fig. 2). We measured the residual effect and showed that it corresponds to an instability below 7×10^{-11} rad s^{-1} (see Supplementary Materials). Although currently negligible, this effect is purely technical and could be resolved by having the MOT and the detection region out of view from the atom interferometer region in future designs.

The most important systematic effects in atom interferometers with separated Raman beams originate from relative wavefront mismatch coupled to deviations of the atom trajectories with respect to the ideal one (*27*, *39*). In our system, a relative angular misalignment $\vec{\delta}\theta$ between the top and bottom mirrors used to retroreflect the Raman beams (Fig. 1), coupled with an error of launch velocity $\vec{\delta}v$ (with respect to a velocity of $-\vec{g}T$ at the first Raman pulse) in the (y, z) plane, results in a phase shift

$$\begin{aligned}\Delta\Phi &= 2Tk_{\mathrm{eff}}(\delta v_y \delta\theta_y + \delta v_z \delta\theta_z) \\ &= 12\mathrm{mrad} \times \left(\frac{\delta v_{y,z}}{1\mathrm{mm.s}^{-1}}\right) \times \left(\frac{\delta\theta_{y,z}}{1\mu\mathrm{rad}}\right) \end{aligned} \quad (3)$$

We explain in Materials and Methods how we set the parallelism between the two Raman beams and the velocity of the atoms to approach the ideal trajectory to achieve an uncertainty on the residual systematic shift of 21 mrad (i.e., 4.6 nrad s^{-1}, from Eq. 2).

After this systematic analysis and the corresponding fine-tuning of the apparatus, we recorded the rotation rate acquisition displayed on Fig. 2. The stability of the gyroscope over the entire acquisition is analyzed in the Supplementary Materials (fig. S5) and is in agreement with that read from Fig. 3 for shorter integration times.

Dynamic rotation rate measurements

We use the unprecedented sampling rate and inertial sensitivity of our gyroscope to perform measurements of weak dynamic rotation rates. To this end, we modulate the orientation of the experiment around the y axis. This was performed by applying a force on the bottom plate linking the experimental frame to the vibration isolation platform via the voice-coil actuator controlling the tilt θ_x of the apparatus. We apply sinusoidal modulations of the form $\theta_x(t) = \theta_0 \sin(\omega t)$ with a period $2\pi/\omega$ and with an amplitude θ_0 of a few 10^{-7} rad. The resulting rotation rate is of the form $\vec{\Omega}(t) = \Omega_0 \cos(\omega t)\hat{u}_y$, with $\Omega_0 = \omega\theta_0$. The measurements are reported in Fig. 4 for modulation periods of 5 and 10 s. The respective modulation amplitudes are 2.3×10^{-7} and 3.4×10^{-7} rad. Figure 4 (A and B) shows the atomic phase extracted from the transition probability, $P(t)$, which follows the sinusoidal modulation. The total rotation signal from the atom interferometer is the sum of this atomic phase and the phase compensated in real time. A Fourier analysis of the total signal is shown in Fig. 4C. Within our frequency resolution, we find that the amplitude of the reconstructed rotation rate signal agrees with the expectation of Ω_0 with a relative precision of 5%. A more detailed analysis is presented in section S5. Our proof-of-principle experiment, performed in a so far unexplored range of time resolution and inertial sensitivity for a cold-atom sensor, demonstrates the impact of interleaved atom interferometry for dynamic measurements.

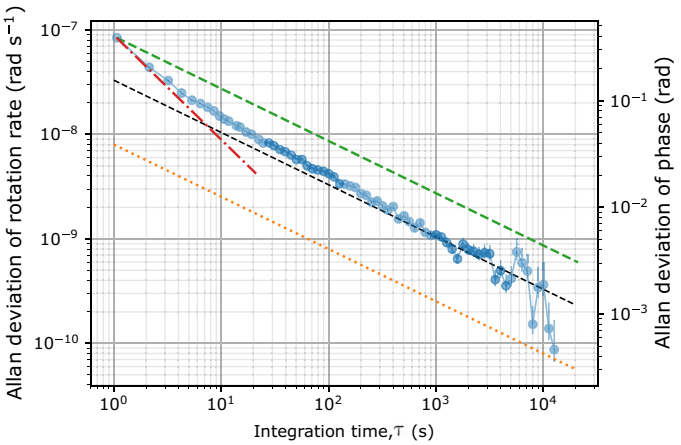

Fig. 3. Gyroscope sensitivity. Stability analysis of an 11.3-hour portion of rotation rate measurements of Fig. 2, between 1:22 a.m. and 12:47 p.m. on 24 September 2017. The error bars represent the 68% confidence intervals on the estimation of the Allan deviation. Dashed black line, 3.3×10^{-8} rad s^{-1} $\times$ $\tau^{-1/2}$; green dashed line, $\tau^{-1/2}$ scaling from the one-shot Allan deviation; red dotted-dashed line, τ^{-1} scaling from the one-shot Allan deviation; orange dotted line, detection noise limit corresponding to 8×10^{-9} rad s^{-1} $\times$ $\tau^{-1/2}$.

DISCUSSION

We have demonstrated the method of interleaving in a large-area atom interferometer, as a way to reach high sampling frequencies and high inertial sensitivities together. Interleaving enables us to efficiently average vibration noise (the largest noise source in cold-atom inertial sensors) and is thus a promising way of reaching the quantum projection noise limit, a necessary condition before increasing the atom flux or implementing schemes to approach the Heisenberg limit. As a result, we demonstrated record short-term sensitivities for a cold-atom gyroscope and could thus characterize systematic effects in a so far unexplored range. The rotation rate sensitivity and stability that we achieved competes with that of the best strategic-grade fiber-optic gyroscopes [long-term stability in the range of 5×10^{-10} rad s^{-1} (*31*)]. Our results thus pave the way for a change of technology in future high-precision inertial navigation systems.

In our setup, the maximum number of interleaved measurements is technically limited to three because of the arrangement of our detection

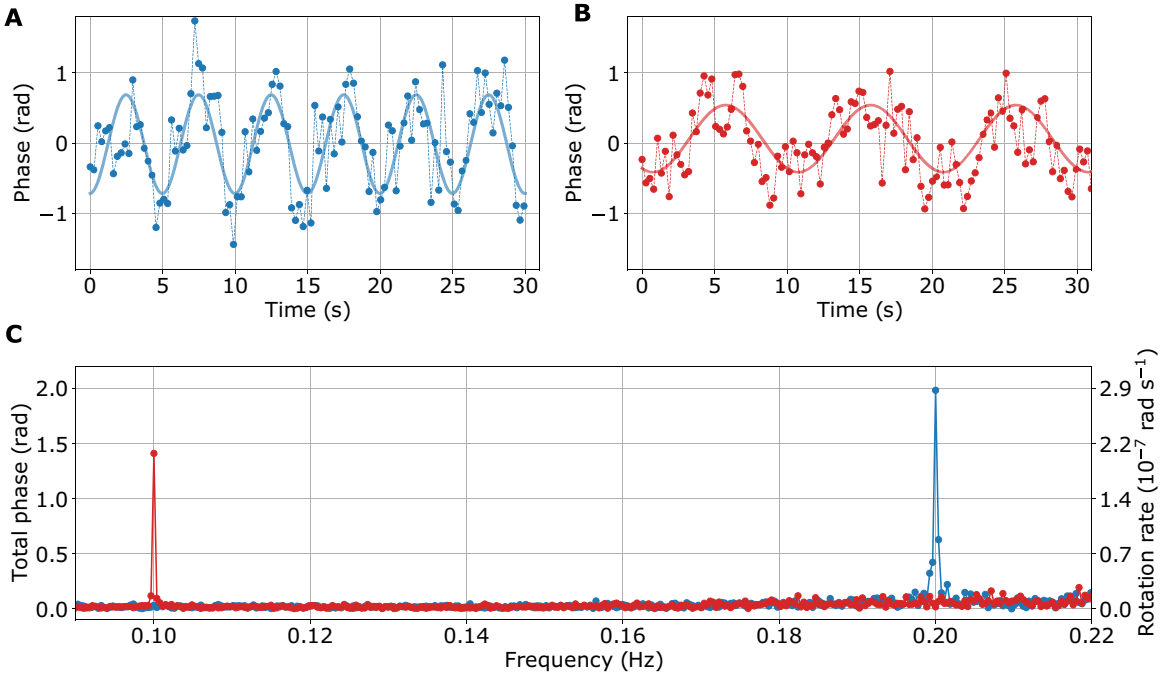

Fig. 4. Measurement of dynamic rotation rates. Atom interferometer phase deduced from the transition probability, for rotation rate modulations of 5-s period (**A**) and 10-s period (**B**). Plain line, sinusoidal fit to guide the eye. (**C**) Fourier analysis of the total rotation rate signal, with a frequency resolution of 0.37 mHz.

system with respect to the MOT region (see Materials and Methods). In a dedicated design, e.g., where the detection region would be out of view from the upcoming clouds, sampling frequencies of 20 Hz or higher could be reached. As an alternative, the use of atoms characterized by different transition wavelengths for the cooling/detection/atom interferometer would be beneficial to circumvent the effects associated with the scattered light from the source or the detected atoms. Our technique is thus well suited for ongoing developments of atom interferometers with alkaline-earth atoms (*40*).

Interleaving ties well with laser-cooling techniques, which are able to rapidly (in less than 100 ms) produce cold samples with more than 10^7 atoms. Laser cooling beyond optical molasses such as degenerate Raman sideband cooling appears as a suitable solution for an increased brightness without compromising the cycling frequency. Interleaving is, in principle, also compatible with the production of ultracold, collimated, atom sources (*16*), provided that they can be produced (*41*) or extracted at sufficiently high (several hertz) repetition rates.

The method of interleaved atom interferometry can be applied to different sensor architectures, such as multi-axis accelerometers (by alternating measurements along different axes at a high repetition rate), gavimeters, or gradiometers. For example, interleaving can be exploited to realize a gravimeter of both high accuracy and high sensitivity in a single instrument, potentially allowing to surpass superconducting gravimeters that currently feature record sensitivities but require regular calibrations. Hence, interleaving is representative of the flexibility of cold atoms for realizing versatile inertial sensors, as compared to architectures involving macroscopic masses and electromechanical systems. Regarding fundamental physics applications, achieving high sampling rates is a prerequisite for future studies on dark matter with atomic accelerometers (*24*), as well as for gravitational wave detection with atom interferometers (*25*, *26*). Interleaving is therefore a key concept for future applications of cold-atom inertial sensors.

MATERIALS AND METHODS

Details of the experiment

Cesium atoms loaded from a two-dimensional (2D) MOT were trapped and laser cooled in a 3D MOT. We launched the atoms vertically at a velocity of 5.0 m s^{-1} using moving molasses with a (3D) cloud temperature of 1.2 μK. After the MOT and before the interrogation, the atoms were prepared in the $|F = 4, m_F = 0\rangle$ state using a selection scheme based on the Stern-Gerlach effect (magnetic deflection of the atoms in $m_F \neq 0$ states). Light pulse interferometry is realized using two phase-locked Raman lasers that couple the cesium clock states (hyperfine splitting of 9.192 GHz). The Raman lasers have a wavelength close to the D_2 line (wavelength $\lambda \simeq 852$ nm) and are detuned by 470 MHz from the excited state to reduce incoherent scattering. The impact of residual relative Raman laser phase noise has been estimated to 50 mrad per shot of atom interferometer phase. The Raman lasers were sent to the atoms through two optical windows separated by $L = \frac{3}{8}gT^2 \simeq 59$ cm, with an interrogation time $2T = 801$ ms. We used Gaussian Raman beams with $1/e^2$ diameter equal to 40 mm and about 120 mW of total power. The interferometer output signal was determined by the probability of transition, P, from the $F = 4$ to the $F = 3$ state, which is read out via fluorescence detection of the two levels' populations after the atom interferometer light-pulse sequence. The probability of transition was modulated according to $P = P_0 + A \sin \Phi$, where $C = 2A$ is the interferometer contrast and Φ is the interferometer phase.

Our experiment uses retroreflected Raman beams, such as to form two pairs of Raman beams inducing two transitions: one in the $+\vec{k}_{\text{eff}}$ direction and another in the $-\vec{k}_{\text{eff}}$ direction. Selectivity of the $\pm\vec{k}_{\text{eff}}$ transitions is provided by tilting the Raman beams by an angle $\theta \simeq 3.80°$ with respect to the horizontal to introduce a Doppler shift ($\pm k_{\text{eff}} gT \sin \theta/2\pi \simeq \pm 611$ kHz at the first and last $\pi/2$ pulses), which is much larger than the width of the atom Doppler distribution (~ 40 kHz). To follow the resonance condition at each Raman pulse, we stepwise

changed the relative frequency between the two Raman lasers during the sequence, to match the values given by the underlying frequency chirp pattern (see details in fig. S2). To apply the frequency steps, we used a direct digital synthesizer driven by an FPGA (field-programmable gate array).

Real-time compensation of vibration noise and mid-fringe lock

We measured the vibrations of the setup with two broadband seismometers (model Trillium Compact 120 s from Nanometrics) located at the bottom and top of the experimental frame (see Fig. 1). From the measured signal, we estimated the interferometer phase shift due to vibrations and applied a corresponding phase jump to the relative phase of the Raman lasers 15 ms before the last pulse. This allows us to reduce the standard deviation (SD) of the interferometer phase from about 3.2 to 0.5 rad. To work within the linear regime where the sensitivity is maximal, we alternated measurements on both sides of a fringe and computed an error signal from two successive measurements of the transition probability. This error signal was integrated and used to servo-lock the interferometer at mid-fringe via a feedback on the Raman laser relative phase. More details are given in section S1.

Efficient averaging of vibration noise

Following Eq. 1 and assuming that the Raman lasers are oriented purely in the x direction, the four-light-pulse atom interferometer phase shift is given by (we neglect the duration of the Raman pulse)

$$\Phi = k_{\mathrm{eff}}[x_{\mathrm{b}}(0) - 2x_{\mathrm{t}}(T/2) + 2x_{\mathrm{t}}(3T/2) - x_{\mathrm{b}}(2T)] \quad (4)$$

with $x_{\mathrm{b,t}}(t)$ as the position of the bottom and top retro-mirrors with respect to the free-falling atom cloud. The phase shift can be rewritten as

$$\begin{aligned}\Phi &= k_{\mathrm{eff}}[x_{\mathrm{t}}(0) - 2x_{\mathrm{t}}(T/2) + 2x_{\mathrm{t}}(3T/2) - x_{\mathrm{t}}(2T)] \\ &\quad + k_{\mathrm{eff}}([x_{\mathrm{b}}(0) - x_{\mathrm{t}}(0)] - [x_{\mathrm{b}}(2T) - x_{\mathrm{t}}(2T)]) \\ &= \Phi_{\mathrm{t}}^{\mathrm{acc}} + k_{\mathrm{eff}}L(\theta_{\mathrm{b}}(0) - \theta_{\mathrm{b}}(2T)) \end{aligned} \quad (5)$$

with $L = \frac{3}{8}gT^2$ as the distance between the bottom and top mirrors and Φ_t^{acc} as the term associated to the linear acceleration of the top mirror. The second term represents pure rotation of the bottom mirror about the position of the top one. Recalling that $T_{\mathrm{c}} = 2T/3$ and writing as $\Phi_i = \Phi(iT_{\mathrm{c}})$ the atom interferometer phase at cycle i, the mean phase after N measurement reads

$$\begin{aligned}\bar{\Phi}_N = \frac{1}{N}\sum_{i=0}^{N-1}\Phi_i = \frac{1}{N}\sum_{i=0}^{N-1}&(k_{\mathrm{eff}}L[\theta_{\mathrm{b}}(iT_{\mathrm{c}}) - \theta_{\mathrm{b}}((i+3)T_{\mathrm{c}})] \\ &+ \delta\tilde{\phi}_i)\end{aligned} \quad (6)$$

The term $\delta\tilde{\phi}_i$ encompasses contributions of detection noise, uncompensated linear acceleration noise, and laser phase noise. When expanding the sum in Eq. 6, most of the θ_{b} terms mutually cancel such that the mean phase reads

$$\bar{\Phi}_N = k_{\mathrm{eff}}L\frac{\theta_{\mathrm{b}}(0) - \theta_{\mathrm{b}}((N+2)T_{\mathrm{c}})}{N} + \frac{1}{N}\sum_{i=0}^{N-1}\delta\tilde{\phi}_i \quad (7)$$

This equation shows that the random rotation noise averages as N^{-1} (first term). The second term represents the uncorrelated noise contributions of SD $\sigma_{\delta\phi}$. Their sum equals $\sqrt{N} \times \sigma_{\delta\phi}$, which corresponds to a scaling of the phase sensitivity as $N^{-1/2}$.

Besides rotation noise, uncompensated linear accelerations in the frequency range [0.1 – 1] Hz contribute, to a large part, to the interferometer phase noise (see section S3 for details). This contribution, estimated to typically about 500 mrad per shot, dominates the noise budget and may prevent from observing a clear τ^{-1} scaling of the gyroscope sensitivity. Interleaving, however, allows us to oversample these fluctuations, thus introducing correlations between successive measurements, which also contribute to the τ^{-1} dependence of the instrument sensitivity.

Alignment of the two Raman beams and atom trajectory

We set the parallelism between the top and bottom Raman beams by means of a two-axis piezo-motorized mirror mount with a resolution of 0.7 μrad. By optimizing the contrast of the interferometer, we approached the parallelism with an uncertainty of about 3 μrad, which is required for the matter waves to recombine at the output of the interferometer. For the fine adjustment, we measured the dependence of the phase shift of Eq. 3, $\Delta\Phi = 2Tk_{\mathrm{eff}}(\delta v_y\delta\theta_y + \delta v_z\delta\theta_z)$, on $\delta\theta_{y,z}$ and $\delta v_{y,z}$ (as defined in the main text). To this end, we set the atom trajectory in the (y, z) directions by varying the tilt of the experiment (y direction) and the launch velocity during the moving molasses phase (z direction). In the z direction, we could zero the systematic effect with an uncertainty of 5 mrad. This amounts to set the velocity of the atoms at the first Raman pulse to the ideal velocity ($v_z = gT$) with an uncertainty of 0.6 mm s^{-1} and to set the parallelism between two mirrors in the z direction with an uncertainty of 0.7 μrad.

The minimization of the systematic shift in the y direction was technically more difficult to achieve than in the z direction: recording the dependence of the phase shift on $\delta\theta_y$ for various velocities required to tilt the entire apparatus by several mrad to vary δv_y by several mm s^{-1}. This procedure required to manually move masses on the base plate of the experiment sitting on a floating vibration isolation platform, which introduced instabilities. We managed to set the y velocity close to the ideal velocity ($v_y = 0$) with an uncertainty of 1.8 mm s^{-1}. The residual shift corresponds to a phase variation of 21 mrad per microradian of $\delta\theta_y$ variation.

Limitation to the number of interleaved interferometers

When trying five interleaved cycles, we observed a marked loss of contrast of the interferometer. The reason is that when a (descending) atom cloud at the output of the interferometer enters the detection region, a part of the light scattered by the atoms is directed toward the (ascending) cloud, which optically pumps atoms to unwanted magnetic states and heats them before they enter the interferometer.

SUPPLEMENTARY MATERIALS

Supplementary material for this article is available at http://advances.sciencemag.org/cgi/content/full/4/12/eaau7948/DC1

Section S1. Real-time compensation of vibration noise, mid-fringe lock, and details of the sequence
Section S2. Raw data
Section S3. Analysis of vibration noise
Section S4. Stability analysis
Section S5. Analysis of the dynamic rotation rate measurements
Section S6. Systematic effect from the scattered light
Fig. S1. Histogram of the vibration phase and of the interferometer phase with real-time compensation of vibration.
Fig. S2. Details of the sequence.
Fig. S3. Raw interferometer measurements corresponding to the data presented in Fig. 2.

Fig. S4. Analysis of vibration noise.
Fig. S5. Stability analysis of the gyroscope.
Table S1. Contribution of the linear acceleration noise to the interferometer phase noise by frequency band.
Reference (*42*)

REFERENCES AND NOTES

1. D. Sheng, S. Li, N. Dural, M. V. Romalis, Subfemtotesla scalar atomic magnetometry using multipass cells. *Phys. Rev. Lett.* **110**, 160802 (2013).
2. I. Gross, W. Akhtar, V. Garcia, L. J. Martínez, S. Chouaieb, K. Garcia, C. Carrétéro, A. Barthélémy, P. Appel, P. Maletinsky, J.-V. Kim, J. Y. Chauleau, N. Jaouen, M. Viret, M. Bibes, S. Fusil, V. Jacques, Real-space imaging of non-collinear antiferromagnetic order with a single-spin magnetometer. *Nature* **549**, 252–256 (2017).
3. R. Jiménez-Martínez, J. Kołodyński, C. Troullinou, V. G. Lucivero, J. Kong, M. W. Mitchell, Signal tracking beyond the time resolution of an atomic sensor by Kalman filtering. *Phys. Rev. Lett.* **120**, 040503 (2018).
4. M. Takamoto, F.-L. Hong, R. Higashi, H. Katori, An optical lattice clock. *Nature* **435**, 321–324 (2005).
5. R. Le Targat, L. Lorini, Y. Le Coq, M. Zawada, J. Guéna, M. Abgrall, M. Gurov, P. Rosenbusch, D. G. Rovera, B. Nagórny, R. Gartman, P. G. Westergaard, M. E. Tobar, M. Lours, G. Santarelli, A. Clairon, S. Bize, P. Laurent, P. Lemonde, J. Lodewyck, Experimental realization of an optical second with strontium lattice clocks. *Nat. Commun.* **4**, 2109 (2013).
6. M. G. Tarallo, T. Mazzoni, N. Poli, D. V. Sutyrin, X. Zhang, G. M. Tino, Test of einstein equivalence principle for 0-spin and half-integer-spin atoms: Search for spin-gravity coupling effects. *Phys. Rev. Lett.* **113**, 023005 (2014).
7. T. Bagci, A. Simonsen, S. Schmid, L. G. Villanueva, E. Zeuthen, J. Appel, J. M. Taylor, A. Sørensen, K. Usami, A. Schliesser, E. S. Polzik, Optical detection of radio waves through a nanomechanical transducer. *Nature* **507**, 81–85 (2014).
8. A. Facon, E.-K. Dietsche, D. Grosso, S. Haroche, J.-M. Raimond, M. Brune, S. Gleyzes, A sensitive electrometer based on a Rydberg atom in a Schrödinger-cat state. *Nature* **535**, 262–265 (2016).
9. Ch. J. Bordé, Atomic interferometry with internal state labelling. *Phys. Lett. A* **140**, 10–12 (1989).
10. M. Kasevich, S. Chu, Atomic interferometry using stimulated Raman transitions. *Phys. Rev. Lett.* **67**, 181–184 (1991).
11. F. Riehle, Th. Kisters, A. Witte, J. Helmcke, Ch. J. Bordé, Optical Ramsey spectroscopy in a rotating frame: Sagnac effect in a matter-wave interferometer. *Phys. Rev. Lett.* **67**, 177–180 (1991).
12. R. Bouchendira, P. Cladé, S. Guellati-Khélifa, F. Nez, F. Biraben, New determination of the fine structure constant and test of the quantum electrodynamics. *Phys. Rev. Lett.* **106**, 080801 (2011).
13. S. Lepoutre, A. Gauguet, G. Trénec, M. Büchner, J. Vigué, He-Mckellar-Wilkens topological phase in atom interferometry. *Phys. Rev. Lett.* **109**, 120404 (2012).
14. L. Zhou, S. Long, B. Tang, X. Chen, F. Gao, W. Peng, W. Duan, J. Zhong, Z. Xiong, J. Wang, Y. Zhang, M. Zhan, Test of equivalence principle at 10^{-8} level by a dual-species double-diffraction Raman atom interferometer. *Phys. Rev. Lett.* **115**, 013004 (2015).
15. M. Jaffe, P. Haslinger, V. Xu, P. Hamilton, A. Upadhye, B. Elder, J. Khoury, H. Müller, Testing sub-gravitational forces on atoms from a miniature in-vacuum source mass. *Nat. Phys.* **13**, 938–942 (2017).
16. P. Asenbaum, C. Overstreet, T. Kovachy, D. D. Brown, J. M. Hogan, M. A. Kasevich, Phase shift in an atom interferometer due to spacetime curvature across its wave function. *Phys. Rev. Lett.* **118**, 183602 (2017).
17. G. Rosi, F. Sorrentino, L. Cacciapuoti, M. Prevedelli, G. M. Tino, Precision measurement of the Newtonian gravitational constant using cold atoms. *Nature* **510**, 518–521 (2014).
18. A. Peters, K. Y. Chung, S. Chu, High-precision gravity measurements using atom interferometry. *Metrologia* **38**, 25 (2001).
19. C. Freier, M. Hauth, V. Schkolnik, B. Leykauf, M. Schilling, H. Wziontek, H.-G. Scherneck, J. Müller, A. Peters, Mobile quantum gravity sensor with unprecedented stability. *J. Phys. Conf. Ser.* **723**, 012050 (2016).
20. Y. Bidel, N. Zahzam, C. Blanchard, A. Bonnin, M. Cadoret, A. Bresson, D. Rouxel, M. F. Lequentrec-Lalancette, Absolute marine gravimetry with matter-wave interferometry. *Nat. Commun.* **9**, 627 (2018).
21. R. Karcher, A. Imanaliev, S. Merlet, F. Pereira Dos Santos, Improving the accuracy of atom interferometers with ultracold sources. *New J. Phys.* **20**, 113041 (2018).
22. J. Lautier, L. Volodimer, T. Hardin, S. Merlet, M. Lours, F. Pereira Dos Santos, A. Landragin, Hybridizing matter-wave and classical accelerometers. *Appl. Phys. Lett.* **105**, 144102 (2014).
23. C. Jekeli, Navigation error analysis of atom interferometer inertial sensor. *Navigation* **52**, 1–14 (2005).
24. P. W. Graham, D. E. Kaplan, J. Mardon, S. Rajendran, W. A. Terrano, Dark matter direct detection with accelerometers. *Phys. Rev. D* **93**, 075029 (2016).
25. W. Chaibi, R. Geiger, B. Canuel, A. Bertoldi, A. Landragin, P. Bouyer, Low frequency gravitational wave detection with ground-based atom interferometer arrays. *Phys. Rev. D* **93**, 021101 (2016).
26. P. W. Graham, J. M. Hogan, M. A. Kasevich, S. Rajendran, Resonant mode for gravitational wave detectors based on atom interferometry. *Phys. Rev. D* **94**, 104022 (2016).
27. A. Gauguet, B. Canuel, T. Lévèque, W. Chaibi, A. Landragin, Characterization and limits of a cold-atom Sagnac interferometer. *Phys. Rev. A* **80**, 063604 (2009).
28. P. Berg, S. Abend, G. Tackmann, C. Schubert, E. Giese, W. P. Schleich, F. A. Narducci, W. Ertmer, E. M. Rasel, Composite-light-pulse technique for high-precision atom interferometry. *Phys. Rev. Lett.* **114**, 063002 (2015).
29. T. L. Gustavson, A. Landragin, M. A. Kasevich, Rotation sensing with a dual atom-interferometer Sagnac gyroscope. *Class. Quantum Gravity* **17**, 2385 (2000).
30. D. S. Durfee, Y. K. Shaham, M. A. Kasevich, Long-term stability of an area-reversible atom-interferometer Sagnac gyroscope. *Phys. Rev. Lett.* **97**, 240801 (2006).
31. H. C. Lefèvre, The fiber-optic gyroscope, a century after Sagnac's experiment: The ultimate rotation-sensing technology? *C. R. Phys.* **15**, 851–858 (2014); for recent performances, see, e.g., iXblue ultimate-performance Fiber-Optic Gyroscope (FOG) (http://web.ixblue.com/cn/aw6ym/fiberoptic-gyroscope).
32. I. Dutta, D. Savoie, B. Fang, B. Venon, C. L. Garrido Alzar, R. Geiger, A. Landragin, Continuous cold-atom inertial sensor with 1 nrad / sec rotation stability. *Phys. Rev. Lett.* **116**, 183003 (2016).
33. B. Canuel, F. Leduc, D. Holleville, A. Gauguet, J. Fils, A. Virdis, A. Clairon, N. Dimarcq, Ch. J. Bordé, A. Landragin, P. Bouyer, Six-axis inertial sensor using cold-atom interferometry. *Phys. Rev. Lett.* **97**, 010402 (2006).
34. J. K. Stockton, K. Takase, M. A. Kasevich, Absolute geodetic rotation measurement using atom interferometry. *Phys. Rev. Lett.* **107**, 133001 (2011).
35. R. Legere, K. Gibble, Quantum scattering in a juggling atomic fountain. *Phys. Rev. Lett.* **81**, 5780–5783 (1998).
36. M. Meunier, I. Dutta, R. Geiger, C. Guerlin, C. L. Garrido Alzar, A. Landragin, Stability enhancement by joint phase measurements in a single cold atomic fountain. *Phys. Rev. A* **90**, 063633 (2014).
37. S. M. Dickerson, J. M. Hogan, A. Sugarbaker, D. M. S. Johnson, M. A. Kasevich, Multiaxis inertial sensing with long-time point source atom interferometry. *Phys. Rev. Lett.* **111**, 083001 (2013).
38. J. M. Hensley, A. Peters, S. Chu, Active low frequency vertical vibration isolation. *Rev. Sci. Instrum.* **70**, 2735–2741 (1999).
39. G. Tackmann, P. Berg, C. Schubert, S. Abend, M. Gilowski, W. Ertmer, E. M. Rasel, Self-alignment of a compact large-area atomic Sagnac interferometer. *New J. Phys.* **14**, 015002 (2012).
40. L. Hu, N. Poli, L. Salvi, G. M. Tino, Atom interferometry with the Sr optical clock transition. *Phys. Rev. Lett.* **119**, 263601 (2017).
41. J. Rudolph, W. Herr, C. Grzeschik, T. Sternke, A. Grote, M. Popp, D. Becker, H. Müntinga, H. Ahlers, A. Peters, C. Lämmerzahl, K. Sengstock, N. Gaaloul, W. Ertmer, E. M. Rasel, A high-flux BEC source for mobile atom interferometers. *New J. Phys.* **17**, 065001 (2015).
42. P. Cheinet, B. Canuel, F. Pereira Dos Santos, A. Gauguet, F. Yver-Leduc, A. Landragin, Measurement of the sensitivity function in a time-domain atomic interferometer. *IEEE Trans. Instrum. Meas.* **57**, 1141–1148 (2008).

Acknowledgments: We thank F. Pereira Dos Santos for careful reading of the manuscript. **Funding:** We acknowledge the financial support from Ville de Paris (project HSENS-MWGRAV), FIRST-TF (ANR-10-LABX-48-01), Centre National d'Etudes Saptiales (CNES), Sorbonne Universités (project SU-16-R-EMR-30, LORINVACC), and Action Spécifique du CNRS Gravitation, Références, Astronomie et Métrologie (GRAM). B.F. was funded by Conseil Scientifique de l'Observatoire de Paris, D.S. by Direction Générale de l'Armement, and M.A. by the EDPIF doctoral school. **Author contributions:** D.S., M.A., and B.F. performed the experiments, and L.A.S. contributed to the dynamic rotation rate measurements. D.S., R.G., and M.A. analyzed the data. R.G. and D.S. wrote the manuscript. A.L. conceived the experiment. R.G. and A.L. supervised the research. All authors discussed the manuscript. **Competing interests:** The authors declare that they have no competing interests. **Data and materials availability:** All data needed to evaluate the conclusions in the paper are present in the paper and/or the Supplementary Materials. Additional data related to this paper may be requested from the authors.

Submitted 17 July 2018
Accepted 19 November 2018
Published 21 December 2018
10.1126/sciadv.aau7948

Citation: D. Savoie, M. Altorio, B. Fang, L. A. Sidorenkov, R. Geiger, A. Landragin, Interleaved atom interferometry for high-sensitivity inertial measurements. *Sci. Adv.* **4**, eaau7948 (2018).

Bibliography

[1] Rym Bouchendira et al. “New Determination of the Fine Structure Constant and Test of the Quantum Electrodynamics”. In: *Phys. Rev. Lett.* 106 (8 Feb. 2011), p. 080801. DOI: 10.1103/PhysRevLett.106.080801. URL: https://link.aps.org/doi/10.1103/PhysRevLett.106.080801.

[2] Richard H. Parker et al. “Measurement of the fine-structure constant as a test of the Standard Model”. In: *Science* 360.6385 (2018), pp. 191–195. ISSN: 0036-8075. DOI: 10.1126/science.aap7706. eprint: https://science.sciencemag.org/content/360/6385/191.full.pdf. URL: https://science.sciencemag.org/content/360/6385/191.

[3] Pierre Cladé et al. “State of the art in the determination of the fine-structure constant and the ratio h/mu”. In: *Comptes Rendus Physique* 20.1 (2019). The new International System of Units / Le nouveau Système international d’unités, pp. 77–91. ISSN: 1631-0705. DOI: https://doi.org/10.1016/j.crhy.2018.12.003. URL: http://www.sciencedirect.com/science/article/pii/S1631070518301701.

[4] B. Canuel et al. “Six-Axis Inertial Sensor Using Cold-Atom Interferometry”. In: *Phys. Rev. Lett.* 97 (1 July 2006), p. 010402. DOI: 10.1103/PhysRevLett.97.010402. URL: https://link.aps.org/doi/10.1103/PhysRevLett.97.010402.

[5] D. S. Durfee, Y. K. Shaham, and M. A. Kasevich. “Long-Term Stability of an Area-Reversible Atom-Interferometer Sagnac Gyroscope”. In: *Phys. Rev. Lett.* 97 (24 Dec. 2006), p. 240801. DOI: 10.1103/PhysRevLett.97.240801. URL: https://link.aps.org/doi/10.1103/PhysRevLett.97.240801.

[6] A. Gauguet et al. “Characterization and limits of a cold-atom Sagnac interferometer”. In: *Physical Review A* 80.6 (Dec. 2009). DOI: 10.1103/physreva.80.063604.

[7] Pierrick Cheiney et al. “Navigation-Compatible Hybrid Quantum Accelerometer Using a Kalman Filter”. In: *Phys. Rev. Applied* 10 (3 Sept. 2018), p. 034030. DOI:

10.1103/PhysRevApplied.10.034030. URL: https://link.aps.org/doi/10.1103/PhysRevApplied.10.034030.

[8] P Gillot et al. "Stability comparison of two absolute gravimeters: optical versus atomic interferometers". In: *Metrologia* 51.5 (June 2014), pp. L15–L17. DOI: 10.1088/0026-1394/51/5/l15. URL: https://doi.org/10.1088%2F0026-1394%2F51%2F5%2Fl15.

[9] C Freier et al. "Mobile quantum gravity sensor with unprecedented stability". In: *Journal of Physics: Conference Series* 723.1 (2016), p. 012050. URL: http://stacks.iop.org/1742-6596/723/i=1/a=012050.

[10] A. Bonnin et al. "Simultaneous dual-species matter-wave accelerometer". In: *Phys. Rev. A* 88 (4 Oct. 2013), p. 043615. DOI: 10.1103/PhysRevA.88.043615. URL: https://link.aps.org/doi/10.1103/PhysRevA.88.043615.

[11] M. G. Tarallo et al. "Test of Einstein Equivalence Principle for 0-Spin and Half-Integer-Spin Atoms: Search for Spin-Gravity Coupling Effects". In: *Phys. Rev. Lett.* 113 (2 July 2014), p. 023005. DOI: 10.1103/PhysRevLett.113.023005. URL: https://link.aps.org/doi/10.1103/PhysRevLett.113.023005.

[12] Xiao-Chun Duan et al. "Test of the Universality of Free Fall with Atoms in Different Spin Orientations". In: *Phys. Rev. Lett.* 117 (2 July 2016), p. 023001. DOI: 10.1103/PhysRevLett.117.023001. URL: https://link.aps.org/doi/10.1103/PhysRevLett.117.023001.

[13] Brynle Barrett et al. "Dual matter-wave inertial sensors in weightlessness". In: *Nature Communications* 7 (Dec. 2016), p. 13786. DOI: 10.1038/ncomms13786. URL: https://doi.org/10.1038%2Fncomms13786.

[14] Nan Yu and Massimo Tinto. "Gravitational wave detection with single-laser atom interferometers". In: *General Relativity and Gravitation* 43.7 (July 2011), pp. 1943–1952. ISSN: 1572-9532. DOI: 10.1007/s10714-010-1055-8. URL: https://doi.org/10.1007/s10714-010-1055-8.

[15] Peter W. Graham et al. "Resonant mode for gravitational wave detectors based on atom interferometry". In: *Phys. Rev. D* 94 (10 Nov. 2016), p. 104022. DOI: 10.1103/PhysRevD.94.104022. URL: https://link.aps.org/doi/10.1103/PhysRevD.94.104022.

[16] W. Chaibi et al. "Low frequency gravitational wave detection with ground-based atom interferometer arrays". In: *Phys. Rev. D* 93 (2 Jan. 2016), p. 021101. DOI: 10.1103/PhysRevD.93.021101. URL: https://link.aps.org/doi/10.1103/PhysRevD.93.021101.

[17] Dong-Feng Gao, Jin Wang, and Ming-Sheng Zhan. "Atomic Interferometric Gravitational-Wave Space Observatory (AIGSO)". In: *Communications in Theoretical Physics* 69.1 (Jan. 2018), p. 37. DOI: 10.1088/0253-6102/69/1/37. URL: https://doi.org/10.1088%2F0253-6102%2F69%2F1%2F37.

[18] Ming-Sheng Zhan et al. "ZAIGA: Zhaoshan long-baseline atom interferometer gravitation antenna". In: *International Journal of Modern Physics D* 0.0 (0), p. 1940005. DOI: 10.1142/S0218271819400054. eprint: https://doi.org/10.1142/S0218271819400054. URL: https://doi.org/10.1142/S0218271819400054.

[19] G. Sagnac. "Effet tourbillonnaire optique. La circulation de l'éther lumineux dans un interférographe tournant". In: *Journal de Physique Théorique et Appliquée* 4.1 (1914), pp. 177–195. ISSN: 0368-3893. DOI: 10.1051/jphystap:019140040017700. URL: http://www.edpsciences.org/10.1051/jphystap:019140040017700 (visited on 08/08/2015).

[20] F. Riehle et al. "Optical Ramsey spectroscopy in a rotating frame: Sagnac effect in a matter-wave interferometer". In: *Phys. Rev. Lett.* 67 (2 July 1991), pp. 177–180. DOI: 10.1103/PhysRevLett.67.177. URL: https://link.aps.org/doi/10.1103/PhysRevLett.67.177.

[21] T L Gustavson, A Landragin, and M A Kasevich. "Rotation sensing with a dual atom-interferometer Sagnac gyroscope". In: *Classical and Quantum Gravity* 17.12 (2000), p. 2385. URL: http://stacks.iop.org/0264-9381/17/i=12/a=311.

[22] P. Berg et al. "Composite-Light-Pulse Technique for High-Precision Atom Interferometry". In: *Phys. Rev. Lett.* 114.6 (Feb. 2015). DOI: 10.1103/physrevlett.114.063002.

[23] Yun-Jhih Chen et al. "Single-Source Multiaxis Cold-Atom Interferometer in a Centimeter-Scale Cell". In: *Phys. Rev. Applied* 12 (1 July 2019), p. 014019. DOI: 10.1103/PhysRevApplied.12.014019. URL: https://link.aps.org/doi/10.1103/PhysRevApplied.12.014019.

[24] Lin Zhang et al. "A Novel Monitoring Navigation Method for Cold Atom Interference Gyroscope". In: *Sensors* 19.2 (Jan. 2019), p. 222. ISSN: 1424-8220. DOI: 10.3390/s19020222. URL: http://dx.doi.org/10.3390/s19020222.

[25] *iXblue ultimate-performance Fiber-Optic Gyroscope (FOG)*. http://web.ixblue.com/cn/aw6ym/fiberoptic-gyroscope.

[26] K. U. Schreiber et al. "How to Detect the Chandler and the Annual Wobble of the Earth with a Large Ring Laser Gyroscope". In: *Phys. Rev. Lett.* 107 (17 Oct. 2011), p. 173904. DOI: 10.1103/PhysRevLett.107.173904. URL: https://link.aps.org/doi/10.1103/PhysRevLett.107.173904.

[27] Thomas Lévèque. "Development of a high sensitivity cold atom gyroscope based on a folded geometry". Theses. Université Pierre et Marie Curie - Paris VI, Sept. 2010. URL: https://tel.archives-ouvertes.fr/tel-00532789.

[28] Matthieu Meunier. "Study of a large area matter wave gyroscope". Theses. Université Pierre et Marie Curie - Paris VI, Dec. 2013. URL: https://tel.archives-ouvertes.fr/tel-01053196.

[29] M. Meunier et al. "Stability enhancement by joint phase measurements in a single cold atomic fountain". In: *Phys. Rev. A* 90.6 (Dec. 2014). DOI: 10.1103/physreva.90.063633.

[30] I. Dutta et al. "Continuous Cold-Atom Inertial Sensor with1 nrad/secRotation Stability". In: *Phys. Rev. Lett.* 116.18 (May 2016). DOI: 10.1103/physrevlett.116.183003.

[31] Indranil Dutta. "Stability improvement of a sagnac cold atom interferometer : towards continuous operation". Theses. Université Pierre et Marie Curie - Paris VI, Nov. 2015. URL: https://tel.archives-ouvertes.fr/tel-01332562.

[32] Denis Savoie. "Continuous and interleaved operation of a cold atom gyroscop and improvement of its stability". Theses. Université Pierre et Marie Curie - Paris VI, Nov. 2017. URL: https://tel.archives-ouvertes.fr/tel-01919499.

[33] D. Savoie et al. "Interleaved atom interferometry for high-sensitivity inertial measurements". In: *Science Advances* 4.12 (2018). DOI: 10.1126/sciadv.aau7948. eprint: https://advances.sciencemag.org/content/4/12/eaau7948.full.pdf. URL: https://advances.sciencemag.org/content/4/12/eaau7948.

[34] Ch.J. Bordé. "Atomic interferometry with internal state labelling". In: *Physics Letters A* 140.1 (1989), pp. 10–12. ISSN: 0375-9601. DOI: https://doi.org/10.1016/0375-9601(89)90537-9. URL: http://www.sciencedirect.com/science/article/pii/0375960189905379.

[35] Mark Kasevich and Steven Chu. "Atomic interferometry using stimulated Raman transitions". In: *Phys. Rev. Lett.* 67 (2 July 1991), pp. 181–184. DOI: 10.1103/PhysRevLett.67.181. URL: https://link.aps.org/doi/10.1103/PhysRevLett.67.181.

[36] Kathryn Moler et al. "Theoretical analysis of velocity-selective Raman transitions". In: *Phys. Rev. A* 45 (1 Jan. 1992), pp. 342–348. DOI: 10.1103/PhysRevA.45.342. URL: https://link.aps.org/doi/10.1103/PhysRevA.45.342.

[37] David S. Weiss, Brenton C. Young, and Steven Chu. "Precision measurement of the photon recoil of an atom using atomic interferometry". In: *Phys. Rev. Lett.* 70 (18 May 1993), pp. 2706–2709. DOI: 10.1103/PhysRevLett.70.2706. URL: https://link.aps.org/doi/10.1103/PhysRevLett.70.2706.

[38] Hervé C. Lefèvre. "The fiber-optic gyroscope, a century after Sagnac's experiment: The ultimate rotation-sensing technology?" In: *Comptes Rendus Physique* 15.10 (2014). The Sagnac effect: 100 years later / L'effet Sagnac : 100 ans après, pp. 851–858. ISSN: 1631-0705. DOI: https://doi.org/10.1016/j.crhy.2014.10.007. URL: http://www.sciencedirect.com/science/article/pii/S1631070514001443.

[39] F. Hasselbach and M. Nicklaus. "An electron optical sagnac experiment". In: *Physica B+C* 151.1 (1988), pp. 230–234. ISSN: 0378-4363. DOI: 10.1016/0378-4363(88)90171-4. URL: http://www.sciencedirect.com/science/article/pii/0378436388901714.

[40] Franz Hasselbach and Marc Nicklaus. "Sagnac experiment with electrons: Observation of the rotational phase shift of electron waves in vacuum". In: *Phys. Rev. A* 48 (1 July 1993), pp. 143–151. DOI: 10.1103/PhysRevA.48.143. URL: https://link.aps.org/doi/10.1103/PhysRevA.48.143.

[41] W. W. Chow et al. "The ring laser gyro". In: *Rev. Mod. Phys.* 57 (1 Jan. 1985), pp. 61–104. DOI: 10.1103/RevModPhys.57.61. URL: https://link.aps.org/doi/10.1103/RevModPhys.57.61.

[42] Benjamin Canuel. "Study of a cold atom rate-gyroscope". Theses. Université Paris Sud - Paris XI, Mar. 2007. URL: https://tel.archives-ouvertes.fr/tel-00193288.

[43] J. Fils et al. "Influence of optical aberrations in an atomic gyroscope". In: *The European Physical Journal D - Atomic, Molecular, Optical and Plasma Physics*

36.3 (Dec. 2005), pp. 257–260. ISSN: 1434-6079. DOI: 10.1140/epjd/e2005-00255-9. URL: https://doi.org/10.1140/epjd/e2005-00255-9.

[44] P. Cheinet et al. "Measurement of the Sensitivity Function in a Time-Domain Atomic Interferometer". In: *IEEE Transactions on Instrumentation and Measurement* 57.6 (June 2008), pp. 1141–1148. DOI: 10.1109/TIM.2007.915148.

[45] Bess Fang et al. "Improving the phase response of an atom interferometer by means of temporal pulse shaping". In: *New Journal of Physics* 20.2 (Feb. 2018), p. 023020. DOI: 10.1088/1367-2630/aaa37c. URL: https://doi.org/10.1088%2F1367-2630%2Faaa37c.

[46] X. Baillard et al. "Interference-filter-stabilized external-cavity diode lasers". In: *Optics Communications* 266.2 (2006), pp. 609–613. ISSN: 0030-4018. DOI: doi.org/10.1016/j.optcom.2006.05.011. URL: http://www.sciencedirect.com/science/article/pii/S0030401806004561.

[47] N. Mielec et al. "Atom interferometry with top-hat laser beams". In: *Applied Physics Letters* 113.16 (2018), p. 161108. DOI: 10.1063/1.5051663. eprint: https://doi.org/10.1063/1.5051663. URL: https://doi.org/10.1063/1.5051663.

[48] G. Santarelli et al. "Frequency stability degradation of an oscillator slaved to a periodically interrogated atomic resonator". In: *IEEE Transactions on Ultrasonics, Ferroelectrics, and Frequency Control* 45.4 (July 1998), pp. 887–894. ISSN: 0885-3010. DOI: 10.1109/58.710548.

[49] Audrey Quessada et al. "The Dick effect for an optical frequency standard". In: *Journal of Optics B: Quantum and Semiclassical Optics* 5.2 (Apr. 2003), S150–S154. DOI: 10.1088/1464-4266/5/2/373. URL: https://doi.org/10.1088%2F1464-4266%2F5%2F2%2F373.

[50] CHRISTOPHER JEKELI. "Navigation Error Analysis of Atom Interferometer Inertial Sensor". In: *Navigation* 52.1 (2005), pp. 1–14. DOI: 10.1002/j.2161-4296.2005.tb01726.x. eprint: https://onlinelibrary.wiley.com/doi/pdf/10.1002/j.2161-4296.2005.tb01726.x. URL: https://onlinelibrary.wiley.com/doi/abs/10.1002/j.2161-4296.2005.tb01726.x.

[51] J. Lautier et al. "Hybridizing matter-wave and classical accelerometers". In: *Applied Physics Letters* 105.14 (Oct. 2014), p. 144102. DOI: 10.1063/1.4897358.

[52] Ken Takase. "Precision rotation rate measurements with a mobile atom interferometer". PhD thesis. Stanford University, Jan. 2008.

[53] G Tackmann et al. "Self-alignment of a compact large-area atomic Sagnac interferometer". In: *New Journal of Physics* 14.1 (Jan. 2012), p. 015002. DOI: 10.1088/1367-2630/14/1/015002. URL: https://doi.org/10.1088%2F1367-2630%2F14%2F1%2F015002.

[54] B. Canuel et al. "Exploring gravity with the MIGA large scale atom interferometer". In: *Scientific Reports* 8.1 (Sept. 2018). DOI: 10.1038/s41598-018-32165-z. URL: http://dx.doi.org/10.1038/s41598-018-32165-z.

[55] T. Lévèque et al. "Enhancing the Area of a Raman Atom Interferometer Using a Versatile Double-Diffraction Technique". In: *Phys. Rev. Lett.* 103 (8 Aug. 2009), p. 080405. DOI: 10.1103/PhysRevLett.103.080405. URL: https://link.aps.org/doi/10.1103/PhysRevLett.103.080405.

[56] Albert Roura. "Circumventing Heisenberg's Uncertainty Principle in Atom Interferometry Tests of the Equivalence Principle". In: *Phys. Rev. Lett.* 118 (16 Apr. 2017), p. 160401. DOI: 10.1103/PhysRevLett.118.160401. URL: https://link.aps.org/doi/10.1103/PhysRevLett.118.160401.

[57] B. Dubetsky and M. A. Kasevich. "Atom interferometer as a selective sensor of rotation or gravity". In: *Phys. Rev. A* 74 (2 Aug. 2006), p. 023615. DOI: 10.1103/PhysRevA.74.023615. URL: https://link.aps.org/doi/10.1103/PhysRevA.74.023615.

[58] J. K. Stockton, K. Takase, and M. A. Kasevich. "Absolute Geodetic Rotation Measurement Using Atom Interferometry". In: *Phys. Rev. Lett.* 107 (13 Sept. 2011), p. 133001. DOI: 10.1103/PhysRevLett.107.133001. URL: https://link.aps.org/doi/10.1103/PhysRevLett.107.133001.

[59] R. Geiger et al. "Detecting inertial effects with airborne matter-wave interferometry". In: *Nature Communications* 2 (Sept. 2011), p. 474. DOI: 10.1038/ncomms1479.

[60] Achim Peters. "High precision gravity measurements using atom interferometry". PhD thesis. STANFORD UNIVERSITY, Oct. 1998.

[61] P. Cheinet. "Conception and realisation of a cold atom gravimeter". Theses. Université Pierre et Marie Curie - Paris VI, Mar. 2006. URL: https://tel.archives-ouvertes.fr/tel-00070861.

[62] Shao-Kai Wang et al. “Shift evaluation of the atomic gravimeter NIM-AGRb-1 and its comparison with FG5X”. In: *Metrologia* 55.3 (Apr. 2018), pp. 360–365. DOI: 10.1088/1681-7575/aab637. URL: https://doi.org/10.1088%2F1681-7575%2Faab637.

[63] R Karcher et al. “Improving the accuracy of atom interferometers with ultracold sources”. In: *New Journal of Physics* 20.11 (Nov. 2018), p. 113041. DOI: 10.1088/1367-2630/aaf07d. URL: https://doi.org/10.1088%2F1367-2630%2Faaf07d.

[64] R. Caldani et al. “Simultaneous accurate determination of both gravity and its vertical gradient”. In: *Phys. Rev. A* 99 (3 Mar. 2019), p. 033601. DOI: 10.1103/PhysRevA.99.033601. URL: https://link.aps.org/doi/10.1103/PhysRevA.99.033601.

[65] Peter Asenbaum et al. “Phase Shift in an Atom Interferometer due to Spacetime Curvature across its Wave Function”. In: *Phys. Rev. Lett.* 118 (18 May 2017), p. 183602. DOI: 10.1103/PhysRevLett.118.183602. URL: https://link.aps.org/doi/10.1103/PhysRevLett.118.183602.

[66] G. D’Amico et al. “Canceling the Gravity Gradient Phase Shift in Atom Interferometry”. In: *Phys. Rev. Lett.* 119 (25 Dec. 2017), p. 253201. DOI: 10.1103/PhysRevLett.119.253201. URL: https://link.aps.org/doi/10.1103/PhysRevLett.119.253201.

[67] Joel M. Hensley, Achim Peters, and Steven Chu. “Active low frequency vertical vibration isolation”. In: *Review of Scientific Instruments* 70.6 (1999), pp. 2735–2741. DOI: 10.1063/1.1149838. eprint: https://doi.org/10.1063/1.1149838. URL: https://doi.org/10.1063/1.1149838.

[68] Biao Tang et al. “A programmable broadband low frequency active vibration isolation system for atom interferometry”. In: *Review of Scientific Instruments* 85.9 (2014), p. 093109. DOI: 10.1063/1.4895911. eprint: https://doi.org/10.1063/1.4895911. URL: https://doi.org/10.1063/1.4895911.

[69] F Matichard et al. “Seismic isolation of Advanced LIGO: Review of strategy, instrumentation and performance”. In: *Classical and Quantum Gravity* 32.18 (Aug. 2015), p. 185003. DOI: 10.1088/0264-9381/32/18/185003. URL: https://doi.org/10.1088%2F0264-9381%2F32%2F18%2F185003.

[70] Min-Kang Zhou et al. “Note: A three-dimension active vibration isolator for precision atom gravimeters”. In: *Review of Scientific Instruments* 86.4 (2015), p. 046108.

DOI: 10.1063/1.4919292. eprint: https://doi.org/10.1063/1.4919292. URL: https://doi.org/10.1063/1.4919292.

[71] V. Schkolnik et al. "The effect of wavefront aberrations in atom interferometry". In: *Applied Physics B* 120.2 (Aug. 2015), pp. 311–316. ISSN: 1432-0649. DOI: 10.1007/s00340-015-6138-5. URL: https://doi.org/10.1007/s00340-015-6138-5.

[72] Min-kang Zhou et al. "Observing the effect of wave-front aberrations in an atom interferometer by modulating the diameter of Raman beams". In: *Phys. Rev. A* 93 (4 Apr. 2016), p. 043610. DOI: 10.1103/PhysRevA.93.043610. URL: https://link.aps.org/doi/10.1103/PhysRevA.93.043610.

[73] Vladan Vuleti ć et al. "Degenerate Raman Sideband Cooling of Trapped Cesium Atoms at Very High Atomic Densities". In: *Phys. Rev. Lett.* 81 (26 Dec. 1998), pp. 5768–5771. DOI: 10.1103/PhysRevLett.81.5768. URL: https://link.aps.org/doi/10.1103/PhysRevLett.81.5768.

[74] Andrew J. Kerman et al. "Beyond Optical Molasses: 3D Raman Sideband Cooling of Atomic Cesium to High Phase-Space Density". In: *Phys. Rev. Lett.* 84 (3 Jan. 2000), pp. 439–442. DOI: 10.1103/PhysRevLett.84.439. URL: https://link.aps.org/doi/10.1103/PhysRevLett.84.439.

[75] Philipp Treutlein, Keng Yeow Chung, and Steven Chu. "High-brightness atom source for atomic fountains". In: *Phys. Rev. A* 63 (5 Apr. 2001), p. 051401. DOI: 10.1103/PhysRevA.63.051401. URL: https://link.aps.org/doi/10.1103/PhysRevA.63.051401.

[76] Remi Geiger. "Airborne matter-wave inertial sensor". Theses. Université Paris Sud - Paris XI, Oct. 2011. URL: https://tel.archives-ouvertes.fr/tel-00651016.

[77] T. Berrada et al. "Integrated Mach–Zehnder interferometer for Bose–Einstein condensates". In: *Nature Communications* 4.1 (June 2013). DOI: 10.1038/ncomms3077. URL: https://doi.org/10.1038/ncomms3077.

[78] T. Kovachy et al. "Quantum superposition at the half-metre scale". In: *Nature* 528.7583 (Dec. 2015), pp. 530–533. DOI: 10.1038/nature16155. URL: https://doi.org/10.1038/nature16155.

Matteo Altorio **04/12/2019**

Sujet: Nouvelles techniques d'interférométrie atomique pour un gyrometre à atomes froids de grande aire de Sagnac

Résumé: Cette thèse décrit la mise en œuvre de nouvelles techniques d'interférométrie atomique améliorant la stabilité et l'exactitude d'un gyromètre à atomes froids situé au laboratoire SYRTE. Des transitions Raman stimulées permettent de séparer et recombiner les ondes atomiques. Une séquence de quatre impulsions lumineuses génère un interféromètre avec une aire Sagnac de 11 cm2.

Je présente la mise en œuvre d'un schéma d'interrogation entrelacé dans un interféromètre dont le temps d'interrogation est de 801 ms, dans lequel trois nuages atomiques sont interrogés simultanément résultant en une cadence de mesure de 3,75 Hz. Avec ce schéma, nous démontrons une sensibilité de 30 nrad/s/√Hz. Nous présentons ensuite des mesures de rotation dynamiques dans une plage jusqu'ici inexplorée pour un capteur à atomes froids.

Un biais important du capteur provient d'un couplage entre un désalignement relatif des miroirs rétroréfléchissant les faisceaux Raman et la trajectoire de l'atome. Une technique est introduite pour réduire ce biais au niveau de 1 nrad/s et atteindre une stabilité à long terme de 0,3 nrad/s qui représente l'état de l'art des gyromètres atomiques.

Le manuscrit décrit ensuite la première caractérisation du facteur d'échelle du gyromètre à l'aide de différentes techniques. En particulier, la mise en place d'une plateforme de rotation sous le capteur permet de faire varier la projection du vecteur rotation de la Terre sur l'interféromètre et donc de moduler le déphasage de rotation.

Les techniques présentées dans cette thèse ouvrent la voie à un test de l'effet Sagnac pour les ondes de matière avec une précision relative inférieure à 100 parties par million.

Mots clés: Interférométrie atomique, capteur inertiel, atomes froids, gyrometre, effet Sagnac

Subject: Novel atom interferometry techniques for a cold-atom gyroscope of large Sagnac area

Abstract: This thesis describes the implementation of new atom interferometry techniques to improve the stability and accuracy of a cold-atom gyroscope located at the SYRTE laboratory. Stimulated Raman transitions are used to split and recombine the atomic waves. A sequence of four light pulses generates an interferometer with a Sagnac area of 11 cm2.

I present the implementation of an interleaved interrogation scheme, where three atomic clouds are interrogated simultaneously in an atom interferometer featuring a sampling rate of 3.75 Hz and an interrogation time of 801 ms.

With this scheme we demonstrate a short-term sensitivity of 30 nrad/s/√Hz. We then present measurements of dynamic rotation rates in a so far unexplored range for a cold atom sensor.

An important bias of the sensor originates from a coupling between a relative misalignment of the mirrors which retro-reflect the Raman beams and the trajectory of the atom. A technique is introduced to reduce this bias at the level of 1 nrad·s-1 and to achieve a long-term stability of 0.3 nrad·s-1 which represents the state of the art for atomic gyroscopes.

The manuscript then describes the first characterization of the scale factor of the gyroscope using different techniques. In particular, the implementation of a rotation stage below the sensor enables us to vary the projection of the Erath rotation rate vector onto the interferometer area and therefore to modulate the rotation phase shift. The implementation of the techniques presented in this thesis pave paving the way to a test of the Sagnac effect for matter waves with a relative accuracy level below 100 parts per million.

Keywords: Atom interferometry, inertial sensor, cold atoms, gyroscope, Sagnac Effect